A STUDY OF MAGNETIC NON-LINEARITY AND FINITE

LENGTH EFFECTS IN SOLID IRON SUBJECTED TO   A

TRAVELLING MMF WAVE

by

ALAN LESLIE BOWDEN

Submitted for the Degree of Doctor of Philosophy

at

The University of Aston in Birmingham .

June 1973

CONTAINS

PULLOUTS

SUMMARY

This thesis describes an experimental and analytic study of the effects of magnetic non-linearity and finite length on the loss and field distribution in solid iron due to a travelling mmf wave.

In the first half of the thesis, a two-dimensional solution is developed which accounts for the effects of both magnetic non-linearity and eddy-current reaction; this solution is extended, in the second half, to a three-dimensional model.

In the two-dimensional solution, new equations for loss and flux/pole are given; these equations contain the primary excitation, the machine parameters and factors describing the shape of the normal B-H curve. The solution applies to machines of any air-gap length. The conditions for maximum loss are defined, and generalised torque/frequency curves are obtained. A relationship between the peripheral component of magnetic field on the surface of the iron and the primary excitation is given.

The effects of magnetic non-linearity and finite length are combined analytically by introducing an equivalent constant permeability into a linear three-dimensional analysis. The equivalent constant permeability is defined from the non-linear solution for the two-dimensional magnetic field at the axial centre of the machine to avoid iterative solutions. In the linear three-dimensional analysis, the primary excitation in the passive end-regions of the machine is set equal to zero and the secondary end faces are developed onto the air-gap surface.

The analyses, and the assumptions on which they are based, were verified on an experimental machine which consists of a three-phase rotor and alternative solid iron stators, one with copper end rings, and one without copper end rings; the main dimensions of the two

stators are identical. Measurements of torque, flux/pole, surface current density and radial power flow were obtained for both stators over a range of frequencies and excitations. Comparison of the measurements on the two stators enabled the individual effects of finite length and saturation to be identified, and the definition of constant equivalent permeability to be verified. The penetration of the peripheral flux into the stator with copper end rings was measured and compared with theoretical penetration curves.

Agreement between measured and theoretical results was generally good.

ACKNOWLEDGEMENTS

LIST OF CONTENTS

LIST OF SYMBOLS

MKSA units are used.

Many of the Equations referred to here may be found in a List of Important Equations at the end of the thesis.

$\left.\begin{array}{l} A \\ a \\ b \end{array}\right\}$ Constants used in the functional representation of the normal B-H curve.

B Flux density (T)

B_s Saturation flux density (T)

$\dot{C}_p$, $\dot{C}_{ph}$ Quantities including the primary permeability. (Chapters 2 and 9 respectively).

c Equation 4.56

D Stator bore (m)

$\dot{D}_s$, $\dot{D}_{sh}$ Quantities describing the effect of the secondary iron and eddy-currents. (Chapters 2 and 9 respectively).

d $\left\{\begin{array}{l} \text{A non-dimensional quantity equal to } \dfrac{(L - L_A)}{2L_A} \text{ (Chapter 9);} \\ \text{a constant in the Fröhlich equation (Equation 4.53).} \end{array}\right.$

E Electric field strength (V/m)

F MMF (A); force (N)

f Frequency (Hz)

g Air-gap length (m)

H Magnetic field strength (A/m)

h Harmonic order

I RMS current (A)

J Current density (A/m^2)

K Current loading (primary current sheet) (A/m^2)

K_b A function of b, Equations 4.24 and 4.25.

K_p Normalised power loss, Equation 4.49.

K_s Equation 6.16

$\dot{k}$ Equals $(\beta + j\gamma)$, in Chapter 2

$\dot{k}_h$ Equals $(\beta_h + j\gamma_h)$, in Chapter 9

L	Developed length of stator (Fig. 9.6).
L_A	Active length
L_s	Axial length of stator.
$\dot{M}, \dot{M}_h$	Quantities in linear field analysis (Chapters 2 and 9 respectively).
m	$\sqrt{\omega \mu_r \mu_o / \rho}$ (Appendix II)
P	Power (W/m^2)
P_A	Power, Agarwal's theory
P_L	Power, limiting non-linear theory.
p	Instantaneous power (W/m^2), pairs of poles.
Q, Q_n	Ratio of wave impedances at surface of secondary iron, Chapters 2 and 6 respectively, (non-dimensional).
q	$2\pi/\lambda$
R	Resistance (Ω)
R_a, r	Radius of bar, radial distance (m)
R_L	Finite length factor, Equation 9.35
S	Ratio of the peripheral and radial components of the magnetic field strength at the surface of the secondary.
$\dot{s}_h$	Equation 9.7.
T	Torque (N-m)
t	Time (s)
U	a quantity defining the shape of the waveform of magnetic field strength (Section 4.7)
V	Voltage (V)
v	Velocity (m/s), instantaneous voltage (v)
W_h	Hysteresis energy loss (J/m^3)
w	π/L
w_h	hw
x, y, z	Space co-ordinates
Z	Wave impedance (Ω)
α	$1/\delta$ (m^{-1})
α_n	$1/\delta_n$ (m^{-1})

β, β_h	attenuation coefficient, Chapters 2 and 9 respectively (m^{-1})
β_n	attenuation coefficient, Chapter 4 (non-dimensional)
γ, γ_h	phase change coeffients, Chapters 2 and 9 respectively (rad/m)
γ_n	phase change coefficient, Chapter 4 (non-dimensional)
Δ, Δ_n	functions of Q and Q_n respectively
δ	depth of penetration , $\sqrt{2\rho/\omega\mu_o\mu_r}$ (m)
δ_n	limiting depth of penetration (m)
δ_A	limiting depth of penetration, Agarwal's theory
δ_L	limiting depth of penetration, limiting non-linear theory
ε	phase change with depth (rad)
η	$q\alpha/\mu_s$
Θ	angle between primary mmf and radial flux density
Θ_h	hysteresis angle
λ	wavelength in the peripheral direction (m)
μ_o	permeability of vacuum ($4\pi \times 10^{-7}$ H/m)
μ_r	relative permeability (non-dimensional)
μ_e	constant equivalent permeability (non-dimensional)
μ_g	permeability of the surface of the secondary iron (H/m)
μ_p	primary relative permeability
μ_s	secondary relative permeability
ξ	wavefront depth (m), Section 3.5.1.1 $\dfrac{d\varepsilon}{dy}$, Appendix III
ρ	resistivity (Ωm)
τ	time constant (s)
Φ	Flux (Wb)
$\emptyset$	power factor angle
ω	angular frequency (rad/s)

SUBSCRIPTS

a	air-gap region
av	mean value
c	applied field, centre of the stator (Chapter 10)
e	eddy current
g	field components at the surface of the secondary ($y = g$)
h	quantities obtained by the three-dimensional analysis (Chapter 9)
m	quantities at maximum torque or loss
max	maximum value
n	present non-linear theory
o	surface value ($y = o$)
p	primary
r	reaction field
s	secondary
t	total
x, y, z	peripheral, radial and axial directions

SUPERSCRIPTS

.	complex quantities
~	complex conjugate
^	peak value of an alternating quantity.

ABBREVIATION

p.u.	per-unit

CHAPTER 1

INTRODUCTION

1.1 BACKGROUND TO THIS THESIS

In recent years, there has been renewed interest in the nature and calculation of eddy-current losses in solid-iron members of electrical machines; this has been due partly to the increase in losses due to a substantial increase in the specific loading of electrical machines[1] and to advances in numerical methods, computer technology and experimental techniques.

The determination of the electromagnetic fields within machines is, in most instances, an essential prerequisite to the calculation of eddy-current losses, and may be achieved either by calculation, using analytic or numerical methods, or by experimental investigation, or by a combination of the two.

Where the design objective is to obtain either the minimum or the maximum possible loss in the iron, a method of calculation is required which shows the relationship between the loss and the machine parameters; this can be achieved by using analytic methods. Analytic solutions for the electromagnetic fields in solid-iron regions of simple geometry are readily obtained if the permeability and resistivity of the iron are assumed constant, but not if these parameters are functions of space and time. Simplifying assumptions must therefore be made at the outset if solutions are to be obtained. A considerable number of approximate solutions have been published, yet few comparative studies of them have been made.

Numerical methods, although more suitable for the solution of non-linear differential equations, are cumbersome, and give particular rather than general solutions. They may, however, provide a standard

by which approximate analytic solutions may be judged.

In some recently published solutions of eddy-current losses in solid iron, a compromise has been sought between analytic and numerical methods, either by developing detailed equivalent circuits which may then be solved by digital computers[2,3], or by producing normalised loss charts by numerical techniques[4].

The quest for more detailed information on field distributions, either to verify or define the simplifying assumptions made in calculations has led to innovations in experimental technique and instrumentation. Although numerous investigations of the flux distribution in the air-gap regions of machines by means of search coils or semi-conductor devices have been reported, relatively few measurements of the flux distribution within solid iron regions or surface eddy currents[5,6] have been attempted.

To obtain analytic solutions for the finite and complex geometries of rotating electrical machines, further simplifying assumptions must be made and idealised mathematical models developed.

An idealised model of a rotating machine, which has a solid-iron secondary member, an air gap and a laminated-iron primary member, is shown in Fig. 1.1. overleaf. If currents are assumed to flow in the axial direction only, the magnetic field in the model is two-dimensional. This model has recently received much attention since it is applicable to studies, albeit introductory, of mmf, tooth ripple and negative-sequence losses in the solid poles of large synchronous machines.

Linear analytic solutions for the field distribution in the air-gap region and the solid-iron secondary of this model have been produced in which the primary excitation is represented by a current sheet, either on the surface, or within the body of the primary member.

solid-iron secondary member

air gap

current sheet
(primary excitation)

laminated-iron primary member
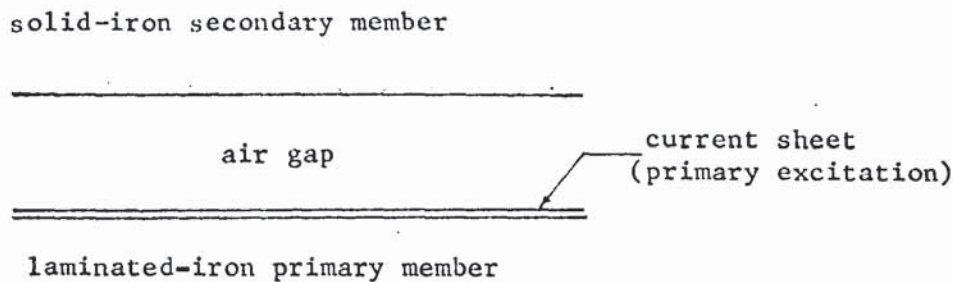
FIG. 1.1   An Idealised Model of a Rotating Machine

Published analytic solutions for this model, which consider
the secondary iron to be magnetically non-linear, either contain
expressions or values derived by the linear analysis, or assume that
the air-gap length is small;   no solution, it is believed, both
accounts successfully for magnetic non-linearity and gives expressions
for power loss and flux/pole which include the primary excitation and
air-gap length.

The determination of the loss in solid-iron secondary members of
finite length has been attempted by many authors, either by the intro-
duction of empirical or theoretically derived factors into solutions
for the two-dimensional model (Fig. 1.1), or by the development of
three-dimensional analyses;   in all cases, the magnetic permeability
of the secondary iron is assumed constant.

The effects of magnetic non-linearity on the loss in machines of
finite length are not fully understood.   Methods of extending two-
dimensional non-linear theories to three-dimensional models have been
suggested, but little theoretical or experimental justification   for

them has been given.   A brief review of publications on finite-length

effects is given in Chapter 9.

1.2   OUTLINE OF THIS THESIS

This thesis may be divided into two distinct, though related,

parts;

(i)   the derivation and verification of a non-linear analytic

solution for the field distribution, and loss, in rotating

electrical machines that may be represented by the idealised

model of Fig. 1.1, and

(ii)   a theoretical and experimental study of the combined effects

of magnetic non-linearity and finite length on the loss in

the solid iron.

It is believed that the analyses given in this thesis are an

advance on theories previously published.   Emphasis is placed on

the experimental verification of the analyses;   many of the experimental

techniques introduced by Davies[5] for the measurement of electromagnetic

fields in eddy-current couplings have been further developed for this

investigation.   Values obtained by the analytic solution are also

compared with those obtained by numerical methods.

1.2.1   The Non-linear Solution

A preliminary theoretical investigation of the two-dimensional

linear analysis of the multiregion model is made in Chapter 2.   Although

this analysis is well-known, certain aspects are extended to provide

a better understanding of the nature of the problem and a basis for the

development of the non-linear theory.

The variation in the value of the magnetic field strength at the

surface of the secondary, the eddy-current reaction mmf, and the

peripheral flux leakage in the air gap, are investigated for a range of

frequencies, ratios of pole-pitch to air-gap length, and permeabilities of both primary and secondary members. A study of the space-distribution of the magnetic field quantities in the air-gap region and the secondary iron leads to a physical interpretation of the field distribution in the model.

The relationship between the dimensions, frequency and physical constants of the model for maximum power loss in the secondary iron is defined; this relationship is also expressed both in terms of radial flux densities at the surface of the iron and the impedances of the model.

The non-linear theory for the multiregion model is developed, in two parts:

(i) Maxwell's equations, embodied in the diffusion equation, are solved for the solid-iron region, (Chapter 4), and

(ii) the electromagnetic field quantities on the surface of the secondary member are related to the primary excitation, (Chapter 6).

In the non-linear analysis for the solid-iron region the normal B-H curve is represented by the function $B = aH^b$. This function, previously used by Davies[7] in his theoretical treatment of the eddy-current coupling, is inserted into the solution of the diffusion equation for the magnetic field at an initial stage. Since the solution is for fundamental sinusoids only, the loss equation is modified to account for the loss due to saturation harmonics of flux density and magnetic field strength. The solution for the loss is expressed as a function of the surface components of the magnetic field; these quantities are related to the primary excitation by means of a solution for the air-gap region of the model. Equations for the loss and torque are thus derived as functions of the excitation, frequency, and

the parameters of the model. Equations are similarly derived for flux/pole and surface current density. The solutions apply to a machine with uniform air gap of any length.

Using the definition of maximum power loss in the secondary iron, obtained in terms of the impedances of the model (Chapter 2), expressions for peak torque and the frequency at peak torque are derived; generalised torque-frequency characteristics are given in terms of these quantities.

The theoretical results for the two-dimensional multiregion model are compared with measurements obtained from a specially designed experimental machine. This machine, described in detail in Chapter 7, consists of a polyphase rotor surrounded by a diametrically split solid-iron stator, which is fitted with copper end-rings[*] to reduce end-region effects and to enable the eddy-currents to pass across the split.

The amplitude of the circumferential component of flux density throughout the depth of the iron was investigated using search coils placed in grooves machined in one of the split surfaces. Measurements of torque, flux/pole, surface current density and power flow across the air gap were also made over a frequency range of 2-100 Hz and for primary excitations up to 20000 A/m. The radial flux density in the air gap and current density at the surface of the secondary, were measured along the axial length of the machine to determine the effectiveness of the copper end-rings.

The non-linear theory for the solid iron region was also verified by two additional investigations.

Firstly, measurements of loss and surface current density were made on a round bar through which an alternating current of known value

---

[*] For simplicity, this stator will be referred to throughout the thesis as 'the end-ring stator'.

was passed. (It is shown that the loss in this bar differs from that in a semi-infinite slab by less than 4% for surface magnetic field strengths up to 15000 A/m). The values of current density, being related to a known value of surface magnetic field strength, provided a cross-check with measured values on the experimental machine. The measured values of loss are compared with those predicted by the present non-linear theory and other analytic solutions.

Secondly, the diffusion equation was solved by numerical techniques to obtain the loss and the harmonic content of both the flux density and magnetic field strength waveforms at various depths into the iron. This was undertaken to evaluate the contribution of the saturation harmonics to the loss, and to provide flux density waveforms which could be compared with those measured within the depth of the iron.

1.2.2 Combined Effects of Non-linearity and Finite Length

To obtain an anlytical solution for machines with a solid-iron secondary member of finite length, a mathematical model is used in which an infinite number of identical machines are arranged end to end with alternate polarity. The permeability of the iron is assumed constant. Solutions for the field distribution throughout the model, the flux/pole and the loss, are developed in Chapter 9; they are applicable to machines whose active length is less than, or equal to, their overall length. A finite length factor, R_L, is defined which relates the loss or torque, for the model of finite length, to that for the linear two-dimensional model.

The loss in a solid-iron secondary which is both magnetically non-linear and of finite length is obtained by using the non-linear two-dimensional solution (Chapter 6) and R_L; this is made possible by equating the linear and non-linear two dimensional solutions, thereby deriving an equivalent constant permeability for the iron with which

R_L may be calculated.   In this method of loss calculation, it is
assumed that the equivalent constant permeability applies at all
points on the surface of the stator;   the validity of this assumption
is discussed in Chapters 9 and 10.

An experimental investigation was carried out on the experimental
machine for a continuous stator without copper end-rings[*].   Measurements,
similar to those on the copper end-ring stator, were made of surface
current density and radial flux density, with particular regard to
their variation over the axial length of the machine.   The torque
and flux/pole were also measured.

The finite length factor was obtained experimentally by comparing
measured torques for the end-ring and the continuous stator, at the
same frequency and excitation.   Considerable care was taken to
ensure that the parameters of both stators were the same.   The
measured values of torque and finite length factor agree well with
calculated values, and the variation of the finite length factor,
flux/pole and surface current density with frequency and excitation
is clearly demonstrated.

[*]   For simplicity, this stator will be referred to throughout the
thesis as 'the continuous stator'.

CHAPTER 2

THE TWO-DIMENSIONAL LINEAR ANALYSIS

2.1   INTRODUCTION

The two-dimensional linear analysis for the idealised model of
a rotating machine (Fig. 1.1) is discussed in this chapter.   The
permeabilities of both the primary and secondary iron are finite and
the primary excitation is considered to be equivalent to an infinitely
thin current sheet at the surface of the primary.

Equations for the field distribution in the solid iron secondary
and the air-gap region are given, and the variation in the magnitude
of the field quantities with the value of permeability of the primary
iron is discussed.

The reaction field of the eddy-currents at the surface of the
secondary is discussed, and relationships between its radial and
peripheral components and those of the applied and resultant fields
are derived.

The depth of penetration for maximum power transfer to the
secondary is defined, and found to occur when the modulus of the input
impedance to the secondary iron is equal to the modulus of the impedance
of the eddy-current field at the surface of the secondary.

Equations for the mmfs acting on the air-gap region are obtained,
and the conditions governing the magnitude of the peripheral flux in
the airgap are investigated.

2.2 THE MATHEMATICAL MODEL.

The model chosen for analysis, and its co-ordinate system are shown in Fig. 2.1.
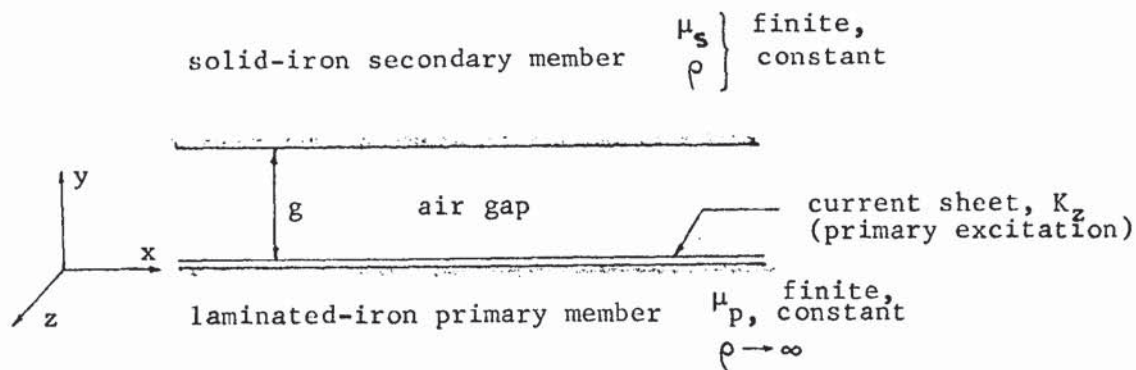
FIG. 2.1

The cylindrical geometry of the rotating machine has been developed so that the air-gap region is bounded by flat surfaces;

y is measured in the radial direction from the surface of

the primary member,

x is measured in the peripheral direction, and

z is measured along the axis of the machine.

The development of a rectilinear model is desirable as analytic solutions for the field distribution will therefore contain hyperbolic rather than Bessel functions and is permissible where the curvature of the cylindrical machine has little effect on the field distribution. Wood and Concordia[8] have compared the results of analyses for a rectilinear model and two and four-pole cylindrical models of the same rotor diameter. These solutions are presented in equivalent impedance form and, although obtained for a rotor iron permeability of 100, are applicable to any value of permeability provided the pole pitch >> depth of penetration (δ) (see Section 2.3). It may be concluded from their study that there is negligible error in assuming a rectilinear model if the ratio of the fundamental pole pitch to depth of penetration is greater than 15, and the ratio of fundamental pole pitch to air-gap length is greater than 12. The dimensions of most

machines, including turbogenerators, comply with these criteria. The complexity of the solution for the cylindrical model prevents more detailed comparisons, and the assumption of a rectilinear model may best be justified by correlating theoretical and experimental results, particularly if saturation of the iron is to be considered.

2.2.1   The Primary Member.

The primary iron is assumed to be composed of infinitely thin, insulated, laminations so that its resistivity in the axial direction is infinite.   The primary excitation is represented by an infinitely thin current sheet in which the current varies sinusoidally in both space and time.   It may be described by the expression:

$$K_z = \hat{K} \cos(\omega t - qx)$$
$$= \text{Re}\,(\hat{K}e^{-jqx}\,e^{j\omega t}) \qquad\qquad 2.1$$

where K_z is the line density of current in amperes per metre, ω is the angular frequency in radians per second, and $2\pi/q$ is the wavelength of the spatial current variation in the x direction.   Equation 2.1 represents a sinusoidally-distributed wave travelling in the + x direction at a uniform velocity, $v = \omega/q$ m/s.

Only the axial (z) component of current is assumed to flow within the boundaries of the model.   Reference is made to a current sheet rather than a primary mmf since it provides a simple boundary condition for solutions of the magnetic-field distribution;   mmfs may be obtained by integrating the solutions between required limits.   Saliency,slotting or other discontinuities are not included in the model, the surfaces of both primary and secondary being flat, smooth, and parallel to the z axis.

A more realistic representation of finite conductors in an axially-slotted structure may be obtained by placing the current sheet at a depth d into the primary iron rather than on its surface.[9]

While this clearly affects the leakage reactance of the current sheet, it has little effect on the field in the air gap and solid-iron regions of the model. (See Section 2.3).

2.2.2 The Secondary Member.

The secondary member is assumed to be composed of an isotropic, homogeneous ferromagnetic material whose electrical resistivity and magnetic permeability are constant.

Only currents in the axial (z) direction are considered to flow in the secondary member. The magnetic field throughout the model will therefore be two-dimensional having components in the x and y directions. In addition, it is assumed that crosspole, or peripheral currents, and radial currents exist only at $z = \pm \infty$ so that they have negligible effect on the magnetic-field distribution in the model.

The depth of the secondary member in the radial direction is assumed to be very great compared to the depth of penetration of the electromagnetic field. Finite length and finite depth effects are considered in Chapters 9 and 10.

2.3 SOLUTION FOR THE ELECTROMAGNETIC-FIELD COMPONENTS.

The specific assumptions made in Section 2.2 with regard to the configuration of Fig. 2.1 are:

(i) The permeabilities of both the primary ($\mu_o \mu_p$) and secondary members ($\mu_o \mu_s$) are constant in time and space.

(ii) The restivity of the primary member is infinite in the axial direction, while that of the secondary member is finite and constant. (ρ)

(iii) The surfaces of the primary and secondary members are smooth, flat, and parallel to the z axis.

(iv) Only the axial component of current exists in the

current sheet and secondary member.

Both primary and secondary members are assumed stationary so that the field moves at the same velocity relative to either member. The frequency, f, at which variations occur in all regions of the model is therefore,

$$f = \frac{\omega}{2\pi}$$

Maxwell's equations for electromagnetic fields in linear conducting media are:

$$\text{curl } \underline{H} = \underline{J} \qquad\qquad 2.2$$

$$\text{curl } \underline{E} = -\frac{\partial \underline{B}}{\partial t} \qquad\qquad 2.3$$

together with

$$\text{div } \underline{B} = 0 \qquad\qquad 2.4$$

$$\text{div } \underline{J} = 0 \qquad\qquad 2.5$$

$$\underline{B} = \mu\underline{H} \qquad\qquad 2.6$$

$$\underline{J} = \frac{1}{\rho} \cdot \underline{E} \qquad\qquad 2.7$$

From these equations and the assumptions (i) and (ii) in Section 2.2.,

$$\left. \begin{array}{l} \nabla^2 \underline{H} = 0 \\[2mm] \nabla^2 \underline{E} = 0 \end{array} \right\} \quad \begin{array}{c} \text{Primary iron} \\ \text{and} \\ \text{Air gap} \end{array} \qquad 2.8$$

$$\left. \begin{array}{l} \text{and } \nabla^2 \underline{H} = \dfrac{\mu_o \mu_s}{\rho} \cdot \dfrac{\partial \underline{H}}{\partial t} \\[4mm] \nabla^2 \underline{E} = \dfrac{\mu_o \mu_s}{\rho} \cdot \dfrac{\partial \underline{E}}{\partial t} \end{array} \right\} \quad \begin{array}{c} \text{Secondary} \\ \text{iron} \end{array} \qquad 2.9$$

As the current sheet varies sinuoidally in space and time, and the permeabilities and resistivities in all regions are constant, all field quantities will vary sinusoidally and may be described by,

$$\underline{H} = \text{Re } \dot{H} e^{j\omega t} \qquad\qquad 2.10$$

$$\underline{E} = \text{Re } \dot{E} e^{j\omega t} \qquad\qquad 2.11$$

where $\dot{H}$ and $\dot{E}$ are complex field vectors.

Equations 2.8 and 2.9 may thus be written :

$$\left. \begin{array}{l} \nabla^2 \dot{H} = 0 \\[2mm] \nabla^2 \dot{E} = 0 \end{array} \right\} \quad \begin{array}{c} \text{Primary iron} \\ \text{and} \\ \text{Air gap} \end{array} \qquad 2.12$$

$$\nabla^2 \dot{H} - \alpha(1 + j)\dot{H} = 0$$

$$\nabla^2 \dot{E} - \alpha(1 + j)\dot{E} = 0$$

Secondary iron   2.13

where

$$\alpha = \left(\frac{\mu_o \mu_s \omega}{2\rho}\right)^{\frac{1}{2}}$$

2.14

The general solution of equations 2.12 and 2.13 has the form

$$\dot{S}_u = (A_u e^{-jky} + G_u e^{jky})$$

2.15

where $\dot{k} = (q^2 + 2j\alpha^2)$ for the secondary iron,

2.16

$k = q$ for the primary iron and air gap,

2.17

$\dot{S}$ refers to any one of the field components $\dot{H}_x$, $\dot{H}_y$ or $\dot{E}_z$, and the suffix u refers to any one of the three regions, so that

  u = s for the secondary iron

  u = a for the air gap

and u = p for the primary iron.

The boundary conditions to be satisfied by the field components are:

(i) $\dot{H}_{xa} - \dot{H}_{xp} = -\hat{k} . e^{-jqx}$
at the primary current sheet (y = o)

(ii) $\dot{H}_x$ is continuous at y = g.

(iii) $\dot{B}_y$ is continuous at y = o and y = g

(iv) $\dot{B} \to 0$ as $y \to \pm \infty$

The coefficients A_u and G_u for each of the three regions may be found from the six boundary conditions.

The most important results are the field components in the air gap and solid-iron secondary. They are:

$$\dot{H}_{xa} = \frac{-\hat{k}}{\overline{C}_p} \left[e^{-qy} - \dot{D}_s e^{-qg} e^{q(y-g)} \right] e^{-jqx}$$

2.18

$$\dot{H}_{ya} = j \frac{\hat{k}}{\overline{C}_p} \left[e^{-qy} + \dot{D}_s e^{-qg} e^{q(y-g)} \right] e^{-jqx}$$

2.19

$$\dot{H}_{xs} = \frac{-2\,\hat{k}}{\overline{C}_p} \left[\frac{\dot{k}}{q\mu_s + \dot{k}} e^{-k(y-g)} e^{-qg} \right] e^{-jqx}$$

2.20

$$\dot{H}_{ys} = j \frac{2K}{\dot{C}_p} \left[\frac{q}{q\mu_s + k} \; e^{-k(y-g)} e^{-qg} \right] e^{-jqx} \qquad 2.21$$

$$\dot{J}_{zs} = -j \frac{4K}{\dot{C}_p} \left[\frac{\alpha^2}{q\mu_s + k} \; e^{-k(y-g)} \; e^{-qg} \right] e^{-jqx} \qquad 2.22$$

where
$$\dot{D}_s = \left[\frac{q\mu_s - k}{q\mu_s + k} \right] \qquad 2.23$$

and
$$\dot{C}_p = \frac{\mu_p + 1}{\mu_p} \left[1 - \frac{\mu_p - 1}{\mu_p + 1} \cdot D_s \cdot e^{-2qg} \right] \qquad 2.24$$

If the current sheet had been placed at a depth d into the primary iron rather than on its surface, it may be shown that the term e^{-qd} would appear in the numerator of equations 2.18 to 2.22.

Equations 2.18 to 2.22 describe the distribution of the sinusoidal components of the electromagnetic field in the radial and peripheral directions.   To arrange them into a more convenient form for analysis, let

$$\dot{k} = \beta + j\gamma \qquad 2.25$$

where, from equation 2.16

$$\beta = 1/\sqrt{2} \left[(q^4 + (2\alpha^2)^2)^{\frac{1}{2}} + q^2 \right]^{\frac{1}{2}} \qquad 2.26$$

$$\gamma = 1/\sqrt{2} \left[(q^4 + (2\alpha^2)^2)^{\frac{1}{2}} - q^2 \right]^{\frac{1}{2}} \qquad 2.27$$

Since β, γ, α and q have dimensions of (m^{-1}), equations 2.26 and 2.27 may be expressed in the following non-dimensional form:

$$\beta/\alpha = \left[(1 + q^4/4\alpha^4)^{\frac{1}{2}} + q^2/2\alpha^2 \right]^{\frac{1}{2}} \qquad 2.28$$

$$\gamma/\alpha = \left[(1 + q^4/4\alpha^4)^{\frac{1}{2}} - q^2/2\alpha^2 \right]^{\frac{1}{2}} \qquad 2.29$$

Equations 2.28 and 2.29 show that

$$\beta \to \gamma \to \alpha$$

and
$$\dot{k} \approx \alpha(1 + j), \text{ if } (q^2/2\alpha^2) << 1 \qquad 2.30$$

i.e. if the depth of penetration ($\delta = 1/\alpha$) is much less than the pole pitch (π/q). β/α and γ/α are plotted against $(q^2/2\alpha^2)$, in figure 2.2, which shows that for a 5% error in the equality, $\beta = \gamma = \alpha$, $(q^2/2\alpha^2) = 0.10.$

Since $\alpha = \left(\frac{\omega\mu_o\mu_s}{2\rho} \right)^{\frac{1}{2}}$, equation 2.30 may not be valid for small values of frequency and peameability.

2.4 EFFECT OF THE PRIMARY IRON

In equations 2.15 to 2.19 the permeability of the primary iron is contained only in the coefficient $\dot{C}_p$ (Equation 2.24) which therefore represents the contribution of the primary iron.

The second term within the square brackets of Equation 2.24 represents a current sheet positioned at a depth of 2g into the primary iron, which is the image of the combined effects of the secondary iron and eddy-current field.

The term $\left[\dfrac{\mu_p - 1}{\mu_p + 1} \right]$ is recognized as the image factor.[10]

Limiting values for $\dot{C}_p$ occur when $\mu_p = 1$ and $\mu_p \to \infty$.

When $\mu_p = 1$,

$$\dot{C}_p = \dot{C}_{p1} = 2, \qquad \left[\frac{\mu_p - 1}{\mu_p + 1} \right] = 0, \qquad \qquad 2.31$$

signifying that the image current-sheet disappears.

When $\mu_p \to \infty$,

$$\dot{C}_p = \dot{C}_{p\infty} = (1 - \dot{D}_s e^{-2qg}), \qquad \left[\frac{\mu_p - 1}{\mu_p + 1} \right] \to 1, \qquad 2.32$$

signifying complete reflection.

Due to the number of variables contained in equation 2.24, $\dot{C}_p$ is difficult to present in graphical form for values of μ_p between 1.0 and ∞ . Simplification of Equation 2.24 is possible if $\beta = \gamma = \alpha$, i.e. if the pole pitch >> depth of penetration, when the expression for $\dot{D}_s$ may be written in the non-dimensional form,

$$\dot{D}_s = \left[\frac{\eta - (1 + j)}{\eta + (1 + j)} \right] \qquad \qquad 2.33$$

$$\text{where} \quad \eta = \frac{q\mu_s}{\alpha} = \left(\frac{2\pi}{\lambda} \cdot \frac{\mu_s}{\alpha} \right) \qquad \qquad 2.34$$

Thus only three non-dimensional quantities exist in the expression for $\dot{C}_p$:-

the primary relative permeability; μ_p ,

the coefficient η ,

the ratio of air-gap length to pole pitch; (qg).

Fig. 2.3 shows the variation of the ratio $\dfrac{|\dot{C}_{p\omega}|}{|\dot{C}_p|}$ with primary permeability, μ_p, for a range of values of η and (qg). The difference between $|\dot{C}_p|$ and $|\dot{C}_{p\infty}|$ is significant only for permeabilities less than 500, and is greatest where both the air gap is small (qg small) and the eddy-current field is weak (η large). Since μ_p for practical machines is normally greater than 500, it will be assumed in all following discussions and derivations that $\mu_p \rightarrow \infty$. Where $\mu_p < 500$ the amplitudes of the field quantities must be multiplied by the appropriate value of $\dfrac{|\dot{C}_{p\infty}|}{|\dot{C}_p|}$.

Most previous authors[11,12,13] set $\mu_p \rightarrow \infty$ at the beginning of their analyses without qualification. Mukherji[14] included μ_p in his analysis but did not isolate or evaluate its effect on the field quantities. Lawrenson[9] calculated the value of the radial flux density $(\dot{B}_y)$ at the surface of the secondary for $\mu_p = 1000$ and found there was little change in $|\dot{B}_y|$ for values of $\mu_p > 500$. He did not obtain a general expression for the effect of the primary iron on the field distribution.

2.5 THE FIELD DISTRIBUTION IN THE SECONDARY MEMBER.

The electromagnetic-field components in the secondary member are described by Equations 2.20, 2.21 and 2.22. Substituting for k from Equation 2.30, (i.e. assuming $\beta = \gamma = \alpha$) and for C_p from Equation 2.32, (i.e. assuming $\mu_p \rightarrow \infty$), these equations may be written,

$$\dot{H}_{xs} = -\frac{\hat{K}(1+j)}{\dot{M}} e^{-\alpha(1+j)(y-g)} e^{-jqx} \qquad 2.35$$

$$\dot{H}_{ys} = j\frac{\hat{K}q}{\alpha\dot{M}} e^{-\alpha(1+j)(y-g)} e^{-jqx} \qquad 2.36$$

$$\dot{J}_{zs} = -j\frac{\hat{K}2\alpha}{\dot{M}} e^{-\alpha(1+j)(y-g)} e^{-jqx} \qquad 2.37$$

where $\dot{M} = \cosh qg \left[\eta . \tan h\, qg + 1 + j \right]$ \qquad 2.38

The attenuation and phase shift of the sinusoids with depth, y,

are described by the terms $e^{-\alpha y}$ and $e^{-j\alpha y}$, respectively. These terms also describe the penetration of a plane electromagnetic wave consisting only of the field components H_x and J_z. The assumption that $\beta = \gamma = \alpha$ thus implies that the radial component of the magnetic field has negligible effect on the penetration of flux and current density into the iron. This conclusion has great importance in considerations of power loss in the secondary, particularly if the iron is magnetically non-linear.

2.5.1 The Field Components on the Surface of the Secondary Member.

The amplitudes of the field components on the surface of the secondary $(y = g)$ and their phase angles with respect to the primary current sheet may be obtained from Equations 2.35 to 2.38 as,

$$\dot{H}_{xg} = - \frac{2 \hat{K}}{|\dot{M}|} \underline{/\dot{H}_{xg}} \; e^{-jqx} \qquad\qquad 2.39$$

$$\dot{H}_{yg} = \frac{q \hat{K}}{\alpha |\dot{M}|} \underline{/\dot{H}_{yg}} \; e^{-jqx} \qquad\qquad 2.40$$

$$\dot{J}_{zg} = \frac{2 \alpha \hat{K}}{|\dot{M}|} \underline{/\dot{H}_{yg}} \; e^{-jqx} \qquad\qquad 2.41$$

$$\text{where } |\dot{M}| = \cosh qg \left[(\eta \tanh qg + 1)^2 + 1 \right]^{\frac{1}{2}} \qquad\qquad 2.42$$

$$\underline{/\dot{H}_{xg}} = (90 - (\phi + \theta)) = \tan^{-1} \left[\frac{\eta \tanh qg}{\eta \tanh qg + 2} \right] \qquad\qquad 2.43$$

$$\text{and } \underline{/\dot{H}_{yg}} = (90 - \theta) = \tan^{-1} \left[\eta \tanh qg + 1 \right] \qquad\qquad 2.44$$

The phase angles θ and ϕ are shown in Fig. 2.4 below measured from the axis of the applied mmf (or primary pole axis).
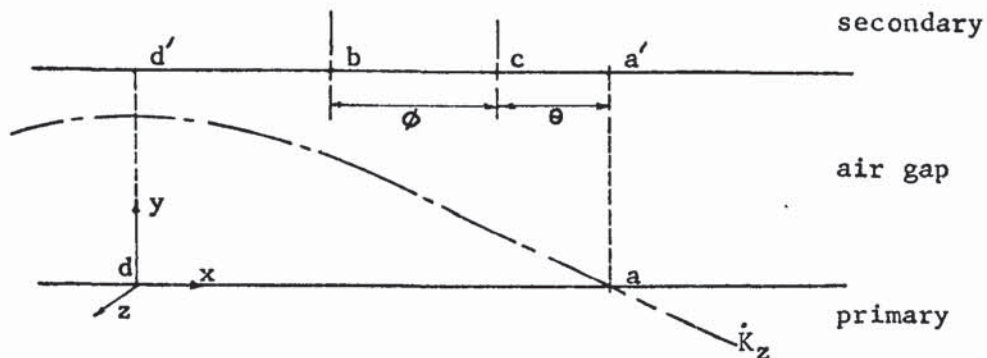
Fig. 2.4

At: $x = d$ Peak primary current density $\left.\begin{array}{}\\\end{array}\right\}$ $y = 0$

$x = a$ Peak primary mmf

$x = c$ Peak $\dot{H}_{yg}$ and $\dot{J}_{zg}$ $\left.\begin{array}{}\\\end{array}\right\}$ $y = g$

$x = b$ Peak $\dot{H}_{xg}$

From Equations 2.39 and 2.40,

$$\frac{\dot{H}_{xg}}{\dot{H}_{yg}} = - \frac{\sqrt{2}\,\alpha}{q} \cdot \underline{/-\phi} \,. \qquad\qquad 2.45$$

where $\tan \phi = 1$, so $\phi = 45^{\circ}$. $\qquad\qquad 2.46$

and thus $\quad 0 < \underline{/H}_{xg} < 45^{\circ}$

$\qquad\qquad 45^{\circ} < \underline{/H}_{yg} < 90^{\circ}$

Note also that $|\dot{H}|_{xg} > |\dot{H}|_{yg}$ since $\sqrt{2}\,\alpha > q$.

The variations of the angles $\underline{/\dot{H}}_{xg}$ and $\underline{/\dot{H}}_{yg}$ with the non-dimensional parameters η and (qg) are given in Fig. 2.5, showing the separate effects of change in the strength of the eddy-current field (α^{1}/η) and machine dimensions (qg). Change in the air-gap length has little effect on the phase angles if the eddy-current field is strong (η small) but considerable effect if it is weak (η large).

If $\beta \neq \gamma \neq \alpha$, but $\mu_p \to \infty$, then from Equations 2.21, 2.22, 2.23 and 2.24,

$$\tan \phi = \frac{\beta}{\alpha} \qquad\qquad 2.47$$

and from Fig. 2.5, $\phi > 45^{\circ}$, becoming 90° when $\left.\begin{array}{}\gamma\\\alpha\end{array}\right\}^{Jz} \to 0$, so that H_y occurs at $x = a$ and H_x at $x = o$ in Fig. 2.4 (on previous page).

2.5.2 <u>Resultant Magnetic Field Strength in the Secondary</u>

The resultant $\dot{H}$ is obtained by combining $\dot{H}_x$ and $\dot{H}_y$, given by Equations 2.35 and 2.36 respectively, and may be described by lines of constant $|\dot{H}|$ as shown in Fig. 2.6 for the condition $\sqrt{2}\alpha > q$. The line cc' is the spatial locus of the current-density maxima throughout the depth of the iron, cc' and all lines parallel to it are therefore isophasals. The variation of $\dot{H}$ at any point may be obtained by considering this field pattern to travel in the x

direction with a velocity of $v = \frac{\omega}{q}$.

2.6 POWER AND TORQUE.

The mean power flow per unit surface area is given by the complex Poynting vector, P,

$$\text{where } P = \tfrac{1}{2} \text{ Re}(E \times \tilde{H})$$

($\sim$ denotes complex conjugate).

The mean power flow into the solid iron secondary, i.e. in the radial or y direction, at any depth (y - g) is thus

$$P_y = \tfrac{1}{2} \text{ Re } (\dot{E}_{zs} \tilde{H}_{xs})$$

giving, from Equations 2.35 and 2.37

$$P_y = \frac{K^2 . \alpha . \rho}{M^2} . e^{-2 \alpha (y - g)} \quad \text{if} \begin{cases} \sqrt{2} \, \alpha > q \\ \mu_p \to \infty \end{cases} \qquad 2.48$$

Note that the index of the exponential term $e^{-2 \alpha (y - g)}$, is twice as great as that for the magnetic or electric field, so that in fact only 14% of the total power into the iron penetrates beyond the depth of penetration δ .

The power into the iron is dissipated as heat so that the total loss in the iron per unit area is given by,

$$P = P_y \Big]_{y = g} = \tfrac{1}{2} \text{ Re } (\dot{E}_{zg} . \dot{H}_{xg})$$

$$= \frac{\hat{K}^2 . \alpha \rho}{|\dot{M}|^2} \qquad 2.49$$

Since both the primary and secondary members are considered to be stationary, the total loss must equal the total power transferred across the air gap so that, in rotating machine terms, $P = \omega_{me} T$, where T is the torque per unit area, and ω_{me} is the mechanical angular velocity of the rotating electromagnetic fields relative to primary or secondary member ($\omega_{me} = \frac{\omega}{p}$).

$$\text{Thus } T = \frac{\hat{K}^2 \, \alpha \rho p}{|\dot{M}|^2 . \omega} \qquad 2.50$$

2.6.1 Maximum Loss and Torque

Substitution of Equation 2.42 into Equation 2.50 gives

$$ T = \frac{\hat{K}^2 p \mu_o \mu_r}{2\cosh^2 qg} \left[\frac{1}{\dfrac{q^2 \mu_s^2}{\alpha} \tanh^2 qg + 2\alpha + 2q\mu_s \tanh qg} \right] \qquad 2.51 $$

The term within the square bracket shows that

when $\alpha \to 0$, $T \to 0$,

and when $\alpha \to \infty$, $T \to 0$,

so that between these limits there must be a maximum torque.
Differentiating Equation 2.51 with respect to α and equating the
resultant expression to zero, the maximum torque is found to occur

$$ \text{when} \quad \alpha_m = \frac{q\mu_s}{\sqrt{2}} \tanh qg \qquad\qquad 2.52a $$

$$ \text{and} \quad \delta_m = \frac{1}{\alpha_m} \qquad\qquad 2.52b $$

where the suffix m denotes the value of any quantity at
maximum torque, δ_m being the required depth of penetration for
maximum power transfer to the secondary. The maximum torque
per unit surface area, T_m, is found by substituting Equation 2.52a
into Equation 2.51:

$$ T_m = \frac{p\mu_o \hat{K}^2}{q \sinh qg \cosh qg} \left[\frac{1}{2\sqrt{2}\,(2 + \sqrt{2})} \right] \qquad 2.53 $$

and the maximum loss in the secondary at the angular frequency 'ω'

$$ \text{is} \quad P_m = \frac{\omega T_m}{p} \qquad\qquad 2.54 $$

Note that T_m and P_m are independent of the secondary parameters
μ_s and ρ, being dependent only on the parameters and dimensions
of the air-gap region. The equation for torque (Equation 2.53)
can be considerably simplified by expressing it in terms of the non-
dimensional quantities T/T_m and α/α_m so that from Equations 2.51,
2.52 and 2.53, the normalised torque, or normalised loss at constant
frequency is,

$$ \frac{T}{T_m} = \frac{P}{P_m} = \frac{2 + \sqrt{2}}{\dfrac{\alpha}{\alpha_m} + \dfrac{\alpha_m}{\alpha} + \sqrt{2}} \qquad 2.55 $$

Writing $Q = \dfrac{\alpha}{\alpha_m}$, 2.56

Equation 2.55 becomes

$$\frac{T}{T_m} = \frac{P}{P_m} = \frac{2 + \sqrt{2}}{Q + Q^{-1} + \sqrt{2}} \qquad 2.57$$

Q may be defined in terms of the machine parameters by substituting Equations 2.14 and 2.52a in 2.56,

$$Q = \frac{1}{q \ \tanh qg} \cdot \left(\frac{\mu_o \ \omega}{\rho \ \mu_s}\right)^{\frac{1}{2}} \qquad 2.58$$

Equation 2.57 was obtained by Davies[7] in developing a general theory for eddy-current couplings, although his expression for Q differs from Equation 2.58 since it contains terms describing the magnetic non-linearity of the secondary iron.

Since Q = 1 for maximum torque (or loss) the angular frequency at maximum torque, ω_m, may be obtained from Equation 2.58 as

$$\omega_m = \frac{q^2 \ \mu_s \ \rho}{\mu_o} \ \tanh^2 qg \qquad 2.59$$

The torque, T, may be described in terms of Q by substituting Equation 2.53 into 2.57, so that,

$$T = \frac{P \ \mu_o \ K^2}{2 \sqrt{2} q \ \cosh qg \ \sinh qg} \cdot \Delta \qquad 2.60$$

where $\quad \Delta = \dfrac{1}{Q + Q^{-1} + \sqrt{2}} \qquad 2.61$

2.7 THE FIELD IN THE AIR-GAP REGION

2.7.1 General

The analysis of machines whose secondary members contain discrete conductors is usually concerned only with the air-gap region, where the fields may be superposed. Two initial assumptions are normally made; firstly, that the permeability of the primary and secondary are much greater than unity, and secondly, that there is negligible peripheral

flux leakage in the air gap. It is thus possible to consider the interaction of the mmf's due to the primary and secondary currents in the air-gap region only. A primary aim of this section is to investigate the possibility of such an analysis for the configuration of Fig. 2.1.

2.7.2 Eddy-Current Reaction

The magnetic field quantities defined in the analysis so far are resultant quantities, i.e. they represent the combined effects of the applied field of the primary current sheet and the reaction field of the eddy-currents. Thus at any point in the model of Fig. 2.1,

$$\dot{H} = \dot{H}_c + \dot{H}_r \hspace{4cm} 2.62$$

where, $\dot{H}$ is the resultant field.

$\dot{H}_c$ is the applied field of the current sheet

$\dot{H}_r$ is the reaction field of the eddy-currents.

In magnetically linear media this equation may be applied to the peripheral (x) or radial (y) field components.

The peripheral and radial components of the magnetic field in the air-gap region, are described by Equations 2.18 and 2.19 respectively. They contain two terms, the first describes the field of the primary excitation if no secondary iron were present, and the second, containing the coefficient $\dot{D}_s$, defines the contribution of the eddy currents plus the secondary iron. The contribution of the second term to the field in the air gap is equivalent to replacing the secondary by a current sheet of value $\dot{D}_s$ positioned a distance g into the secondary iron. Stoll and Hammond[15] examined the field of this equivalent current sheet for a model without primary iron ($\mu_p = 1$, and $\dot{C}_p = 2$), but did not separate the contributions of secondary iron and eddy currents.

Only Rüdenberg,[16] to the author's knowledge, has solved Maxwells equations for the secondary iron making the initial assumption that the resultant field is equal to the applied plus the reaction fields. These fields may be derived more simply however, from the expressions for the resultant field and Equation 2.62.

2.7.2.1 The Peripheral Field Components

The resultant peripheral magnetic field on the surface of the secondary($y = g$) is obtained from Equation 2.35 as,

$$\dot{H}_{xg} = - \frac{\hat{K}\ (1 + j)\ e^{-jqx}}{\cosh qg\ (\eta\tanh qg + 1 + j)} \cdot \begin{cases} \text{if}\sqrt{2}\,\alpha > q \\ \text{and}\ \mu_p \to \infty \end{cases} \qquad 2.63$$

When $\rho \to \infty$, $\alpha \to 0$, and from Equation 2.22, $\dot{J}_{zs} \to 0$

Thus from Equation 2.16

$$\dot{k} \to q \quad \text{if there is no eddy current field.} \qquad 2.64$$

Substituting Equation 2.64 into 2.18, 2.23 and 2.24, the applied field is obtained,

$$\dot{H}_{xgc} = \frac{-\hat{K}.e^{-jqx}}{\cosh qg\ (\mu_s.\tanh qg + 1)} \qquad 2.65$$

The reaction field on the surface, $\dot{H}_{xgr}$, may be obtained by substitution of Equations 2.63 and 2.65 in Equation 2.62. The resultant expression is complicated and, for simplicity, only three specific cases are noted;

(i) If, in Equation 2.65, $\mu_s . \tanh qg \gg 1$

and in Equation 2.63, $\eta.\tanh qg \ll 1$, i.e. the eddy-current field is strong, then,

$$\dot{H}_{xg} \gg \dot{H}_{xgc}, \text{ and so } \dot{H}_{xgr} \to \dot{H}_{xg}$$

(ii) If in Equation 2.65, $\mu_s \tanh qg \ll 1$

and in Equation 2.63, $\eta \tanh qg \ll 1$, i.e. the eddy-current field is strong,then,

$$\dot{H}_{xgc} \to \dot{H}_{gx}, \text{ and so } \dot{H}_{xgr} \to 0$$

This condition represents complete reflection of the eddy-current field in the primary iron. It would occur, for example, in a short air-gap machine having a solid copper secondary. ($\mu_s = 1$)

(iii) If in Equation 2.65 $\mu_s \tanh qg = 1$,

and in Equation 2.63, $\eta \tanh qg << 1$,

then $\dot{H}_{xgr} \rightarrow \dot{H}_{xgc} \rightarrow \dot{H}_{xg}/2$

This condition may exist in a large air-gap machine having a solid copper secondary. ($\mu_s = 1$).

Case (i) clearly applies to machines having solid iron secondaries, where $\mu_s \tanh qg >> 1$. $\Big($ It should be noted that μ_s in Equation 2.65 is the value of the secondary-iron permeability in the absence of eddy currents, which, in all probability, will be much greater than the value of μ_s in the equation for the resultant field (Equation 2.63)$\Big)$

2.7.2.2 The Radial Field Components

The resultant radial flux density at the surface of the secondary ($y = g$) is given by Equations 2.36, 2.38 and 2.6 as

$$\dot{B}_{yg} = \frac{j \eta \cdot \tanh qg \cdot \mu_o \cdot \hat{K} \cdot e^{-jqk}}{\sinh qg \cdot (\eta \tanh qg + 1 + j)} \left\{ \begin{array}{l} \text{if } \sqrt{2}\,\alpha > q \\ \text{and } \mu_p \rightarrow \infty \end{array} \right. \qquad 2.66$$

(The radial flux density is considered here as it is continuous across the air/iron boundary).

The flux density at the surface of secondary, $\dot{B}_{ygc}$, due to the applied field is found by substituting Equation 2.64 in Equation 2.21,

$$\dot{B}_{ygc} = \frac{j \hat{K} \cdot e^{-jqx} \cdot \mu_o \mu_s}{\cosh qg \, (\mu_s \tanh qg + 1)}$$

and $\qquad \dot{B}_{ygc} = \dfrac{j \mu_o \hat{K} \cdot e^{-jqx}}{\sinh qg}$, if $\mu_s \tanh qg >> 1$. $\qquad 2.67$

Thus, the flux density at the surface of the secondary due to the eddy currents, is from Equations 2.62, 2.6, 2.66, and 2.67,

$$\dot{B}_{ygr} = \frac{-j(1+j)\mu_o\hat{K}.e^{-jqx}}{sinhqg\left(\eta\ tanhqg + 1 + j\right)} \qquad 2.68$$

Comparison of Equation 2.68 with Equation 2.63 for $\dot{H}_{xg}$ shows that

$$\dot{B}_{ygr} = j\ \frac{\mu_o}{tanhqg}\ .\ \dot{H}_{xg} \qquad if \begin{cases} \mu_p \to \infty \ and\ \sqrt{2}\ \alpha \ > \ q \\ \\ \mu_s\ tanhqg\ >>1 \end{cases} \qquad 2.69$$

An equation of similar form may be obtained for the flux density at the surface of the primary current sheet (y = 0) in the absence of eddy currents. From Equation 2.19 when $\dot{k} = q$ (Equation 2.64),

$$\dot{B}_{yoc} = j.\frac{\mu_o\ \hat{K}}{tanhqg} \qquad if \begin{cases} \mu_p \to \infty \\ \\ \mu_s\ tanhqg\ >>1 \end{cases} \qquad 2.70$$

Thus the total effect of the eddy currents may be represented by an equivalent current sheet on the surface of the secondary whose line current density is equal to $\dot{H}_{xg}$.

From Equations 2.66 and 2.68

$$\frac{\dot{B}_{yg}}{\dot{B}_{ygr}} = -\ \frac{\eta\ tanhqg}{(1+j)} \qquad 2.71$$

and

$$\frac{|\dot{B}_{yg}|}{|\dot{B}_{ygr}|} = \frac{\eta tanhqg}{\sqrt{2}} = \frac{1}{Q} \quad (Equations\ 2.58\ and\ 2.34) \qquad 2.72$$

so that for peak torque or maximum power transfer, i.e. when Q = 1

$$|\dot{B}|_{yg} = |\dot{B}|_{ygr} \qquad 2.73$$

Also from Equations 2.67 and 2.63

$$\frac{|\dot{H}|_{ygc}}{|\dot{H}|_{xg}} = \frac{Q}{tanhqg} \qquad 2.74$$

where $\dot{H}_{ygc}$ is the radial field strength on the air-gap side of the surface of the secondary (y = g).

The vector diagram representing the relationship $\dot{B}_{yg} = \dot{B}_{ygr} + \dot{B}_{ygc}$ may be constructed from Equations 2.69, 2.72, 2.63, 2.67 and is shown in Fig. 2.7

2.7.2.3   Impedance Relationships

The input impedance to the secondary iron (at y = g) is

defined as,

$$Z_y \Big]_{y = g} = Z_{yg} = \frac{\dot{E}_{zg}}{\dot{H}_{xg}} \qquad 2.75$$

and from equations 2.35 and 2.37,

$$\dot{Z}_{yg} = \rho \alpha \ (1 + j)$$

or $\quad \dot{Z}_{yg} = \sqrt{2} \rho \alpha \ \underline{/45^{\circ}} \qquad 2.76$

The radial flux density at the surface of the secondary due to the eddy currents, $\dot{B}_{ygr}$, will induce an emf in the surface of the secondary equal to

$$\dot{E}_{zgr} = j \ \frac{\mu_o \ \omega}{q \tanh qg} \cdot \dot{H}_{xg} \qquad 2.77$$

If $\mu_s \tanh qg \gg 1$ and $\eta \tanh qg \ll 1$ then $\dot{H}_{xgr} \approx \dot{H}_{xg}$, and the

impedance of the eddy-current field at the surface of the secondary

is $\quad \dot{Z}_{ygr} = \frac{\dot{E}_{zgr}}{\dot{H}_{xg}} = j \ \frac{\mu_o \cdot \omega}{q \tanh qg} \qquad 2.78$

The ratio of the moduli of $\dot{Z}_{yg}$ and $\dot{Z}_{ygr}$ is

$$\frac{|\dot{Z}_{yg}|}{|\dot{Z}_{ygr}|} = \frac{\sqrt{2} \rho \alpha q}{\mu_o \omega} \ \tanh qg \qquad 2.79$$

substituting $\omega = \frac{2\alpha^2 \rho}{\mu_o \mu_s}$ (Equation 2.14), into Equation 2.78,

$$\frac{|\dot{Z}_{yg}|}{|\dot{Z}_{ygr}|} = \frac{\eta \tanh qg}{\sqrt{2}} = \frac{1}{Q} \qquad 2.80$$

Thus, maximum power is transferred when $|\dot{Z}_{yg}| = |\dot{Z}_{ygr}|$ i.e. when the impedances are 'matched' - a familiar requirement in circuit theory. $|\dot{Z}_{ygr}|$ is seen to be purely reactive (Equation 2.77), being a function only of the air-gap permeance, since both $\mu_s \gg 1$ and $\mu_p \gg 1$, and the impedance of the primary current sheet is equal to $\dot{Z}_{ygr}$ if $\mu_p \gg 1$ and $\mu_s \gg 1$, which may be seen by comparing Equations 2.69 and 2.70. Both impedances are therefore similarly related to the rate at which energy is stored in the air-gap region. Maximum power is transferred across the air gap when the rate of change of energy

stored in the air gap is equal to the rate energy is transferred to the secondary iron, a condition implied by Equation 2.80. Since it is assumed that $\dot{H}_{xg} = \dot{H}_{xgr}$, if the primary current circuit was opened, the decay of the eddy-current field would be governed by the same equality, i.e. that $|\dot{Z}_{yg}| = |\dot{Z}_{ygr}|$, and the time constant of the decay is therefore given by,

$$\tau_s = \frac{L_s}{R_s} \qquad \qquad 2.81$$

where, from Equation 2.78, $L_s = \dfrac{\mu_o}{q \tanh qg}$ $\qquad$ 2.82

and from Equations 2.76 and 2.56, $R_s = \rho \alpha_m$ $\qquad$ 2.83

since R_s is the resistance of the iron when $Q = 1$.

Thus from Equations 2.82 and 2.83,

$$\tau_s = \frac{\mu_o}{q^2 \mu_s \rho \tanh^2 qg} \qquad \qquad 2.84$$

2.7.3 Peripheral Flux Leakage.

In the absence of eddy currents, peripheral flux leakage in the air gap occurs due to the sinusoidal distribution of the applied mmf around the circumference of the machine and thus $|\dot{B}_{yg}| < |\dot{B}_{yo}|$. Eddy-current reaction affects the value of the peripheral flux leakage and causes the radial flux density to be shifted from the axis of the applied mmf by the spatial angle Θ . In addition, due to the exponential decay of both the eddy-current reaction (from the surface of the secondary) and applied fields (from the surface of the primary) across the air gap, the angle Θ varies with radial distance from the surface of the primary. The resultant curvature of constant $|\dot{B}|$ lines in the air gap is shown in Fig. 2.6.

The effect of the eddy-current reaction on the magnetic field in the air gap is shown in Fig. 2.8 and 2.9. In Fig. 2.8 the ratio of the flux density at the surface of the secondary $|\dot{B}_{yg}|$ to that at

the surface of the primary $|\dot{B}_{yo}|$ is plotted against η for several values of (qg). The curves were computed from Equation 2.19, and clearly show that the peripheral flux leakage increases with eddy-current reaction (α $^1/_\eta$), particularly for large air gaps. Where $\eta > 10$ the eddy-current field has negligible effect on the peripheral flux leakage. Fig. 2.9 gives $\underline{/\dot{B}}_{yo}/ \underline{/\dot{B}}_{yg}$ against η for various values of (qg). At small values of (qg) there is little difference between the angles, while at large values of (qg) there is considerable difference if the eddy-current reaction is large. ($\dot{\eta}$ small).

It should be remembered that the calculated value of peripheral flux-leakage is less for the equivalent rectilinear model than for the cylindrical model having a solid iron rotor. Thus the calculated loss may be correspondingly greater in the rectilinear model, and significantly so if both the air gap and armature reaction are large.

2.7.4 The MMF Diagram

Consider the path aa' d'd in Figure 2.6 which encloses the primary current sheet but no secondary eddy currents. Applying Ampere's circuital law round this path,

$$\int \dot{K}_z.dx = \dot{F}_g - \int \dot{H}_{xg}.dx \qquad \qquad 2.85$$

where F_g is the resultant mmf acting on the air gap.

Let $\dot{F}_c = \int \dot{K}_z dx$, which is the mmf of the current sheet, $\qquad$ 2.86

and $\dot{F}_r = \int \dot{H}_{xg} dx$, which is the mmf of the eddy current $\qquad$ 2.87

field, if μ_s $\tanh qg \gg 1$ and $\eta \tanh qg \ll 1$

(Section 2.7.2.1),

so that Equation 2.85 becomes,

$$\dot{F}_c = \dot{F}_g - \dot{F}_r \qquad \qquad 2.88$$

Solving the integrals in Equations 2.86 and 2.87,

$$\dot{F}_r = j\frac{\dot{H}_{xg}}{q} \qquad\qquad 2.89$$

$$\dot{F}_c = j\frac{\hat{K}}{q} \qquad\qquad 2.90$$

so that from Equations 2.89, 2.90, Equation 2.88 may be written

$$\dot{F}_g = {}^j\!/_q \left[\hat{K} + \dot{H}_{xg} \right] \qquad\qquad 2.91$$

The modulus of $\dot{F}_g$ is obtained in terms of $\dot{F}_r$ from Equations 2.35, 2.91 and 2.89 (after some manipulation) as,

$$|\dot{F}_g| = \frac{|\dot{F}_r|}{2} \left[(\eta \tanh qg \cosh qg + (\cosh qg - 1))^2 + (\cosh qg - 1)^2 \right]^{\frac{1}{2}} \quad 2.92$$

Thus, if the ratio of air-gap length to pole pitch is very small, i.e., $qg \ll 1$, then, $\cosh qg \to 1$,

and $\tanh qg \to qg$

so that $\dfrac{|\dot{F}_g|}{|\dot{F}_r|} \simeq \dfrac{qg}{2}$, if $qg \gg 1$, $\qquad\qquad 2.93$

and from Equation 2.72,

$$\frac{|\dot{F}_g|}{|\dot{F}_r|} \quad \frac{|B_{yg}|}{|B_{ygr}|} = \frac{1}{Q} \text{, if } qg \gg 1. \qquad\qquad 2.94$$

Also, from Equations 2.69 and 2.89, and 2.67 and 2.90,

$$\left.\begin{aligned}\dot{B}_{ygr} &= \frac{\mu_o \dot{F}_r}{g} \\[2em] \dot{B}_{ygc} &= \frac{\mu_o \dot{F}_c}{g}\end{aligned}\right\} \text{ if } \left\{\begin{aligned}\mu_s \; &qg \gg 1 \\ &qg \ll 1 \\ \mu_p &\to \infty \\ \sqrt{2}\alpha &> q\end{aligned}\right. \qquad 2.95$$

Thus, the vector diagram relating the flux densities at the surface of the secondary, given in Fig. 2.7, may be converted to an mmf diagram from Equation 2.95 and Equation 2.94 if $qg \ll 1$.

An expression for $|\dot{F}_r|$ in terms of $|\dot{F}_c|$ may be obtained from Equation 2.39 using Equations 2.88 and 2.87 as,

$$|\dot{F}_r| = \frac{\sqrt{2}.|\dot{F}_c|}{\cosh qg \left[(\eta \tanh qg + 1)^2 + 1 \right]^{\frac{1}{2}}}$$

which may be expressed in terms of Q from Equation 2.72 as

$$|\dot{F}_r| = \frac{|\dot{F}_c| \cdot Q}{\left[Q^2 + \sqrt{2}Q + 1 \right]^{\frac{1}{2}} \cosh qg} \qquad 2.96$$

An approximate form of Equation 2.96 is obtained if it is assumed that $qg \ll 1$.

The non-dimensional quantity $\dfrac{|\dot{F}_r|}{|\dot{F}_c|}$, derived from Equation 2.96, is shown plotted against η for a range of (qg) values in Fig. 2.10. The error in the calculation of $|\dot{F}_r|/|\dot{F}_c|$, due to the use of the approximate form of Equation 2.96 (qg $\ll$ 1), is shown by comparison of the full, and dotted curves plotted for qg = 1.0 and qg = 0.33. When the eddy-current field is weak (η large) there is little error for all practical values of (qg). When the eddy-current field is strong, (η small), there is considerable error for large values of (qg), due to the greater effect of the coshqg terms in Equation 2.96 when η is small (or, the (coshqg - 1) terms in Equation 2.92).

The power loss or torque, may also be expressed in terms of $|\dot{F}_r|$. By substituting Equations 2.88, 2.96 and 2.42 into Equation 2.50, the torque is obtained as

$$T = \frac{|\dot{F}_r|^2 \alpha.\rho.q^2.p}{2\omega} \qquad 2.97$$

2.8 CONCLUSIONS

The linear two-dimensional solution of the electro-magnetic field in the configuration of Fig. 2.1 has been discussed in this chapter.

The permeability of the primary iron is contained in a single, complex term $\dot{C}_p$. It has been shown (Section 2.4), that the values of the field quantities do not change for $500 < \mu_p < \infty$.

When $\sqrt{2}\alpha > q$, $\beta \simeq \gamma \simeq \alpha$, and the field equations can be simplified; this condition implies that $\dfrac{\partial \dot{H}_x}{\partial y} >> \dfrac{\partial \dot{H}_y}{\partial x}$ and $|\dot{H}_x| > |\dot{H}_y|$, so that the field distribution within the iron approximates to that of a plane electro-magnetic wave.

In Sections 2.5 to 2.7 inclusive, it was assumed that both $\mu_p \rightarrow \infty$ and $\sqrt{2}\alpha > q$.

An equation for the torque per unit area was obtained (Section 2.6), and differentiated to define the maximum torque per unit area, T_m, and the depth of penetration, $\delta_m (= 1/\alpha_m)$, at which it occurs. Both torque per unit area and α are normalised to a base of T_m and α_m respectively; the normalised value of α is given by Q, so that maximum torque occurs when $Q = 1$.

Q is found to be equal to the ratio of the moduli of the input impedance of the secondary iron, $|\dot{Z}|_{yg}$, and the impedance of the eddy-current field at the surface of the secondary $|\dot{Z}|_{ygr}$, provided $\mu_s \tanh qg >> 1$ and $\eta \tanh qg << 1$. Since $\dot{Z}_{ygr}$ is a function of frequency and the air-gap parameters only, this definition of Q may be used when the secondary iron is considered magnetically non-linear.

When $\eta \tanh qg << 1$ or $Q >> 1$ (Equation 2.80), i.e. the eddy-current field is strong, and $\mu_s \tanh qg >> 1$, the peripheral components of the resultant magnetic-field strength, $\dot{H}_{xg}$, and the magnetic-field strength

due to the eddy-currents, $\dot{H}_{xgr}$, are approximately equal;   if these

conditions cannot be stated, $\dot{H}_{xgr} \neq \dot{H}_{xg}$, the difference between them

being due to the applied field of the primary current sheet, $\dot{H}_{xgc}$

(Equation 2.62).

In discussing the nmfs acting on the air-gap, it has been shown

(Section 2.7.4) that the ratio of $|\dot{F}_r|$ to $|\dot{F}_g|$ is equal to Q if $qg \ll 1$.

In Equation 2.97, the torque has been expressed in terms of $|\dot{F}_r|$.

If $|\dot{F}_r|$ is calculated from the approximate form of Equation 2.96, which

is obtained by assuming $qg \ll 1$, the largest error in the calculations

will occur when the eddy-current effect is strong.

CHAPTER 3

A LITERATURE SURVEY:

NON-LINEAR THEORIES AND PROPERTIES OF FERROMAGNETIC MATERIALS

3.1 INTRODUCTION

The magnetic and electric characteristics of commercially available ferromagnetic materials, excluding those used for permanent magnets, are defined and discussed in the first two sections of this chapter. Several observations are also made which have an important bearing on experimental investigations of electromagnetic fields in solid iron. The next section details the effects that the characteristics of ferromagnetic materials have on the electromagnetic fields described in Chapter 2; these effects include the variation of permeability with depth, hysteresis loss and saturation harmonics of the magnetic quantities.

The remainder of the Chapter contains a literature survey of published solutions for the estimation of eddy-current loss that include the effects of magnetic non-linearity. The majority of the theories discussed are analytic, but a brief statement on finite difference methods is included for completeness. This survey is divided into two parts, the first concerns the penetration of plane waves into solid iron, and the second the two dimensional fields in solid iron due to a travelling mmf wave. By showing the deficiencies in previously published work, this chapter indicates the need for the work described in Chapters 4 to 8 in this thesis.

3.2 FERROMAGNETIC MATERIALS

The electric and magnetic characteristics of ferromagnetic materials are described by the resistivity ρ of the material and the non-linear relationship between the flux density, B, and the magnetic field strength, H.

The two B-H curves for magnetic materials are shown in Fig. 3.1 below. A single valued curve OA, which will be referred to as the normal B-H curve, is obtained when an unmagnetized specimen of the material is subjected to a slowly increasing magnetic field. This curve is not reversible, for if on reaching a magnetic field strength of H_{max} the field is cyclically varied between $\pm H_{max}$, a hysteresis loop is traced. A number of hysteresis loops is obtained by selecting different values for H_{max}, and the locus of their maximum values - the B_{max} - H_{max} curve - is almost coincident with the normal B-H curve. Fig. 3.2 shows a number of hysteresis loops for a sample of EN1A mild steel.
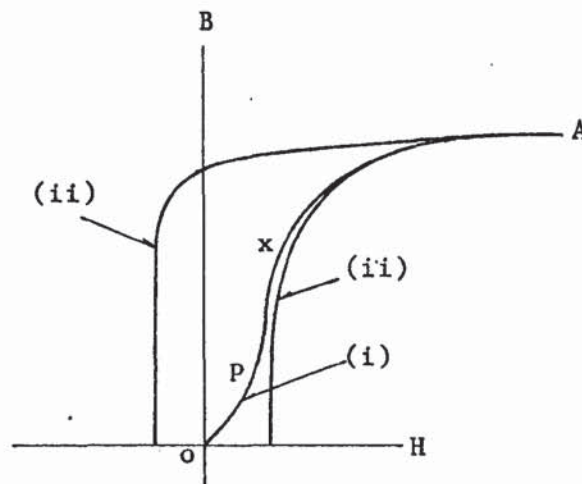
Fig. 3.1   Upper half of B-H curves for magnetic materials
             (Symmetrical about the H axis)

             (i) normal B-H curve
             (ii) hysteresis loop.

Three regions of the normal B-H curve may be identified[17] as -

(i)   the initial magnetization, OP where hysteresis is
      negligible so that the curve is approximately reversible.

(ii) the region of greatest slope, PX, which extends up to the
      knee of the curve.   In this region $dB/dH \gg B/H$ and the
      curve is irreversible.

(iii) the region beyond the knee of the curve, XA - here the
      slope of the curve decreases as the iron becomes saturated.

The magnetic behaviour of the material is also described by its

permeability μ which is given by the ratio B/H.

Both the magnetic and electric quantities of ferromagnetic

materials are dependent on chemical composition, crystal structure

and temperature.   The effects of temperature are discussed separately

in Section 3.3.

At room temperature, the electrical resistivity of steel is very

sensitive to composition and structure and particularly to the amount

of carbon.   The addition of carbon and other alloying elements to

iron increases its resistivity and useful data for estimating the

resistivity of low alloy steels is given by Woolman and Mottram.[18]

The B-H relationship for steel is sensitive to changes in the chemical

composition, and to the processes of fabrication and heat treatment

at values of H at and below the knee of the curve, but is sensitive

to changes only in chemical composition at values of magnetic field

strength within the saturated region of the B-H curve.[17, 19, 20] Effect of

change in the chemical composition on the magnetic properties of steel

is illustrated in Fig. 3.3 below;   curve (a) is for mild steel (not

annealed) having 0.2% carbon and curve (b) is for iron containing

0.02% carbon and annealed at 900°C.   Since the carbon content which

is specified for EN1A steel is 0.07 - 0.15%. , it is clearly necessary
to ensure that all specimens used in related experimental work must
originate from the same ingot. Variation in composition within the
steel, or heterogeneity, has an adverse effect on magnetic character-
istics by altering the composition of regions of the steel from the
preferred specification; it also has various second-order effects
and results, for example, in non-uniform flux distribution.
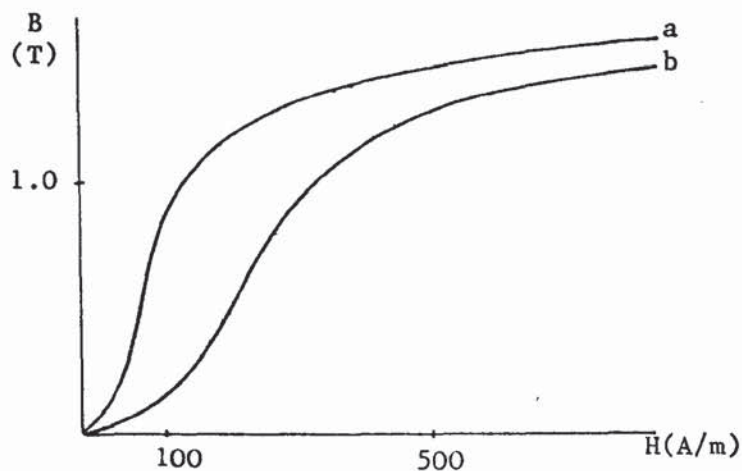
Fig. 3.3   Effect of Change in Chemical Composition on the
            Normal B-H curve (Bozorth [17])

            (a) 0.2% carbon
            (b) 0.02% carbon

Strains in the material by fabrication cause magnetic anisotropy,
which may be removed by annealing. The final state of the crystal
structure of any specimen depends on its history of manufacture and,
while no two specimens can be pointwise identical, overall differences
can be minimised by similar processes of machining and heat treatment.

Knowledge of the surface conditions of a steel specimen are of
particular importance in experimental studies of eddy-current losses,
but are extremely difficult to determine.[19]   The chemical composition

and the crystal structure at the surface may differ from that within the body of the specimen, and are determined by the processes of production and manufacture. Specimens cannot always be bright annealed after surface machining, and even if it is carried out it does not guarantee magnetic homogeneity or isotropy of the surface layers. (Electro-chemical machining[21] may however be used to remove surface layers without inducing further strains.) It is therefore inadvisable to attempt verification of any theory which is based on an overall B-H relationship for the material by localised measurements, unless many similar measurements of the field quantities are made over the surface of the material.

It is also preferable, if possible, that measurements are made at flux levels above the knee point of the B-H curve where the magnetic characteristics are least sensitive to changes in the crystal structure of the material.

3.3   EFFECT OF TEMPERATURE ON MAGNETIC AND ELECTRIC PROPERTIES

3.3.1   Magnetic Properties

The attenuation of the power loss density with depth into the steel is described by Equation 2.48. If the electric and magnetic properties of the material are functions of temperature, the temperature distribution and the loss distribution must be interdependent.

The greatest effect of temperature on the magnetic characteristics of the material occurs near the Curie point (about 770° C for normal mild steel) where the relative permeability at any value of magnetic field strength rapidly drops to unity. Between 100°C and 500°C there is virtually no temperature coefficient of permeability for field strengths above 250 A/m, but at smaller field strengths the temperature coefficient of permeability may vary considerably and is dependent on both the field strength and the temperature. Eddy-current losses are

important when they raise the temperature excessively and, since it is probable that the surface layers of the iron will be saturated to cause losses sufficient to raise the temperature to 100 - 500°C, the temperature coefficient of permeability may be considered insignificant. The probable variation of permeability with temperature is indicated by the normal B-H curves for iron shown in Fig. 3.4 below. At temperatures between 23°C to 300°C, the shape of the curve changes only at magnetic field strengths at and below the knee point so that the permeability increases.
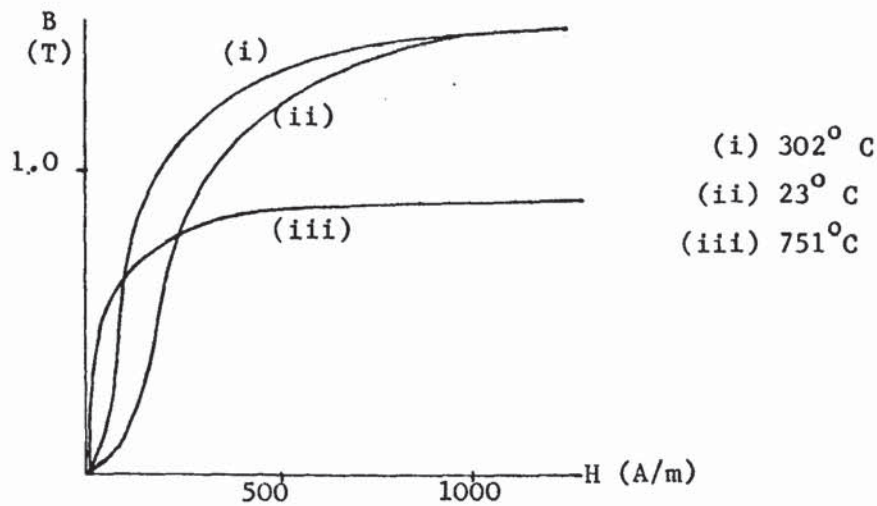
Fig. 3.4   Normal B-H curves of iron at different temperatures
(Bozorth [7])

3.3.2   Electrical Properties

The resistivity of steel increases when it is heated from room temperature, and the temperature coefficient of resistance is dependent to a lesser degree on temperature. The non-uniform heating of the steel due to eddy currents produces a temperature gradient which varies throughout the heating time. At the start of the heating process the temperature is greatest at the surface of the iron, whereas during the total heating time the temperature distribution may become

more uniform due to a decrease in permeability at high values of H
and an increase in radiation loss from the surface. The variation
in resistivity during the heating process is therefore dependent on
many factors, some of which are extremely difficult to define.

Resistivity also changes with the applied magnetic field
strength,[7] but the magnitude of the change is usually only a few
percent at temperatures much lower than the Curie temperature.

3.4   THE FORMULATION OF NON-LINEAR THEORIES

3.4.1   General

From the discussion in the previous Section (3.3), the following
characteristics of ferromagnetic materials should be included in a
mathematical solution of iron losses:

(i)   the non-linear B-H relationship.

(ii)   the resistivity-temperature characteristic.

The inclusion of the resistivity-temperature characteristic
implies that the electromagentic and heat conduction equations should
be solved simultaneously; this solution would be complicated, and
as the heat conduction equation includes many ill-defined quantities
(Section 3.3.2),it is also impracticable. For this reason the
effects of temperature are neglected in this thesis. It is also
necessary to assume that the material is homogeneous and isotropic
to obtainatheory that is generally applicable.

3.4.2   The Non-Linear B-H Relationship

The linear theory (constant permeability), described in Chapter 2,
shows that the electromagnetic quantities vary periodically in time at
any spatial point, their amplitudes varying with depth throughout the
medium. There is therefore, a unique hysteresis loop at every depth
throughout the medium. The derivation of a mathematical solution that

accounts for an infinite number of hysteresis loops is clearly an impossibility and approximations and assumptions must be made at the outset.   In considering the initial approximations that may be made it is useful to note the significant differences which the inclusion of non-linearity will make to the linear solution.

3.4.2.1 The Distribution of the Electromagnetic Quantities

The flux density, current and loss densities will no longer attenuate with depth into the medium as defined by the linear theory since any change of amplitude of the magnetic field strength results in a change in permeability, as defined by the normal μ-H curve. The change of phase with depth of the electromagnetic quantities can no longer be constant due to the change in permeability with depth. If the value of the magnetic field strength at the surface of the iron (H_o) is greater than the value at the knee point of the B-H curve (H_k), then the permeability will increase with depth into the iron, so that the attenuation and phase change with depth will increase but the velocity of the penetrating wave will decrease;   the opposite of these effects will occur if $H_o < H_k$.

As the main object of this work is to provide a means of calculating the total loss in the iron, a solution for the spatial distribution of the electromagnetic quantities is of secondary importance. It is however important to the designer that a concept of depth of penetration be retained and, as the definition of this quantity by the linear theory is no longer valid, an attempt must be made to define an equivalent quantity under non-linear conditions.   In the linear theory, the depth of penetration δ applies to both the distribution of flux density and current density, whereas the loss distribution has a penetration depth of $\delta/2$;   in the non-linear theory it is probable that the penetration depth will be different for each of the three

quantities. The problem is therefore to find a basis for defining a single equivalent depth of penetration.

3.4.2.2 SATURATION HARMONICS

Saturation harmonics of flux density and magnetic field strength must be generated in the medium due to the non-linear relationship between them. It is unlikely that either the magnetic field strength or flux density will be sinusoidal except at the surface of the medium where these quantities are functions primarily of the primary excitation or voltage if the air-gap is small. If a sinusoidal magnetic field strength was considered to exist at every point in the medium, the flux density and induced emf waveforms would be non-sinusoidal. Since the resultant magnetic field strength at any point is obtained by combination of the applied field and the reaction field due to the eddy currents, it too must be non-sinusoidal.

The loss due to the saturation harmonic of the field quantities must therefore be included in the theory; this may be implicit in the development of the theory or may have to be added as a separate factor.

3.4.2.3 Hysteresis Loss

The total loss in the iron includes both hysteresis and eddy current losses.

The overall magnetization characteristic of a ferromagnetic specimen, when determined at power frequencies, is a B-H loop which is referred to as the dynamic hysteresis loop; the area of this loop is proportional to the total loss (eddy-current and hysteresis). The deformation of the normal hysteresis loop (Fig. 3.1) to the dynamic hysteresis loop is due to eddy-current reaction. The normal rather than the dynamic hysteresis loop must therefore be included in analyses to obtain solutions for the eddy-current density within the iron.

Whilst functions representing the hysteresis loop have been

reported , the hysteresis loss may be simply accounted for by an equivalent elliptical B-H representation which allows an estimation of the effects of hysteresis to be made.[22,23] The relationship between B and H for the equivalent loop is

$$B = \mu \, He^{-\Theta_h}$$

where $\mu = B_{max}/H_{max}$

Θ_h is termed the hysteresis angle and is taken to be the value which makes the area of the equivalent ellipse equal to the normal hysteresis loop for the same maximum values of B and H. Hence if W_h is the area of the normal hysteresis loop per unit volume per cycle, then

$$W_h = \oint H \, dB = \pi \, H_{max} \, B_{max} \, \sin \Theta_h$$

and

$$\Theta_h = \arcsin \frac{W_h}{\pi \, H_{max} \, B_{max}}$$

Typical values of Θ_h for values of H_{max} are shown in Fig. 3.5.
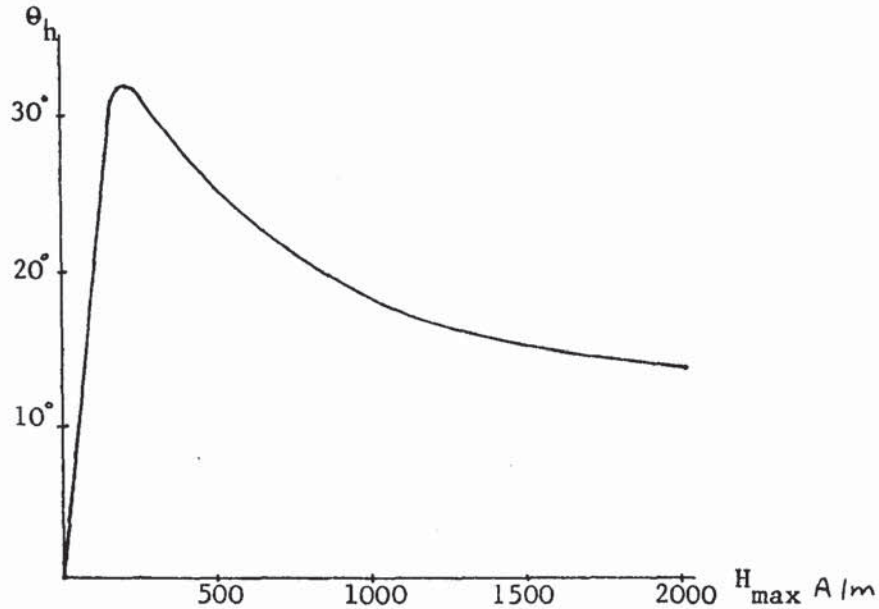
Fig. 3.5 Variation of Hysteresis Angle, Θ_h, with H_{max} for EN1A steel.

The total eddy current and hysteresis loss P_t, the power factor angle $\emptyset$, which the angle between the sinusoids of B and H for the dynamic hysteresis loop, and the power factor in a semi-infinite slab have been shown by Pohl[23] to be:

$$P_t = P \sqrt{1 + \sin\theta_h}$$

$$\phi = \pi/4 - \theta_h/2$$

$$\cos \phi = 0.707 \sqrt{1 + \sin\theta_h}$$

and the eddy current loss alone is

$$P_e = P/ \sqrt{1 + \sin\theta_h}$$

where

$$P = \frac{H_o^2}{2} . \alpha\rho \qquad\qquad 3.1$$

and α is given by Equation 2.14.

P is equal to the eddy current loss in the absence of hysteresis, i.e. when $\theta = 0$.

Thus the effects of hysteresis on the power loss obtained by this analysis are,

(i)   the increase of the total loss by the factor $\sqrt{1 + \sin \theta_h}$

and   (ii)   the decrease of the eddy current loss by the factor

$$1/ \sqrt{1 + \sin\theta_h}$$

The penetration of magnetic field strength is also obtained by Pohl as

$$h = \text{Re } H_o e^{j\omega t} .e^{-\alpha\sqrt{1 + \sin\theta_h}.y} .e^{-j\alpha\sqrt{1 - \sin\theta_h}.y} \qquad 3.2$$

where y is the depth into the slab.

Equation 3.2 indicates that the effect of hysteresis is to increase the attenuation but to decrease the phase shift with depth from the surface compared with the values obtained for a magnetically linear material.

A survey of the literature reveals a definite reluctance by most authors to determine the effects of hysteresis on the field distribution or total loss either theoretically or experimentally.   The reason for

this is that, not only is it difficult to achieve, but the contribution of the hysteresis loss appears to be small at value of $H_o > H_k$. In addition, theories not including the effects of hysteresis have produced results which agree well with measured values even when $H_o < H_k$. This is discussed further in Section 3.6.

3.5 NON-LINEAR ONE-DIMENSIONAL ANALYSES

This section contains a brief review of non-linear analytical methods of calculating the loss in solid iron.

Most analyses may be classified as either using a straight line representation or a functional representation for the normal B-H curve. Those analyses that fall outside this classification are the graphical method and the assumed permeability distribution with depth into the iron. Examples of all these solutions are given in the following sections.

3.5.1 Straight-Line Representation

Four straight-line approximations of the normal B-H curve are shown in Fig. 3.6 overleaf. The method of analysis is to solve Maxwell's equations subject to the assumed B-H relationships.

Solutions for mmf and voltage impact excitation only have been obtained for the characteristics in Fig. 3.6c[24,25] and Fig. 3.6d[26]. The field distribution for each of these characteristics is described by two separate differential equations and in the case of Fig. 3.6d one of the differential equations is non-linear. The difficulty in obtaining solutions for these characteristics for $H > H_s$ (see Fig. 3.6) is in determining the point in the space-time plane at which transition takes place from one differential equation to the other.

Solutions for alternating field excitations have been obtained for the limiting non-linear characteristic[27,28] (Fig. 3.6a) and the
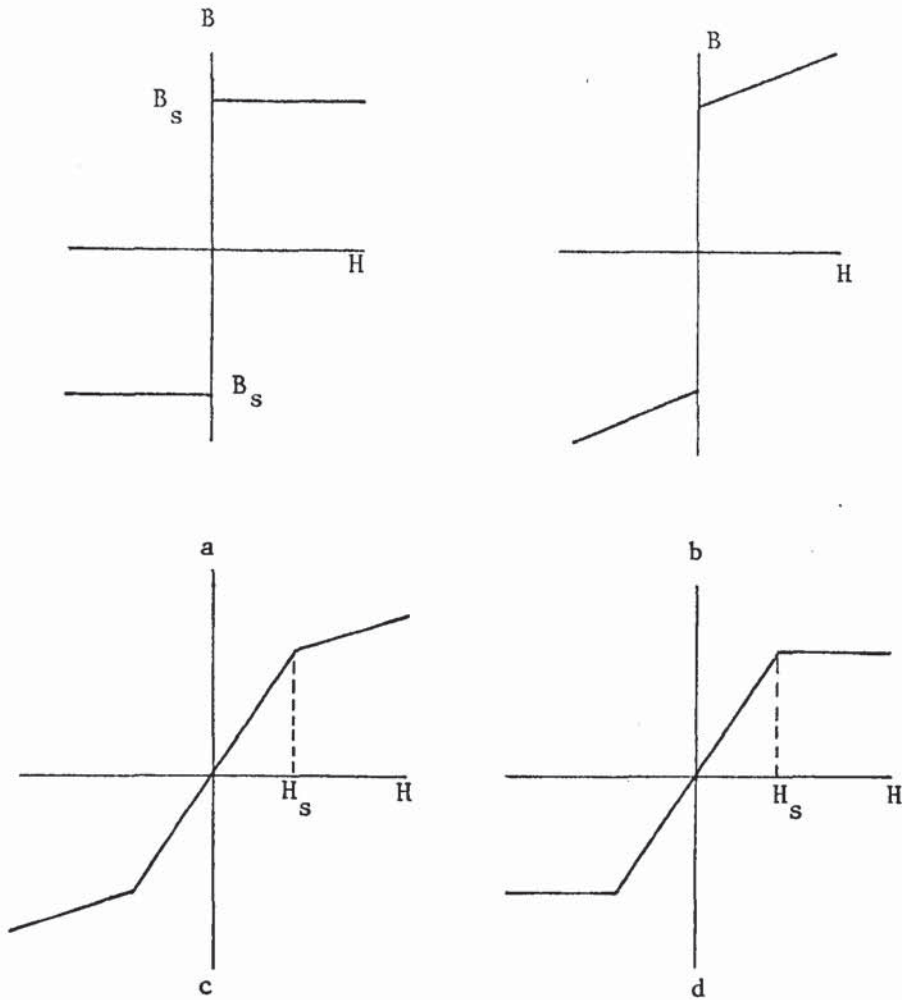
Fig. 3.6   Straight line representations of the Normal B-H curve

    a : limiting non-linear curve, References 27 and 28
    b : modified limiting non-linear curve, Reference 29
    c : References 24 and 25
    d : Reference 26

modified limiting non-linear characteristic[29] (Fig. 3.6b) which

describe only two states of magnetisation.   The linear and limiting

non-linear characteristics are extreme representations of the B-H

curve;   the true solution for the loss in iron must therefore lie

somewhere between solutions which are obtained using these

characteristics.   The limiting non-linear theory will be briefly

reviewed here for reference;   solutions for both sinusoidal flux

and mmf are given and compared in the literature[30,31] but only the

solutions for sinusoidal mmf is relevant here.

3.5.1.1 The Limiting Non-Linear Theory

As the sinusoidal magnetic field intensity at the surface of the steel increases from zero to a positive maximum and decreases again to zero, a constant, saturated wave front of flux density $+ B_s$ propagates into the steel. At the end of the half cycle, the wavefront has penetrated to a depth δ_L. During the following negative half cycle, a constant wavefront of flux density $- B_s$ propagates into the steel demagnetizing the density $+ B_s$ as it progresses. The flux changes only between the surface and the wavefront (see Fig. 3.7 below), and hence eddy currents are only induced in this region.
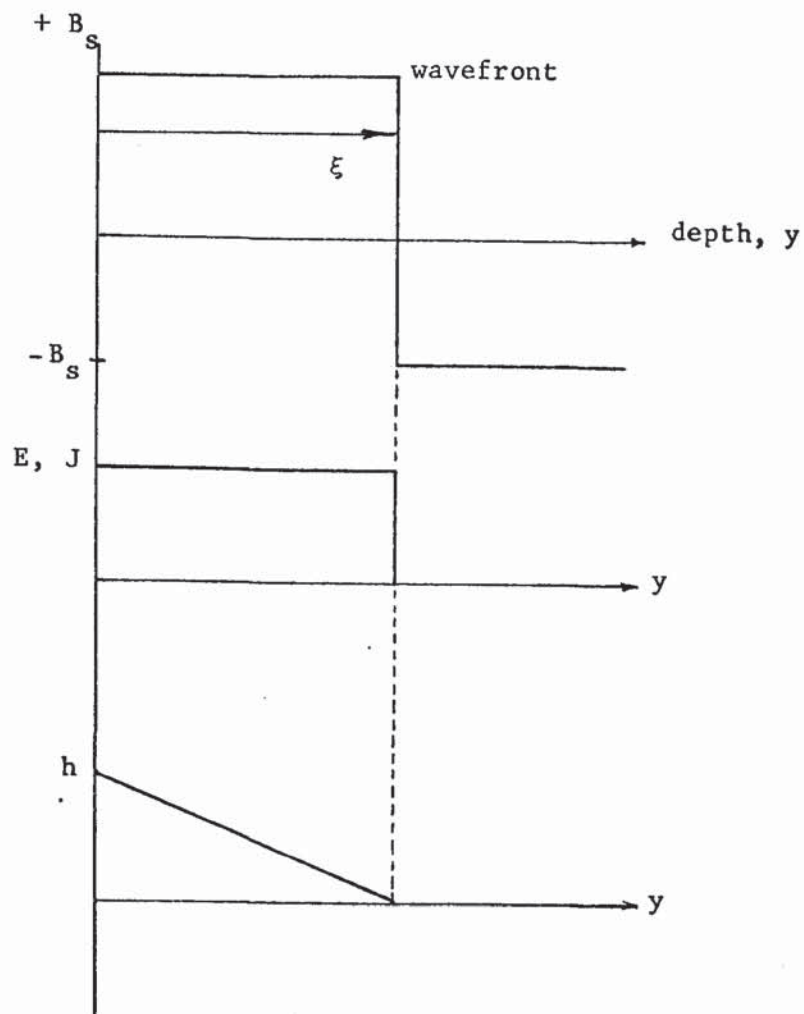
Fig. 3.7   Illustrating the limiting non-linear theory.

Thus $J = \frac{1}{\rho} \frac{d}{dt} \left[B_s (\xi - y) - B_s (\delta_A - \xi) \right]$

$= \frac{2}{\rho} \cdot B_s \frac{d\xi}{dt} \; , \; y < \xi$

$= 0 \qquad \quad y > \xi$

The current density is therefore uniform up to the wavefront, and the magnetic field intensity, H, must increase uniformly from zero at the wavefront to the surface value at any instant of time; that is,

$h = H_o \sin\omega t = \frac{2}{\rho} \cdot \xi \cdot \frac{d\xi}{dt} B_s$

$= \frac{B_s}{\rho} \cdot \frac{d}{dt} \cdot (\xi)^2$

Hence $\xi = \sqrt{\frac{H_o 2 \rho}{\omega B_s}} \cdot \sin \frac{\omega t}{2} \; , (0 < t < \pi/\omega)$

The maximum value of ξ, δ_L, occurs when $t = \pi/\omega$, so

i.e $\delta_L = \sqrt{\frac{2 \rho H_o}{\omega B_s}}$ \hfill 3.3

The power dissipated in the steel is given by,

$P_L = \frac{\rho \omega}{\pi} \cdot \int_o^{\pi/\omega} J^2 \, \xi \, dt$

and hence

$P_L = \frac{4}{3\pi} \cdot \omega B_s \, \delta_L \, H_o$

or $P_L = 1.7 \frac{H_o^2 \rho}{2 \delta}$ \hfill 3.4

Substituting for δ_L in Equation 3.4 from Equation 3.3

$P_L = 1.7 \sqrt{\frac{\rho B_s \omega}{8}} \cdot H_o^{1.5}$ \hfill 3.5

These final expressions for power loss can be compared with that obtained by the linear theory (Equation 3.1).

Two observations can be made from this comparison:

(i) Consider Equation 3.4. If δ_L is made equal to δ at all values of H_o then $P_L = 1.7P$, and the exponent of H_o in each case is 2.0. δ_L can only be made equal to δ by varying B_s so that $\frac{B_s}{H_o}$ for the non-linear theory equals

$(\mu_o \mu_r)$ for the linear theory.

(ii) Consider equation 3.5. If B_s is a constant, then the exponent of H_o is 1.5, and the constant of proportionality is $1.7 \sqrt{\dfrac{\rho B_s \omega}{8}}$

The general equation for the power loss may be stated as,

$P = pH_o^r$ where p and r are constants.

From the previous discussion both p and r are dependent on the choice of the saturation flux density, B_s.

Extensive experimental work was carried out by Agarwal[32] to determine a suitable definition of B_s; he concluded that $B_s = 0.75 B_m$, where B_m corresponds to H_o on the magnetization curve for the material.

Thus at any value of H_o, the loss may be calculated from the expression

$$P_A = 1.47 \frac{H_o^2 \rho}{2 \delta_A} \qquad\qquad 3.6$$

where $\qquad\qquad\qquad\qquad\qquad\qquad\qquad\qquad 3.7$

$$\delta_A = \sqrt{\frac{2H_o \rho}{\omega B_m}}$$

(The subscript A denotes Agarwal's solution.)

This empirical equation gives fairly good results (within 10%) for a wide range of H_o for a variety of steels.

The difference between measured and calculated results however is not constant. Measured losses are smaller at low H_o and larger at high H_o than those obtained by Agarwal's equation. Clearly the single empirical factor of $B_s = 0.75 B_m$ does not give the true exponent of H_o which should be between 1.5 and 2.0. Experimental evidence shows that $r \simeq 1.6$, (Thornton[33] :1.57) .

The results of Agarwal's investigations show that the linear theory underestimates the loss, whereas the non-linear theory overestimates it. The reasons for this are discussed by Mc Connell,[34]

who concludes that the non-linear theory both over-estimates the contribution of the saturation harmonics and the amplitude of the penetrating waves at all depths beyond the surface of the material.

The expressions for the depth of penetration for the linear and non-linear theories are similar, yet their physical interpretations are different. The depth of penetration, δ, in the linear theory, relates to the exponential decay of the field quantities as they diffuse into the material, whereas δ_A for the limiting non-linear theory defines the depth beyond which there is no penetration of any field quantity. δ_A depends on the total flux while δ depends on the material parameters and frequency of the applied field. Neither theory can be expected to give the correct field distribution within the solid iron although they may be useful in estimating the power loss.

The magnetization process within the material described by the limiting non-linear theory differs from that described by the linear theory. The modern theory of ferromagnetism is based on the existence of domains which are considered to be small permanent magnets. In the unmagnetised state the orientation of the domains are such that the resultant magnetisation is zero. The process of magnetisation due to an applied field consists of the orientation of domains towards parallelism with the applied field. Eddy-current losses have been determined by considering domain movement, particularly in attempts to account for the anomalous loss in this steel laminations[35,36]. If the iron is considered to be progressively magnetised so that a line of separation between the randomly orientated domains and the orientated domains penetrates the iron[36], the magnetisation process resembles that described by the limiting non-linear theory. There is however, no evidence that such a process occurs in steel slabs whose dimensions

are much greater than domain sizes.

3.5.2 Functional Representations

A rigorous solution for the electromagnetic field distribution may be obtained if an analytic function representing the normal B-H curve can be inserted into Maxwell's equations. The difficulty in obtaining such a solution is not only in finding a function which accurately represents the B-H curve, but in finding a function for which a solution of Maxwell's equations may be obtained.

Fishcher and Moser[37] have studied 15 functions that may represent the normal B-H curve. Those that are applicable to the region above the knee of the curve and into saturation, yet have a simple form, are:

$$B = \exp \frac{H}{a + bH} \qquad\qquad 3.8$$

$$B = \frac{H}{a + bH} \qquad\qquad 3.9$$

$$B = aH^b \qquad\qquad 3.10$$

$$B = a - b/H \qquad\qquad 3.11$$

where a and b are constants.

Equation 3.9, the Fröhlich equation, and Equation 3.11 are most suitable for representing the region around the knee of the B-H curve (typically 100-5000 A/m for mild steel). The parabola, Equation 3.10, is most suitable for representing the saturated region of the curve (typically 1500 - 30,000 A/m for mild steel), but can be used with fair accuracy to represent the whole of the B-H curve except at very low magnetic field strengths. It is interesting to note that, as the temperature of the material increases from room temperatures, the B-H curve approaches a parabolic shape and may be more accurately represented by Equation 3.10 (see Fig. 3.4).

Davies[7] used the equation $(\mu\mu_o)^{\frac{1}{4}} H = kH^m$, which may be derived from $B = aH^b$ (Equation 3.10) in developing an analytic theory for

eddy-current couplings and brakes, and Pillai[38] has also used Equation 3.10 in developing a theory for solid rotor induction machines. These are discussed in Section 3.7. Lim[4] uses the Frohlich equation in obtaining a finite difference solution for the loss in solid iron; this is discussed in Section 3.6.

The 'perturbation' method may be used to solve non-linear partial differential equations which have been obtained by using analytic functions to represent the B-H curve. In the method described by Poritsky and Butler,[25] the B-H curve is represented by the cubic equation

$$H = CB + DB^3 \hspace{3cm} 3.12$$

where C and D are constants.

H and B are expanded in powers of a perturbation parameter λ,

$$\text{e.g. } B = B_o + \lambda B_1 + \lambda^2 B_2 \text{ ---}$$

Substituting these series for B and H into Equation 3.12 and then into the equation

$$\frac{\partial^2 H}{\partial y^2} = \frac{1}{\rho} \cdot \frac{\partial B}{\partial t}$$

yields a sequence of partial differential equations for B_o, B_1 etc., by equating like powers of λ. These equations may be progressively solved to obtain B_o, B_1 etc.

The number of terms required in a perturbation solution depends on the degree of saturation. For values of H well into saturation, convergence of the series for B and H is slow, and the method has little or no advantage over numerical methods of solution.

3.5.3 Functional Representation of the Permeability - Depth Relationship

Several authors have solved Maxwell's equations using a function which relates permeability to depth into the iron. This method of solution therefore considers only sinusoids of B and H at any point

in the iron since the variation of permeability with time is neglected.
As there is no theoretical or experimental information regarding the
variation of permeability with depth, this solution and the function
assumed for the (μ - depth) characteristic can only be verified by
correlation of measured and calculated results.

A simple exponential function has been used by Ollendorff[39]
so that

$$\mu = \mu_s e^{my} \qquad\qquad 3.13$$

where m is a constant and y is the depth.

Nejman[40] uses the substitution

$$\mu = \frac{1}{(b - ay)^2} \qquad\qquad 3.14$$

which contains two constants a and b.

In both cases a general solution is obtained in terms of the
constants a, b or m;   the particular solution, and the evaluation
of the constants, is obtained by matching the general solutions for
μ and H with the μ-H curve for the material.   Nejman used the
analytical function given in Equation 3.10 for this purpose.

The simple exponential function has the advantage that a
two-dimensional magnetic field solution may be obtained, although
the solution for both one and two-dimensional magnetic fields is
given as Bessel functions.

3.5.4 The Graphical Method

An alternative to approximating the B-H curve to a series
of straight lines is to divide the ferromagnetic material into a
number of thin layers (Δy), each of which is considered to have
a constant, yet different, permeability.   Starting by defining H_o,
and therefore B_o and E_o at the surface (y = 0) the now linear
differential equation is solved for the first surface layer to

determine the field quantities at $(y + \Delta y)$. The value of the magnetizing force at $(y + \Delta y)$ determines the new permeability for the next layer. A graphical solution of this step by step method is given by Pohl[23] and Kesavamurthy and Rajagopalan.[41] This solution is less accurate than the piece wise linearisation of the normal B-H curve for the same number of linear steps since the permeability for each step is defined by the ratio B/H rather than the slope of the B-H curve; it is also a lengthy technique and has since been superceded by more accurate numerical methods.

3.6   FINITE DIFFERENCE SOLUTIONS

In finite difference methods the differential equations of the problem are converted into a set of algebraic equations by the use of Taylor series approximations. These equations are solved numerically at every point on a grid constructed to cover the required space or space-time domain. The use of finite difference techniques has grown rapidly in recent years due to the availability of high speed computers. Problems of the convergence of the numerical solution and it's stability arise, which are not encountered in analytic solutions. Several authors have applied these techniques to eddy current problems in saturated iron, either employing the normal B-H curve or a nest of hysteresis loops.

The numerical studies made by Gillot and Calvert[42] and Gillot and Abrahams[43] are of particular interest. The former calculated the loss in steel rods using the normal B-H curve only, whilst the latter calculated the loss for the same steel rods using a nest of hysteresis loops. The computed losses agreed, in both cases, with measurements to within 10% over a wide range of magnetic field strength (up to 4,850 A/m), although the agreement was better when the nest of hysteresis loops were used. The eddy-current loss is less when hysteresis is considered although the total calculated loss increases.

From a short table of results in Ref.43 it is seen that the
hysteresis part of the total loss decreases with H_o, and is less
than 10% for values just into saturation ($H_o < 5000$ A/m).   At a
value of H_o below the knee point the hysteresis loss was 37% of the
total loss, although the difference between the total losses
calculated with and without hysteresis was only 5%;   this shows
that calculations of eddy-current losses using the B-H curve alone
must account for a considerable part of the hysteresis loss.   The
numerical method of Gillot and Calvert[42] using the normal B-H curve
is discussed in greater detail in Section 5.6.

Numerical solutions have the major disadvantage that they
cannot be expressed by an equation in which the main variables
are represented.   Lim[4] and Hensman[44] have recently published
solutions for the loss in solid iron which, although using numerical
techniques, overcome this disadvantage . This was achieved by presenting
the solution in the form of a universal loss chart from which the
power loss may be calculated for a range of surface magnetic field
strengths and for a variety of steels.   The universal loss chart
is therefore equivalent to an analytic solution.   A depth of
penetration δ_F is defined by the equation $P = \dfrac{H_o{}^2 \rho}{\delta_F}$, where   P   is
the computed loss. δ_F is therefore an equivalent linear depth
of penetration, and as such it has little physical significance;
it cannot give information on the flux level at a particular depth
as δ or δ_A (Equation 3.7) can, unless it is related to the computed
values of the field quantities throughout the depth of the material.
Thus, although extensive computations are not required to obtain
the total loss in the material, they are still required for
determining the field distribution.   A limitation of the theories
given by Lim and Hensman is the use of Frohlich's equation to
represent the B-H curve;[37,45] this equation accurately represents the

region around the knee of the normal B-H curve and into saturation, but increasingly diverges from the B-H curve with further increase of magnetic field strength.

3.7   TWO-DIMENSIONAL SOLUTIONS FOR THE CONFIGURATION OF FIG. 1.1

In the analytic solutions so far discussed, and the loss charts produced by finite difference solutions, it has been assumed that the surface magnetic field strength H_o is known.   In Chapter 2 however, it has been shown that H_o cannot be equated directly to the primary current sheet for the machine configuration given in Fig. 2.1, but is dependent on the frequency, dimensions and physical constants of the machine.   It is reasonable to assume that this will also be true for magnetically non-linear iron, so that it is not possible to assume an air gap of negligible length.

To include the air-gap region in a numerical solution for the loss in the iron would increase the length of the iterative process, and it is preferable that even an approximate analytic solution be found so that the dependence of the loss and eddy-current reaction on the excitation and parameters of the machine may be directly seen.

Few authors have obtained an analytic solution for the two-dimensional fields in non-linear iron produced by a travelling mmf, and in some cases sweeping approximations are made to obtain solutions of acceptable complexity.

Gonnen and Stricker[46] obtained a two-dimensional solution in the solid iron secondary of an eddy-current brake in terms of Bessel functions on the basis that the permeability did not vary with time but varied exponentially with depth into the iron.   The permeability is defined as $\mu = \mu_s e^{my}$ where μ_s is 'the average permeability on the rotor surface', and was found by 'measuring the pole flux as a function of excitation'.   m is chosen so that the solution for the peak values

of B and H at any depth into the iron correspond as close as possible to values from the B-H curve; an iterative solution is therefore required. A comparison of calculated and measured B-H curves given in Reference [46] shows that the permeability does not vary exponentially with depth, although the error is not large; the maximum deviation in B is estimated as 10%. Gonnen and Stricker find that provided $q^2/2\alpha_g^2 << 1$ where $\alpha_g = (\frac{\omega\mu_o\mu_s}{2\rho})^{\frac{1}{2}}$ then the tangential component of H in the iron is very much greater than the radial component. The total analysis for the eddy-current brake is simplified by assuming no airgap between stator and rotor so that eddy-current reaction and loss are incorrectly determined.

More recently, Pillai[38] has given a solution of the two-dimensional magnetic field within solid iron on the assumption that the relationship between the peripheral components of B and H is represented by an expression of the form $B = aH^b$, whilst the relationship between the radial components of B and H is linear. The relationship $B = aH^b$ relates the fundamental components of B and H; although not stated in his paper, it is therefore assumed that the relationship applies for all possible waveforms of B and H at any depth into the iron (see Section 3.4.2.2.). The solution is applied approximately to an induction motor, with a solid iron rotor having a constant applied voltage. Some measurements of torque, primary current and power factor were taken on a solid rotor induction motor without copper end rings and correlated with calculated values; the end region effects were accounted for 'by increasing the resistivity of the rotor material'.

Pillai states that the choice of different functions relating B and H in the radial and peripheral directions was based on 'calculations which show that even when the peripheral component of

B is highly saturated, the radial component of B is well within the
linear range'. This statement may be true, but it does not mean that
the permeabilities in the peripheral and radial directions may be
chosen independent of each other; the components of the flux density
are obtained from a resultant B which might be into saturation.

Dorairaj and Krishnamurthy[47] have carried out a two-dimensional
graphical solution by extending the method given by Pohl[23]. The
instantaneous values of the radial and peripheral components
of flux density at any layer, b_y and b_x respectively, are dependent
on h_y and h_x (instantaneous values of H_y and H_x which are assumed
sinusoidal), but their actual values are determined by the resultant
magnetic field strength h, which is equal to $\sqrt{h_y^2 + h_x^2}$, in relation
to the normal B-H curve. A Fourier analysis of the instantaneous
flux densities is carried out giving the fundamental components B_y and
B_x. For the remainder of the step-by-step construction, which is
carried out in accordance with Maxwell's field equations, the B_1-H
curve is used where B_1 is the peak fundamental flux density
corresponding to a peak fundamental magnetic field strength. Maxwell's
equations (Equations 2.2 to 2.7) for the two-dimensional field
are written as

$$J_z = \frac{\partial H_x}{\partial y} - \frac{\partial H_y}{\partial x} \qquad\qquad 3.15$$

$$\frac{\partial E_z}{\partial y} = \frac{\partial B_x}{\partial t}$$

and

$$\frac{\partial B_x}{\partial x} + \frac{\partial B_y}{\partial y} = 0$$

The authors state that,'extensive constructions made for the case of
solid rotor machines with different pole pitches and slip frequencies
show that no appreciable error occurs in neglecting the second term',
in Equation 3.15, so that

$$J_z \approx \frac{\partial H_x}{\partial y} \qquad\qquad 3.16$$

Thus, the field distribution and loss may be determined by simply considering the penetration of a plane wave into the iron.

Lasocinski[6] assumes that the one dimensional solution obtained by Nejman[40] may be applied to the solid iron rotor of an induction machine, i.e. Equation 3.16 applies. The author considers the field distribution in the air gap for magnetically linear and non-linear iron and travelling mmfs, but investigates chiefly the effects of variation of the permeability of the secondary iron on the field distribution around the periphery of the rotor due to pulsating fields.

Mc Connel and Sverdrup[48] calculate the torque in an induction motor with solid iron rotor using the limiting non-linear theory to account for magnetic non-linearity. They assume also that the two-dimensional magnetic fields may be reduced to a one-dimensional field for the calculation of torque i.e. Equation 3.16 applies. The value of the flux density across the air gap is assumed constant. The value of the saturation flux density B_s used in the loss calculations is taken from the normal B-H curve corresponding to the peak value of the surface magnetic field strength. The theoretical values of torque given in Reference 48 , are much greater than the experimental values at the same slip; and the reasons for this are evident from the results of the later investigation by Agarwal[32] (see Section 3.5.1.1.)

Davies[5,7] extended and developed the design procedure proposed by Gibbs[49] for eddy-current couplings, into a generalised theory which is completely analytic. Expressions for loss, torque and flux/pole are given. A linear theory was used to develop an equation for the loss in the secondary in terms of the peripheral component of the surface magnetic field, and it was assumed that Equation 3.16 applies. The value of permeability chosen for the

iron corresponds to the peak value of the surface magnetic field strength, H_o, the $\mu - H_o$ relationship being given as $(\mu\mu)^{\frac{1}{4}} H = kH^m$ (which is equivalent to $B = aH^b$) and may be derived directly from the normal B-H curve. It was realised by Davies that once the value of permeability was chosen it is assumed to apply at all points in the iron for the whole sinusoidal excursion of the flux density. Even so, the correlation between calculated and experimental results for couplings was good, particularly with regard to the variation of torque and flux with applied mmf; reasons for this are given in Section 5.4.3.1.2.

Davies also calculated the resultant mmf and the eddy-current reaction mmf acting on the air gap and related the reaction mmf to the surface magnetic field strength. Both mmfs were also related to the torque, so that by obtaining their phasor differences the torque could be related to the applied mmf. The air gap was assumed to be small, so that the flux density was constant along its length.

By differentiating the expression for torque and equating to zero, the peak torque and the frequency at peak torque is obtained. Normalised expressions for torque were obtained in terms of a non-dimensional quantity Q which was defined in terms of normalised torque and frequency . Normalised torque/slip curves were also obtained.

The evaluation of the eddy-current reaction mmf and its relation to the surface magnetic field strength, the development of normalised torque/slip curves and, most important, the relationship between torque and applied mmf, were not attempted by any of the other authors whose published work is discussed in this Chapter.

3.8 CONCLUSIONS

This Chapter has been concerned mainly with the effects of magnetic non-linearity on the evaluation of the loss and field distribution in solid iron and theories which have been proposed so far to account for these effects.

Finite difference solutions have not been considered in any detail as the object of this thesis is to produce solutions in which the influence of individual parameters may be directly seen. Although universal loss charts are equivalent to analytic solutions, they are not applicable to multiregion models and, as their title indicates, give information only on power loss.

Hysteresis has been omitted from most non-linear theories due to the difficulties of including it, and the small errors that exist between measured values and values calculated from theories that neglect hysteresis - even for values of magnetic field strength below the knee of the B-H curve. The finite difference studies of Gillot and Calvert,[42] and Gillot and Abrahams[43] show that the loss that is calculated t considering only the normal B-H curve contains a major part of the hysteresis loss. Hysteresis may therefore be excluded from loss calculations. It should be noted that it is not known if hysteresis may also be excluded from the calculation of power factor and eddy current reaction.

There are many one-dimensional non-linear theories for solid iron that are based on the normal B-H curve, yet rarely are they compared or their advantages and disadvantages shown by experimental work. The form of the solution must be as simple as possible if the theory is to be extended to a two-dimensional multiregion model. There is little point therefore in choosing a perturbation method (Section 3.5.2) which has little advantage over numerical solutions.

Where the loss due to saturation harmonics is implicit in the theory, the solution is complicated if the normal B-H curve is represented by functions other than the limiting non-linear B-H curve. The limiting non-linear theory, however, over-estimates the loss and the saturation flux density B_s, must be empirically defined; the definition given by Agarwal,[32] which was based on the results of extensive experimental work, has been widely used. It would be preferable if, either some factor dependent on the actual shape of the normal B-H curve could be included in a non-linear theory, or B_s could be defined analytically; it is likely that the first solution would lead to the second.

To solve Maxwell's equations subject to a representative function of the normal B-H curve, and to obtain a solution of acceptable complexity, it would appear necessary to ignore the saturation harmonics of B and H and to consider only the variation of permeability with depth into the iron. This implies that the wave-forms of B and H at every depth in the iron are sinusoidal and only their peak values relate to the normal B-H curve for the iron; these are the assumptions made in the graphical method of solution (Section 3.5.4). The effects of saturation harmonics are accounted for approximately by considering the fundamental sinusoids of the actual B and H waveforms.

If the solution is to be completely analytic, an analytic function for the normal B-H curve must be included in the theory. The function $B = aH^b$ is preferred for its simplicity and accuracy of representation of the B-H curve, particularly at and above the knee point.

In considering the extension of the one-dimensional non-linear theory to the two-dimensional multiregion model it has been shown that it is permissible to consider only the penetration of the

peripheral component of the magnetic field strength into the iron provided $q^2/2\alpha^2 \ll 1$ at the surface of the secondary. This assumption has been used by several authors[6,48] in calculating the loss or torque in solid rotor machines. Only Davies[7] however has produced a general expression for the torque in terms of the applied mmf which includes the effects of non-linearity; the analytic function used to represent the normal B-H curve, $(B = aH^b)$ was not however included in the solution at an initial stage.

There is therefore a need for a theory of the multiregion model which will enable the torque or loss, flux/pole, eddy-current reaction and field distribution to be calculated directly from the excitation and parameters of the machine, and includes a solution of Maxwell's equations subject to a representative function of the normal B-H curve; such a theory is given in Chapters 4 and 6 of this thesis.

It is also necessary that experiments be devised so that all aspects of the theories may be verified or its limitations discovered; such experiments are described in Chapters 5, 7 and 8 of this thesis. (Notes concerning the measurement of electromagnetic field quantities in ferromagnetic materials have been made in Section 3.2).

CHAPTER 4

A NON-LINEAR THEORY FOR THE SOLID-IRON REGION

4.1   INTRODUCTION

In this chapter, a theory is developed for the solid-iron secondary of the model configuration in Fig. 1.1, taking into account magnetic non-linearity.

The initial assumptions in the theory are,

(i)   that the secondary member is a homogeneous, semi-infinite block of ferromagnetic material,

(ii)   that the currents in the primary and secondary regions flow only in the axial (z) direction, and the magnetic field throughout the model is due only to the axial currents, and

(iii) that rectangular co-ordinates, rather than cylindrical co-ordinates, are used, the effects of curvature being neglected.

In the linear analysis of this model, the same form of general solution (Equation 2.15) is applicable to both the air-gap and the solid-iron region.   In the non-linear analysis, the differential equations for the solid-iron region and the air-gap region are different, and solutions for each region must be obtained independently and combined by matching boundary conditions. A solution for the solid-iron region is developed in this chapter, and combined with the solution for the air-gap region in Chapter 6.

In the following analysis for the solid-iron region, it is assumed that permeability varies with depth only and not with time, so that Maxwell's equations, embodied in the diffusion equation, are solved for fundamental sinusoids of the electro-magnetic

quantities. It is also assumed in the analysis that at any depth in the iron, the peripheral component of magnetic field strength H_x, is very much greater than the radial component H_y. The values of B and H at any depth are related, initially, by the normal B-H curve for the material, (the effect of neglecting hysteresis has been discussed in Section 3.6). The normal B-H curve is represented in the analysis by the function $B = aH^b$. The effects of the saturation harmonics of the magnetic quantities, that actually exist at any point in the iron, are discussed at the end of the analysis and the function $B = aH^b$ is suitably modified.

The final sections of this chapter include a comparison of the theory developed here (the present theory), with the limiting non-linear theory and other theories using functions of the form $B = aH^b$.

4.2 THE MAGNETIC FIELD DISTRIBUTION WITHIN THE SOLID-IRON REGION

4.2.1 General

In the linear analysis (Chapter 2), is was shown that $H_x \gg H_y$ in the solid iron region if $\sqrt{2}\,\alpha \gg q$. This condition implies that only the peripheral components of the magnetic field, H_x, need be considered in determining the distribution of the eddy-current field and the loss in the iron. The use of this approximation is especially desirable in the present non-linear analyses of the two-dimensional model, where the permeability is considered to vary with depth, and H_x and H_y cannot be considered independently. This complication is avoided if $\hat{H}_x \gg \hat{H}_y$ in magnetically non-linear iron. Where $\mu = \text{fn} \,(\,\hat{H}\,)$, the permeability will increase with depth into the iron, provided $\hat{H}$ at the surface is greater than that at the maximum value of μ (i.e. at the knee of the normal B-H curve). It is logical to assume, therefore, that if $\sqrt{2}\,\alpha \gg q$ at the surface layer then this condition applies at any depth. Both Dorairaj and Krishnamurthy[47] and Gonnen and Stricker[46] (see Section 3.7.), have found this to be so, although no numerical values are given. Since $\sqrt{2}\,\alpha \gg q$ in most practical cases, even for permeabilities < 100, it is assumed that $H_x \gg H_y$ in the following analysis. This assumption appears to be valid from the results of the experimental investigation. The electromagnetic field distribution in the secondary iron is therefore assumed to be the same as that of a one-dimensional, or plane, electromagnetic wave. The solution that is derived here is later modified (Chapter 6), to allow for the field distribution around the periphery of the secondary.

4.2.2 Solution for The Magnetic Field Distribution

The co-ordinate system used in this analysis is given in Fig. 2.1. Since it is assumed that,

$$H_y = H_z = 0$$

and $\quad J_x = J_y = 0$ $\qquad\qquad$ 4.1

then the magnetic field distribution within the solid iron is governed by the Diffusion Equation, obtained from Equations 2.2, 2.3, and 2.7, as,

$$\frac{\partial^2 H_x}{\partial y^2} = \frac{1}{\rho} \cdot \frac{\partial B_x}{\partial t} \qquad\qquad 4.2$$

The fundamental sinusoids of the magnetic field at the surface of the solid iron region are given by:

$$\left.\begin{array}{l} H_{xg} = \hat{H}_{xg} \cos \omega t \\[2mm] B_{xg} = \hat{B}_{xg} \cos \omega t \end{array}\right\} \text{at } y = g \qquad \begin{array}{l} 4.3 \\[2mm] 4.4 \end{array}$$

(where $\hat{H}_{xg} > 0$ and $\hat{B}_{xg} > 0$)

At any depth into the iron, i.e. at $y' = (y - g)$, the fundamental sinusoids of B_x and H_x will be shifted in phase with respect to the surface quantities. As discussed in the previous section (Section 4.2.1), H_x and B_x are sinusoidal functions of time, and are in time phase, since hysteresis is neglected. Thus,

$$\left.\begin{array}{l} H_x = \hat{H}_x \cos (\omega t + \varepsilon) \\[2mm] B_x = \hat{B}_x \cos (\omega t + \varepsilon) \end{array}\right\} \text{at } y' = (y - g) \qquad \begin{array}{l} 4.5 \\[2mm] 4.6 \end{array}$$

where ε represents the phase shift, and $\hat{H}_x$ $\hat{B}_x$ and ε are all functions of y.

It is assumed that the amplitudes of the fundamental sinusoids, $\hat{B}_x$ and $\hat{H}_x$ may be related by the normal B-H curve for the material. Up to this point, the statement of the problem is similar to that given in the graphical solution[23,41]; but in the following analysis the function,

$$B = a\, H^b \qquad\qquad 4.7$$

is used to represent the normal B-H curve,

where a and b are constants.   (See Section 3.5.2).

From Equation 4.6,

$$\frac{\partial B_x}{\partial t} = \omega \hat{B}_x \sin(\omega t + \varepsilon) \qquad\qquad 4.8$$

Substituting Equation 4.7 and 4.8 into the Diffusion equation (Equation 4.2), to obtain an equation in H_x only:

$$\frac{\partial^2 H_x}{\partial y^2} = \frac{\omega . a}{\rho} H_x^b \sin(\omega t + \varepsilon) \qquad\qquad 4.9$$

From Equation 4.5,

$$\frac{\partial H_x}{\partial y} = \cos(\omega t + \varepsilon) . \frac{d\hat{H}_x}{dy} - \hat{H}_x . \sin(\omega t + \varepsilon) . \frac{d\varepsilon}{dy},$$

and

$$\frac{\partial^2 H_x}{\partial y^2} = \cos(\omega t + \varepsilon) \frac{d^2 \hat{H}_x}{dy} - \frac{2 \, d\hat{H}_x}{dy} . \frac{d\varepsilon}{dy} \sin(\omega t + \varepsilon)$$
$$- \hat{H}_x . \sin(\omega t + \varepsilon) . \frac{d^2\varepsilon}{dy^2} - \cos(\omega t + \varepsilon) . \hat{H}_x . \left(\frac{d\varepsilon}{dy}\right)^2 \qquad 4.10$$

Thus, equating the (cos) and (sin) terms on the right hand side of Equations 4.10 and 4.9,

$$- 2 . \frac{d\hat{H}_x}{dy} . \frac{d\varepsilon}{dy} - \hat{H}_x \frac{d^2\varepsilon}{dy^2} = \frac{\omega}{\rho} . (a.\hat{H}_x^b) \qquad\qquad 4.11$$

$$\frac{d^2\hat{H}_x}{dy^2} - \hat{H}_x \left(\frac{d\varepsilon}{dy}\right)^2 = 0 \qquad\qquad 4.12$$

Eliminating ε between Equations 4.11 and 4.12,

$$\frac{d}{dy}\left[\hat{H}_x^{1.5}\left(\frac{d^2\hat{H}_x}{dy^2}\right)^{\frac{1}{2}}\right] = \frac{\omega a}{\rho} . \hat{H}_x^{(b+1)} \qquad\qquad 4.13$$

A solution of this differential equation was found by assuming the following general form of solution for the attentuation of $\hat{H}_x$ with depth into the iron:

$$\hat{H}_x = \hat{H}_{xg} (1 - f\, y')^m , \quad (f\acute{y}) < 1, \qquad\qquad 4.14$$

where m and f are constants.

Substitution of Equation 4.14 into Equation 4.13 gives

$$\hat{H}_{xg}^2 \cdot m^{\frac{1}{2}}(m - 1)^{\frac{1}{2}} \cdot (2m - 1) \cdot f^2 (1 - fy')^{(2m - 2)} = \frac{\omega a}{\rho} \cdot \hat{H}_{xg}^{(b+1)}(1 - fy')^{m(b+1)}$$
4.15

Both sides of this equation are of the form $K(1 - fy')^X$ so that, for

Equation 4.14 to be a solution to Equation 4.13,

$$(1 - fy')^{2m - 2} = (1 - fy')^{m(b + 1)}$$
4.16

and $\qquad \hat{H}_{xg}^2 \cdot m^{\frac{1}{2}}(m - 1)^{\frac{1}{2}} (2m - 1)f^2 = \frac{\omega a}{\rho} \cdot \hat{H}_{xg}^{(b + 1)}$
4.17

From Equation 4.16,

$$(2m - 2) = m(b + 1) ,$$

so that ,

$$m = \frac{2}{(1-b)} \quad ,$$
4.18

and from Equations 4.18 and 4.17,

$$\hat{H}_{xg}^2 \frac{\sqrt{2(1 + b)}}{(1 - b)} \cdot \frac{(3 + b)}{(1 - b)} \cdot f^2 = \frac{a\omega}{\rho} \cdot \hat{H}_{xg}^{b + 1}$$

thus $\qquad f = \left[\frac{\omega a}{\rho \sqrt{2}} \cdot \hat{H}_{xg}^{(b - 1)} \right]^{\frac{1}{2}} \left[\frac{(1 - b)}{(3+b)(1+b)^{\frac{1}{2}}} \right]^{\frac{1}{2}}$
4.19

From Equation 4.7, $\mu = a.H^{b - 1}$,
4.20

so that, at the surface of the secondary, when $y = g$,

$$\mu_g = a \cdot \hat{H}_{xg}^{b - 1}$$
4.21

Substituting Equation 4.21 into Equation 4.19,

$$f = \alpha_g \left[\frac{\sqrt{2} \cdot (1 - b)^2}{(3+b)(1+b)^{\frac{1}{2}}} \right]^{\frac{1}{2}}$$
4.22

where $\qquad \alpha_g = \sqrt{\frac{\omega \mu_g}{2 \rho}}$
4.23

(f must be positive for $\hat{H}_{xg}$ to decrease as y' increases).

Since $f \propto \alpha_g$, and has dimensions of (m^{-1}), it is preferable to

define,

$$\alpha_n = f = K_b \cdot \alpha_g,$$
4.24

where $\qquad K_b = \left[\frac{\sqrt{2} \cdot (1 - b)^2}{(3+b)(1+b)^{\frac{1}{2}}} \right]^{\frac{1}{2}}$
4.25

Also, since m (Equation 4.14) relates to the rate of attenuation of the amplitude of H_x, which in the linear analysis is dependent on the quantity β ,

$$\text{let} \quad \beta_n = n = \frac{2}{1 - b} \qquad\qquad 4.26$$

Thus, $\qquad \hat{H}_x = \hat{H}_{xg} (1 - \alpha_n y')^{\beta n} \qquad\qquad\qquad 4.27$

The subscript n denotes the non-linear solution.

Equation 4.27 is an exact solution of the differential equation (Equation 4.13).

To obtain ε as a function of y', Equation 4.27 is substituted into Equation 4.12. On integrating the resultant equation and resolving the constant of integration from the boundary conditions, $\varepsilon = 0$ when $y' = o$,

$$\varepsilon = \gamma_n \ln. (1 - \alpha_n y') \qquad\qquad 4.28$$

$$\text{where} \quad \gamma_n = \pm \frac{\sqrt{2(1 + b)}}{1 - b} \qquad\qquad 4.29$$

Thus, from Equation 4.5, the complete solution for H_x is

$$H_x = \hat{H}_{xg}(1 - \alpha_n y')^{\beta n} . \cos (\omega t + \gamma_n . \ln (1 - \alpha_n y')) \qquad 4.30$$

$$\text{of} \quad H_x = \text{Re}. \hat{H}_{xg} (1 - \alpha_n y')^{\beta n + j \gamma_n} . e^{j\omega t} \qquad\qquad 4.31$$

4.2.2.1 The Limiting Depth of Penetration

Since α_n has the dimension of (m^{-1}) the term $(1 - \alpha_n y')$ is non-dimensional, and so from Equation 4.30,

$$H_x = 0 \text{ when } y' = \delta_n = \frac{1}{\alpha_n} \qquad\qquad 4.32$$

δ_n may be called the 'limiting depth of penetration'. For Equation 4.32 to be possible, the permeability must become infinite when $y' = \delta_n$. This result is due to the inclusion of the function $B = a H^b$ in the above analysis. For this function to represent the normal B-H curve above the knee point (Section 3.2), the exponent $b < 1$.

Therefore, from Equation 4.20,

$\mu \rightarrow \infty$, as $H \rightarrow 0$ if $b < 1$.

A typical μ/H curve and function $\mu = a H^{b-1}$ for $b < 1$ are compared in Fig. 4.1a .

(a)   (b)
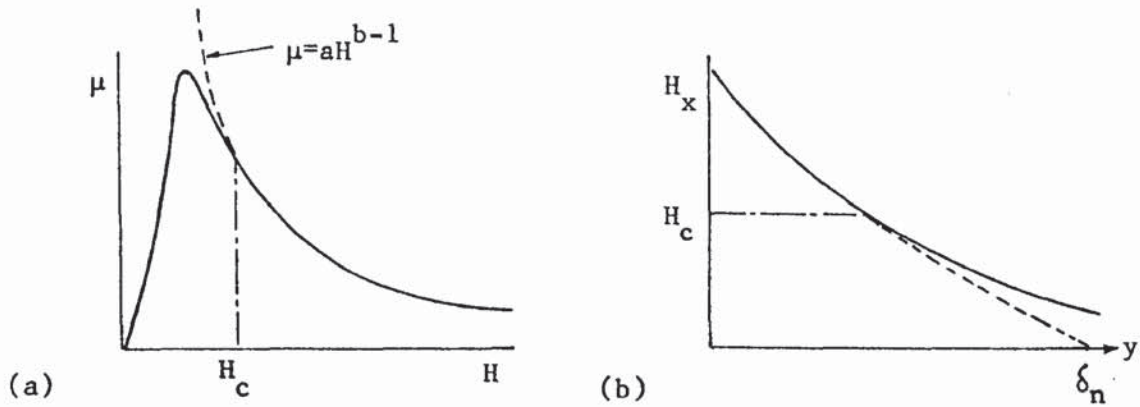
Fig. 4.1   Effect of Representing the Normal B-H Curve by $B = aH^{b}$.

Thus Equation 4.30 must be inaccurate for values of $\hat{H}_x$ below a value H_c (Section 5.5), as illustrated in Fig. 4.1b . This inaccuracy of representation has less effect on the range of application of the theory than might at first be thought;   it is discussed in Section 5.6

4.2.2.2   The Linear Case

It is interesting to consider the form of Equation 4.31 when the permeability is assumed constant, i.e. $b = 1$.

When $b = 1$, Equations 4.7 and 4.20 become,

$$B = a H$$

and $\mu = a;$ respectively.

Also from Equations 4.24, 4.25 and 4.32,

$$\alpha_n = 0 \text{ and } \delta_n \rightarrow \infty$$

Equation 4.31 can be written in the alternative form,

$$H_x = \text{Re } \hat{H}_{xg} \cdot e^{(\beta_n + j\gamma_n) \ln.(1 - \alpha_n y')} \cdot e^{j\omega t} \qquad 4.33$$

ln $(1 - \alpha_n y')$ may be expressed as,

$$\ln (1 - \alpha_n y') = - \alpha_n y' - \tfrac{1}{2} (\alpha_n y')^2 - 1/3 (\alpha_n y')^3 \text{ ---} \qquad 4.34$$

so that, from Equations 4.26 and 4.29,

$$(\beta_n + j\gamma_n) \ln (1 - \alpha_n y') = - \alpha_n y' \left| \frac{2}{1 - b} + j \frac{\sqrt{2(1+b)}}{(1- b)} \right| \left| 1 + \frac{\alpha_m y'}{2} \text{ ---} \right.$$

α_g may be substituted for α_n from Equations 4.24 and 4.25, so that, when b = 1,

$$(\beta_n + j\gamma_n) \ln (1 - \alpha_n y') \rightarrow - (1 + j) \alpha_g y'$$

and Equation 4.33 becomes,

$$H_x = \text{Re } \hat{H}_{xg} e^{-\alpha_g y'} . e^{-j\alpha_g y'} . e^{j\omega t}$$

4.3 THE CURRENT DENSITY DISTRIBUTION

From Equation 2.3, and the assumptions stated in Equation 4.1, the current density, J_z is related to the magnetic field component H_x by,

$$J_z = \frac{dH_x}{dy} \qquad\qquad 4.35$$

Thus, from Equation 4.31 and 4.35,

$$J_z = \text{Re.} \left[(\beta_n + j\gamma_n) \alpha_n \hat{H}_{xg}(1 - \alpha_n y')^{(\beta_n - 1 + j\gamma_n)} \right] e^{j\omega t}$$
$$4.36$$

and the amplitude of the surface current density is

$$\hat{J}_{zg} = (\beta_n + j\gamma_n) \alpha_n \hat{H}_{xg} \qquad\qquad 4.37$$

4.4 ALTERNATIVE DESCRIPTION OF THE DISTRIBUTION OF THE ELECTROMAGNETIC WAVE

The distribution of the magnetic and electric fields into the depth of the iron have been described in Sections 4.2.2 and 4.3. By means of the series expansion given in Equation 4.34, the distribution of the electromagnetic quantities may be written as,

$$H_x = \text{Re} \left[H_{xg} e^{- K_b \alpha_g(\beta_n + j\gamma_n) y'} . e^{-\tfrac{1}{2} (K_b \alpha_g)^2 (\beta_n + j\gamma_n) y'^2} \text{ ---} e^{j\omega t} \right.$$

$$E_z = Re \; E_{zg} \; e^{-K_b \; \alpha_g (\beta_n - 1 + j\gamma_n)y'} \cdot e^{-\frac{1}{2} (K_b \; \alpha_g)^2 (\beta_n - 1 + j\gamma_n)y^2} e^{j\omega t}$$

The attenuation with depth of the electromagnetic field is dependent on the quantities $(K_b \; \beta_n)$ and α_g, and the change in phase with depth is dependent on $(K_b \; \gamma_n)$ and α_g; both the attenuation and change in phase are therefore dependent on b, i.e. the shape of the normal B-H curve, and the surface magnetic field strength, which is included in the expression for α_g. The variation of K_b, β_n and γ_n with b is shown in Fig. 4.2.

If the permeability is constant (b = 1) and equal to μ_g, $(K_b \cdot \beta_n)$, $(K_b \cdot \beta_n - 1)$, and $(K_b \cdot \gamma_n)$ become equal to unity, while the remaining terms become equal to zero, (Section 4.2.2.2). When b < 1, i.e. the permeability increases with depth into the iron, $K_b \beta_n > 1$, so that the attenuation with depth of $\hat{H}_x$ is greater than that in the linear case, while the attenuation of $\hat{E}_z$ is less than that in the linear case.

Qualitatively, the quantities K_b, β_n and γ_n account for both the change in permeability with depth and the shape of the normal B-H curve, whilst the quantity α_g accounts for the level of saturation in the iron.

4.5 POWER FACTOR ANGLE AND IMPEDANCE OF THE SOLID IRON

The phase angle, $\emptyset_n$, between $\hat{H}_{xg}$ and $\hat{J}_{zg}$, (or $\hat{E}_{zg}$) may be called the power factor angle (see Equation 4.44a).

From Equation 4.37,

$$\hat{J}_{zg} = R_n \cdot \alpha_n \cdot \hat{H}_{xg} \; \underline{/\emptyset_n},$$

where $R_n = \sqrt{\beta_n^2 + \gamma_n^2}$ \hfill 4.38a

so that $R_n = \sqrt{6 + 2b}/(1 - b)$ \hfill 4.38b

and $\emptyset_n = \tan^{-1} \dfrac{\gamma_n}{\beta_n}$ \hfill 4.39

Thus, $\cos \emptyset_n = \beta_n/R_n$ \hfill 4.40

and $\sin \emptyset_n = \gamma_n/R_n$ \hfill 4.41

The wave impedance of the solid iron is given by

$$Z_{yn} = \frac{E_z}{H_x} ,$$

and from Equations 4.36 and 4.31

$$Z_{yn} = \rho . R_n . \alpha_n . \underline{/\phi_n} . (1 - \alpha_n y')^{-1} \qquad 4.42$$

(Note that the impedance increases with depth ($Z_n \rightarrow \infty$ as $y' \rightarrow \delta_n$) unlike the linear case where the impedance is constant.)

At the surface of the secondary, i.e. at $y = g$,

$$Z_{ygn} = (\rho . R_n . \alpha_m) \underline{/\phi_n} \qquad 4.43$$

4.6 LOSS IN THE SOLID IRON

The mean power flow/unit area into the solid iron, at any depth, is given by,

$$P_y = \tfrac{1}{2} \text{Re.} (E_z . \tilde{H}_x) \qquad 4.44a$$

substituting for E_z and H_x from Equations 4.36, and 4.31,

$$P_y = \frac{H_{xg}^2}{2} \rho . \beta_n . \alpha_n . (1 - \alpha_n y')^{(2\beta_n - 1)} \qquad 4.44$$

The total power/unit area into the secondary at $y = g$ is equal to the power loss, P_n, where, from Equation 4.44

$$P_n = \frac{\hat{H}_{xg}^2}{2} . \rho \beta_n \alpha_n \qquad 4.45$$

4.6.1 True Exponent of $\hat{H}_{xg}$ in the Loss Equation

The true exponent of $\hat{H}_{xg}$ in Equation 4.45 is not 2, as α_n is a function of $\hat{H}_{xg}$. Thus, substituting Equation 4.21 for μ_g into Equation 4.23,

$$\alpha_g = \hat{H}_{xg}^{\frac{(b-1)}{2}} . \sqrt{\frac{a\omega}{2\rho}} \qquad 4.46$$

so that, from Equations 4.46, 4.45 and 4.24,

$$P_n = \hat{H}_{xg}^{\frac{(b+3)}{2}} \frac{\beta_n K_b \sqrt{\omega\rho a}}{2\sqrt{2}} \qquad 4.47$$

and the true exponent of $\hat{H}_{xg}$ is $\frac{(b+3)}{2}$.

4.6.2 Normalised Power

If the permeability of the secondary iron is considered constant and equal in value to the permeability at the surface, μ_g, then $b = 1$ and from Equations 4.25, 4.26 and 4.24, $(\beta_n \cdot \alpha_n) = \alpha_g$, so that Equation 4.45 becomes

$$P = \frac{\hat{H}_{xg}^2}{2} \cdot \rho \alpha_g \qquad 4.48$$

Thus a loss ratio, K_p, may be defined as

$$K_p = \frac{P_n}{P} = \frac{\alpha_n \cdot \beta_n}{\alpha_g} \qquad (K_p \geqslant 1) \qquad 4.49$$

where P_n is obtained from Equation 4.45.

Substituting for α_n from Equation 4.24 into Equation 4.49

$$K_p = K_b \cdot \beta_n \qquad 4.49a$$

so that from Equation 4.25 and 4.26

$$K_p = \left[\frac{4\sqrt{2}}{(3+b)(1+b)^{\frac{1}{2}}} \right]^{\frac{1}{2}} \qquad 4.50$$

K_p is plotted against the exponent b in Fig. 4.2 between the limiting values of $b = 0$ and $b = 1$. The value $b = 1$ refers to the linear case (Section 4.2.2.2) when $P = P_n$.

When $b = 0$, K_p has a maximum value of 1.375, and Equation 4.7 becomes,

$$B = a \qquad 4.51$$

which is the expression for the rectangular B-H curve.

The limiting non-linear theory, based on the rectangular B-H curve (see Section 3.5.1.1), gives

$$P_L = C_L P$$

where

$$C_L = \frac{16}{3\pi} \simeq 1.7 \qquad \text{(Equation 3.4)}$$

K_p is not equal to C_L since the effect of saturation harmonics is

implicit in the limiting non-linear theory. In fact, both the
saturation harmonics and the level of flux density throughout the depth
of the iron are over-stated in the limiting non-linear theory, so that
Agarwal[32] found it necessary to reduce C_L from 1.7 to an empirical factor
of 1.47. This value is obtained by taking the value of $B_s = 0.75 B_{xg}$.
The advantages of the present theory over Agarwal's theory are that
both the variation of the flux density with depth into the iron, and the
dependence of this variation on the shape of the B-H curve and the value
of $\hat{H}_{xg}$, are accounted for. The disadvantage of the present theory is
that the effects of the saturation harmonics of the magnetic quantities
have not been included. From a comparison of experimental and theoretical
results, the contribution of saturation harmonics to the total loss is
not greater than 15%

4.7 SATURATION HARMONICS

In the analysis so far, it has been assumed that peak values of
the sinusoids of flux density and magnetic field strength at the surface
of the iron, $\hat{B}_{xg}$ and $\hat{H}_{xg}$, have been related by the normal B-H curve for
the iron. If it is assumed that the waveform of the magnetic field
strength only is sinusoidal, then the actual waveform of flux density
will be of the form shown in Fig. 4.3 below.

FIG. 4.3
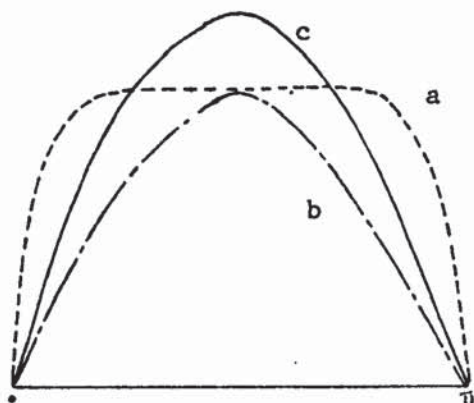
(a) waveform of B_{xg}, derived
from the normal B-H curve
for sinusoidal H_{xg}.

(b) Sinusoid of B_{xg}, assumed
in the analysis so far.

(c) fundamental component of
waveform (a).

Waveform (a) in Fig. 4.3 should describe the flux density on the surface of the secondary of the model (Fig. 1.1), if the primary current sheet varies sinusoidally with time, and the pole pitch is very much greater than the air-gap length;   if this is the case, the power loss in the iron will be given by the product of the fundamental sinusoids of H_{xg} and the flux density (waveform (c), in Fig. 4.3), at the surface of the secondary.   If H_{xg} is sinusoidal, a B_1-H_1 curve* for the surface of the iron may be obtained from the normal B-H curve.   At any other point in the depth of the iron, a different B_1-H_1 curve may be obtained, since both H_x and B_x contain varying percentages of harmonics (Section 3.4.2)

4.7.1 Analytic Derivation of B_1- H_1 Curves

Consider the general case where neither B_x nor H_x are sinusoidal. The relationship between the amplitudes of the waveforms at any depth in the iron is illustrated in Fig. 4.4 overleaf.   The amplitudes of the actual waveform of B_x (waveform (b)) and H_x (waveform (d)), correspond at point P on the normal B-H curve for the iron.   The fundamental component of H_x (waveform (e)), corresponds to a value of B_{h1}, and the fundamental component of B_x (waveform (f)), is B_1. The B_1 - H_1 curve may thus be obtained from the normal B-H curve by multiplying B_{h1} by the ratio R_b, where,

$$R_b = \frac{B_1}{B_{h1}}$$ 4.52

The ratio R_b is obtained by the following analysis.   The normal B-H curve is represented in this analysis by the Frohlich expression, where

$$B = \frac{H}{d + kH,}$$ 4.53

The Frohlich expression is preferred to the function $B = aH^b$

---

*   the subscript 1 denotes fundamental component.

Fig. 4.4.   Illustrating the Analytic Derivation of B_1-H_1 Curves.

in this analysis since it is more accurate at, and below, the knee point of the B-H curve where the ratio R_b has its greatest variation.   The Frohlich constants, d and k, for the sample of EN1A steel used in the experimental investigation, are

$$d = 288$$

$$k = 0.512 \qquad \qquad 4.53a$$

The B-H curve given by Equation 4.53 is shown in Fig. 5.3   where it may be compared both with the normal B-H curve and the curve given by $B = aH^b$.

The waveform of the magnetic field strength, H_x may be represented by the expression,

$$h_x(\omega t) = \frac{H \sin \omega t}{1 - U \sin \omega t} \qquad \qquad 4.54$$

The shape of the waveform is governed by the value of U, so that, in Fig. 4.5

waveform (a) U < 0

(b) U = 0, h = Hsinωt

(c) U > 0
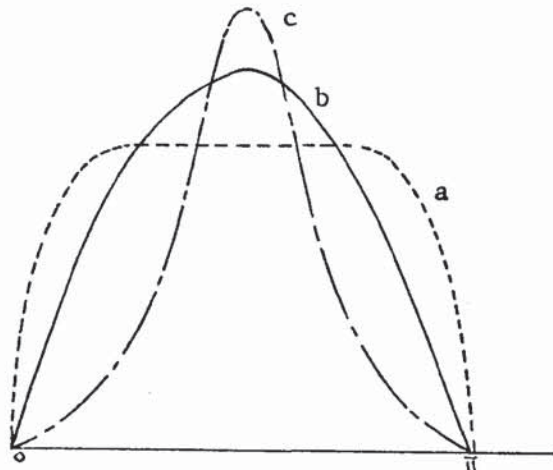
Fig. 4.5

Thus, from Equations 4.53 and 4.54,

$$b_x(\omega t) = \frac{H}{kH - dU} \left[\frac{\sin\omega t}{c + \sin\omega t} \right] \qquad 4.55$$

where

$$c = \frac{d}{(kH - dU)} \qquad 4.56$$

The fundamental component of $b_x(\omega t)$, B_1, is obtained by Fourier analysis, so that,

for $c^2 < 1$

$$B_1 = \frac{2H}{\pi(kH - dU)} \left[2 - c\pi \mp \frac{c^2}{\sqrt{1 - c^2}} \ln \left| \frac{1 - \sqrt{1 - c^2}}{1 + \sqrt{1 + c^2}} \right| \right] \qquad 4.57a$$

and for $c^2 > 1$,

$$B_1 = \frac{2H}{\pi(kH - dU)} \left[2 - c\pi \pm \frac{c^2}{\sqrt{c^2 - 1}} \left| \pi - 2 \tan\frac{\pm 1}{\sqrt{c^2 - 1}} \right| \right] \qquad 4.57b$$

where the upper signs are for c > 0.

and the lower signs are for c < 0.

Derivation of these expressions is given in Appendix I. H_1, the fundamental component of $h_x(\omega t)$ may be obtained by a similar analysis of Equation 4.54. The results of the computation of R_b for the normal B-H curve for EN1A steel are shown plotted against H_1 in Fig. 4.6. It is seen in this figure that R_b is substantially constant for values of $H_1 > 2500$ A/m. If the $B_1 - H_1$ curve is to be represented by a function of the form $B_1 = AH_1^m$, the exponent m will therefore be approximately the same as b in the function $B = aH^b$, and only the constant A will vary.

Thus, let $B_1 = AH_1^b$ 4.58a

where $A \simeq a R_b$ 4.58b

It is also seen from Fig. 4.6. that there is little change in the value

of A for considerable change in the waveform of H_x;   as most curves

lie within $1.2 < R_b < 1.3$, for $H_1 > 5000$ A/m, a reasonable approximation

for A is,

$$A \simeq 1.25a$$ 4.59a

so that

$$B_1 = 1.25aH_1^b$$ 4.59b

and from Equation 4.59a and 4.21,

$$\mu_g = 1.25a \, H_{xg}^{b-1}$$ 4.59c

The inclusion in the theory of the fundamental components of the actual

waveforms of B_x and H_x, by means of the curve $B_1 = AH_1^b$, may account

for the effects of saturation harmonics.   No consideration is given

here to the effect of saturation harmonics on the distribution of B_1 and

H_1 in the depth of the iron.   The use of the function $B_1 = AH_1^b$ must

therefore be judged by comparing calculations from the present theory

with the results of experimental and other theoretical work.

4.8 COMPARISON OF THE PRESENT THEORY WITH THE LIMITING NON-LINEAR

THEORY

4.8.1 Power Loss and Power Factor Angle

Since the effects of saturation harmonics of the magnetic quantities

may now be accounted for in the present theory by the use of the function

$B_1 = AH_1^b$, the expression for the loss, P_n, (Equation 4.45) may be compared

with the loss given by the limiting non-linear theory, P_L, (Equation 3.4).

In Table 4.1, the ratios P_n/P (Equation 4.49) and P_L/P are compared,

where P is the power loss in the iron when the permeability is constant

and equal to μ_g (Section 4.5.2).

The ratio P_n/P when $B_1 = AH_1^{0.112}$ is approximately equal to P_L/P

when $B_s = 0.75\ B_{xg}$, which is the definition of B_s proposed by

Agarwal[32]; both these ratios relate to mild steel for values of $\hat{H}_{xg}$

above the knee of the normal B-H curve. The function $B_1 = AH_1^{0.112}$

applies specifically to EN1A mild steel for $2500 < \hat{H}_{xg} < 20000$ A/m

so that P_n/P should be constant for this range of $\hat{H}_{xg}$. Agarwal found

there was good correlation between experimental and theoretical

results for a wide range of $\hat{H}_{xg}$ if $B_s = 0.75\ B_{xg}$.

Although there is agreement between the power loss calculated by

the present non-linear theory and Agarwal's limiting non-linear theory,

the calculated values of power factor angle ϕ_n do not agree; for the

limiting non-linear theory $\phi_n = 26.6°$ (a constant value), whereas for

the present non-linear theory and $b = 0.112$, $\phi_n = 36.7°$ (Equation 4.40)

which is approximately constant for 2500 A/m $< \hat{H}_{xg} < 20000$ A/m.

4.8.2 A Definition of the Saturation Flux Density B_s

By equating the loss obtained by the present theory with that obtained

by the limiting non-linear theory, the saturation flux density, B_s,

may be defined in terms of b and A.

If $P_n = P_L$ for the same value of $\hat{H}_{xg}$,

then from Equations 4.45 and 3.4

$$\beta_n \cdot \alpha_n = \frac{16}{3\pi} \cdot \alpha_L$$

Substituting for $(\beta_n \alpha_n)$ from Equation 4.49

$$\alpha_g K_p = \frac{16}{3\pi} \cdot \alpha_L \qquad\qquad 4.60$$

Substituting for α_g and α_L in Equation 4.60 from Equations 4.23 and

3.3 respectively, and putting $\mu_g = R_b \cdot \dfrac{\hat{B}_{xg}}{\hat{H}_{xg}}$, where $\hat{B}_{xg}$ corresponds to

$\hat{H}_{xg}$ on the normal B-H curve,

$$B_s = \frac{3\pi K_p^2}{16} R_b \cdot \hat{B}_{xg} \qquad\qquad 4.61$$

Since K_p is a function of the exponent b only (Equation 4.49), and R_b is

a function of $\hat{H}_{xg}$ and the shape of the normal B-H curve (Equation 4.57),

B_s may be defined in terms of $\hat{B}_{xg}$ from a knowledge of the normal B-H curve of the material.

For 2500 A/m $< \hat{H}_{xg} <$ 15000 A/m,

$b = 0.112$ (Equation 5. ⎞

$K_p = 1.31$ (Fig. 4.5) ⎬ EN1A Mild Steel

$R_b \simeq 1.25$ ⎠

Substitution of these values into Equation 4.61 gives,

$B_s \simeq 0.75 \hat{B}_{xg}$.

4.9 COMPARISON OF THE PRESENT THEORY WITH OTHER THEORIES USING A FUNCTION OF THE FORM $B = aH^b$

The development of the present theory followed the work of Davies[5,7] as it was realised that the function $B = aH^b$ should be inserted into the diffusion equation at the initial stage of its solution.

It is however, interesting to compare this solution with others which also use the function $B = aH^b$; due to the nature of this function, all such solutions should have a 'limiting depth of penetration', since $\mu \to \infty$ as $H \to 0$. This is so for both the solutions of Nejman[40] and Pillai[38].

Nejman's solution differs from the present solution and, in the opinion of the author, is less credible, since he defines arbitrarily a function for permeability with depth which is introduced into the diffusion equation. The solution of the resulting equation is 'matched' with the function $B = aH^b$ to define the arbitrary constants. On investigation, however, it is found that these constants are the same as those obtained by the present solution. Nejman does not, it is believed, consider the power loss in the iron, its variation with H, or introduce factors K_b and K_p.

Pillai, more recently, gives a 'complete solution' for the two-

dimensional fields in solid iron, but has not published his method of analysis; the permeability on the radial axis is assumed constant, while that on the peripheral axis varies as $\mu = aH^{b-1}$. Pillai's solution is different from the present solution, and from the two-dimensional solution given in Chapter 6, but in its approximate form, when $H_x \gg H_y$, it is found to give the same form of anlytic results (after some manipulation) as that by Nejman and the present theory.

The difference between the final solutions obtained by these theories is in the method of accounting for saturation harmonics, which not only affect the final equation for the loss, but also the field distribution within the depth of the iron.

The author's analysis, which it is believed has not been previously published, is verified in Chapter 5, although its verification has been partly achieved by its comparison with the limiting non-linear theory (Section 4.8). It is felt that the nature of the factors accounting for magnetic non-linearity can be identified more easily in the present theory than in the theories of the other authors.

The theory developed in this chapter is later extended to two-dimensional and three-dimensional cases to obtain solutions chiefly for power loss and flux/pole; the theories by Nejman and Pillai have not been extended in the manner described in this thesis.

4.10   CONCLUSIONS

A non-linear theory has been developed in this chapter for the solid-iron secondary of the model configuration given in Fig.2.1. Although the formulation of the method of solution is similar to that of the graphical solution[23] , the diffusion equation (Equation 4.2) is solved here for the magnetic field quantities subject to the function $B_1 = AH_1{}^b$, where A and b are constants for a stated range of $\hat{H}_{xg}$. The use of the quantities B_1 and H_1 enables the loss due to saturation harmonics to be accounted for (Section 3.4.2.2 and 4.7);   this has not been verified in this chapter. As the normal B-H curve is represented by the function $B = aH^b$, the inclusion in the theory of the quantities B_1 and H_1 is embodied only in the constant A.   The B_1-H_1 curve is related approximately to the normal B-H curve by a theoretical investigation (Section 4.7.1).

The distribution of the electromagnetic field in the depth of the iron has been described in Section 4.2.2, 4.3 and 4.4, where the quantities K_b, β_n and γ_n have been defined;   these quantities account for both the variation of permeability with depth into the iron and the shape of the normal B-H curve.

If P_n is normalised by expressing it as a multiple, K_p , of the power loss, P, (Equation 4.48),

$$K_p = \cdot \frac{P_n}{P} = K_b \, \beta_n \quad \text{(Equation 4.49)}$$

For mild steels, K_p is approximately 1.47 for values of $\hat{H}_{xg}$ above the knee of the normal B-H curve.

It has been shown that the loss equation for the present non-linear theory is approximately equal to that obtained by Agarwal's theory for similar steels and a similar range of surface magnetic field strengths.

CHAPTER 5

COMPARISON OF THE NON-LINEAR ANALYTIC SOLUTION

with

(i) AN EXPERIMENTAL INVESTIGATION ON A ROUND FERROMAGNETIC BAR

(ii) FINITE DIFFERENCE SOLUTIONS.

5.1 INTRODUCTION

Experimental verification of the non-linear theory developed in Chapter 4 (the present theory), is given in this chapter. An experimental investigation of the loss and surface current density in a round ferromagnetic bar is described, and the results obtained are compared with the present analytic solution. This investigation was additional to that on the experimental machine (Chapters 7 and 8).

The present analytic solution is also compared with finite difference solutions. Firstly, a finite-difference solution of the differential equation for the fundamental sinusoid only (Equation 4.13), using the normal B-H curve, gives the distribution of the magnetic field in the depth of the iron. Secondly, a finite difference solution of the diffusion equation (Equation 4.2), using the normal B-H curve, gives the magnetic field quantities in the iron, their waveforms and the loss.

The experimental investigation was carried out on a round bar of EN1A mild steel. The normal B-H curve for this steel was used in calculations both for the present analytic solution and the finite-difference solutions.

5.2. THE PARAMETERS OF THE STEEL USED IN THE EXPERIMENTAL INVESTIGATION

The steel used in all experimental work (Chapters 5, 8, 10) was EN1A Grade 4, Mild Steel (B.S.970) of chemical composition C 0.11%, S 0.25%, Mn 1.15%. The two stators used with the experimental machine (Chapter 7), were flame cut from the same billet and two short bars and a ring specimen were machined from the remaining material; these were annealed at 880° C. Where practicable, annealing was carried out in an inert atmosphere after the final machining operations. The normal B-H curve obtained for the ring specimen , and the derived μ-H curve, are given in Fig . 5.1.

The resistivity of the steel was measured on a cylindrical bar. The resistivity, ρ , at 33° C was found to be:

$$\rho = 1.9 \times 10^{-7} \ \Omega m.$$

5.3 THE CONSTANTS a AND b FOR THE STEEL

The constants a and b in the function $B = aH^{b}$ may be found by plotting the normal B-H curve on log-log paper. The equation represented is,

$$\log B = \log a + b \log H \qquad\qquad 5.1$$

so that b is equal to the slope of the curve and a is then obtained by inserting corresponding values of B and H into Equation 5.1. Fig. 5.2 shows log B against log H for the sample of EN1A steel (Section 5.2). Both a and b are approximately constant for values of H greater than 2500 A/m but change below this value.

In Fig. 5.3, the normal B-H curve is compared with the function $B = aH^{b}$ for,

$$\left. \begin{array}{l} a = 0.664 \\ b = 0.112 \end{array} \right\} \qquad\qquad 5.2$$

There is good agreement between the two curves for 15000 > H > 2500 A/m.

For values of H < 2500 A/m, the function $B = aH^b$ may represent the normal B-H curve with a fair degree of accuracy over a smaller range of H. In Fig. 5.3, the function $B = aH^b$ is compared with the normal B-H curve for

$$\left. \begin{array}{l} a = 0.214 \\ b = 0.258 \end{array} \right\} \qquad 5.3$$

There is close agreement between the curves over a range 500A/m < H < 2500A/m.

5.4 THE EXPERIMENTAL INVESTIGATION

The power loss and surface current density were measured on a round bar of EN1A steel, which was obtained from the same billet as the stators and ring specimen (Section 5.2). 50 Hz a.c. current was passed axially through the bar; this current produced a magnetic field in the peripheral direction. The magnetic field strength at the surface of the bar is given by,

$$H_R = \frac{I}{2\pi R_a}, \qquad 5.4$$

where R_a is the radius of the bar.

The resultant electric field strength along the axis of the bar at any depth is related to the current density by,

$$\underline{E} = \rho \underline{J} \qquad 5.5$$

The distribution of the electro-magnetic field in the bar is governed by the diffusion equation. If the radius of the bar is much greater than the depth of penetration then rectangular co-ordinates may be used; if the radius of the bar is not greater than the depth of penetration then the diffusion equation must be expressed in cylindrical co-ordinates. The diameter of the bar was chosen so that rectangular co-ordinates could be used with negligible error for all surface magnetic field strengths up to and including 15000 A/m.

The choice of bar diameter was based on a comparison of the solutions of the diffusion equation using rectangular and cylindrical co-ordinates in which the permeability of the bar was assumed constant. Mc Lachlan[50] compares the two solutions, for values of the ratio of depth of penetration to radius of the bar. Since the depth of penetration is a function of the permeability, the radius of the bar may be determined for any value of permeability and for any specified difference between the two solutions. A brief description of the comparison of the solutions is given in Appendix II .

In the non-linear analysis, the permeability of the bar varies with depth from the surface. If the magnetic field strength at the surface is greater than that at the knee of the normal B-H curve, the permeability increases with depth into the iron, so that the actual depth of penetration is less than that calculated by the linear theory for a permeability equal to that at the surface. If, therefore, the value of permeability at the surface is chosen for a comparison of the solutions, a 'pessimistic' value for the bar diameter will be determined. For $\hat{H}_R$ = 15000 A/m, the error in assuming rectangular co-ordinates is found to be less than 4% for a nominally 7.6 cm diameter bar.

5.4.1 The Experimental Rig

The bar of EN1A steel, which was machine ground and bright annealed, was connected across the secondary winding of a 10 V, 25 KVA transformer whose primary winding was fed, via a regulator, from 2 lines of a 415 V, 3-phase supply.

To ensure that the current, and therefore the surface magnetic field strength in the bar (H_R), was sinusoidal three large air-cored reactors were connected in series with the bar, whose reactance was greater than the impedance of the bar.

The ends of the bar were drilled and tapped and the bar was bolted between two aluminium busbars, this is shown in Fig. 5.4. To obtain good electrical contact between bar and busbars, the ends of the bar were coppered.
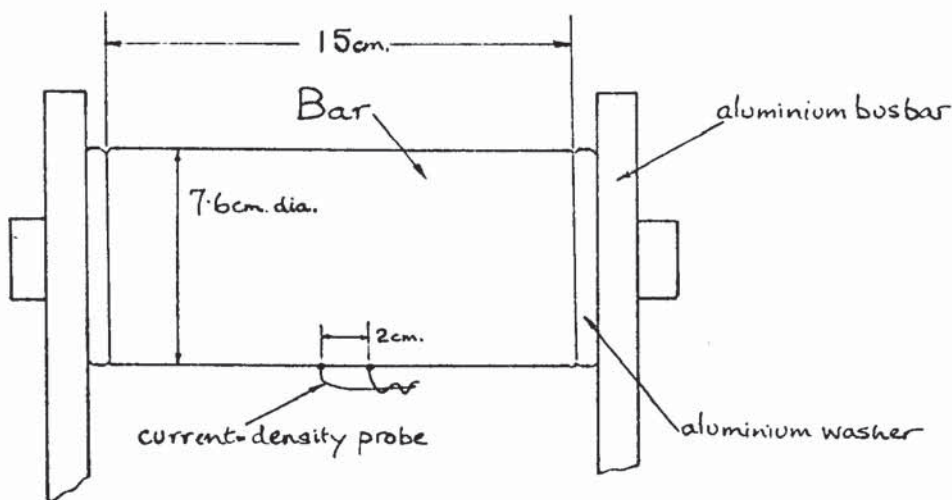
Fig. 5.4 Round Bar of EN1A Steel used in the Experimental Investigation

5.4.2 Measurement Techniques

5.4.2.1 Current Density Probes

The surface current density was obtained by measurement of the voltage drop along the surface of the bar. If a voltage V is measured between two points a distance L_p apart on the bar, the average value of current density over the length L_p is,

$$J = \frac{V.L_p}{\rho}$$

5.6

The probes used to measure the voltage drop consisted of two 0.01 mm diameter nickel-copper wires spot-welded to the surface of the bar. (Section 7.3.3). The distance L_p between the welds was 2 cm (Fig.5.6).

5.4.2.2   Measurement of Power Loss

The loss in the bar is proportional to the product of the voltage from the current-density probes and the total current in the bar. A voltage proportional to the current in the bar was obtained by integration of the output from a linear coupler placed around the bar. This consisted of 1620 turns of copper wire wound on a flexible former. The two ends of the former could be linked to form a toroid around the bar.

5.4.2.3   Instrumentation

An electronic multiplier was used to obtain the product of the voltage signals from the current-density probe and the linear coupler. This instrument had a specified error of 0.1% at its full output of 10 V (peak). It was found that, if both signals were less than 1V, the error was greater than 1%, but, if one signal was maintained near its maximum of 10 V, and the second signal was not lower than 0.5V (peak), the error was no greater than 1%.

To attain the voltage levels required, both signals were amplified. The complete circuit used is shown in Fig. 5.5. Checks were made on the gain of the amplifiers, the phase shift through the circuits, and the effect of the loading of the amplifiers on the signal level. The mean power was obtained by connecting the output from the multiplier to a d.c. digital voltmeter. The amplifiers were adjusted for minimum drift and minimum d.c. bias at each gain setting. The rate of change of the d.c. bias at the output terminals of the integrator was significant at high amplifications, and a decoupling capacitor of 0.1 μF was inserted between the integrator and the preceding amplifier. A check on the resultant phase shift and attenuation due to the capacitor was made and found to be negligible. As a final check on the d.c. bias at the output of the multiplier, the

polarity of the mean power relative to that of the d.c. bias could be reversed by interchanging the leads of the current density probe. (Switch S, Fig. 5.5). The d.c. bias could then be evaluated by taking the difference in the readings.

5.4.2.4. Calibration for Power Loss Measurement

If v_1 and v_2 are a.c. input voltages to the multiplier, the output voltage is

$$v_o = \frac{v_1\, v_2}{10} \qquad\qquad 5.7$$

Let the output voltage from the linear coupler be v_L, then the input to the multiplier is, from Fig. 5.5 and assuming v_L to be sinusoidal,

$$v_1 = \frac{v_L\, A_1\, A_4}{\omega RC} \qquad\qquad 5.8$$

Let the voltage output from the current density probe be v_E, then the input to the multiplier is, from Fig. 5.5,

$$v_2 = v_E\, A_2 \qquad\qquad 5.9$$

Thus from Equations 5.7, 5.8, 5,9,

$$v_o = \frac{v_E\, v_L\, A_2\, A_1\, A_4}{.\, 10\omega RC} \qquad\qquad 5.10$$

But the instantaneous power/m^2, p is,

$$p = \frac{v_E}{L_p} \cdot \frac{v_L}{Y\, 2\pi\, R_a} \qquad\qquad 5.11$$

where Y is the output voltage of the linear coupler per ampere.

Substituting Equation 5.10 into Equation 5.11,

$$P = \frac{10\, V_o . \omega RC}{A_1 . A_2 . A_4 . L_p . 2\pi R_a Y} \qquad\qquad 5.12$$

P is the mean power loss/m^2 if V_o is the d.c. voltage indicated by the digital voltmeter.

5.4.2.5 Phase Angle Measurement

The angle ϕ between the sinusoids of H_R and J was measured by obtaining oscillograms of V_E and V_L (Section 5.7.2.4) and analysing the waveform of V_E. This method of measuring phase angles was

calibrated using the variable phase supply of a signal generator;
the generator produced a d.c. level proportional to the phase
difference between the signals which enabled the phase to be set
to $\pm$ .05°. The method of phase angle measurement was found to
be accurate to $\pm$ 1°.

5.4.3. Discussion of Results

5.4.3.1 The Loss in the Bar

The measured and calculated values of loss are shown in Table
5.1 for peak values of the surface magnetic field strength, $\hat{H}_R$, between
2850 A/m and 15000 A/m, and are plotted in Fig. 5.6 for $\hat{H}_R$ < 3000 A/m.

In Table 5.1, there is good agreement between the measured
values and those calculated by the present theory based on the
function $B_1 = AH_1^{\,b}$ (Equations 4.59 and 5.2).

For $\hat{H}_R$ < 2500 A/m (Fig. 5.8), the present theory gives values
of loss less than those measured, the deviation between them becoming
> 10% for $\hat{H}_R$ < 1250 A/m. The value of A for this region of the
normal B-H curve was determined from Equation 4.58 and Fig. 4.6
for U = 0.

For correlation of measured and calculated loss at values of
$\hat{H}_R$ near the knee of the normal B-H curve it was essential that the
bar underwent the same annealing process as the ring specimen from
which the B-H curve was taken. Loss measurements on a non-annealed
bar of EN1A steel were made and found to be less than the calculated
values by up to 30%.

5.4.3.1.1 The Limiting Non-Linear Theory (Agarwal)

The loss was also calculated by the limiting non-linear theory ,
using Agarwal's empirical equation, $B_s = 0.75 \, B_R$, (Table 5.1);

these calculations agree well with the measured values of loss,
which is not unexpected, as the empiricism in Agarwal's theory has been
justified by the present theory (Section 4.8).   The loss calculated
by Agarwal's theory is less than the measured loss at large values
of $\hat{H}_R$ and is greater than the measured loss at values of $\hat{H}_R$ below
the knee of the normal B-H curve.   (Fig. 5.6 and Table 5.1).

     5.4.3.1.2   The Linear Theory and the Exponent of $\hat{H}_R$

The measured loss is also compared with the loss calculated
from the linear theory (Table 5.1) for,

(i)   relative permeabilities of 250 and 1000

(ii)   permeabilities obtained from Fig. 5.2 which corresponds to

       the magnetic field strength on the surface of the bar ($\hat{H}_R$)

       These will be discussed in turn.

For a relative permeability of 250, the measured and calculated
loss agree approximately at 14700 A/m, whereas the calculated value
is only 68% of the measured value at 2950 A/m.   For a relative
permeability of 1000, the measured and calculated loss agree
approximately for $\hat{H}_R <$ 2950 A/m, whereas at 14700 A/m the calculated
loss is 82% greater than the measured loss.   Since the loss calculated
by the linear theory is proportional to $\hat{H}_R^{\,2}$, it is clear from these
calculations that the exponent of $\hat{H}_R$ for the measured loss is less
than 2.   Log-log plots in Fig. 5.7 of the measured loss against
H_R show that the exponent of $\hat{H}_R$ (given by the gradient of the line)
is equal to 1.57.   By the present theory (Equation 4.47) the
exponent of $\hat{H}_R$ is ($\dfrac{b + 3}{2}$), which is equal to 1.55 when b = 0.112
(Equation 5.2).

For values of permeability obtained from Fig. 5.2 corresponding
to $\hat{H}_R$, the calculated loss was considerably less than the measured

loss, but from a log-log plot of calculated loss against $\hat{H}_R$, the exponent of $\hat{H}_R$ is 1.59 . If μ_g, given by Equation 4.21, is substituted into the linear loss equation (Equation 3.1), the exponent of $\hat{H}_R$ is obtained as $(\frac{b+3}{2})$, which is equal to that obtained by the present theory; this substitution cannot however account for the variation of permeability with depth into the iron.

5.4.3.2 The Surface Current Density and Power Factor Angle

Measured and calculated values of surface current density are tabulated against peak surface magnetic field strength, $\hat{H}_R$, in Table 5.2. The calculated values (fundamental amplitudes) were obtained by Equation 4.37. Two sets of measured values are given, one being the actual peak values of the surface current density and the other the corresponding fundamental amplitudes. The correlation between calculated and measured fundamental amplitudes is good, over the experimental range of excitation.

Plate 5.1 shows typical oscillograms of the voltages from the current density probes (Section 5.4.2.1). Computer analysis of these oscillograms showed that the fundamental amplitudes were 0.92 to 0.96 of the actual peak values. The predominant harmonic components, namely the 3rd, 5th and 7th, are tabulated in Table 5.3 for three values of excitation; the third harmonic component is considerably greater than other components, and increases with an increase in $\hat{H}_R$.

Superimposed on the oscillograms of the voltages from the current-density probes are voltages proportional to the bar current, which were obtained by means of the linear coupler. The bar current is proportional to the magnetic field strength $\hat{H}_R$. The power factor angle, ϕ_n, between the fundamental component of surface current density and surface magnetic field strength was found to be within the range $30.3°$ to $31.2°$ over the experimental range of excitation. The calculated phase angle, ϕ (Equation 4.39) is

36.7° for EN1A mild steel for 2500 A/m $< \hat{H}_R <$ 20000 A/m, (b = 0.112.)
Although the measured values of ϕ_n are lower than the calculated
value of 36.7°, they are virtually constant over the experimental
range of excitation.

5.5 FINITE DIFFERENCE SOLUTION OF EQUATION 4.13

Finite-difference techniques (Section 3.6) were used to solve
Equation 4.13, which defines the penetration of the magnetic field
into the iron subject only to a change of permeability with depth.

Equations 4.11 and 4.12, from which Equation 4.13 is obtained,
were written in finite-difference form. Initial values of H were
obtained by assuming the region of the normal B-H curve between
H = 0 and H = 250 A/m to be linear; these values of H were assumed
to occur at a depth y into the iron. The finite-difference equations
were progressively solved, subject to the normal B-H curve (Fig. 5.2),
for decreasing values of y. A brief description of the solution
is given in Appendix III.

The results of the computation for a frequency of 5 Hz are
shown in Fig. 5.8 . Δy was chosen as 0.02 mm in order to limit
oscillations of $\frac{d\varepsilon}{dy}$ to negligible proportions. Also plotted in Fig.
5.8 are the results of the analytic solution using the values of
b and a given in Equation 5.2. The solutions are almost coincident
for 2500 A/m < H <15000 A/m, but diverge below about 2500 A/m.
Inaccuracies in the solution are thus due to the difference between
the function $B = aH^b$ and the normal B-H curve rather than the form
of solution (Equation 4.30). The effect of these inaccuracies
on the loss calculation are discussed in the next section.

5.6   ANALYTIC SOLUTION FOR THE DISTRIBUTION OF THE ELECTROMAGNETIC

      FIELD IN THE IRON

As the wave of magnetic field strength penetrates into the iron,
its amplitude decreases and the values of a and b will change (Fig.5.4).
Since the theory is based on the assumption that a and b are constants,
it is only strictly applicable to peak values of the surface magnetic
field strength, $\hat{H}_{xg}$, much greater than 2500 A/m, when changes in a
and b occur only at considerable depth into the secondary.   For
values of $\hat{H}_{xg}$ near the value at the knee of the normal B-H curve,
the range of $\hat{H}_x$ represented by any single function $B = aH^b$ is small.
If however, the power is dissipated within this range of $\hat{H}_x$, there
is little error in the loss calculation.   The accuracy of the theory
may thus be judged by comparing the attentuation of $\hat{H}_x$ (Equation 4.27)
and the loss density, P_y, (Equation 4.44) with depth into the iron.

Fig. 5.9   shows the attenuation of the field quantities with
depth into the iron at 5 Hz for a surface field strength of 15000
A/m using the values of a and b given in Equation 5.2.   It is seen
that $\hat{H}_x$ attenuates to 2500 A/m, 0.167 p.u. of the surface value,
at a depth of 9.2 mm.   The loss density has reduced to 0.062 p.u.
of the total loss in the iron at this depth, and there is little
error in the loss calculation.   Fig. 5.10 shows the attenuation
with depth at 5 Hz of the field quantities for a surface field strength
of 5000 A/m for the same values of a and b, (Equation 5.2).   At 2500
A/m, where the B-H curve and the function $B = aH^b$ diverge, the loss
density is 0.34 p.u.   This does not mean that the error in the
calculation of the total loss is 0.34 p.u.   The magnetic field
penetrates into the iron beyond 9.2 mm but attenuates at a greater
rate than that determined using the normal B-H curve, (Fig. 5.8).
The error in the loss will, therefore, be some fraction of 0.34 p.u.

The magnitude of this error is determined by comparison of the calculated loss with that obtained by an experimental investigation and the finite difference solution of the diffusion equation. This also applies to the loss calculations for surface field strengths less than 2500 A/m where mean values of a and b are chosen.

5.7   FINITE DIFFERENCE SOLUTION OF THE DIFFUSION EQUATION

The finite-difference technique applied by Gillot and Calvert[42] was used to obtain solution to the diffusion equation (Equation 4.2). Although more refined techniques now exist, this method has been successfully applied by a number of researchers and is used here to provide only a comparison with the analytic and experimental results.

Gillot and Calvert considered the case of an infinitely long, flat plate of thickness 2d with a time-varying magnetic field applied parallel to its surfaces. Due to the symmetry of the resultant field about the centre line of the plate, only half the plate thickness need be considered in the computation. If the plate thickness is very much greater than the depth of flux penetration, the solution approximates to that of an infinitely thick slab.

A brief description of the finite difference method is given in Appendix IV. Both the flux penetration and the loss in the plate at 50 Hz were computed for peak values of surface magnetic field strength, H_o, of 5000 A/m and 10000 A/m. The half width of the plate was assumed to be 0.01 m and the waveforms of the magnetic field quantities were computed at depths of y = 0, 1, 2 .....mm. Each half cycle of the waveforms was divided into 180 ordinates.

5.7.1   Results of the Computation

5.7.1.1 Loss

The computed values of loss are given in Table 5.4 ; these results agree well with those obtained from the experimental

investigation on the bar and by the present theory (Section 5.4.3.1 and Table 5.1).

5.7.1.2   Analysis of the Waveforms

The peak values and analysis of the flux density and magnetic field strength waveforms are given in Table 5.5   for a surface magnetic field strength, H_o, of 10000 A/m;   typical waveforms of these quantities are given in Fig. 5.11.   Since the present analytic theory is for fundamental components only, the following observations are made concerning the fundamental components of the computed waveforms (Table 5.5).

(i)   The ratio of the flux density corresponding to the fundamental component of H on the normal B-H curve (B_{h1}) to the fundamental component of B (B_1), are in reasonable agreement with the calculated values of R_b given in Fig. 4.6 (Section 4. 7.1).

(ii)   The attenuation with depth of H, calculated by the present non-linear theory for $\hat{H}_o$ = 10000 A/m, is shown in Fig. 5.8. The attenuation with depth for the theory based on $B_1 = AH_1^b$ is greater than that for $B = aH^b$, and the values of the fundamental component of H obtained by the finite-difference solution (Table 5.5) at 1 mm and 2 mm are seen to be almost equal to the values obtained by the theory based on $B_1 = AH_1^b$.

5.8 CONCLUSIONS

A comparison of theoretical and experimental results has been given in this chapter to verify the non-linear theory developed in Chapter 4. The finite-difference solution of Equation 4.13 (Section 5.5) which defines the penetration of the magnetic field into iron whose permeability changes only with depth, has shown that the present theory may be inaccurate due to the analytic representation of the normal B-H curve. The divergence between the finite difference solution and the analytic solution (Fig. 5. 8) occurs only at depths near to the limiting depth of penetration, δ_n , if the surface magnetic field strength is greater than that at the knee of the normal B-H curve. The error in the loss calculation should be small, since the attenuation with depth of power loss density is greater than that of the magnetic field (Section 5.5); this is verified by the good agreement between the loss calculated by the present analytic solution for $\hat{H}_{xg} > 2500$ A/m, the loss measured in the bar (Table 5.1), and the loss obtained by the finite difference solution of the diffusion equation, (Equation 4.2). Hysteresis loss may be the reason for the measured values of loss being greater than the calculated values for values of $\hat{H}_{xg}$ near the knee of the normal B-H curve (Fig. 5. 6).

The finite-difference solution of the diffusion equation (Equation 4.2), gave values of the fundamental component of the magnetic field strength which were approximately equal to the corresponding values obtained by the present theory. This evidence, together with the agreement between the measured and calculated values of loss and surface current density, support the view that the function $B_1 = AH_1^b$ adequately represents the distribution of the fundamental component of B_x and H_x in the iron. The calculated

and measured values of power factor angle, ϕ, do not however, agree (Section 5.4.3.2) the calculated angle being 36.70°, and the mean value of the measured angle, 30.70°. As predicted by the present theory, there is little variation in the measured angle for 2950 A/m $< \hat{H}_{xg} <$ 15000 A/m. Hysteresis (Section 3.4.2.3) may account for part of the difference between the angles, but not to the extent of 5° at values of $\hat{H}_{xg}$ well above the knee of the normal B-H curve. Although this difference in angle appears significant, the difference in power loss that it produces is within acceptable limits.

The measured waveforms of surface current density (Plate 5.1) are similar to those obtained by the limiting non-linear theory. As waveforms of this shape were obtained experimentally at values of $\hat{H}_{xg}$ near the knee of the normal B-H curve, they do not necessarily indicate saturation of the iron; their shape must be due to the shape of the hysteresis loop rather than that of the normal B-H curve.

The loss calculated by Agarwal's theory is greater than the measured loss at small values of $\hat{H}_{xg}$ and less than the measured loss at large values of $\hat{H}_{xg}$, although the differences are small; this indicates that the empirical relationship, $B_s = 0.75 \hat{B}_{xg}$, is strictly true for only one value of $\hat{H}_{xg}$. There is also little difference between the values of loss calculated by Agarwal's theory and the present theory for 2950 A/m $< \hat{H}_{xg} <$ 15000 A/m (Table 5.1), since B_s is a function of the exponent b, which is virtually constant over this range of $\hat{H}_{xg}$. An advantage of the present theory over Agarwal's theory is that it contains factors (a and b) which describe the shape of the normal B-H curve for the material and may therefore be used with greater accuracy at very large values of $\hat{H}_{xg}$; the author has demonstrated[51] that the loss in directly heated ferromagnetic billets ($\hat{H}_{xg}$ = 150000 A/m), is approximately 11% greater than that calculated by Agarwal's theory.

CHAPTER 6

AN ANALYSIS OF THE TWO-DIMENSIONAL MODEL INCLUDING
MAGNETIC NON-LINEARITY

6.1 . INTRODUCTION

In this chapter, the one-dimensional non-linear theory given
in Chapter 4 is included in an analysis of the two-dimensional model
of Fig. 1.1.

A general relationship between the peripheral component of
magnetic field on the surface of the secondary, $\dot{H}_{xg}$, and the primary
excitation, $\hat{K}$, is derived in Section 6.2. In Sections 6.3 and 6.4
the non-linear solution obtained in Chapter 4 is introduced into the
general relationship between $\dot{H}_{xg}$ and $\hat{K}$ and the resulting equation
enables the loss in the iron to be defined in terms of the primary
excitation.

The conditions for maximum torque or loss are defined by
equating the moduli of the input and output impedances of the
secondary region; the ratio of the moduli of the impedances is
given by a new dimensionless quantity Q_n, so that maximum torque
occurs when $Q_n = 1$. Q_n is obtained in terms of the dimensions and
physical constants of the machine. This method of obtaining the
conditions for maximum torque was derived for the linear analysis
(Section 2.7.2.2) but is shown in this chapter to be applicable to
magnetically non-linear regions.

Expressions for loss, torque, eddy-current reaction and
flux/pole are obtained in terms of Q_n, the parameters of the machine
and the primary excitation, by using the relationship between $\dot{H}_{xg}$
and $\hat{K}$ which is derived in Sections 6.2 to 6.4. From the expression
for Q_n and torque, generalised torque/frequency curves are obtained.
The work in this chapter is believed to be original.

6.2 GENERAL SOLUTION FOR THE FIELD COMPONENTS ON THE SURFACE OF THE SECONDARY IN TERMS OF THE PRIMARY CURRENT SHEET.

Referring to Fig. 2.4, which illustrates the field in the air gap,

$$\text{let } \dot{H}_{yga} = \dot{S} \dot{H}_{xg} \qquad \qquad 6.1$$

where both $\dot{H}_{yga}$ and $\dot{H}_{xg}$ are complex quantities with respect to the co-ordinate system (Fig. 2.4) and $\dot{H}_{yga}$ is the radial component of the magnetic field in the air gap at the surface of the secondary ($y = g$).

The general solution for the field in the air gap is given by Equation 2.15 so that

$$\dot{H}_{xa} = (Ae^{-qy} + Ge^{qy})\, e^{-jqx} \qquad \qquad 6.2$$

When $y = 0$, $\dot{H}_{xao} = -\hat{K}e^{-jqx}$

and Equation 6.2 becomes $A + G = -\hat{K}$ $\qquad \qquad 6.3$

When $y = g$ Equation 6.2 becomes

$$\dot{H}_{xg} = (Ae^{-qg} + Ge^{qg})\, e^{-jqx} \qquad \qquad 6.4$$

From Equation 2.8

$$\frac{\partial \dot{H}_{ya}}{\partial x} = \frac{\partial \dot{H}_{xa}}{\partial y}$$

and therefore

$$\dot{H}_{ya} = \int \frac{\partial \dot{H}_{xa}}{\partial y} \cdot dx$$

which becomes, from Equation 6.2

$$\dot{H}_{ya} = j\,(Ge^{qy} - Ae^{-qy})\, e^{-jqx}$$

and at $y = g$, using Equation 6.1,

$$\dot{S}\dot{H}_{xg} = j\,(Ge^{qg} - Ae^{-qg})\, e^{-jqx} \qquad \qquad 6.5$$

From Equations 6.3 and 6.4

$$(\dot{H}_{xg} + \hat{K}e^{-qg}) = 2G\ \sinh qg\ e^{-jqx} \qquad \qquad 6.6$$

and from Equations 6.4 and 6.5,

$$(1 - j\dot{S})\,\dot{H}_{xg} = 2Ge^{qg}\ e^{-jqx} \qquad \qquad 6.7$$

Thus substituting for G, from Equation 6.7, into 6.6.,

$$\dot{H}_{xg} = \frac{- \hat{K}_c e^{-jqx}}{\cosh qg \ (1 - j \dot{S} \tanh qg)} \qquad 6.8$$

$\dot{H}_{yg}$ may be obtained from Equations 6.8 and 6.1.

6.3 RELATIONSHIP BETWEEN THE FIELD QUANTITIES ON THE SURFACE OF THE SECONDARY IRON ($\dot{S}$) FOR THE PRESENT NON-LINEAR THEORY

In the previous Section (6.2), $\dot{H}_{xg}$ was expressed in terms of the primary excitation, the dimensions of the machine and the complex quantity $\dot{S}$ (Equation 6.1). $\dot{S}$ may be obtained using the one-dimensional non-linear solution (Chapter 4) for the solid iron, provided it is assumed that the current-density distribution is dependent only on the distribution of the peripheral component of the magnetic field; this has been discussed in Section 3.7 and 4.2 where it was shown that this assumption is valid if $\frac{q^2}{2\alpha^2} \ll 1$ at the surface of the secondary.

The amplitude of the current density at the surface of the secondary iron ($y = g$) obtained by the one-dimensional non-linear theory is given in Equation 4.37 as

$$\hat{J}_{zg} = \alpha_n (\beta_n + j\gamma_n) \hat{H}_{xg}$$

so that from Equation 2.7

$$\hat{E}_{zg} = \rho \alpha_n (\beta_n + j\gamma_n) \hat{H}_{xg} \qquad 6.9$$

Considering now the two-dimensional model of Fig. 1.1, the electric field (Equation 6.9) must be induced, as in the linear case, by a radial component of flux density rotating in the peripheral (x) direction at uniform velocity. Since it is assumed, in Chapter 4, that the electromagnetic field quantities vary sinusoidally in time, the distribution of these quantities in the peripheral direction must also be sinusoidal.

Thus Equation 6.9 becomes, in the notation of Equations 2.10 and 2.11,

$$\dot{E}_{zg} = \rho \alpha_n (\beta_n + j\gamma_n) \dot{H}_{xg} \qquad 6.10$$

where $\dot{H}_{xg} = \hat{H}_{xg} e^{-jqx}$ and $q = \dfrac{2\pi}{\lambda}$

For the linear air-gap region, Equation 2.3 applies, so that

$$\frac{\partial E_z}{\partial y} = - j\omega B_x$$

and $\dfrac{\partial E_z}{\partial x} = j\omega B_y$ 6.11

Thus, from Equation 6.10 and 6.11

$$\dot{B}_{yg} = \frac{-q\rho}{\omega} \cdot \alpha_n (\beta_n + j\gamma_n) \dot{H}_{xg} \qquad 6.12$$

Thus the radial component of the surface magnetic field strength in the air gap is,

$$\dot{H}_{yga} = \frac{-q\rho\alpha_n}{\omega\mu_o} (\beta_n + j\gamma_n) \dot{H}_{xg} \qquad 6.13$$

so that, from Equation 6.1,

$$\dot{S} = \frac{-q\rho\alpha_n}{\omega\mu_o} (\beta_n + j\gamma_n) \qquad 6.14$$

(The quantity $\dot{S}$ is used not only in this chapter but also in the three-dimensional analysis given in Chapter 9).

6.4 THE PERIPHERAL COMPONENT OF MAGNETIC FIELD STRENGTH, $\dot{H}_{xg}$

Substituting Equation 6.14 into 6.8, the peripheral component of the magnetic field strength at the surface of the secondary is obtained as,

$$\dot{H}_{xg} = \frac{-\hat{K} e^{-jqx}}{\cosh qg (1 - jK_s\beta_n + K_s\gamma_n)} \qquad 6.15$$

where $K_s = \dfrac{q\rho\alpha_n}{\omega\mu_o} \cdot \tanh qg$ 6.16

Thus the modulus of H_{xg} may be obtained as

$$|\dot{H}_{xg}| = \frac{\hat{K}}{\cosh qg (1 + 2K_s\gamma_n + K_s^2 R_n^2)^{\frac{1}{2}}} \qquad 6.17$$

where $R_n^2 = \gamma_n^2 + \beta_n^2$

Now from Equations 4.24, 4.23 and 4.21 and 4.58, Equation 6.16

may be written,

$$K_s = \frac{qK_b}{\sqrt{2}\mu_o} \cdot \left[\frac{\rho A}{\omega}\right]^{\frac{1}{2}} \cdot |H_{xg}|^r \cdot \tanh qg \qquad 6.18$$

where $\quad r = \dfrac{b - 1}{2}$

The effects of magnetic non-linearity are included in Equation 6.18 by means of quantities r, K_b and A, where,

(i)   the exponent r accounts for the variation of permeability with magnetic field strength, i.e. when the permeability is constant, $b = 1$ and $r = o$.

(ii)   the quantity $A = aR_b$ (Equation 4.58) where R_b accounts for the effects of the saturation harmonics of the magnetic quantities

and (iii)   the quantity K_b (Equation 4.25) accounts for the variation of permeability with depth into the secondary iron.

Substituting Equation 4.41 into Equation 6.17,

$$|\dot{H}_{xg}| = \frac{\hat{K}}{\cosh qg \left[1 + 2 \sin\phi_n K_s R_n + K_s^2 R_n^2\right]^{\frac{1}{2}}} \qquad 6.19$$

$|\dot{H}_{xg}|$ may be calculated from this equation if the following data is available,

(i)   the amplitude and frequency of the primary excitation,

(ii)   the dimensions of the machine.

(iii) the resistivity of the secondary iron.

(iv) the normal B - H curve for the secondary iron.

Once $|\dot{H}_{xg}|$ has been determined, the loss and surface current density may be obtained from Equations 4.45 and 4.37 respectively.

6.5   LOSS AND TORQUE, AND THE FACTOR Q_n

In Section 2.7.2.3 it was shown that for maximum loss in

the secondary iron,

$$|\dot{Z}_{yg}| = |\dot{Z}_{ygr}| \qquad\qquad 6.20$$

when $\left.\begin{array}{c}\mu_p \\ \mu_s\end{array}\right\} \gg 1$ and the eddy current field is strong (η tanhqg $\ll 1$).

It was also shown that, for the same conditions, the combined

effect of the eddy-current field is equivalent to a current sheet

on the surface of the secondary whose line current density is

equal to $\dot{H}_{xg}$. Under these conditions $|\dot{Z}_{ygr}|$ is given by

Equation 2.78 which does not include the secondary iron

parameters. Thus Equation 2.78 also applies to the non-linear

case if $\mu_g \gg 1$. $|\dot{Z}_{yg}|$ is obtained from Equation 4.43, so that

Equation 6.20 becomes,

$$\rho \cdot R \cdot \alpha_n = \frac{\mu_o \cdot \omega}{q \cdot \text{tanhqg}} \qquad\qquad 6.21$$

and in general

$$\frac{|\dot{Z}_{yg}|}{|\dot{Z}_{ygr}|} = Q_n = \frac{\mu_o \omega}{q \cdot \rho \cdot R_n \cdot \alpha_n \cdot \text{tanhqg}} \qquad\qquad 6.22$$

where $Q_n = 1$ for maximum loss and the suffix n denotes the non-

linear case.

Substituting for α_n from Equations 4.49, 4.23, and 4.21

into Equation 6.22,

$$Q_n = \frac{\sqrt{2}\,\mu_o}{q \cdot R_n \cdot \text{tanhqg} \cdot K_b \cdot |\dot{H}_{xg}|^r} \left[\frac{\omega}{\rho A}\right]^{\frac{1}{2}} \qquad\qquad 6.23$$

Comparison of Equation 6.23 with Equation 6.18 shows

that

$$Q_n = \frac{1}{K_s R_n} \qquad\qquad 6.24$$

Substituting Equation 6.24 into 6.19 and noting that

$|\dot{F}_r| = \dfrac{|\dot{H}_{xg}|}{q}$ and $|\dot{F}_c| = \dfrac{\hat{K}}{q}$ (from Section 2.7.3), then

$$|\dot{F}_r| = \frac{|\dot{F}_c| \cdot Q_n^{\frac{1}{2}}}{\text{coshqg}\left[Q_n^{-1} + Q_n + 2\,\sin\phi_n\right]} \qquad\qquad 6.25$$

Equation 6.25 has the same form as Equation 2.96 for the linear case (b = 1) where $2 \sin\emptyset_n = \sqrt{2}$.

The loss unit area, P_n may also be given in term of $|\dot{F}_r|$ from Equations 4.45 and 2.89,

$$P_n = \frac{|\dot{F}_r|^2}{2} \cdot \rho \beta_n \alpha_n q^2 \qquad\qquad 6.26$$

P_n may be expressed in terms of the primary excitation $|\dot{F}_c|$ by substituting Equation 6.25 into 6.26 and using Equation 6.22 and 4.40,

$$P_n = \frac{|\dot{F}_c|^2 \cdot \mu_o \cdot \omega \cdot q \cdot \cos\emptyset_n \cdot \Delta_n}{2 \cdot \sinh qg \cdot \cosh qg} \qquad\qquad 6.27$$

and the torque is

$$T_n = \frac{P_n P}{\omega} (\pi D\, L_A) \qquad\qquad 6.28$$

where $\Delta_n = \dfrac{1}{Q_n^{-1} + Q_n + 2 \sin\emptyset_n}$ \qquad\qquad 6.29

The maximum loss unit area, P_{nm}, occurs when $Q_n = 1$, so that

$$P_{nm} = \frac{|\dot{F}_c|^2 \cdot \mu_o \cdot \omega \cdot q \cdot \cos\emptyset_n \cdot}{4 \cdot (1 + \sin\emptyset_n) \sinh qg \cdot \cosh qg} \qquad\qquad 6.30$$

and

$$T_{nm} = \frac{P_{nm} P}{\omega} (\pi D\, L_A) \qquad\qquad 6.31$$

where T_{nm} is the maximum torque

Thus, the normalised torque is given by,

$$\frac{T_n}{T_{nm}} = \left[\frac{2 + 2 \sin\emptyset_n}{Q_n^{-1} + Q_n + 2 \sin\emptyset_n} \right] \qquad\qquad 6.32$$

(Equation 6.32 reduces to Equation 2.57 when b = 1).

For any particular machine, Q_n varies only with excitation and frequency. At constant excitation, there will be a frequency at which the torque is a maximum, i.e. when $Q_n = 1$.

ω_{mm}, the angular frequency at maximum torque, may be obtained in terms of the primary excitation $|\dot{F}_c|$ from Equations 6.23 and 6.25

by putting $Q_n = 1$,

$$\omega_{nm} = \frac{q^{(b + 1)} . A . \rho . R_n^2 . K_b^2 \sinh^2 qg . \left[2 + 2 \sin \emptyset_n\right]^{\frac{(1 - b)}{2}}}{2 . |\dot{F}_c|^{(1 - b)} . \mu_o^2 . \cosh^{(b+1)} qg} \qquad 6.33$$

(Note that ω_{nm} becomes independent of $|\dot{F}_c|$ when $b = 1$)

The development of the expressions for maximum loss and torque in this section has been based on the general criterion of impedance matching at the secondary surface. The maximum loss or torque, and thus Q_n, could have been obtained by the more fundamental, though lengthier, method of differentiating the expression for loss or torque and equating the resultant expression to zero.

Two significant differences from the linear analysis are noted. Firstly, that Q_n and ω_{nm} are dependent on the primary excitation (represented by $\dot{F}_c$ or indirectly by $\dot{H}_{xg}$). The inclusion of the excitation, and the constant A, in the expressions for these quantities is indicative of the change in the value of permeability with excitation.

Secondly, that P_{nm} and T_{nm} are dependent on the angle $\emptyset_n$ and therefore on the shape of the normal B-H curve, whereas in the linear analysis ω_m and T_m were only dependent on the airgap quantities. The maximum loss or torque may be increased by as much as 25% due to the non-linearity of the iron (the maximum difference occurs when $b = 0$).

Q_n may also be expressed in terms of the primary excitation and the parameters of the machine. From Equations 6.23 and 6.25,

$$N_\Delta = \frac{2 . \mu_o^2 . \omega . |\dot{F}_c|^{(1 - b)} . \cosh^{(b - 1)} qg .}{q^{(b + 1)} . \rho . R_n^2 . K_b^2 . A . \tanh^2 qg .} \qquad 6.34$$

where $N_\Delta = (Q_n^{\frac{b + 3}{2}} . \Delta_n^{\frac{b - 1}{2}})$ \qquad 6.35

from which Q_n may be calculated. (Δ_n is expressed in terms

of Q_n in Equation 6.29).

6.5.1   Generalised Torque/Frequency Characteristics.

Q_n may be expressed in terms of the normalised torque, from Equations 6.23, 6.25, 6.32 and 6.33 as

$$Q_n = \left[\frac{\omega}{\omega_{nm}}\right]^{\frac{2}{3+b}} \cdot \left[\frac{T_n}{T_{nm}}\right]^{\frac{1-b}{3+b}} \qquad\qquad 6.36$$

so that T_n/T_{nm} may be plotted against ω/ω_{nm} from Equation 6.31 for values of the exponent b.

The graph of T_n/T_{nm} against ω/ω_{nm} for b = 0.112 (Equation 5.2) is shown in Fig. 6.1, together with the curve for b = 1.   Note that the T_n/T_{nm} is symmetrical about ω/ω_{nm} = 1 when b = 1, but is asymmetric about ω/ω_{nm} = 1 when b < 1.   Graphs so obtained are normalised torque/frequency characteristics, but since T_{nm} and ω_{nm} are defined in terms of the primary excitation and the parameters of the machine by Equations 6.31 and 6.33 respectively, they become generalised torque/frequency characteristics where $1/T_{nm}$ and $1/\omega_{nm}$ are the torque and frequency coefficients respectively.

From Equation 6.34, when b = 1, $Q_n = (\omega/\omega_{nm})^{1/2}$ $\qquad$ 6.37

and   when b = 0 $Q_n = (\omega/\omega_{nm})^{2/3} \cdot (T_n/T_{nm})^{1/3}$ $\qquad$ 6.38

The exponents in Equation 6.37 and 6.38 were also obtained by Davies for the same limiting conditions.   In fact many of the exponents obtained in this chapter are approximately equal in value to those derived by Davies[7]   for the same B-H curve;   this might be expected for it has been shown in Section 5.7.3.1 that the substitution of the function $B = aH^b$ into the linear loss Equation (Equation 3.1), which in principle is the method used by Davies, gives the same exponent of $\hat{H}_{xg}$ as obtained in the non-linear loss equation (Equation 4.45).

The difference between the loss expressions occurs in the

constant of proportionality which is greater in the present non-linear theory due to the inclusion of K_b, which accounts for the variation of the permeability with depth, and the constant A (Equation 4.58) which accounts for the contribution of the saturation harmonics of flux density and magnetic field strength.

6.6   THE FLUX/POLE-TORQUE RELATIONSHIP

The mean value of the air gap flux density at the surface of the secondary (y = g) is,

$$B_{y \, mean} = \frac{2}{\pi} \left| \dot{B}_{yg} \right|$$

The flux/pole = $(B_y \, mean)$ x (pole area)

Thus from Equation 6.12 the flux/pole is

$$\Phi = \frac{2\rho \alpha_n R_n L_A}{\omega} \cdot \left| \dot{H}_{xg} \right| \qquad 6.39$$

The flux per pole, Φ, may also be expressed in terms of $\left| \dot{F}_c \right|$ and Q_n.

From Equation 6.39, 6.22 and 6.25,

$$\Phi = \frac{2 \left| \dot{F}_c \right| \mu_o}{\sinh qg} \cdot \frac{\Delta_n}{Q_n^{\frac{1}{2}}} \qquad 6.40$$

The torque may be related to $\left| \dot{H}_{xg} \right|$ from Equation 4.45

giving
$$T_n = \frac{\left| \dot{H}_{xg} \right|^2 \cdot P^2 \cdot \beta_n \cdot \alpha_n \cdot L_A}{\omega q} \qquad 6.41$$

Thus, eliminating $\left| \dot{H}_{xg} \right|$ between Equations 6.39 and 6.41, and substituting for α_n from Equation 4.24 ,

$$\Phi = R_n \cdot \left[\frac{1}{P} \right]^{\frac{2+2b}{3+3b}} \cdot \left[\frac{qT_n}{\beta_n} \right]^{\frac{1+b}{3+b}} \cdot \left[\frac{2AK_b}{\omega} \right]^{\frac{1}{3+b}} \cdot \left[\frac{1}{\rho} \right]^{\frac{b+2}{b+3}} \qquad 6.42$$

so that,

$$\Phi \alpha \left[T_n \right]^{\frac{b+1}{b+3}} \qquad 6.43$$

or ,
$$T_n \alpha \left[\Phi \right]^{\frac{b+3}{b+1}} \qquad 6.44$$

which has limiting values of ,

$$T_n \, \alpha \, \Phi^2 \quad \text{when } b = 1 \qquad 6.45$$

$$T_n \, \alpha \, \Phi^3 \quad \text{when } b = 0 \qquad 6.46$$

6.7   CONCLUSION

A general solution has been obtained for the magnetic field components on the surface of the secondary in terms of the primary excitation, the dimensions of the machine and the complex quantity $\dot{S}$ (Equation 6.1). $\dot{S}$ was determined for the present non-linear theory by equating the solutions for the solid-iron region and air gap at the iron/air boundary. Thus the magnetic field at the surface of the secondary is given in terms of the primary excitation and the dimensions and parameters of the machine (Equation 6.19). Since the loss in the secondary iron has been expressed in terms of the magnetic field at its surface (Equation 4.45), equation 6.19 enables the loss to be obtained in terms of the primary excitation (Equation 6.27).

Maximum torque or loss occurs when the non-dimensional quantity $Q_n = 1$. Q_n has been obtained in terms of the parameters and dimensions of the machine (Equation 6.23) by using the condition that Q_n equals the ratio of the input and output impedances of the solid iron region if the eddy-current field is strong and $\left.\begin{array}{c}\mu_p \\ \mu_s\end{array}\right\} \gg 1$. This proves to be a simple way of defining the conditions at maximum torque compared with the more usual method of obtaining the differential of the torque with respect to frequency. It is, in principle, a form of the maximum power transfer theorem and could no doubt be obtained by means of a lumped-parameter equivalent circuit[*]. It has however been deduced in Chapter 2 by a full and detailed analysis of the field distribution in the machine; all qualifying conditions are therefore clearly defined in applying the principle of impedance matching to a machine containing distributed parameters throughout.

Using the definition of Q_n in Equation 6.23 and the relationship between $\dot{H}_{xg}$ and $\hat{K}$ in Equation 6.19, the eddy-current reaction mmf $\dot{F}_r$

---

[*] This method, using an equivalent circuit, has since been derived by Chalmers[67] to obtain a general theory for solid rotor induction machines, based on the limiting non-linear B-H characteristic.

the flux/pole and the torque, or loss, have been obtained in terms of the primary excitation and Q_n.

By putting $Q_n = 1$ expressions for maximum loss or torque were obtained (Equations 6.30 and 6.31). It is noted that the maximum torque or loss are functions of the angle $\emptyset_n$ and therefore vary with the shape of the B-H curve. If the curve changes from a linear (b = 1) to a rectangular (b = 0) relationship, all other quantities being the same, the maximum torque will increase by approximately 25%. Physically, this is equivalent to a reduction in the reactance to the secondary currents due to saturation of the iron.

ω_{nm}, the angular frequency at maximum torque, has been obtained from the definition of Q_n (Equation 6.23) and is expressed in terms of the primary excitation, the dimensions and physical constants of the machine in equation 6.33. The primary excitation together with the constant A (Equation 4.58) define the permeability of the secondary iron, so that ω_{nm} becomes independent of the primary excitation when the permeability is constant (b = 1).

By defining Q_n in terms of the normalised torque (T_n/T_{nm}) and (ω/ω_{nm})(Equation 6.36), generalised torque/frequency characteristics have been obtained for values of b. These curves are asymmetric about $Q_n = 1$ for all values of b < 1. (It must be remembered that all expressions may be simplified if qg << 1 when sinh qg $\rightarrow$ qg and cosh qg $\rightarrow$ 1).

The derivation of a relationship between torque and flux/pole concludes the analysis of this chapter. It is found that there is considerable difference in the relationship between torque and flux/pole for linear and non-linear conditions (Equations 6.45 and 6.46) so that by plotting measured torque against measured flux/pole it should be possible to obtain a clear indication of the validity of the theory.

CHAPTER 7

THE EXPERIMENTAL MACHINE AND EXPERIMENTAL PROCEDURE

7.1   INTRODUCTION

The non-linear theory developed in Chapters 4 and 6, and its modification to account for finite length effects (Chapter 9) were verified by measuring torque, surface current density, air-gap flux and flux penetration on a specially designed experimental machine.   The machine is of a cylindrical form, having a 4-pole polyphase rotor and alternative solid-iron stators, one with copper end rings and one without copper end rings.   Measurements were taken over a range of frequency of 1 to 100 Hz and rotor excitations up to 20,000 A/m.

At the start of the project much of the proposed experimental work had not been attempted by previous researchers, particularly many aspects of the flux penetration measurements and the estimation of the current-density distribution over the surface of the stator.   Considerable development of experimental techniques was required, so that a preliminary investigation was carried out on a machine consisting of a polyphase rotor and solid iron stator (without copper end rings), using existing equipment in the laboratory.   This Chapter commences with a brief description of part of the preliminary investigation to indicate the formulation of the experimental machine and procedure.

The experimental machine is described in Section 7.3.   The experimental techniques and instrumentation used to measure flux penetration, surface current density and airgap flux density are described in Section 7.4.   The final section of this Chapter (Section 7.7) contains a description of tests carried out on the experimental machine to determine the effectiveness of the copper rings.

7.2 THE PRELIMINARY INVESTIGATION

7.2.1 General

The experimental machine for the preliminary investigation consisted of a 4-pole, 3-phase rotor and a solid stator of EN1A steel (see Section 5.2). The rotor was coupled to a 4-pole d.c. machine having manual Ward Leonard control, so that by supplying the rotor winding from a 50 Hz, 3-phase supply, the speed of the rotating field relative to the stator could be varied from very low speeds to twice synchronous speed. The inverted construction of the machine was chosen to eliminate slip rings in the search-coil circuits and so that the end and back boundaries of the solid iron were clearly defined. Tests carried out on this machine included the measurement of loss, surface current density and flux penetration in the stator.

7.2.2 Loss Measurements

The eddy-current loss in the stator was measured at 50 Hz (i.e. when the rotor was locked) by the 2 wattmeter method. At frequencies below and above 50 Hz, the d.c. machine acted as a generator or motor respectively. At 100 Hz, half the power fed to the stator is fed from the d.c. machine, and half from the a.c. supply.[52] In general, at any frequency, f, the total power, P, fed to the stator is -

$$P = \frac{f}{(50\sim f)} \left[I_A V \pm (I_A{}^2 R_A + \text{No load losses of d.c. machine}) \right] \quad 7.1$$

Where I_A, R_A and V are the armature current, armature resistance and voltage, respectively, of the d.c. machine.

This method simplifies the loss measurement, but the overall accuracy of Equation 7.1 is dependent on that of its individual parts, and is greater at low frequencies than at frequencies near to 50 Hz when ($I_A V$) is small.

7.2.3   Preliminary Flux Penetration Tests.

7.2.3.1 The Search Coils

For minimum interference to the electromagnetic fields, search wires should be inserted into the iron through holes drilled axially through the stator.   Holes of 0.3 mm diameter can be drilled through 10 cm. of solid steel by electro-chemical machining but, as only limited control over the direction of the drill is possible at such depths, it was not considered a practicable method.   The stator was therefore diametrically split and one of the mating surfaces grooved for the location of the search wires.

The grooves, 0.15 mm wide, were milled with a cutter. Insulated copper wires of 0.1 mm diameter were placed and secured in the grooves with epoxy resin.   A sketch of the half stator and the search coil arrangement is shown in Fig. 7.1.

7.2.3.2 Measurements

Both the magnitude of the peripheral component of flux density and its change in phase with depth were measured using the search coil array described in Section 7.2.3.1 (Fig. 7.1)   these results are given in Appendix V but three observations are noted here which influenced the design of the final experimental machine.

   (i)   A considerable percentage of flux penetrated to the back end of the stator (Fig. A5.1);   this is due to finite length effects (Chapter 9).   At the axial ends of the machine the eddy-current reaction is considerably reduced and the flux may penetrate deeper into the iron.   Since the search coils run the whole axial length of the machine (Fig. 7.1), the flux at the axial ends of the stator predominates at depths greater than the limiting depths of penetration, δ_n ;   this was confirmed by measuring the flux distribution along the axial length of the machine, both within and on the surface of the stator (Appendix V).

(ii) Tooth ripple was evident in the flux waveforms at all frequencies other than at 50 Hz and was greatest at 100 Hz and 1 Hz. At 100 Hz the ripple flux was approximately 5% of the fundamental and voltages were induced by the ripple flux in search coils up to 5 mm from the stator surface.

(iii) The peak values of the flux density at the surface of the secondary were considerably lower than the calculated values ($|\dot{B}_{xg}|$) and were independent of changes in frequency; this indicates that the actual values of the eddy-current reaction field in the region of the split are less than the theoretical values. Both the finite length of the stator (Chapter 9) and the split must influence the magnetic and electric circuits in the stator and might cause a reduction of the eddy-current reaction field at its surface.

7.2.3.3 Effects of Splitting the Stator

One possible cause of the apparent reduction in the eddy-current reaction at the split is flux redistribution due to the variation in the spacing between the grooves (see Fig. 7.1), or unevenness in the mating surfaces. Since the eddy-currents are distributed throughout the whole medium, the flux distribution will be governed more by the reluctance of the total magnetic circuit in the iron than by the split.

The total peripheral flux in the stator at the split was compared with that a pole pitch away from the split over a range of excitation and frequency. The difference in the measured values was never greater than 7%, the value at the split being the smaller of the two. It was concluded, therefore, that the pole pitch was sufficiently large for the additional air-gap due to the split to have negligible effect on the reluctance of the magnetic circuit.

Comparison of the waveforms of the flux at the two positions however, showed that the iron was less saturated at the split, even though the flux levels were virtually the same, which indicated a reduction of eddy-current reaction in this region.

Since the machine has finite length, peripheral currents as well as axial currents will flow in the secondary and must therefore cross the split. The effect of the contact resistance between the mating surfaces on the eddy-current distribution is not easy to assess. Current density probes (see Section 7.2.4) were placed on the stator surface to measure both the axial and circumferential current densities at the split, and again a pole pitch away from the split. Despite the inconsistency of the waveforms from the probes (Section 7.2.4), a definite decrease in the current densities was detected near the split, and it was felt that this was associated with the reduction in eddy-current reaction in this region.

Measurements were made on sample blocks of EN1A steel to determine the surface conditions required for minimum contact resistance. The results are given in Table 7.1, and it is seen that the finer the texture of the surface the higher is the contact resistance. A layer of copper, approximately 2.5 μm thick, was electro-deposited onto the mating surfaces of the sample blocks and a considerable decrease in contact resistance was observed. It was considered however, that the introduction of copper between the surfaces in the stator might have undesirable effects on the distribution of the eddy-currents, particularly as uniformity of the thickness of the copper layer could not be guaranteed. It was concluded that the results of flux penetration tests from stators not fitted with copper end rings were too inaccurate to be of value.

7.2.4   Preliminary Surface Current Density Measurements

The magnitude of the eddy-current density in the surface of the stator was estimated by measuring the voltage difference between two points, 1 cm apart on the surface. The probes used to measure the voltage were formed by swaging copper wires into holes in the surface of the stator. The voltage waveforms obtained with the probes were not consistent with the waveforms of the airgap flux density; this was believed due to the unreliable contact between wire and steel and the indeterminate depth of the probes in the surface of the stator.

7.3   THE EXPERIMENTAL MACHINE

The arrangement of the experimental machine, whose development was based on the preliminary tests (Section 7.2), is shown in Fig.7.2 and Plates 7.1 and 7.2. The specification of the machine is given in Tables 7.2 and 7.3, and the following notes are made on its design and construction.

(i)   The 4-pole rotor has a 3-phase, star-connected, winding which was designed to reduce the mmf harmonics (Table 7.2).

(ii)   The rotor was held stationary throughout the tests and was supplied from a variable frequency source (Section 7.3.1). This method of varying the fundamental frequency of the eddy-currents in the stator eliminated tooth-ripple and enables the loss to be determined by measuring the reaction torque on the rotor; it also eliminated the possibility of damage to the search coils due to rotation.

(Although the 'rotor' was held stationary, the terms 'rotor' and 'stator' will be retained for convenience throughout the thesis).

(iii) The torque was measured by means of a strain-gauge torque

transducer, which consists of a high-tensile steel shaft to which is cemented a strain-gauge bridge network. One end of the torque transducer was coupled to the rotor shaft and the other to a fixed bracket (Fig. 7.2). The output from the torque-transducer circuit was indicated on a digital meter. The output from the torque transducer was calibrated by the manufacturers as:

$$1 \text{ V} = 27.1 \text{ N-m}$$

(maximum total error due to non-linearity was $\pm$ 0.12% of F.S.D.) The calibration of the transducer was checked by means of a torque-arm and spring balance. The bearing stiction torque was estimated experimentally as equivalent to 0.003V, which was not greater than 12% of the torque reading at 4800 A/m, 6% at 7200 A/m and 3.4% at 9600 A/m, and a negligible percentage at all higher excitations. To minimise the error due to bearing stiction, the torque was read both for increasing and decreasing excitations and the mean value of the readings taken.

(iv) Two solid stators of EN1A mild steel were used, one was diametrically split and fitted with copper end-rings[*], and the other was neither split nor fitted with copper end-rings[†]. The overall dimensions of these stators were identical. In view of the effects of both the finite length of the stator and of the split on the eddy-current distribution (Section 7.2.3), flux penetration tests were carried out only on the stator with copper and rings (Section 7.3.2 and 7.4.1) The airgap surfaces and end faces of the stators were marked out on a milling machine for accurate positioning of the search coils and current density probes.

---

[*] the diametrically split stator, fitted with copper end rings, will be referred to in following sections as the end-ring stator,

[†] the continuous stator, without copper end rings, will be referred to in following sections as the continuous stator.

(v) In the preliminary investigation, the half stators were clamped together at the flanges at the back end of the stator (Fig. 7.1). To equalize the pressure over the split surfaces, the clamping arrangement shown in Plates 7.1 and 7.2 was used. The clamping shoes were made of bakelite so that the stator was electrically and magnetically isolated from the rest of the experimental rig, which was earthed at a single point.

7.3.1 Supplies

Two generators were used to obtain supplies over the required frequency range of 0.75 Hz to 100 Hz; these are detailed as follows:

(1) An a.c. generator, driven by a 4-pole induction motor through an eddy-current coupling, provided a supply whose frequency could be varied from 0.75 Hz to 60 Hz. The rating of the generator was 150/200 KVA 415/550V, 208A. The field of the generator was fed from an electronic power supply capable of operation in a constant voltage or constant current mode. The speed of the generator was controlled to with $\pm$ 5 rev/min.

(2) A synchronous motor-generator set was used to provide a 100 Hz. supply. The 6-pole synchronous generator, whose rating is 7.5 kVA, 230 volts, 10.8A, 50 Hz, was driven by a belt drive at twice its rated speed.

7.3.2 The End-Ring Stator

The end-ring stator is shown in Fig. 7.3 and in Plate 7.3. The copper rings were brazed on to the stator with silver solder (42% silver) at a temperature of 630° C in an atmosphere of nitrogen and hydrogen. All surfaces of the copper bridging pieces and the mating surfaces on the copper rings (Fig. 7.3) were ground flat; (these surfaces could have been silvered, but experimental tests showed this to be unnecessary).

The copper rings served two purposes:

(i)   to provide a path of relatively low impedance to the cross-pole currents (Section 9.1.1) so that the magentic field throughout the machine was essentially two-dimensional.

(ii)   to provide a path of low resistance across the split for the eddy-currents;   this presupposes that the eddy-currents prefer to flow to the ends of the machine and through the copper, rather than between the poles within the active region of the machine.   This is discussed further in Section 7.7.2.

7.3.2.1   The Plate

A plate 12.7 mm thick was inserted between the stator halves (Fig. 7.3).   Copper pieces were brazed to the ends of the plate so that the eddy-currents could flow through the plate to the bridging pieces and the stator halves.   The plate was located between the stator halves before the final machining of the stator bore and the surfaces of the copper rings.   The plate surfaces were finely ground. A plate was used for the following reasons:

(i)   it was not possible to spark machine grooves on the stator surfaces for the location of search coils due to the limited size of the available machine.

(ii)   the plate was made interchangeable with an axially slotted stator (associated with a project not contained in this thesis), whose tooth width was 25.4 mm so that the plate formed half a tooth when inserted between the stator halves.   The search coils in the plate surface were thereby placed on the tooth axis.

7.4   INSTRUMENTATION OF THE EXPERIMENTAL MACHINE

The experimental machine was instrumented for the measurement of:-

(i)   flux penetration into the stator,

(ii) the current density distribution on the surface of the stator,

(iii) the air gap flux density and flux/pole,

(iv) and torque, from which the loss in the stator iron may be obtained.

The experimental techniques and instrumentation used for the measurement of (i) to (iii) above are described in the following sections.

7.4.1   Flux Penetration

Flux penetration measurements were made using two arrays of search coils, one on the surface of the plate and the other on a split surface diametrically opposite the plate (Fig. 7.3).   The search wires run axially through the stator and are connected, in each array, to a common strip at one end of the stator, while at the other end they are twisted together and taken to a selector switch;   this arrangement enables any two wires to be selected to form a search coil.   Both arrays were similar to that used in the preliminary investigation, (Fig. 7.1), but differed in the dimensions and spacing of the grooves.

7.4.1.1. Search Coil Array in the Plate

Grooves, 0.625 mm wide and 0.15 mm deep, were spark machined in a surface of the plate (Fig. 7.3) and 0.04 mm diameter, insulated, copper wires were located in the grooves and secured with epoxy resin. The spacing between the grooves was approximately 1.25 mm, so that the width of the grooves was only 5% of the distance between the search wires.   A magnified picture of the groove array was projected on to a ground glass screen so that the spacing between search wires could be measured accurately;   the measured spacings are given in Table 7.4.   A photograph of the grooves is shown in Plate 7.4.

7.4.1.2 Search Coil Array in Split Surface

Grooves, 0.15 mm wide and 0.15 mm deep were milled in a split surface of a stator diametrically opposite the plate (Fig. 7.3).   The

spacing between the grooves was 2.5 mm.

7.4.2 Surface Current Density

The faults in the probes used in the preliminary investigation (Section 7.2.4) were eliminated by welding the wires to the surface of the stator. Nickel-copper wires of 0.1 mm diameter, and insulated with a double layer of rayon, were used; these wires have a relative magnetic permeability of approximately unity and therefore have little effect on the field distribution in the air-gap region. It was not found possible to weld copper wires to steel due to their dissimilar melting points.

The welds between wire and stator were obtained by passing a pulse of energy from a capacitor discharge unit through the relatively high contact resistance between them. Both the amplitude and time of the pulse could be controlled. Successful welds were obtained by trial and error as the contact resistance is dependent on the pressure applied and the cleanliness of the surfaces. The diameter of the weld area was little more than the diameter of the wire itself. A photograph of a typical weld is shown in Plate 7.5.

To measure the voltage drops due to the eddy-currents in the surface only, the voltages induced in the search coil circuits by time-varying flux are minimised, not only by twisting the wires between the probe and the recording instruments, but also by keeping the active conductor between the weld points as close to the surface as possible.[53] The probes used were all of 1 cm pitch; this was considered to be the minimum allowable distance for reasons of accuracy, both in defining the length of the probe and in obtaining a voltage signal greater than the pick-up voltage and noise level of the amplifiers. ('Dummy' search coils of 'zero' area were inserted into the gap of the machine to determine these levels).

The location of the current density probes on the stators is shown in Figs. 7.4 and 7.5.

7.4.3 Air Gap Flux and Flux Density

7.4.3.1 Search Coils

Search Coils, each consisting of a single turn of 0.1 mm, double rayon covered, nickel-copper wire, were attached to the stator surface with epoxy resin.

The location of the search coils, all full pitched, is shown in Figs. 7.6 and 7.7; these search coils were used to measure:-

(i) the flux/pole over the total active length of the machine,

and (ii) the flux/pole per cm of axial length.

7.4.3.2 Hall Probe

The air gap flux density was measured by means of a Hall probe which consisted of a thin semi-conductor plate mounted on a Beryllia backing. The dimensions of the probe were 3mm by 12 mm by 0.41 mm thick, and the effective area of the semi-conductor plate was 4 sq.mm. The probe was attached to a 0.125 mm thick melinex strip which enabled it to be moved in an axial or peripheral direction in the airgap region. The variation of flux density with axial length was measured more accurately by means of the probe, but the readings and waveforms were considerably affected by localised effects due to the rotor slotting and surface irregularities. The full-pitch search coils were not so sensitive to change in position relative to the rotor, the variation of the measured peak value of air gap flux around the stator being no greater than $\pm$ 3%.

7.5 MEASUREMENT PROCEDURES

7.5.1 Flux Measurement

The voltage from the search coils were fed to the amplifiers

and integrator shown in circuit A of Fig. 5.5. If the output from a search coil is v_i, the flux linking the coil, Φ, is

$$\Phi = \int_0^t v_i \, dt$$

The output from circuit A of Fig. 5.5 is,

$$v_o = - \frac{1}{A_1 A_4 RC} \int_0^t v_i \, dt = - \frac{\Phi}{A_1 A_4 RC}$$

so that

$$\Phi \cong \frac{RC}{A_1 A_4} \cdot v_o \quad \text{(volts)}$$

7.5.2 Current Density Estimation

Oscillograms of the voltages from the probes were analysed by using the Stanley Harmonic Analyser.[*] If the amplitude of the fundamental component of a waveform is V volts, then the fundamental component of the mean value of current density over a length, L_p, is,

$$J_1 = \frac{V}{\rho L_p}$$

where $\rho = 1.9 \times 10^{-7} \, \Omega - m$ (Section 5.2)

For the probes in the experimental machine, $L_p = 1.0$ cm.

7.6 EFFECT OF TEMPERATURE ON THE MEASUREMENTS

The temperature of the stator and rotor surfaces was monitored by means of thermocouples secured to the surfaces with epoxy resin.

Measurements may be affected by variation in temperature from the following causes,

(i) variation in the resistivity of the steel

and (ii) change in the radial airgap length.

The increase in resistivity with temperature of EN1A steel is of the order of 0.35% per $^\circ$C between 20° - 100°C, so that little

---

[*] The Stanley Harmonic Analyser is a product planimeter

change in the readings should occur for a 10°C change in temperature. All measurements were taken within the temperature range of 25 - 35°C by taking the readings as quickly as possible.

A decrease in the radial airgap length was found to occur during low frequency, high excitation, tests when the rotor temperature rose more than that of the stator (in some instances, only 0.125 mm nett gap existed between the coils and the rotor surface).

7.7 INITIAL TESTS ON THE EXPERIMENTAL MACHINE

7.7.1 Adjustment of the Airgap Length

To ensure uniformity of the airgap, the voltages induced in the full pitch search coils (Figures 7.6 and 7.7) were compared at low frequencies (i.e. when the eddy-current reaction is small). This provided a check on the airgap length around the machine and over its axial length. Although this was a lengthy process, the airgap had only to be set once prior to the whole test procedure.

7.7.2 The Waveform of the Rotor MMF

To obtain an indication of the effect of eddy-current reaction on the mmf waveform, the flux linkage with a full-pitch search coil on the rotor surface and the line current to the rotor were measured, both in the absence of either stator and with the end-ring stator.

Without either stator, the waveforms of both the flux and the line current had negligible harmonic content.

For the experimental machine with the end-ring stator, analysis of the waveforms of line current, taken over the experimental range of excitation for both the 150 KVA and the 7.5 KVA generators, showed that the 5th and 7th harmonic components were never greater than 1%

of the fundamental. The 3rd harmonic components of current were eliminated by the star connection of the winding.

These tests showed that the mmf wave produced by the rotor excitation was approximately sinusoidal, despite the distorting effect of the eddy-current reaction (Section 8.5.2).

7.7.3   Location of the Axes of the Rotor MMF

To measure the phase difference between the rotor excitation and any of the field quantities on the surface of the stator, it was necessary to locate the axes of the rotor mmf.

The mmf axes of the star-connected rotor winding were located for the instant that the current in the red phase was a maximum. A d.c. current was passed through the red phase in series with the parallel yellow and blue phases and point of maximum flux density in the airgap was detected using a Hall probe. As the rotor could be locked at any position, these mmf axes could be located with respect to the search coils and current density probes on the stator.

To determine the variation of the rotor mmf with time on these axes, a voltage proportional to the current in the red phase was obtained by integrating the output from the linear coupler (Section 5.7.2.2) placed around the red phase lead; this voltage is therefore equivalent to the variation of mmf with time at the spatial points located by the Hall probe.

7.7.4   Effectiveness of the Copper End Rings

The effectiveness of the copper end rings was assessed by comparing the values of the following quantities measured over the experimental range of frequency and excitation.

(i)   Current density, measured with the probes shown in Fig. 7.4.

(ii)   (Flux/pole)/cm length measured with the search coils shown in Fig. 7.6.

There was negligible variation over the surface of the stator ($< \pm$ 5%) in the values of these quantities which shows that the peripheral components of the eddy currents were negligible throughout the active region of the machine.

Since the axial pitch of the search coils and the current density probes were equal (1 cm), the voltage induced by the flux density wave (E_z) may be compared directly with the corresponding voltage drop due to the eddy currents (ρJ_z). Both the amplitudes and waveforms of these voltages were compared over a wide range of frequency and excitation and found to be in good agreement. This result shows that the voltage drop due to the cross-pole currents, which flow mainly in the copper end rings, is negligible compared to the voltage drop due to the axial currents.

CHAPTER 8

DISCUSSION OF EXPERIMENTAL AND THEORETICAL RESULTS

for the

MACHINE WITH THE END RING STATOR

8.1 INTRODUCTION

This chapter contains a discussion of the results of tests
carried out on the machine with the end-ring stator described in
Section 7.3.   The aim of these tests was to verify the non-linear
theory presented in Chapters 4 and 6.   As the non-linear theory for
the solid-iron region (Chapter 4) has been verified by the tests
described in Chapter 5, emphasis is placed here on the importance of
the relationship between the magnetic field strength at the surface
of the secondary* $|\dot{H}_{xg}|$, and the primary† excitation $\hat{K}$ (Equation 6.19);
this links the non-linear theory of Chapter 4 to the multiregion two-
dimensional model   (Fig. 1.1).

Verification of the theory in Chapters 4 and 6 is given by
correlation of measured and calculated values of torque, surface current
density and flux/pole.   Measured loss and current density in the
experimental machine are also compared with similar measurements on
the bar (Chapter 5), which show that the non-linear one-dimensional
theory may be applied to the solid-iron secondary of the multiregion
model when $q^2/2\alpha^2 \ll 1$ at its surface.

The non-dimensional factor Q_n (Chapter 6) is calculated for the
experimental machine and its possible use as a design factor is
demonstrated.

---

*   The stator of the experimental machine represents the secondary
    of the multiregion model (Fig. 1.1)

†   The rotor of the experimental machine represents the primary
    of the multiregion model.

Measurements of the penetration of the peripheral component of flux into the stator by means of the search coils described in Section 7.4.1 are compared with theoretical penetration curves derived by the non-linear theory (Equations 6.19 and 4.31)   A primary aim of these tests was to confirm the calculation of surface magnetic field strength $|\dot{H}_{xg}|$ from Equation 6.19.

8.2   TORQUE AND POWER LOSS

8.2.1   Measured Torque

The torque was measured by means of the torque transducer described in Section 7.3 for values of the primary mmf, $|\dot{F}_c|$, from 275 to 1100 At/pole (Table 7.3), and over a frequency range of 1.5 Hz to 100 Hz.

The values of measured torque are given in Table 8.1.

8.2.2   Calculated Torque

The torque may be calculated by any one of three methods, each revealing different aspects of the present theory:

(i)   The value of the magnetic field strength on the surface of the secondary iron $|\dot{H}_{xg}|$ may be determined by means of Equation 6.19 from a knowledge of the primary excitation, the physical constants and dimensions of the machine.   Knowledge of $|\dot{H}_{xg}|$ enables the loss to be calculated from Equation 4.45 and the torque from Equation 6.28.

This method demonstrates the importance of defining $|\dot{H}_{xg}|$, or $|\dot{F}_r|$ the eddy-current reaction, accurately;   it is discussed in detail in Section 8.2.3.

(ii)   The value of Q_n may be determined by means of Equation 6.34, from a knowledge of the primary excitation and the parameters of the machine.   The torque may then be determined from Equations 6.27 and 6.28.   This method is described in detail in Section 8.2.5.

(iii)   The torque may be obtained directly from the generalised torque/frequency characteristics (Fig. 6.1, Section 6.5.1) if T_{nm} is calculated from Equation 6.31 and ω_{nm} is calculated from Equation 6.33.   This is the most direct method of obtaining the torque, since the reaction of the eddy currents is implicit in the calculations.

Values of T_n/T_{nm}, ω/ω_{nm}, T_{nm} and f_{nm} for the experimental machines are given in Table 8.2 for excitations of 275, 550, and 1100 At/pole and frequencies from 1.5 to 100 Hz.

Calculated values of torque for the end ring stator are plotted in Figs. 8.1 and 8.2 (the continuous lines) against values of primary excitation from 4800 A/m to 19200 A/m and for frequencies of 1 Hz to 100 Hz. The constants a and b in the function $B = aH^b$ are given by Equation 5.2 for $|\dot{H}_{xg}| > 5000$ A/m and Equation 5.3 for $|\dot{H}_{xg}| < 5000$ A/m. R_b (Equation 4.52) was assumed to be 1.25 so that $A = 1.25a$ (Equation 4.59).

8.2.3   Surface Magnetic Field Strength ($\dot{H}_{xg}$)

In determining the torque by method (i) described in Section 8.2.2, the primary excitation, $\hat{K}$, was calculated from Equation 6.19 for a range of values of $|\dot{H}_{xg}|$ and frequency.   The results of these calculations have been superimposed on the graphs of torque against excitation shown in Figs. 8.1 and 8.2, to indicate directly the effect of the difference between $\hat{K}$ and $|\dot{H}_{xg}|$ (which is proportional to the resultant air-gap mmf) on the torque.   The broken lines in Fig. 8.1 and 8.2 are constant $|\dot{H}_{xg}|$ lines, i.e. they represent the variation in $\hat{K}$ for fixed values of $|\dot{H}_{xg}|$.   For example, in Fig. 8.1, for a value of $\hat{K}$ at 2 Hz of 19 000 A/m the value of $|\dot{H}_{xg}|$ is 15 000 A/m.   It is seen from both Figs. 8.1 and 8.2.that $(\hat{K} - |\dot{H}_{xg}|)$ decreases as the frequency increases which was also observed in the linear case (see Fig. 2.10   where $\eta \alpha 1/f$ (Equations 2.34 and 2.14))

The importance of correctly calculating the value of $|\dot{H}_{xg}|$ is demonstrated in Fig. 8.1 and 8.2   In the example previously quoted, i.e. $\hat{K} = 19\ 000$ A/m at 2 Hz, the torque is 26 N-m.   If it had been assumed that $|\dot{H}_{xg}| = \hat{K} = 19\ 000$ A/m then the torque would have been calculated as 37 N-m i.e. a difference of 42%.   If a line is drawn

from $\hat{K}$ = 19 000 A/m and parallel to the nearest broken line, the torque is given by the intersection of this with the torque line for 2 Hz). By carrying out a similar exercise at 50 Hz it may be seen that the percentage difference in the torque is far less than at 2 Hz.

8.2.4 Comparison of Measured and Calculated Torques

The variation of calculated and measured torque with frequency and excitation is shown in Fig. 8.3. The maximum deviation between calculated and measured values is 7% (calculated values as base). The calculated values are seen to be greater than the measured values at high frequencies and less than the measured values at low frequencies, particularly at the higher excitations. The differences are small however and could be due to variation in one or several of the machine parameters, particularly the air gap length, resistivity, or temperature.

8.2.5 The Factor Q_n

The method of obtaining the loss or torque from Equations 6.27 and 6.28, using the value of Q_n calculated from Equation 6.34, is illustrated graphically for the experimental machine in Figs. 8.4 to 8.6.

N_Δ (Equation 6.34) is shown plotted against the primary excitation $|\dot{F}_c|$ in Fig. 8.4, for a frequency of 1 Hz. Its value at any other frequency may be obtained by multiplying the ordinate of the graph by the frequency.

Q_n is shown plotted against N_Δ (Equation 6.35) in Fig. 8.5. Q_n for the experimental machine may thus be obtained for any value of frequency and excitation from Figs. 8.4 and 8.5.

Fig. 8.6 shows a graph of Δ_n against Q_n computed from Equation 6.29. For any given value of primary excitation and

frequency, Δ_n may be obtained and the torque calculated from Equations 6.27 and 6.28. Values of N_Δ, Q_n, Δ_n, obtained from Figs. 8.4 to 8.6 are given in Table 8.2 for excitations of 275, 550 and 1100 At/pole and frequencies from 1.5 to 100 Hz. The range of Q_n calculated for the experimental machine is 1.3 to 23.3.

8.2.5.1 Torque or Loss in Terms of Machine Parameters and Excitation

It is possible to simplify the method of torque or loss calculation for $Q_n \gg 1$ and $Q_n \ll 1$, when the torque or loss may be expressed directly in terms of the machine parameters and primary excitation.

When $Q_n \gg 1$,

from Equation 6.29, $\Delta_n \to 1/Q_n$

from Equation 6.35 $N_\Delta \to Q_n^2$

so that, from Equation 6.27

$$P_n \ \alpha \ \frac{|\dot{F}_c|^2 . \omega}{g . Q_n} \quad \text{if } qg \ll 1 \qquad\qquad 8.1$$

and from Equation 6.34

$$Q_n \ \alpha \ \omega^{\frac{1}{2}} . |F_c|^{(1-b)/2} . \frac{1}{g . \rho^{\frac{1}{2}} q^{(b+3)/2}} \qquad\qquad 8.2$$

substituting Equation 8.2 into Equation 8.1,

$$P_n \ \alpha \ |\dot{F}_c|^{\frac{(b+3)}{2}} . (\omega \rho)^{\frac{1}{2}} q^{\frac{(b+3)}{2}} \quad \text{if } \begin{cases} Q_n \gg 1 \\ qg \ll 1 \end{cases} \qquad 8.3$$

and from Equation 6.28,

$$T_n \ \alpha |\dot{F}_c|^{\frac{(b+3)}{2}} (\rho/\omega)^{\frac{1}{2}} . q^{\frac{(b+3)}{2}} \qquad\qquad 8.4$$

(Note that the loss and torque are independent of the air-gap length, g.)

When $Q_n \ll 1$,

from Equation 6.29, $\Delta_n \to Q_n$

and from Equation 6.35 $N_\Delta \to Q_n^{(b+1)}$

so that from Equation 6.27

$$P_n \propto |F_c|^2 \cdot \frac{\omega . Q_n}{g} \text{ , if } qg \ll 1 \tag{8.5}$$

and from Equation 6.34

$$Q_n \propto \frac{\omega^{1/(b+1)} |\dot{F}_c|^{(1-b)/(1+b)}}{q^{(b+3)/(b+1)} g^{2/(1+b)} \rho^{1/(1+b)}} \tag{8.6}$$

substituting Equation 8.5 into 8.4,

$$P_n \propto \left[\frac{|\dot{F}_c|}{qg}\right]^{\frac{b+3}{b+1}} \cdot \omega^{\frac{b+2}{b+1}} \left[\frac{1}{\rho}\right]^{\frac{1}{b+1}} \tag{8.7}$$

and from Equation 6.28,

$$T_n \propto \left[\frac{|\dot{F}_c|}{qg}\right]^{\frac{b+3}{b+1}} \cdot \left[\frac{\omega}{\rho}\right]^{\frac{1}{b+1}} \tag{8.8}$$

Between these two limiting conditions, when $Q_n = 1$, from Equations 6.27 and 6.29

$$P_n \propto \frac{|\dot{F}_c|^2 \omega}{g} \text{ , if } \begin{cases} Q_n = 1 \\ qg \ll 1 \end{cases} \tag{8.9}$$

This analysis indicates three distinct modes of operation of the machine, each differently expressed in terms of the machine parameters and dimensions and each specified by the value of Q_n. Thus Q_n may be useful as a design factor, particularly as the eddy-current reaction and flux/pole may also be expressed in terms of Q_n.

8.2.5.2 Variation of Torque with Excitation

For the solid iron stator $b = 0.112$ (Equation 5.2) for EN1A steel. Substituting this value of b into Equations 8.4, 8.8 and 8.9

$$T_n \propto |\dot{F}_c|^{1.55} \text{ , if } Q_n \gg 1 \tag{8.10}$$

$$T_n \propto |\dot{F}_c|^{2.78} \text{ , if } Q_n \ll 1 \tag{8.11}$$

$$T_n \propto |\dot{F}_c|^2 \text{ , if } Q_n = 1 \tag{8.12}$$

Fig. 8.7 shows a log-log plot of measured torque against excitation for two values of frequency. Line (i) corresponds to 2 Hz ($1.55 < Q_n < 3.1$) and has a slope of 1.92 which approaches the index of 2 given in Equation 8.12. Line (ii) corresponds to 100 Hz ($12 < Q_n < 23$) and has a slope of 1.6, which is closer to the index of 1.55 given by Equation 8.10 for large Q_n. It is not possible to check the index of 2.78 given in Equation

8.11 since the smallest value of Q_n obtainable for the experimental machine was 1.3.

8.3   FLUX PER POLE

The flux/pole maybe computed by Equation 6.39 or by Equation 6.40.   The results of the computation are plotted against excitation in Fig. 8.8.   The broken lines indicate the variation of $\hat{K}$ with frequency for a particular value of $|\dot{H}_{xg}|$ and their construction has been discussed in Section 8.2.4.   Also given in this figure are the measured values of fundamental flux/pole which were obtained using the full-pitch search coils shown in Fig. 7.6 (Section 7.4.3).

The measured readings are generally lower than the calculated values, the maximum difference between them being 9% (calculated value as base) which occurs at 2 Hz and 4800 A/m.   A probable reason for the difference between the measured and calculated values are the effects of the split on the electromagnetic circuits in the stator. To investigate the effect of the split on the flux/pole, measurements were made with a full pitch search coil attached to the rotor surface. Moving the position of the rotor search coil relative to the split showed that the pole flux was 4% greater when the axis of the search coil was coincident with the split than when it was a pole pitch away from the split.   It may be concluded therefore that there is some reduction in pole flux due to the split but the small differences generally found between measured and calculated values could be due to errors already discussed in Section 8.2.4.

8.3.1   Flux/Pole - Torque Relationship

The variation of measured torque with measured flux/pole may be obtained by cross-plotting from Figs. 8.8 and 8.3 and is shown plotted to log-log scales in Fig. 8.9 for four values of frequency.

From Equation 6.44,

$$\frac{\log T_n}{\log \Phi_n} = \frac{3 + b}{1 + b}$$

$$= 2.78 \text{ for } b = 0.112$$

The agreement between this calculated value of 2.78 and the slopes
of the graphs in Fig. 8.9 shows that the exponent b must be
substantially constant over the range of excitation and frequency
in the experimental investigation.

8.4   SURFACE CURRENT DENSITY

The surface current density was determined experimentally by
means of the probes (Section 7.4.2) positioned on the surface of
the stator (Fig. 7.4).   The peak values of the fundamental
components of the surface eddy-currents J_{z1} were obtained   (Section
7.5.2) for values of primary excitation from 4800 to 19200 A/m and
frequencies of 2.0 to 100 Hz.

Typical values of J_{z1} obtained with the probes A to F shown
in Fig. 7.4 are given in Table 8.3. J_{z1} is seen to be substantially
constant over the surface of the stator and the significance of
this has been discussed in Section 7.7.2.   The mean value of J_{z1}
over the surface of the stator was determined for each value of
frequency and excitation, and are shown plotted against primary
excitation (K) for several values of frequency in Fig. 8.10.   Also
shown in this figure are the values of current density (fundamental)
computed from Equation 6.9.   The agreement between calculated and
measured values of $\dot{J}_{z1}$ is good.   The broken lines again represent
the variation of $\hat{K}$ with $|\dot{H}_{xg}|$ as described in Section 8.2.4.

8.5   COMPARISON OF MEASUREMENTS IN THE BAR AND TEST MACHINE

8.5.1   Comparison of Magnitudes

It has been stated in Section 4.2.1 that, if $q^2/2\alpha_g^2 \ll 1$,
then the non-linear theory of Chapter 4 may be applied to the

secondary of the multiregion model (Fig. 1.1). Thus, the values

of loss and surface current density measured on the bar (Section 5.7)

should agree with similar measurements made on the experimental

machine for the same value of surface magnetic field strength. In

Table 8.4, values of current density and loss measured at 50 Hz

on the bar and on the experimental machine, are compared when the

calculated magnetic field strength on the surface of the stator

($|\dot{H}_{xg}|$) is equal to the applied magnetic field strength at the

surface of the bar ($\hat{H}_R$). There is generally good agreement between

the measurements made on the bar and the stator.

8.5.2 Comparison of Waveforms

Oscillograms of surface current density, J_z, and air-gap flux

density, B_y, taken with the probes and search coils on the end-ring

stator (Figs. 7.4 and 7.6), are shown in Plate 8.1 for excitations

of 19200 A/m and 4800 A/m at 50 Hz. The waveforms of J_z and B_y

are clearly similar at the same values of excitation; they were

also found to be in phase.

The waveforms of J_z (Plate 8.1) contain a smaller percentage

of the higher harmonics than the waveforms of surface current density

in the bar, J_B (Plate 5.1.). At corresponding values of excitation

in the bar and the experimental machine, the third harmonic components

in J_z and J_B are of the same order (approximately 14 – 20% of the

fundamental), but the fifth and seventh harmonics in J_z are less than

those in J_B.

Superimposed on the oscillograms of air gap flux density at the

surface of the stator (Plate 8.1) are waveforms of line current

which are proportional to the current sheet (K), of the rotor winding

Section 7.7.3). The phase angle between the fundamental components of

the flux density and the current sheet (K), obtained by computer analysis

of the oscillograms, is within the range 35°-37° for all excitations

in the experimental range. The phase angle between the fundamental components of surface magnetic field strength and the surface current density in the bar were found to be about 30° for excitations $>$ 2500 A/m (Section 5.4.3.2). Thus, the fundamental components of the equivalent current sheet of the rotor excitation must lag the surface magnetic field strength on the stator by $5-7^\circ$. This field pattern within the machine is consistent with that given in Fig. 2.6.

8.6 FLUX PENETRATION TESTS

The objective of the tests described in this section was to measure the peripheral component of the flux density at the surface of the stator and the penetration of the peripheral flux into the stator.

Measurement of the magnitude of the peripheral component of flux within the stator was made using the search coils in the surface of the plate and in the surface of the half stator (Section 7.3, 7.4.1 and Fig. 7.3).

Measurement of the change in phase of the flux with depth into the stator was not obtained; at low frequencies, where such measurements would have been of value in checking the theory the readings were too unstable for reasonable accuracy.

8.6.1 The Peak Value of the Mean Flux Density.

The voltage induced in each search coil was electronically amplified, integrated (using circuit A in Fig. 5.5) and the amplitude of the resultant signal indicated on a peak reading valve-voltmeter; the peak value of the flux was determined from this reading as described in Section 7.5.1. The peak value of the mean flux density over the area of the search coil, B_{av}, was obtained by dividing the measured peak value of the flux by the area of the search coil (Table 7.4 and Section 7.4.1). The tests were carried

out for a range of excitation of 4800 to 19200 A/m and a range of
frequency from 2 to 50 Hz.

It was observed that the values of B_{av} varied with excitation
and frequency in a manner contrary to theoretical prediction (Chapter 4).
Fig. 8.11 shows that the values of B_{av} for the surface layer in the
plate and the calculated value of peak flux density at the surface, B_c,
diverge as the frequency increases and the excitation decreases.
($B_c = B_{xg}/1.25$, on the assumption that $B_1 = 1.25a\ H_1^b$ in Equation
4.58). As the search coils measure mean values of flux linkage,
the attenuation and change in phase of the flux density with depth may
affect the readings in the manner observed in Fig. 8.11, since both
factors increase with frequency, yet decrease with excitation, due to
saturation.

The attenuation and change in phase of the fundamental component
of flux density with depth calculated by the present non-linear theory
are given in Fig. 8.12, for various excitations and frequencies. (These
curves were obtained assuming a magnetization curve represented by
$B_1 = 1.25a\ H_1^b$). Also shown in Fig. 8.12 are the calculated mean values
of flux density over a depth of 1.25 mm. These were obtained by computing
the line integral of the emf around the search coils (using Equation 4.6
for E_z). The mean values of flux density are plotted in Fig. 8.12 at
the centre of the search coils i.e. at depths of $(n \times 0.625)$ mm. where
$n = 1, 2, 3....$ It is seen that at 5 Hz, there is no significant
difference between the actual and mean flux density curves for surface
magnetic fields of 15000 A/m and 5000 A/m. At 50 Hz, the difference
between the actual and mean flux density is significant and appears to
increase (the actual value being the greater), and then decrease with
depth into the iron, so that when the surface magnetic field strength
is 5000 A/m, there is a point where the mean value of flux density is
greater than the actual value. The increase in the difference between

the actual and mean flux density appears to be due predominantly to the change in phase with depth (Fig. 8.12b); the decrease in the difference indicates that it is incorrect to plot the mean value of flux density at the centre of the search coil, particularly where the rate of change of flux density with depth is itself changing rapidly over the width of the search coil.

The difference between the mean flux density measured at the surface, B_{av}, and the computed surface flux density, B_c, shown in Fig. 8.11 is much greater at 2 Hz, and primary excitations less than 16000 A/m, than is indicated in Fig. 8.12.

The effects of hysteresis may be an additional cause of the divergence between B_{av} and B_c as the excitation decreases, since the non-linear theory assumes sinusoidal waveforms and a B-H relationship given by the d.c. magnetization curve for the material. Fig. 3.2, shows several hysteresis loops obtained on the ring sample of EN1A Steel on which the normal B-H curve was obtained (Section 5.2). The B-H relationship is approximately single valued, at values of $H \gg 5000$ A/m, but at values of $H < 5000$ A/m, hysteresis effects become significant. At values of $H \gg 5000$ A/m therefore, the single valued saturation curve must govern the nature of the flux penetration, but at lower excitations hysteresis may have a significant effect on the field distribution. Until the effects of hysteresis on the field distribution are accounted for theoretically, no positive conclusions can be made about the measured field distribution at low values of surface magnetic field strength. At a primary excitation of 19200 A/m and a frequency of 2 Hz however, conditions of large saturation and small phase change over the search coil width (1.25 mm or 2.5 mm) should apply for the surface layers at least, and would seem likely from Fig. 8.11; the measured surface flux density is, in fact, greater than the calculated flux density at this frequency

and excitation, and two possible reasons for this discrepancy are discussed in the following sections.

8.6.1.1   Fundamental Components of the Flux

Typical oscillograms of the flux waveforms from the search coils in the plate surface are shown in Plate 8.1, for a frequency of 2 Hz and a primary excitation of 19200 A/m.   (The input impedance to the oscilloscope was set for minimum distortion of the signals).   The fundamental components of the flux waveforms obtained with the search coils in the plate and the split surface are shown in Table 8.5;   they were measured from the oscillograms using a Stanley Harmonic Analyser.

It is seen from Table 8.5 that the ratio of the fundamental amplitude to the measured peak value of flux density is less than that predicted theorectically if the waveform of the magnetic field strength is considered to be sinusoidal   (Fig. 4.6) ;   the difference between the measured and calculated values of the ratio may be due to the finite width of the search coils.

If the wave length of the harmonic of the flux is comparable to the width of the search coil, the measured value of that harmonic will be much less than its real value.   The measured peak flux density may therefore appear greater due to the reduction of higher harmonics. Theoretical evidence which includes the effects of hysteresis is not available to verify this, and it was therefore felt that a complete analysis of the waveforms would be unrewarding.

Penetration curves, both measured and theorettical of the fundamental component of flux density for a frequency of 2 Hz and an excitation of 19200 A/m are shown in Fig. 8.13.   In Fig. 8.13 it is noted that the measured values of flux density at the surface are still greater than the calculated fundamental values, and that the attenuation with depth of the measured values is greater than that of

the calculated values. Reasons for these observations may be given from a comparison of the results obtained with the search coils in the split surface of the half stator and the plate surface.

8.6.2   Effect of the Split between Half Stators

The flux was measured in the plate to a depth of 27 mm. which is approximately the radial extent of the copper end rings (Section 7.4.1). Search coils were inserted in the split surface so that the flux could be measured over the total stator depth. The peak values of the mean flux density at 14420 A/m and 2 Hz, measured with the coils in the split surface are given in Fig. 8.14; the values are expressed as p.u. of the peak value of the mean flux density obtained from the search coil nearest the air-gap surface. It is seen in Fig. 8.14 that there is a small rise in the flux density at the outer surface of the stator. The flux was also progressively summed across the stator commencing at the air-gap surface and the values of flux are shown plotted in Fig. 8.14 as p.u. of the total peripheral flux. It is clear that there is a rise in flux near the outer surface of the stator. The corresponding increase in the current density at the outer surface of the stator indicates that current is flowing in the y - z plane, i.e. radially in the end faces and axially in the outer surface of the stator. The majority of the current at the axial ends of the machine flows through the low impedance path provided by the copper end rings and the fact that a small percentage of the current flows in the y - z plane indicates that the fitting of copper end rings does not produce a field distribution exactly equivalent to that in a machine of infinite length - it would be optimistic to expect it to be so, since the copper has a finite conductivity and is itself split between stator halves.

The measured values of flux linking the search coils obtained

with the copper bridging pieces removed are also shown in Fig. 8.14.
There is an increase of flux at the air-gap and outer surfaces and
a decrease of flux in the middle of the stator cross section. Since
the impedance to the cross-pole currents has been increased by
removing the bridging pieces the current flow in the y - z plane must
also be increased. The result of this diversion of current is to
increase the eddy current reaction acting in a peripheral direction
in the stator, thereby causing the flux to increase near the air-gap
and outer surfaces. The impedance of the cross-pole eddy current
paths must be greater for the plate than for the single split and, on
the basis of the observations made from the removal of the bridging
pieces, the measured flux near the air-gap surface and the attenuation
of flux density with depth should be greater at the plate than the
single split. This is observed in Fig. 8.13, where the flux
penetration curves of the fundamental flux density are shown both for
the plate and the split for an excitation of 19200 A/m at 2 Hz. It
must be expected that the flux readings near to the surface at the
single split are also too high. If the flux readings with the single
split are reduced by the percentage difference that exists between the
readings of the single split and plate, the final values lie very
close to the calculated values. Whilst this is conjecture, there is
sufficient agreement between calculated and experimental results to
give some confidence in the theory, considering the practical
difficulties of measuring field distributions within solid iron.

8.7 CONCLUSION

The torque has been calculated in three ways to show different aspects of the present theory (Chapters 4 and 6). The most direct method is by means of the generalised torque/frequency curves given in Fig. 6.1. Equations for the peak torque (Equation 6.31) and frequency at peak torque (Equation 6.33), together with Fig. 6.1, provide a relatively simple means of calculating torque.

Torque may also be obtained from Equations 6.27 and 6.28 using the curves of Δ_n against Q_n (Fig. 8.6). Note that, since there is little variation in Δ_n with b, (Fig. 8.6), it may be allowable to use only one curve for all shapes of normal B-H curve. Q_n may be determined from the primary excitation, the dimensions and physical constants of the machine using Equations 6.34 and 6.35, or graphically from curves such as Figs. 8.4 and 8.5. Both the flux/pole and eddy-current reaction may also be calculated if Q_n is known (Equations 6.40 and 6.25 respectively).

Q_n has the added virtue of indicating the change in loss with the dimensions and physical constants of the machine (Section 8.2.5.1). For example,

$$P_n \propto \left[|F|_c \lambda \right]^{\frac{b+3}{b+1}} \left[\frac{1}{\rho} \right]^{\frac{1}{b+1}} , \text{ when } Q_n \ll 1,$$

but

$$P_n \propto \left[\frac{|F|_c}{\lambda} \right]^{\frac{b+3}{2}} . \rho^{1/2} , \text{ when } Q_n \gg 1,$$

i.e. when the eddy current field is very strong. Note that the loss is independent of both ρ and λ when $Q_n = 1$. The range of Q_n calculated for the experimental machine is 1.3 to 23.3. Whilst it was disappointing that the theory could not be checked at values of $Q_n < 1.0$, i.e. weak eddy-current fields, the values of Q_n for the experimental machine are most likely to apply in practice where eddy-current losses are important; for example, for negative sequence losses in large turbo-generator rotors or for induction heating at power frequencies by a travelling mmf wave.

Due mainly to the values of the ratio(air gap length/pole pitch) for the experimental machine, the frequency at peak torque was low.

The frequency at peak torque, f_{nm} (Equation 6.33), is approximately proportional to g^2/λ^3 if $qg \ll 1$ and the secondary iron is highly saturated ($b = 0$), while for constant permeability ($b = 1$), f_{nm} is proportional to g^2/λ^4.

The large pole pitch of the experimental machine also ensures that $q^2/2 \alpha g^2 \ll 1$ and $H_x > H_y$ in the stator, so that the one-dimensional non-linear theory of Chapter 4 may be applied to the stator. This is shown by the agreement between the measurements of surface current density and loss in the bar and in the end-ring stator. The bar tests provided an excellent means of cross checking results obtained in the experimental machine.

The deviation between measured and calculated values of torque, flux/pole and surface current density is not greater than 9% and is generally better than 7% (calculated values as base). The cross plotting of torque with excitation and flux/pole provides an extra check on the theory. It must be emphasised that the readings given were not taken by one probe or search coil only, but are the mean values of readings taken from a pattern of probes and search coils around the circumference of the stator so as to avoid any local variation in the surface conditions (Section 3.2). There was, however, little difference in the readings from the probes or search coils.

The flux penetration tests were not as successful as was hoped due to the considerable difference between measurement and theory at low excitations and high frequencies; for these conditions, the present theory cannot be correlated with localised field measurements, due either to limitations of the measurement techniques, or to approximations in the theory (e.g. neglect of hysteresis).

The discussion in Section 8.6 shows that sufficiently accurate

measurement of the field distribution in solid iron due to a travelling wave can be made at a primary excitation of 19200 A/m and 2 Hz; the fairly good agrecment between the measured and calculated value of the peripheral flux density at the surface of the secondary is significant, as the accuracy of the loss calculation depends greatly on the accuracy in determining $|\dot{H}_{xg}|$, particularly at low frequencies (see Section 8.2.3).

The effect of the split has been assessed in Section 8.6.2. It is found that the flux penetration curve can be changed by a relatively small percentage of current flowing in the z - y plane. Thus the flux density at the air-gap surface of the stator of finite length may be significantly increased due to considerable current flow in the z - y plane; this is discussed in Chapters 9 and 10.

CHAPTER 9

FINITE LENGTH EFFECTS AND MAGNETIC NON-LINEARITY

9.1   INTRODUCTION

This Chapter deals primarily with the derivation of power loss and flux/pole in a machine having a solid iron secondary of finite length. After a short statement on the nature of finite length effects and a brief literature survey, a linear three-dimensional analysis is given. The solution obtained by this analysis is later modified to account approximately for the effects of magnetic non-linearity.

The mathematical model used in the linear analysis consists of an infinite number of machines placed end to end whose primary excitations have alternate polarity. By this means the primary current sheet and the resulting field distribution may be described by Fourier series. Wood and Concordia[54] proposed this model to calculate the operational impedances of a solid rotor induction machine of finite length. The present solution is more general than previous solutions, since the permeability of the primary iron is finite. To obtain a more realistic description of the fields, the axial component of the primary current sheet is set equal to zero in the passive end regions and the stator cross section is developed on to the air-gap surface.

The effects of magnetic non-linearity are accounted for by means of the present non-linear theory. It is shown that the field distribution at the surface of the secondary and the axial centre of the machine may be determined approximately by the present two-dimensional non-linear theory (Chapter 6). By equating the linear and the present non-linear two-dimensional theories an equivalent

- 149 -

constant permeability for the iron is derived.   On the assumption
that this permeability applies to all points on the surface of the
secondary, the linear solution for the machine of finite length may
be used to determine the power loss and flux/pole.   This method
is believed to be new.

9.1.1   The Nature of Finite Length Effects

Eddy-currents may flow in the peripheral and radial directions
as well as the axial direction within the secondary of the machine of
finite length to complete the eddy-current paths.   The distribution
of the currents within the secondary is dependent on the relative
self-inductances of their paths between the poles.   The preferred
paths for the cross-pole currents[*] clearly lie in the passive end
regions[†] of the machine where the self inductance of the currents
is lower than that in the active region.

An idealised current distribution within the secondary of the
experimental machine is shown in Fig. 9.1.   Both the peripheral
(x) and the radial (y) components of current density must be zero at
the axial centre of the machine if the field distribution is
symmetrical about this axis.   In the passive end regions, the
currents flowing at the iron/air interface are linked by flux
whose paths are partly in air and are therefore mainly resistance
limited.   The penetration of these currents into the iron must
however be governed by their reactance and must be expressed
mathematically as a function of the depth of penetration δ if
the medium is assumed to be magnetically linear.

The effect of the additional impedance in the eddy-current
paths is that the total power transferred to the secondary (proportional
to $B_y \times H_x$) must be greater than the loss due to the axial component
of the secondary currents alone (proportional to $\left(\rho \, J_z\right) \times H_x$).   The
resultant change in the power equation of the machine is achieved
by a change in the eddy-current reaction acting on the air gap.

---

[*]   'Cross-pole currents' is used here to describe the currents which
link the poles and are additional to those in a machine of infinite
length;   they may therefore have peripheral and radial components
together with axial components in the passive end regions.

[†]   'Passive end region' refers here to the air-gap surface outside
active length of the machine and to the end faces and the outer
surface of the secondary.

9.2   A REVIEW OF LINEAR THREE-DIMENSIONAL ANALYSES

This section includes a brief review of published analyses that account for the effects of finite length which are related to the theory developed in this chapter.   The many empirical factors used to account for the additional resistance in the cross-pole paths will not be discussed here, but Gibb's development[49] of a 'resistivity multiplier' must be noted as he recognises that the eddy-currents must flow near to the air/iron interface and in the 'radial side faces and the whole of the outer surfaces of the secondary', in order to find the path of least resistance.   He neglects however, the reactance to the cross-pole currents.

Many three-dimensional linear analyses[55,56,57] in which the impedance of the cross-pole currents is implicit have been based on the mathematical model proposed by Wood and Concordia.   Their model, shown in Fig. 9.2, assumes an infinite number of identical machines placed end to end with alternate polarity.   Wood and Concordia defined the axial component of the primary current sheet (z direction) by the rectangular waveform shown in Fig. 9.3a.   This may be represented by a Fourier series which contains only odd harmonic terms.   At the boundaries between the machines ($z = \pm L/2$), $J_z = 0$, $B_z \neq 0$ and J_y is assumed zero throughout.   Since the exciting current sheet in each machine must satisfy div $J = 0$, the peripheral current sheet (x direction) must be of the form shown in Fig. 9.3b. It is clear however, that this model does not represent the air/iron boundary existing at the end faces in an actual machine and the axial flux density in the secondary at $z = \pm L/2$ for the model is considerably larger than that in an actual machine.   It would be more realistic perhaps to assume $B_z = 0$ at these boundaries.

This latter boundary condition is included in the analysis of

Bondi and Mukherji.[58]   They obtain a solution for J_x, J_y and J_z, and H_x, H_y and H_z in the secondary member in Fourier series form, and distinguish three types of field in the secondary member;

Type (a) $H_z = 0$ for all z but $J_z \neq 0$ except at the axial interfaces $(z = \pm L/2)$

Type (b) $J_z = 0$ for all z but $H_z \neq 0$ except at the axial interfaces

Type (c) $H_z = 0$ and $J_z = 0$ for all z.

(Type (c) is included within types (a) and (b) but is singled out for convenience).   Since the secondary medium is assumed electromagnetically linear, any field can be represented by super-position of fields of these types.   The first harmonic component of the series solution of fields of type (a) and (b) and the distribution of fields of type (c) are shown in Fig. 9.4.   In fields of type (a), the components may be expressed as Fourier series containing only odd order terms, whereas, in fields of type (b), they may be expressed as Fourier Series containing only even order terms.   The field components in type (a) and (b) penetrate in the radial (y) direction to a depth determined by the classical depth of penetration δ .   Fields of type (c), which are not described by a series solution consist of currents circulating in the x - y plane only;   they penetrate to a much greater depth radially but attenuate rapidly in the axial direction to a depth expressed as a function of δ.

If, for fields of type (b), it is assumed that $H_z \neq 0$ at the axial boundaries $(z = \pm L/2)$ and the primary current sheet is represented by a Fourier series containing odd order terms, the solution of Wood and Concordia[54] may be derived.   It is also shown that the radial component of current density, which was assumed to

be zero by Wood and Concordia, cannot exist in this solution.

Several authors[59,60] concerned with the field solution in linear motors have combined the fields of type (a) and (c) only, so that series solutions for all field components except H_z are obtained. (Their solutions however were not derived from that of Bondi and Mukherji).

Yee's solution[61] for finite length effects in solid rotor induction motors is based directly on Bondi and Mukherji's analysis. The amplitude of the axial component of the primary current sheet is assumed constant for $-\infty < z < \infty$ and peripheral flux leakage in the air gap is neglected. An approximate solution in closed form is, obtained for the field components in the secondary iron. The calculated values of the field components obtained by this solution are inaccurate at the axial ends of the machine, which may lead to error in the calculation of power loss due to cross-pole currents. Similar appoximations were made by Lasocinski[56] in obtaining a solution in closed form from Wood and Concordia's analysis for the field components in the air gap. This solution was necessitated by the slow convergence of the series solutions.

Although the general nature of Bondi and Mukherji's analysis was realised, a solution on this basis was not pursued as it was felt that approximations, made necessary to simplify the solution and to account for the effects of non-linearity, would detract from the advantages gained in its use.

9.3 THE THREE-DIMENSIONAL LINEAR ANALYSIS

The theory developed in this section is for the configuration given in Fig. 9.2, with the assumptions and modifications detailed in this and the following sections.

It is assumed that the machine is one of an infinite series of machines in the axial direction whose primary excitations have

alternate polarity and may therefore be represented by a Fourier series. Since it is assumed that no current may flow in the axial direction across the end boundaries of the machine ($z = \pm L/2$), the axial component of the primary current sheet is an even function of z and may be defined by the expression,

$$K_{zh} = e^{-jqx} \sum_{h=1,3}^{\infty} K_h \cdot \cos w_h z \qquad\qquad 9.1$$

also $\qquad w_h = hw$ $\qquad\qquad\qquad\qquad\qquad$ 9.2

where $\qquad w = \pi/L$, L is the total length of the model $\qquad$ 9.3

and K_h is the Fourier coefficient of the current distribution. The actual distribution of the primary current and the resulting definition of K_h is described in Section 9.4.2.

Several of the basic assumptions listed in Section 2.3 with regard to the configuration of Fig. 2.1 apply also to the configuration of Fig. 9.2 but will be repeated here for clarity;

(i) The permeabilities of both the primary ($\mu_o \mu_p$) and secondary members ($\mu_o \mu_s$) are constant in time and space.

(ii) The resistivity of the primary member is infinite, while that of the secondary member is finite and constant (ρ).

(iii) The surfaces of the primary and secondary members are smooth, flat and parallel to the z-axis.

9.3.1 Solution of the Electromagnetic Field Equations

Maxwell's equations for the primary iron, airgap and the secondary iron may be written in the form given in Equation 2.12, 2.13, and 2.14.

If the variation of the electromagnetic field quantities in the axial (z) direction may be represented by Fourier series then the general solution of Equations 2.12 - 2.13 for the configuration

of Fig. 9.2 is

$$\dot{S}_{uh} = \sum_{h=1,2}^{\infty} (A_{uh}e^{jk_h y} + G_{uh}e^{jk_h y})(X_{uh}\cos w_h z + Y_{uh}\sin w_h z)e^{jqx} \qquad 9.4$$

where $\dot{S}_{uh}$ refers to any one of the field components and the suffix

u denotes any one of the three regions of the model

where u = s for the secondary iron

u = a for the air gap

u = p for the primary iron

and $\quad k_h^2 = (s_h^2 + 2j\alpha^2)$ for the secondary iron, $\qquad 9.5$

and $\quad k_h^2 = s_h^2 \quad$ for the primary iron and air gap regions. $\quad 9.6$

where $s_h^2 = q^2 + w_h^2$ $\qquad\qquad 9.7$

The boundary conditions to be satisfied by the field components

are:

(i) $\dot{H}_{xah} - \dot{H}_{xph} = -K_h$ at the primary current sheet

(ii) $\dot{H}_{xh}$ is continuous at y = g.

(iii) $\dot{B}_{yh}$ is continuous at y = o and y = g.

(iv) $\dot{B} \rightarrow 0 \quad$ as $y \rightarrow \pm\, \infty$

The coefficients A_{uh}, G_{uh}, x_{uh} and Y_{uh} may be found from these

boundary conditions.

The field components in the air gap and solid iron secondary

are:

$$\dot{H}_{xah} = -e^{jqx} \cdot \sum_{h=1,3}^{\infty} \frac{K_h}{\dot{C}_{ph}}\left[e^{-s_h y} - \dot{D}_{sh}e^{-2s_h g}\cdot e^{s_h y}\right]\cos w_h z \qquad 9.8$$

$$\dot{H}_{yah} = \frac{-e^{-jqx}}{jq} \cdot \sum_{h=1,3}^{\infty} \frac{K_h s_h}{\dot{C}_{ph}}\left[e^{-s_h y} + \dot{D}_{sh}e^{-2s_h g}e^{s_h y}\right]\cos w_h z \qquad 9.9$$

$$\dot{H}_{xsh} = -e^{-jqx} \cdot \sum_{h=1,3}^{\infty} \frac{2K_h \dot{k}_h \cdot e^{-s_h g}\cdot e^{-k_h(y-g)}}{\dot{C}_{ph}(s_h\mu_s + k_h)}\cos w_h z \qquad 9.10$$

$$\dot{H}_{ysh} = \frac{-2e^{-jqx}}{jq} \cdot \sum_{h=1,3}^{\infty} \frac{s_h^2 \cdot K_h \cdot e^{-s_h g} \cdot e^{-k_h(y-g)}}{\dot{C}_{ph}(\mu_s s_h + k_h)}\cos w_h z \qquad 9.11$$

$$\dot{H}_{zah} = \frac{-e^{-jqx}}{jq} \cdot \sum_{h=1,3}^{\infty} \frac{w_h \, K_h}{\dot{C}_{ph}} \left[e^{-s_h y} - \dot{D}_{sh} \cdot e^{-2s_h g} \right] \sin w_h z \qquad 9.12$$

$$\dot{H}_{zsh} = \frac{-e^{-jqx}}{jq} \cdot \sum_{h=1,3}^{\infty} \frac{2w_h \cdot K_h \cdot k_h \cdot e^{-s_h g} \cdot e^{-k_h (y-g)}}{\dot{C}_{ph}(\mu_s s_h + k_h)} \sin w_h z \qquad 9.13$$

$$\dot{J}_{zsh} = -j4 \, \alpha^2 \cdot \sum_{h=1,3}^{\infty} \frac{K_h \, e^{-s_h g} \cdot e^{-k_n(y-g)}}{C_{ph} (\mu_s s_h + k_h)} \cos w_h z \qquad 9.14$$

$$\dot{J}_{xsh} = \frac{4\alpha^2 e^{-jqx}}{q} \cdot \sum_{h=1,3}^{\infty} \frac{K_h \, w_h \, e^{-s_h g} \, e^{-k_h (y-g)}}{C_{ph}(\mu_s s_h + k_n)} \sin w_h z \qquad 9.15$$

$$\text{where,} \quad \dot{D}_{sh} = \left[\frac{s_h \mu_s - k_h}{s_h \mu_s + k_n} \right] \qquad 9.16$$

$$\text{and} \quad \dot{C}_{ph} = \frac{\mu_p + 1}{\mu_p} \left[1 - \left| \frac{\mu_p - 1}{\mu_p + 1} \right| \dot{D}_{sh} \right] e^{-2s_h g} \qquad 9.17$$

These equations have the same form as Equations 2.18 to 2.24 for the two dimensional linear model.

If the length of the machine becomes very large (i.e. $L \to \infty$) then,

$$\left. \begin{array}{l} W_h \to 0 \\ s_h \to q \\ \text{and } \dot{k}_h \to \dot{k} = (q^2 + j2\,\alpha^2) \end{array} \right\} \quad L \to \infty$$

and Equations 9.8 to 9.11, 9.14 9.16 and 9.17 reduce to Equations 2.18 to 2.25.

9.3.2 The Primary Current Sheet

The axial and peripheral components of the primary current sheet used by Wood and Concordia[54] and Angst[55] are shown in Figs. 9.3a and 9.3b respectively. They made no attempt to represent the distribution of the axial and peripheral currents at the end regions of the machine, as it is clearly unrealistic for the peripheral current density to have an infinite value at $z = \pm L/2$.

To obtain an accurate solution for the electromagnetic fields in the model, it is important to define the boundary conditions at the iron/air interface (y = o) correctly; these depend on both the current sheet and the primary permeability, (μ_p). If $\mu_p \to \infty$, the peripheral component of the magnetic field at y = o is identical in value to that of the current sheet. In an actual machine, where the primary conductors are placed in axial slots, the magnetic field at y = o due to the axial currents falls sharply at the axial ends of the primary iron and may be accounted for approximately by the axial current distribution shown in Fig. 9.5a. The peripheral component of the current sheet must therefore, from the condition div J = 0, be defined as in Fig. 9.5b. In an actual machine, the peripheral currents flow outside the active region and their relatively small magnetic field will be incorrectly represented in the model, because the current sheet producing it is not only concentrated at the point z = $\pm$ L/2, but is also assumed to be backed by iron of infinite permeability over the total length of the machine. The nett result is that the peripheral magnetic field at the surface of the secondary is too great. To achieve a correct representation of the field distribution, the change in primary permeability must be correctly stated as well as the distribution of the current sheet.

The problem is further complicated by the fact that the primary permeability may not have the same value for the axial and peripheral components of the magnetic field within the active region of the machine. Since the flux paths due to the peripheral currents are perpendicular to the plane of the primary laminations the resulting reaction field due to eddy currents within them may cause an effective decrease in the primary permeability in the axial direction. To account for variations in the primary permeability over the axial length of the machine, however, would make the solution considerably more complicated.

Preston and Reece[57] have investigated finite length effects in a double-sided linear motor having a non-magnetic secondary whose width is greater than the active length of the primary. They assume the axial component of the primary current sheet has the shape shown in Fig. 9.5a, and is backed by primary iron of infinite permeability over the total length of the secondary. The Fourier coefficient for this waveform is considerably more complicated than that of the square wave and, as there is little difference between the low order harmonics for these two waveforms, it is doubtful whether the additional complication makes a significant difference to the loss and flux/pole calculation, although it will clearly affect the magnetic field distribution at the ends of the' active region.

It will be assumed in this thesis that the axial-current distribution is given by the waveform shown in Fig. 9.5a, and that it is backed by iron of infinite permeability over the whole length of the machine.

The Fourier coefficient of the waveform given in Fig. 9.5a is

$$K_h = \frac{4}{h\pi} \hat{K} \sin\left(\frac{h\pi}{2}\right) . \cos(h.d) \qquad 9.18$$

$$\text{where } d = \frac{(L - L_A)}{2L} . \pi \qquad 9.19$$

9.3.2.1 The Length of the Secondary Member

Bondi and Mukherji[58] have shown that the eddy currents remain within a skin depth not only on the air gap surface but also on the radial surfaces at the ends of the machine. On this basis the end and outer surfaces of the secondary are developed on to the z - x plane (air gap surface) for the purposes of calculating the power and flux per pole. This development is shown in Fig. 9.6 and the axial length of the developed secondary is assumed to be equal to

the length around the periphery of its cross section since this
length is generally very much greater than the depth of flux
penetration.

There is far more justification in stating that the axial
component of current density is zero at $z = \pm L/2$ for this
representation than when the actual axial length of the secondary
is used. This boundary condition is still not completely accurate
however since no account is taken of the current that may circulate
in the z - y plane as well as in the z - x plane between the poles
and J_z will only approach zero when $L \rightarrow \infty$.

By shaping the primary current sheet and developing the
secondary profile the value of B_z decreases towards the ends of the
machine, which is similar to the distribution of B_z obtained in
Bondi and Mukherji's model where $B_z = 0$ at the axial boundaries of the
secondary (Fig. 9.4). The values of B_z are however still over-stated
in the present model since μ_p is assumed constant over the total
axial length L of the machine.

9.3.3 Electromagnetic Field Components on the Surface of the Secondary

These components of the electromagnetic field must be derived
in order to determine the power loss in the secondary, the surface
current density and the flux/pole.

To rearrange Equations 9.8 to 9.17 into a form more convenient
for analysis, let

$$\overset{.}{k}_h = \beta_h + j\gamma_h \qquad\qquad 9.20$$

Thus from Equation 9.5 and 9.20

$$\beta_h = \frac{1}{\sqrt{2}} \left[(s_h^4 + 4\alpha^4)^{\frac{1}{2}} - s_h^2 \right]^{\frac{1}{2}} \qquad\qquad 9.21$$

$$\gamma_h = \frac{1}{\sqrt{2}} \left[(s_h^4 + 4\alpha^4)^{\frac{1}{2}} + s_h^2 \right]^{\frac{1}{2}} \qquad \qquad 9.22$$

and $\qquad R_h^2 = \beta_h^2 + \gamma_h^2 \qquad \qquad 9.23$

No attempt is made to simplify the expressions by assuming $\beta_h = \gamma_h$ in a manner similar to that used in the linear two-dimensional analysis, since $(S_h^2 / 2\alpha^2)$ may not be very much less than unity for the higher order harmonics ($h \gg 1$), and there is no reason at present for discounting their contribution to the loss and the field at the surface of the secondary. It may be assumed however that $\mu_p \gg 1$, so that Equation 9.17 becomes,

$$\dot{C}_{ph\infty} = \left[1 - \dot{D}_{sh} e^{-2s_h g} \right] \qquad \qquad 9.24$$

Assuming that $\dot{k}_h$ is given by Equation 9.20, and C_{ph} by Equation 9.24 ($\mu_p \gg 1$), the components of the magnetic field on the surface of the secondary ($y = g$) are:

$$\dot{H}_{xgh} = -e^{-jqx} \sum_{h=1,3}^{\infty} \frac{K_h R_h}{|\dot{M}_h|} \underline{/\dot{H}}_{xgh} \cdot \cos w_h z \qquad \qquad 9.25$$

$$\dot{H}_{ygh} = \frac{je^{-jqx}}{q} \sum_{h=1,3}^{\infty} \frac{K_h s_h^2 \mu_s}{|\dot{M}_h|} \underline{/\dot{H}}_{ygh} \cdot \cos w_h z \qquad \qquad 9.26$$

$$\dot{H}_{zgh} = \frac{je^{-jqx}}{q} \sum_{h=1,3}^{\infty} \frac{K_h w_h R_h}{|\dot{M}_h|} \underline{/\dot{H}}_{xgh} \cdot \sin w_h z \qquad \qquad 9.27$$

$$\dot{J}_{xgh} = \frac{\alpha^2}{q} e^{-jqx} \sum_{h=1,3}^{\infty} \frac{K_h w_h}{|\dot{M}_h|} \underline{/\dot{H}}_{ygh} \cdot \sin w_h z \qquad \qquad 9.28$$

$$\dot{J}_{zgh} = -j \frac{\alpha^2}{\rho} e^{-jqx} \sum_{h=1,3}^{\infty} \frac{K_h}{|\dot{M}_h|} \underline{/\dot{H}}_{ygh} \cdot \cos w_h z \qquad \qquad 9.29$$

$$\underline{/\dot{H}}_{xgh} = \tan^{-1} \left[\frac{\gamma_h \mu_s s_h \sinh s_h g}{(\beta_h^2 \cosh s_h g + \mu_s s_h \beta_h \sinh s_h g + \gamma_h^2 \cosh s_h g)} \right] \qquad 9.30$$

$$\underline{/\dot{H}}_{ygh} = \tan^{-1} \left[\frac{-\gamma_h \cosh s_h g}{(\beta_h \cosh s_h g + \mu_s s_h \sinh s_h g)} \right] \qquad \qquad 9.31$$

and $\dot{M}_h = \left[(\beta\cosh s_h g + \mu_s s_h \sinh s_h g) + j\gamma_h \cosh s_h g \right]$ 9.32

9.4 POWER LOSS AND TORQUE

The total power, P_t, into the secondary may be calculated by means of the Poynting vector[62] so that,

$$P_t = \oiint (\underline{E} \times \underline{H}).ds$$

and the mean power loss is,

$$P_t = \frac{\omega}{2\pi} \int_0^{2\pi/\omega} \oiint \left[(\underline{E} \times \underline{H}).ds\right].dt$$

$$= \frac{1}{2} \left[\mathrm{Re} \oiint (\underline{E} \times \tilde{\underline{H}}).ds \right]$$

where $\tilde{\underline{H}}$ is the complex conjugate of $\underline{H}$.

Thus the mean loss/unit surface area may be obtained as,

$$P = \frac{1}{2L} \mathrm{Re} \int_{-\frac{L}{2}}^{+\frac{L}{2}} \left[E_z \tilde{H}_x - E_x \tilde{H}_z \right]_{y=g} -dz$$ 9.33a

Substituting Equations 9.25, 9.27, 9.28 and 9.29 into Equation 9.33a,

$$P_h = \frac{1}{L} \sum_{h=1,3}^{\infty} \frac{K_h^2 \gamma_h^2 \alpha^2 \rho}{|\dot{M}_h|^2} \left[1 + \frac{w_h^2}{q^2} \right] \int_{-\frac{L}{2}}^{+\frac{L}{2}} (\cos^2 w_h z + \sin^2 w_h z)dz$$

so that,

$$P_h = \sum_{h=1,3}^{\infty} \frac{K_h^2 \gamma_h^2 \alpha^2 \rho}{2|\dot{M}_h|^2} \left[1 + \frac{w_h^2}{q^2} \right]$$ 9.33

The second term in the square bracket (Equation 9.33) may be expanded from Equations 9.2, and 9.3 so that

$$\frac{w_h^2}{q^2} = \left[\frac{h\lambda}{2L} \right]^2$$ 9.34

$\dfrac{w_h^2}{q^2}$ is the ratio of $\dfrac{\text{peripheral current loss}}{\text{axial current loss}}$

The torque, T_h is given as,

$$T_h = \frac{P_h p \, \pi \, DL}{\omega}$$

If Equation 9.33 is divided by Equation 2.49, the ratio of,

$$\left[\frac{\text{Mean loss/unit area in the machine of finite length}}{\text{Loss/unit area in a machine of infinite length}}\right] \text{at constant}$$

frequency is obtained as,

$$\sum_{h=1,3}^{\infty} \frac{K_h^2 \, \gamma_n \, \alpha R_n \, |\dot{M}|^2}{2 \hat{K}^2 \, |\dot{M}_h|^2} \left[1 + \frac{w_h^2}{q^2}\right]$$

Whereas the loss for the machine of finite length is obtained

for a total developed length L, it is more usual, when using the

two-dimensional theory (Chapter 2) only, to calculate the loss over

the active length of the machine L_A.   Thus, a finite length factor,

R_L, may be defined for a machine as,[68]

$$R_L = \frac{\text{Total loss in the machine of finite length, L}}{\text{2-dimensional loss in its active length } L_A}$$

at constant frequency and excitation.

Thus,

$$R_L = \sum_{h=1,3}^{\infty} \cdot \frac{K_h^2 \cdot \gamma_h \alpha R_n \cdot |\dot{M}|^2 \cdot L \cdot \left[1 + \frac{w_h^2}{q^2}\right]}{2 \, \hat{K}^2 \cdot |\dot{M}_h|^2 \cdot L_A} \qquad 9.35$$

Computations of R_L for the experimental machine, at constant

frequency and excitation, are given in Chapter 10 where they are

compared with measured values.

9.5   FLUX/POLE

The flux/pole may be defined as the peak flux linking an area

$(\frac{\lambda}{2} \times L_A)$ and may be obtained by integrating Equation 9.24 over a

pole pitch and over the axial length of the machine so that

$$\Phi_h = \int_{-\lambda/4}^{+\lambda/4} \int_{-L/2}^{+L/2} H_{ygh} \, dx. \, dz \qquad 9.36$$

Substituting Equation 9.26 into 9.36, and carrying out the integration

$$\Phi_h = \frac{4}{q} \sum_{h=1,3}^{\infty} \frac{K_h s_h^2 \mu_s}{w_h \, |\dot{M}_h|} \underline{/\dot{H}}_{ygh} \, \sin \frac{h\pi}{2} \qquad 9.37$$

K_h in this expression is given by Equation 9.17, and it will be
seen therefore that the real part of Equation 9.37 for any single
harmonic, Re (Φ), is

(i)   negative when $-\frac{\pi}{2} > hd > \frac{\pi}{2}$

and   (ii)   positive when $-\frac{\pi}{2} < hd < \frac{\pi}{2}$

Since Re (Φ) for some of the low order harmonics, (mainly 3,5)
become negative, it is found that the flux/pole Φ_h decreases as
the developed length of the secondary L increases, while L_A remains
constant.   The reduction in the value of the flux may be considerable,
e.g. for the experimental machine, Φ_h for $L = 4 L_A$ was one third of
Φ_h for $L = 1.2 L_A$.   Physically, this implies that a considerable
proportion of the flux is returning from the secondary to the
primary in the end regions (axial lengths $> L_A$), whereas in reality
this does not occur due to the considerable increase in air gap
length in these regions.

The calculation of the flux/pole was therefore modified to
account for the misrepresentation of the model in the end region
by integrating $\dot{H}_{ygh}$ over the active length, i.e. $+\frac{L_A}{2} > z > -\frac{L_A}{2}$,
rather than the total length to give Φ_{ha}, where

$$\Phi_{ha} = \frac{4}{q} \sum_{h=1,3}^{\sim} \frac{K_h \; s_h^2 \; \mu_s}{W_h \; |\dot{M}_h|} \cdot \angle\dot{H}_{ygh} \cdot \sin \frac{\pi h \, L_A}{2L} \qquad\qquad 9.38$$

so that Re (Φ_a) is positive for all harmonics for $L \geq L_A$.

Computations of the flux/pole over the active length, Φ_{ha}
are given in Section 10.3 where they are compared with measured
values of flux/pole.

9.6   ACCOUNTING FOR MAGNETIC NON-LINEARITY

9.6.1   General

The permeability of the secondary iron must vary not only with
depth (y - g) but also with axial length due to the variation in

$|\dot{H}_{xh}|$, $|\dot{H}_{zh}|$ and $|\dot{H}_{yh}|$. The typical variation in $|\dot{H}_{xgh}|$, $|\dot{H}_{zgh}|$ and $|\dot{H}_{ygh}|$ over the axial length of the experimental machine, computed from Equations 9.25, 9.27 and 9.26, is shown in Fig. 9.7. It is virtually impossible to relate variation of permeability with that of the components of the magnetic field over the axial length of the secondary; for this reason most authors have first obtained linear analytic solutions for finite length effects which have been later modified to account for non-linearity.

Angst[55] used the limiting non-linear theory to obtain the impedance of a machine of infinite length; this impedance is then multiplied by an 'end-effect factor' derived by a linear analysis based on Wood and Concordia's model. Yee and Wilson[63] use the limiting non-linear theory[28] together with Yee's linear analysis[61]. They account for saturation for the peripheral component of the magnetic field only on the assumption that E_z and H_x exist mainly in the active region, whereas all other field components exist mainly in the passive end regions. This may appear a justifiable assumption on the basis of previous discussion (e.g. Section 9.1), although it is clearly impossible to make any demarcation between saturated and non-saturated regions for either the peripheral or axial components of the magnetic field; the extent of saturation in the secondary is dependent on the machine configuration and operating conditions.

The major problem in these or any other modified linear theory is the choice of value for the permeability of the secondary iron (μ_s) in the linear analysis and, in the case of the above methods, in the choice of B_s, the saturation flux density. Yee and Wilson[63] choose arbitrarily a value of B_s corresponding to $|\dot{H}_{xgh}|$

at the centre of the machine and the value of μ_s corresponding to

0.707 $|\dot{H}_{xgh}|$ at the ends of the machine which must be determined

by an iterative process. Angst[55] uses the method of Mc Connel

and Sverdrup[48] to derive B_s and a value of μ_s of $\dfrac{B_s}{\mu_o|\dot{H}_{xg}|}$

The method of accounting for the combined effects of

finite length and magnetic non-linearity in this thesis is based

on two assumptions, which are,

(i)   that the peripheral component of surface magnetic field, the

surface current density and the loss at the axial centre of

the secondary may be determined approximately by the present

non-linear theory,

(ii)   that the level of saturation at the axial centre of the

secondary applies approximately to the peripheral and axial

components of the magnetic field at all points on the surface

of the secondary.

These assumptions are discussed in the following sub-sections

and later in the experimental investigation (Chapter 10);   but if

they apply approximately to the solid iron secondary, then magnetic

non-linearity may be included in the calculation of loss or torque

and flux/pole for the machine of finite length.   The inclusion of

non-linearity in these calculations is achieved by deriving an

equivalent constant permeability μ_e for the secondary iron by

equating the linear and non-linear two-dimensional solutions for

the field distribution at the surface of the secondary;   this

derivation is given in sub-section 9.6.2.

Thus, on the basis of the assumptions (i) and (ii) above,

the torque or loss may be obtained by,

(a)   calculating μ_e for the excitation, dimensions and parameters

of the machine (see Section 9.6.2 below).

(b)   calculating R_L from Equation 9.35 using the value of μ_e

obtained in (a), and

(c)   multiplying the loss or torque for the active length of the

machine L_A, calculated by the present non-linear two-dimensional

theory (Chapter 6) by R_L.

Alternatively, the loss or torque may be determined from Equation

9.33 using the value of μ_e obtained in (a).   The flux/pole may be

determined from Equation 9.38 using the value of μ_e obtained in (a).

9.6.2   An Equivalent Constant Permeability

It is possible to define an equivalent constant permeability

μ_e for the secondary iron which if used in the linear two-dimensional

theory would give the same field distribution on the surface of the

secondary, and therefore the same loss, as obtained by the non-linear

theory for the same excitation, frequency and machine dimensions.

Thus, from the previous discussion, the permeability μ_e must also

apply approximately at the axial centre of the secondary.

It is seen from Equations 6.1 and 6.8 that the field distribution

at the surface of the secondary is described by the value of $\dot{S}$, which

relates $\dot{H}_{xg}$ to $\dot{H}_{yga}$.

For the present non-linear theory, (Section 6.3)

$$\dot{S} = \frac{-q \, \rho \, \alpha_n}{\omega \mu_o} \, (\beta_n + j\gamma_n)$$

9.39

For constant permeability

$$\dot{S}_e = \frac{-q\mu_e}{2\alpha_e} \, (1 + j)$$

9.40

where the subscript e denotes equivalent linear quantities.

Equating $\dot{S}_e$ and $\dot{S}$ from Equations 9.40 and 9.39

$$\alpha_e = \frac{\alpha_n \, R_n}{\sqrt{2}} \, \underline{/\phi_n - 45^\circ}$$

9.41

and $\quad \mu_e = \dfrac{\mu_g}{\mu_o} \ K_e \ \underline{/2\phi_n - 90}$ $\qquad\qquad$ 9.42a

where $\quad K_e = R_b . (K_b^2 . R_n^2) \ /2$ $\qquad\qquad\qquad$ 9.42b

$\qquad$ The method of obtaining $|\mu_e|$ is detailed as follows:

(i) $\quad$ The value of $|\dot{H}_{xg}|$ is obtained for the required excitation

$\qquad$ and frequency from Equation 6.19.

(ii) $\quad$ A value of permeability, μ, corresponding to this value of

$\qquad$ $|\dot{H}_{xg}|$ is obtained from the μ-H curve, Fig. 5.2.

(iii) This value of permeability, μ, is inserted into Equation 9.42,

$\qquad$ to obtain the equivalent constant permeability $|\mu_e|$.

$(R_b$ is obtained from Fig. 4.6, corresponding to the value of $|\dot{H}_{xg}|$

obtained in (i) for $U = 0$, and K_b and R_n are obtained from Equation

4.25 and 4.38b for a value of b obtained for the normal B-H curve

for the material).

9.6.3 $\quad$ Field Distribution at the Axial Centre of the Secondary

$\qquad$ At the centre of the machine the magnetic field is two-

dimensional and only the axial component of the current density exists.

The impedance in the current paths between the poles of the machine

causes the eddy-current reaction acting on the gap to decrease, and

the radial flux density in the gap to increase, compared with that in

a machine of infinite length for the same values of excitation and

frequency. $\quad$ Even so, there may be little significant decrease in the

peripheral component of the surface magnetic field at the axial centre

of the machine if the pole pitch is much greater than the air gap

length. $\quad$ In addition, if the pole pitch is much greater than the

depth of penetration $\left(s_h^2 / \ 2\alpha^2 << 1\right.$ for the theory in this chapter)

then the current density distribution within the iron must be

governed mainly by the distribution of the peripheral component of

the magnetic field. $\quad$ It is suggested therefore that, at the centre

of the machine, the linear two-dimensional theory may be used to determine approximately the peripheral component of the magnetic field, the surface current density and the loss in the iron but not the radial flux density;   this is verified analytically in Section 9.6.3.   (If it appears contradictory that the current density, but not the flux density, may be determined by the two-dimensional theory, it must be remembered that the loss at the centre of the machine is not equal to the power flow across the gap at this point, as it is in a machine of infinite length, the difference between them being due to the additional loss of the cross-pole currents.   The loss in the iron α (J_z x H_x) but the power flow $\alpha(B_y$ x $H_x)$).   Consideration of Equations 9.21 and 9.22 shows that the error in the approximation must increase as the $\left[\dfrac{\text{pole pitch}}{\text{length, L}}\right]$ ratio increases.

If the linear two-dimensional theory, rather than the three-dimensional theory, may be used to determine field quantities at the axial centre of the secondary, magnetic non-linearity may be accounted for by using the present non-linear theory, if $s_h^2/2\alpha_g^2 < 1$. Thus the permeability μ_e must also apply approximately at the axial centre of the secondary.

In Table 9.1 a comparison is given of $|\dot{H}_{xgh}|$ and $|\dot{H}_{xg}|$, and $|\dot{J}_{zgh}|$ and $|\dot{J}_{zg}|$ computed from Equations 9.25, 9.29, 2.39 and 2.41, for two values of the excitation and three values of frequency for the experimental machine.   The value of permeability for each frequency and excitation was obtained by Equation 9.42.   The modulus of μ_e was taken to simplify the calculations.   (Since $\emptyset_n$ for EN1A steel is approximately 37°, there seemed little need to complicate the solution by including the angle$\left(\emptyset_n - 45\right)$, considering the approximations that had already been made).

As expected, $|\dot{H}_{xg}| > |\dot{H}_{xgh}|$, the difference between them
varying from 7% to 20% ($|\dot{H}_{xg}|$ as base); similar percentage
differences were obtained for the corresponding values of
permeability (Fig. 5.2). Considering that the ratio of $\left[\dfrac{\text{active length}}{\text{pole pitch}}\right]$
for the experimental machine is 0.58, these results are perhaps
surprisingly good. The close agreement between $|\dot{J}_{zg}|$ and $|\dot{J}_{zgh}|$ is
confirmed by the experimental investigation discussed in Chapter 10.

9.6.4 Level of Saturation throughout the Secondary

The assumption that μ_e applies to the whole of the secondary
surface cannot be verified analytically. The variation in effective
permeability μ_e of the fundamental components of the field throughout
the secondary is however less than might be thought by considering
the variation in $|\dot{H}_{xg}|$ with axial length. For $|\dot{H}_{xg}|$ = 15000 A/m,
K_e = 1.67 if R_b = 1.25, so that $\mu_e = 1.67 \mu_g/\mu_o$ (see Equations 9.42
and 4.58). Due to the decrease of K_e with $|\dot{H}_{xg}|$, μ_e does not
increase as much as the permeability read from the μ - H curve
(Fig. 5.2). Admittedly, for H less than 2500 A/m, $\delta\mu/\delta H$ is
large and must be the predominant factor in determining the value
of permeability for this range of H. For the axial component of
current, the majority of the loss or flux/pole occurs within the
active region. As $|\dot{H}_{xg}|$ is also associated with this part of the
loss, μ_e is best defined at the centre of the machine since only
a small fraction of the loss or flux/pole due to axial currents
will occur in the passive end region. The majority of the loss
or flux/pole due to the cross-pole currents must occur at the
ends of the active region where $|\dot{H}_{zg}|$ approaches a maximum value.
It is likely that the iron will not be as saturated as indicated
in Fig. 9.2, due to the misrepresentation of the axial current sheet
given in Fig. 9.5a. Since the level or extent of saturation in

the secondary cannot be determined theoretically, verification of the definition of μ_e for both axial and peripheral components of current must be sought experimentally.

9.7   CONCLUSION

Expressions have been obtained for the power loss and flux/
pole in a machine of finite length whose solid iron secondary was
assumed to be magnetically linear.   The solution for these
quantities was obtained by the analysis of a mathematical model
in which all field quantities were expressed as series containing
only odd order terms.   The basic model for the analysis was proposed
by Wood and Concordia[54], but two modifications have been made,
which are,

(i)   the primary current sheet has been defined by the waveform
       given in Fig. 9.5 which represents zero axial current in the
       passive end regions, (Section 9.3.2).

(ii)   the stator profile (z-y plane) has been developed on to the
       air gap surface to account approximately for the current that
       flows in the radial end faces and outer surface of the
       stator, (Section 9.3.2.1).

It is realised that, even with these modifications, the field
distribution in the passive end regions will be incorrect due to
the assumption that the primary iron extends over the whole length
of the machine.

The loss in a machine of finite length has been normalised
by expressing it as p.u. of the two-dimensional loss over the
active length, L_A, of the machine (Chapter 2), the ratio of the
two losses being termed the finite length factor, R_L.

Magnetic non-linearity may be accounted for by multiplying
the torque or loss calculated from the non-linear theory of Chapter
6 by R_L.   It is clearly preferable that magnetic non-linearity is
also included in the derivation of R_L, and this has been achieved

approximately by defining an equivalent constant permeability μ_e for the secondary iron. μ_e is obtained by equating the linear and non-linear two-dimensional solutions at the axial centre of the machine on the assumption that the increase in radial flux density at this point in the machine of finite length has little effect on the values of the peripheral component of the magnetic field or the current density. This assumption is verified by computation of these quantities for the two and three dimensional linear analysis. By defining μ_e on the basis of the two-dimensional solution, iterative solutions are avoided.

In applying μ_e to the whole of the secondary surface, it is assumed that the level of saturation throughout the secondary is the same, so that μ_e is the effective permeability seen by waves of both peripheral and axial components of magnetic field at the surface of the secondary. This assumption has not been disproved, although it is generally considered that most of the loss due to the peripheral currents occurs in a less saturated region than that of the axial currents. Measurements of surface current density should indicate the level of saturation in the stator; this is discussed in Chapter 10. Although the use of μ_e is based on simplifying assumptions, it is considered a preferable method to the use of an arbitrary value of permeability.

It should be noted that the definition of μ_e (Equation 9.42) includes the effect of saturation harmonics of the magnetic quantities. Since the effect of saturation harmonics decrease as the surface magnetic field strength decreases, μ_e will not increase by as much as the permeability read from the normal μ-H curve. (Fig. 5.2).

The flux/pole has been defined as the peak flux linking an area ($\lambda/2 \times L_A$) and is determined by integrating B_{ygh} over this

area.   The derived expression for flux/pole, ϕ_{ha}, is given in
Equation 9.38.   In the actual machine, the flux flows in the y-x
plane and also into the end regions in an axial direction before
passing between the poles.   The axial component of flux is greatest
at the ends of the active length and is prevented from passing back
to the primary in the passive end regions by the large air gap.
In the theoretical model, the flux which passes axially into the
passive end regions may pass back to the primary since the air gap
is assumed to be the same over the whole length of the machine.
Thus it was found that the integration of $\dot{B}_{ygh}$ should be carried
out over the active length, L_A, and not the total length L of the
machine, (Section 9.5).   Magnetic non-linearity may be accounted
for in the calculation of flux/pole by using the equivalent
constant permeability μ_e, on the assumption that it applies for both
the peripheral and axial components of the flux.

CHAPTER 10

DISCUSSION OF EXPERIMENTAL AND THEORETICAL RESULTS

for the

MACHINE WITH THE CONTINUOUS STATOR

10.1   INTRODUCTION

The aim of this chapter is to assess the theory presented in
Chapter 9, and the validity of the assumptions on which it is based,
by comparing calculations with experimental results obtained on the
experimental machine with the continuous stator[*] (see Section 7.3).

The theory in Chapter 9 was developed primarily for the
calculation of torque or power loss and flux/pole, so that the first
sections of this chapter contain a direct comparison of measured and
calculated values of these quantities.

As it is felt that the results of tests given in Chapter 8 show
that the non-linear theory for the machine with the end-ring stator
(Chapter 6) may be used with confidence, the measured and calculated
values of the ratio,

$$\left[\frac{\text{Flux/pole, or torque, for the machine with continuous stator}}{\text{Flux/pole, or torque, for the machine with end-ring stator}} \right]$$

are also compared for the same excitation and frequency.   This was
made possible by ensuring that the main dimensions of the two stators
were identical.   Comparisons of the ratio defined here show differences
between theory and measurement that are not so clearly evident from
direct comparisons of torque or flux/pole.   Of prime importance is
the experimental result that the ratio of the eddy-current reaction
for the two stators (end-ring stator as base) must decrease with
increasing frequency from 2 to 20 Hz, but increase with frequency
from 20 to 100 Hz.   It is suggested that this variation in eddy-
current reaction is due either to the change in the length of the

---

* 'Continuous stator' is the stator without copper end rings that
  is not diametrically split.

air gap at the ends of the machine or to saturation effects, or a combination of both. The remaining tests described in this chapter were designed to investigate these ideas; they include the measurement of the distribution along the axial length of flux/pole, surface current density and power flow to the secondary.

The chapter ends with a summary of the conclusions made in each Section.

10.2   TORQUE

10.2.1 Measured Torque

The torque was measured by means of the torque transducer
described in Section 7.3, for a range of excitation of 4800 to
19200 A/m, and frequencies of 2 to 100 Hz.   The measured torque
for the continuous stator is shown plotted against frequency in
Fig. 10.1, and is tabulated in Table 8.1, where the values may be
compared directly with the torque measured on the end-ring stator.
The measured finite length factor R_{Lm}, may be obtained from Table
8.1. as the ratio of $\left[\dfrac{\text{torque for continuous stator}}{\text{torque for end-ring stator}}\right]$ at the same value
of excitation and frequency.

Two observations may be made from a comparison of the measured
torque for the continuous stator (Fig. 10.1) with the computed
values of torque for the end-ring stator (Fig. 8.3).

(i)   The frequency at maximum torque for the end-ring stator
        is lower than that for the continuous stator.   This is
        due to the greater resistance of the eddy-current paths
        in the continuous stator.

(ii)   The maximum measured torque for the continuous stator
        appears to be less than the computed torque for the
        end-ring stator for the same excitation.   This may be
        due to the greater extent of saturation in the end-ring
        stator causing the effective reactance of the eddy-current
        paths to be less than that in the continuous stator.

10.2.2 Calculated Torque

The torque was calculated by means of the non-linear theory
described in Chapters 6 and 8, and the finite length factor derived
in Section 9.4.   The method of determining R_L, and thereby the

torque or loss at any frequency, is given in Sections 9.6.1 and 9.6.2. The finite length factor, R_L, was computed for the continuous stator by this method, and is shown plotted against permeability for a range of frequencies in Fig. 10.2. Calculated torques for the continuous stator are shown in Fig. 10.1.

Values of $|\dot{H}_{xg}|$, μ_e, R_L, R_{Lm}, and $\frac{R_{Lm}}{R_L}$ for the continuous stator, for excitations of 4800, 9600 and 19200 A/m and for frequencies from 2 to 100 Hz, are given in Table 10.1. Computed values of torque, obtained by multiplying the torque for the two-dimensional model by the corresponding value of R_L, are shown plotted in Fig. 10.1.

10.2.3 Comparison of Measured and Calculated Torque

Since the calculated and measured torques for the end-ring stator compare favourably (see Section 8.2.3), the accuracy of the torque calculations for the continuous stator may be judged by comparing the calculated finite length factor, R_L, with the measured finite length factor, R_{Lm}, which are given in Table 10.1 for the experimental range of frequency and excitation.

The overall deviation in the ratio $\frac{R_{Lm}}{R_L}$ varies from 0.86 to 1.20, values less than 1 occuring between 50 Hz and 100 Hz, and values greater than 1 occuring at the relatively lower frequencies. The increase of R_{Lm} with frequency is therefore less than that of R_L.

Variation of R_L with excitation is accounted for approximately because μ_e is determined from the normal B-H curve for the material. Variation of R_L due to eddy-current reaction is shown by the variation of $|\dot{H}_{xg}|$ with frequency in Table 10.1. Both R_L and R_{Lm} increase with excitation at constant frequency, but the increase of R_{Lm} with excitation is less than that of R_L. A discussion of these results

is contained in Section 10.4.

10.2.3.1 Variation of R_L with Permeability and Length

The calculated value of R_L could be increased at low frequencies to bring the ratio (R_{Lm}/R_L) closer to unity by, either (a) decreasing μ_e, or (b) decreasing the developed length of the stator (L). These will be discussed in turn.

(a) To decrease μ_e at the lower frequencies is contrary to physical reasoning since H_{xg} decreases with frequency, and not only will there be less saturation at the centre of the machine but a greater proportion of the volume of the stator should be in an unsaturated state. It has not been verified that the value of μ_e may be chosen on the assumption that H_{xg} at the centre of the machine is approximately equal to that in the two-dimensional model for the same excitation and frequency, and, even if this were verified, there is no reason to suppose this value is a fair compromise for the variation in permeability over the axial length of the machine. The value of permeability at any frequency is however, unlikely to be less than the value of μ_e derived for saturated conditions at the centre of the machine.

(b) The variation of R_L with the developed length of stator is demonstrated in Fig. 10.3. It is seen that for a permeability of 180 and a frequency of 5 Hz, R_L decreases from 1.85 to an approximately constant value of 1.24 for a total axial length of $L > 2.5\ L_A$. Thus a 'correct' value of R_L could be obtained by selecting an equivalent length for the machine. But this equivalent length is dependent on frequency, a fact shown in Fig. 10.4, where R_L for a permeability of 180 is given over a range of frequency from 5 to 50 Hz for both the actual length

of the machine (L_S = 0.133 m, see Fig. 9.6) and the developed length of the machine, L, i.e. including length of radial end faces and outer surface (0.406 m). The value of R_L for the actual length is approximately 30% greater than that for the developed length of stator over the range of frequency given. Thus, choosing an equivalent length for the machine does not improve the accuracy of the loss or torque calculation over a wide frequency range.

Since the value of R_L is approximately constant for large values of L, an expression in closed form might be obtained for $\left.\frac{L}{h}\right\} \to \infty$. The expression would be complicated, however, and there would be little gain in achieving it, particularly as convergence of the series solution for loss is extremely rapid.

10.3 FLUX/POLE

10.3.1 Measured Flux/Pole

The flux/pole was measured by means of full-pitch search coils (attached to the surface of the stator), whose axial length was equal to the active length L_A (Sections 7.4.3. and 7.5.1). Values of the fundamental flux/pole were measured at excitations from 4800 to 19200 A/m and frequencies from 2 to 100 Hz and are shown plotted in Fig. 10.5 and tabulated in Table 10.2 (Φ_{hm}). Also shown in Table 10.2 are values of the ratio of the flux/pole measured on the stators with and without copper end rings. (Φ_{hm}/Φ).

10.3.2 Calculated Flux/Pole

The flux/pole was computed from Equation 9.38 for values of permeability from 100 - 750 and frequencies from 2 to 100 Hz. (Convergence of the series solution is slow and some 200 harmonic terms were required). The results of the computations are shown

plotted against permeability in Fig. 10.6 for an excitation of 1000 A/m. Since the permeability is assumed constant, the flux/pole is proportional to excitation.

The flux/pole for each value of frequency and excitation was determined by,

(i) determining the value of the equivalent constant permeability, $|\mu_e|$, for each excitation and frequency. The procedure for determining $|\mu_e|$ has been described in Section 9.6.2 and the values obtained are given in Table 10.1.

(ii) A value of flux/pole is read from Fig. 10.6 for the required values of $|\mu_e|$ and frequency and then multiplied by the excitation, to obtain the required value of flux/pole.

The computed values of flux/pole (Φ_{ha}), and the ratio Φ_{ha}/Φ are also given in Table 10.2.

10.3.3 Comparison of Measured and Calculated Flux/pole

The deviation between measured and calculated values of flux/ pole is generally < 10% between 2 and 20 Hz, but becomes progressively greater at frequencies > 20 Hz. The decrease of Φ_{ha} with increase in frequency is less than that of Φ_{hm} ; the increase of Φ_{ha} with increase in excitation is greater than that of Φ_{hm}. These results are discussed in the following sections.

10.4 DISCUSSION OF MEASURED VALUES OF FLUX/POLE AND FINITE LENGTH FACTOR

In Table 10.2 it is seen that, whereas values of $\dfrac{\Phi_{ha}}{\Phi}$ increase with frequency, values of $\dfrac{\Phi_{hm}}{\Phi}$ increase with frequency up to 20 Hz and then decrease; this indicates that the ratio of the eddy-current reaction for the two stators (end-ring stator as base), must decrease with frequency from 2 to 20 Hz but increase with

increasing frequency from 20 to 100 Hz. The occurrence of a maximum value for $\dfrac{\Phi_{hm}}{\Phi}$ indicates a difference between the three dimensional model and the actual machine, due either to a change in the physical parameters or the boundary conditions of the machine.

The level and extent of saturation in the stator is a function of excitation and frequency. (The term 'extent of saturation' means the axial length of the secondary surface that may be considered in a qualitative sense, to be saturated). As in the case of the finite length factor, R_L, variation of the level of saturation with excitation and frequency is accounted for approximately by the definition of μ_e, but variation in the extent of saturation with excitation and frequency is not wholly accounted for. It may be that, as the frequency rises, the extent of saturation increases causing the flux/pole to decrease to values lower than those predicted by theory. It seems unlikely, however, that saturation should have such a large effect on the ratio $\dfrac{\Phi_{hm}}{\Phi}$ at the relatively low excitation of 4800 A/m.

An alternative explanation may be given, based on the large increase in the length of air gap that occurs at the ends of the active length of the actual machine but not in the model. In the passive end regions of the actual machine where the length of the air gap is large, the permeance of the flux paths linking the eddy currents is relatively low, compared to that in the active region, so that the impedance of the current paths is also relatively low. If a greater proportion of current passes into the passive end regions as the frequency increase, the effects of the lower impedance in these regions to the currents will become increasingly significant. An effect of lowering the impedance of the current paths is to increase the eddy-current reaction within the active region causing the flux/pole to decrease. It would appear from the measurements of flux/pole that the effects of the relatively low impedance to

the currents in the passive end region become sufficiently large at frequencies greater than 20 Hz to cause a decrease in the ratio $\dfrac{\overset{\Phi}{\phi}_{hm}}{\phi}$.

A reduction in the finite length factor, R_{Lm}, should also be observed between 50 and 100 Hz if this hypothesis is correct; this is only seen to be so at 4800 A/m (Table 10.1), although $\delta R_{Lm}/\delta f$ decreases with increase in frequency for all excitations.

It is interesting to note that a comparison of the calculated and measured results of Yee and Wilson[63], who used the more realistic boundary conditions for the secondary given in Fig. 9.4, shows that exactly the same deviation with frequency and excitation occurs between measured and calculated torque as is given in this thesis. It cannot be concluded that this deviation is therefore independent of the boundary conditions at $z = \dfrac{\pm L_A}{2}$ since it may be due to some other assumption in their theory.

The effects of saturation and/or change of airgap length at the ends of the active length of the machine may be more easily detected by measurement of the distribution of the radial component of the air gap flux along the axial length of the stator.

10.5   VARIATION OF AIR-GAP FLUX WITH AXIAL LENGTH

The (flux/pole)/cm of axial length was measured using the 7 full-pitch search coils of 1cm width attached to the surface of the stator and shown in Fig. 7.7.   Measurement of the air-gap flux density by means of a Hall probe was also obtained, (see Section 7.4.3.2).

Fig. 10.7 shows the measured variation of the air-gap (flux/pole)/cm length at 50 Hz compared with the variation of air-gap flux density obtained with the Hall probe.   So far as could be detected, the maximum value of flux density measured by the probe occurred at

a point 2 mm within the active length of the machine for all frequencies and excitations. These curves are similar to those obtained by other authors[56,57].

The values of the measured (flux/pole)cm length at the centre of the continuous stator, ϕ_{hc}, is compared with that for the end-ring stator, ϕ_c in Table 10.3. The ratio of $\frac{\phi_{hc}}{\phi_c}$ at an excitation of 4800 A/m is seen to increase from 2 to 20 Hz but to decrease from 20 to 100 Hz in a manner similar to the variation of $\frac{\phi_{hm}}{\phi}$ discussed in Section 10.3. Whether this variation is due to the change in the air-gap length at the ends of the machine cannot be detected from observing only the (flux/pole)/cm length at the centre of the machine. There is, however, a definite increase with frequency in the values of the ration $\frac{\phi_{hc}}{\phi_c}$ at an excitation of 4800 A/m between 5 to 20 Hz, whereas there is little difference in this ratio at 19200 A/m between 5 to 20 Hz; this is probably due to the effects of saturation, which are explained as follows by reference to the waveforms of the air-gap flux density.

Plate 10.1a shows the flux density waveforms at the surface of the stator for excitations of 4800 A/m and 19200 A/m. The greater distortion due to saturation at the higher excitation is clearly recorded. Plate 10.1b shows the waveforms of flux density at the surface of the stator obtained with the search coils given in Fig. 7.7. Three effects are noted:

(i) An increase in the magnitude of the flux density between the axial centre and the ends of the stator and,

(ii) A change in phase between the flux density and primary excitation between the axial centre and ends of the stator.

(iii) The waveforms of the flux density at the ends of the stator are less distorted than those at the centre of the stator, which

indicates greater saturation of the iron at the centre.

All three effects are due to a decrease in eddy-current reaction between the centre and ends of the stator.

The greater saturation at the centre of the stator may cause a greater proportion of the flux/pole to pass across the air gap at the ends of the stator. This suggestion is confirmed by the following results.

The (flux/pole)/cm length measured by the search coils, 1, 5, and 6 (Fig. 7.7), are shown plotted against frequency for excitations of 4800 A/m and 19200 A/m in Fig. 10.8. The values are given as p.u. to a base of total flux/pole, (Φ_{hm}). The variation of the flux at the end of the stator (coil 6) with frequency for constant excitation is seen to differ from that at the centre of the stator (coil 1), and clearly indicates that a progressively higher percentage of the total flux/pole exists at the ends of the machine as the frequency increases. Comparison of curves a, b and d, e, in Fig. 10.8 shows that the displacement of flux from the centre to the ends of the stator is more pronounced at 19200 A/m than at 4800 A/m. (This effect is similar to the increase in the flux penetration into the stator in the radial direction as saturation occurs in the surface layers).

The results of the measurements of flux/pole and (flux/pole)/cm length thus show that the change in the air gap length at the axial ends of the machine causes the eddy-current reaction to be higher than theoretically predicted at frequencies where the lower impedance presented to the currents in the passive end regions becomes significant, and that saturation, which occurs primarily at the centre of the machine, may modify this situation in causing a greater percentage of the flux to cross the air gap at the axial ends of the stator, even at the lower frequencies.

10.6 SURFACE CURRENT DENSITY DISTRIBUTION

10.6.1 General

The suggestion made in Section 10.4 that a large percentage of the eddy-currents in the stator flow outside the active region of the machine, needs experimental confirmation. It is also informative to study the current density distribution on the surface of the stator since this quantity is related to the loss density distribution in the stator, whereas the radial flux density in the air gap is related to the power transferred to the stator.

10.6.2 Measurement of Surface Current Density

The current density was estimated from measurements made using the probes (Fig. 7.5) described in Section 7.4.2 for a range of excitation from 4800 A/m to 19200 A/m and frequencies from 2 Hz to 100 Hz. The method of estimating the fundamental components of current density from the voltages obtained from these probes has been described in Section 7.5.2.

Variation of the peripheral and axial components of current density, J_{xh1} and J_{zh1} respectively, obtained by means of the probes shown in Fig. 7.5, are given in Fig. 10.9 for excitations of 4800 A/m and 19200 A/m and frequencies of 5 Hz and 50 Hz. These curves are typical of measurements made over the full range of excitation and frequency. Note that the currents flowing in the radial direction in the end faces are given as J_{zh1} on the assumption that the stator profile is developed onto the air-gap surface.

Typical waveforms obtained with the probes are given in Plate 10.2. The waveforms of J_{zh} within the active length are similar to those obtained on the surface of the end-ring stator and the bar, whereas waveforms of J_{zh} outside the active length are sinusoidal. Waveforms of J_{xh} within the active length have a

more pronounced peak than J_{zh}; waveforms of J_{xh} outside the active length are sinusoidal.

A portable probe was used to measure the current density at other points on the stator surface. Typical examples of the measurements obtained are given in Table 10.4. The waveforms in each case were sinusoidal.

10.6.3 Computed Surface Current Densities

The values of $|J_{zhg}|$ and $|J_{xhg}|$ computed from Equations 9.29 and 9.28 respectively, are shown in Fig. 10.9. (About 30 harmonic terms were required for convergence of the series solution). Values given in this figure are p.u., where the base value is the amplitude of the current density computed at the axial centre of the stator.

10.6.4 Discussion of Results

The following observations are made from the results presented in Fig. 10.9.

(i) The curves of J_{xh1} and J_{zh1} are continuous from the air gap surface to the radial end faces - there is no discontinuity at $Z = \pm L_S/2$ (see Fig. 9.6). The agreement between measured and theoretical values of J_{zh1} is fairly good, considering the approximations made in the model, and is better at 5 Hz than 50 Hz. There is considerable difference, however, between the measured and theoretical values of J_{xh1}. Firstly the theoretical maximum value of J_{xh1} is much greater than the corresponding measured value. Secondly, the maximum value of J_{xh1} occurs outside the active length, whereas the corresponding calculated value occurs at the axial ends of the machine; this clearly shows that the eddy currents are forced into the end regions $(Z > L_A)$ in seeking paths of minimum impedance.

It is felt that these results justify the development of the secondary profile on to the air gap surface, but also show the effects of misrepresentation of the primary current sheet and end regions in the analytical model.

(ii)   The measured p.u. values of axial and peripheral current density are greater in the end regions at 19200 A/m than at 4800 A/m, whereas the computed values of p.u. current in the end region are less for the higher excitation. The reason for the variation in the computed values of current density is the choice of $|\mu_e|$, i.e. a decrease in $|\mu_e|$ results in less current in the end region, and a greater concentration of peripheral current at the ends of the active length of the machine. The increase in the measured p.u. current in the end region is presumed due to saturation at the axial centre of the machine causing flux to be forced towards the ends of the machine and thereby causing a greater percentage of current to be forced into the end regions. It would appear, therefore, that the change in current distribution with excitation is governed more by the combined effects of saturation and the change in air gap length in the end regions than by the level of saturation alone.

(iii)   Although the maximum value of J_{xh1} is much smaller than the theoretical value, it is not less than 78% of the value of J_{zh1} at the axial centre of the stator. There is also little variation in the maximum value of J_{xh1} with frequency and excitation. It would appear from these observations that the maximum level of saturation for the axial component of the magnetic field could be close to that for the peripheral component. Although the region of saturation is not so extensive for the

axial component of the magnetic field as it is for the
peripheral component, a large proportion of the loss due
to the axial component must occur under saturated conditions.
This is an important observation, as the use of an equivalent
linear permeability for the stator is based on the assumption
that the whole of the stator surface is at the same level of
saturation.

The values of J_{xh1} and J_{zh1} given in Table 10.4 show that a
considerable proportion of the eddy currents flow outside the developed
length of stator to which the current density probes were attached
(9.2 cm). Considering that the length of the end face is 7.1cm ,
it is surprising that such a large percentage of current flows in the
z - y plane.

10.6.4.1 Current Density at the Axial Centre of the Stator

In Table 10.3 the surface current density measured at the centre
of the continuous stator, J_{zc1} is compared with that measured on the
surface of the end ring stator, J_{z1}. The agreement between these
readings is very good (except at 2 Hz when J_{zc1} is considerably lower
than J_{z1}), and is in fact better than that predicted in Table 9.1.
It is believed that as a greater proportion of the current is forced
into the end regions than theoretically predicted, the effect of the
cross pole currents on the field distribution at the centre of the
stator is less than that suggested in Table 9.1; this statement is
verified by the measurements of the air gap flux at the centre of
the continuous stator (Section 10.5), which show that the eddy-current
reaction is greater than that predicted theoretically at the higher
values of frequency. Thus, the assumption on which the choice of μ_e
is based, that $|\dot{H}_{xg}|$ at the axial centre of the stator may be determined
approximately by the two-dimensional non-linear theory, appears to be

justified, even for a machine of relatively small (length/pole pitch) ratio for all frequencies >2 Hz, and for all excitations within the experimental range.

10.7 RADIAL POWER FLOW

10.7.1 General

The power flow to the stator is dependent on the magnitude of the primary excitation K, the air gap flux density $\dot{B}_y$ and its phase with respect to the primary excitation $/\dot{B}_y$. It was felt that measurement of the total power to both the continuous and end-ring stators would enable the distribution of the additional power for the peripheral current losses to be determined.

Methods of measuring power flow in the air gap of machines have been tried[64,65], but not, it is believed, by obtaining the product of primary current and air gap flux density.

10.7.2 Theory and Calibration

The power flow to the secondary may be measured by obtaining the product of $\dot{B}_{yg}$ and $\dot{K}$, if $|B_{yg}|$ is constant across the air gap.

The net force exerted on a unit volume of current is given by the vector equation,

$$\underline{F} = \left[\underline{J} \times \underline{B} \right]$$

Thus the mean force per unit surface area, on the current sheet K in the peripheral direction is

$$F_x = \frac{1}{\lambda} \int_0^\lambda \left[K.B_y \right].dx \Big]_{y=0}$$

so that,

$$F_x = \frac{1}{2} \cdot Re \left[\dot{K}.\tilde{\dot{B}}_y \right]\Big]_{y=0} \qquad 10.1$$

F_x represents the reaction force on the current sheet. The rate of working against this force must equal the power leaving the primary

member. The velocity v of the current sheet and associated flux density wave is

$$v = \frac{\omega}{q} \text{ m/sec.}$$

Hence the power/unit area of the primary surface P is,

$$P = F_x \cdot v$$

so that, from 10.1

$$P = \frac{\omega}{2q} \text{Re}\left[\dot{K} \ \tilde{B}_y\right]_{y = o}$$

which is equal to the power entering the secondary.

If $\dot{B}_y\Big]_{y = g} \simeq \dot{B}_y\Big]_{y = o}$, then the search coils attached to the stator surface may be used to obtain $B_y\Big]_{y = o}$. A set of full pitched search coils, similar to those on the stator (Fig. 7.7), was attached to the rotor surface. Measurement of the flux density with these coils showed negligible difference between $\left|\dot{B}_y\right|\Big]_{y = o}$ and $\left|\dot{B}_y\right|\Big]_{y = g}$ over a wide range of frequency and excitation.

The primary current sheet is assumed to be equivalent to discrete windings placed in slots in laminated iron. While it is realised that there will be primary iron loss, it is considered that the eddy-current reaction and loss in the secondary iron is much greater than that in the primary iron, even at the ends of the active region ($Z = \pm \frac{L_A}{2}$) where the value of air gap flux is greatest. This assumption may be verified by comparing the total torque obtained from the power flow measurements with that measured by the torque transducer (see Section 10.5.3).

10.7.2.1 The Method of Measurement

A voltage proportional to the radial flux density $\dot{B}_{yg}$ was obtained by means of the full pitch search coils shown in Fig. 7.7.

The mmf axes of the rotor were located by the method described in Section 7.7.3. The variation of mmf with time on these axes was

determined by integrating the output from a linear coupler placed around one of the supply leads to the rotor (Section 7.7.3).

An mmf axis was aligned with the axis of the search coils as shown in Fig. 10.10 below, so that the product of the integrated linear coupler output and the voltage from the search coil was proportional to $\dot{K} \times \dot{B}_y$.
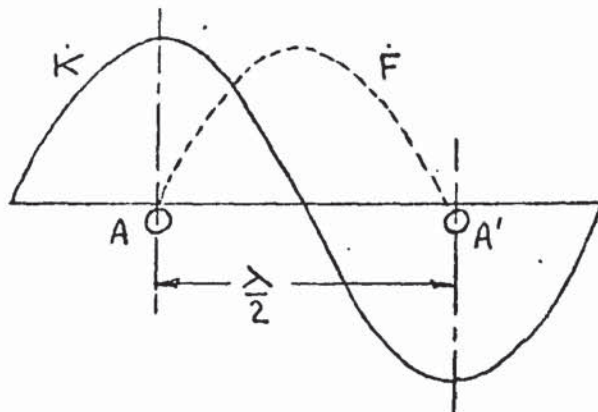
<u>Fig. 10.10</u>

Position of primary mmf ($\dot{F}$) and equivalent current sheet ($\dot{K}$) of the rotor winding at the instant the current in the supply lead to the rotor is a maximum. AA' : Search coil.

The instruments used to obtain this product are given in circuits A and B of Fig. 5.5.

10.7.2.2 Calibration Procedure

If v_1 and v_2 are the input voltages to the multiplier (Fig. 5.5) then the output voltage is,

$$v_o = \frac{v_1 v_2}{10} \qquad \qquad 10.2$$

Let the output voltage from the linear coupler be v_L, then the input to the multiplier is, from Fig. 5.5. (circuit A),

$$v_1 = \frac{v_L A_1 A_4}{\omega RC} \qquad \qquad 10.3$$

Let the voltage output from the search coil be v_e, then the input to the multiplier is, from Fig. 5.5 (circuit B),

$$v_2 = v_e \cdot A_2 \qquad \qquad 10.4$$

Thus from Equations 10.2, 10.3 and 10.4

$$v_o = \frac{v_e \, v_L \, A_2 \, A_1 \, A_4}{10 \, \omega RC} \qquad \qquad 10.5$$

But the power $p = \dfrac{v_e}{2 \times 10^{-2}} \cdot \dfrac{v_L}{Y}$ W /m^2 10.6

where Y is volts/A/m from the coupler.

Substitute Equation 10.5 into Equation 10.6, so that, the loss,P, is

$$P = \dfrac{10\ V_o\ \omega RC}{A_1\ A_2\ A_4\ 2.10^{-2}\ Y}\ \text{W /m}^2 \qquad\qquad 10.7$$

and V_o is now the d.c. voltage indicated by the digital voltmeter. (Fig.5.5)

The torque/cm axial length,

$$T = P\ (\lambda\ p)\ 10^{-2} \cdot \dfrac{P}{\omega}$$

$$= \left[\dfrac{P}{\omega}\right] \cdot 1.42 \times 10^{-2}\ (N - m)$$

for the experimental machine.

10.7.3 Discussion of Results

The power flow to the end-ring stator was measured at 50 Hz only using the full-pitch search coils of 1 cm length shown in Fig. 7.6. This was undertaken as an additional check on the method of measurement. There was negligible difference in the readings obtained from the search coils and Table 10.5 compares the total torque measured by the present method and that measured by the torque transducer.

The power flow to the continuous stator was measured at 50 Hz and 20 Hz for excitations of 2400 A/m to 19200 A/m. (At lower frequencies the readings were too unstable for reasonable accuracy. This was also found to occur in the measurement of phase angles,and was believed to be due to fluctuations in the speed of the supply generator. The torques obtained are given in Table 10.6. Also given in Table 10.6 are the torque/cm length of the continuous and the end-ring stator,expressed as p.u. of the mean torque/cm of the continuous stator.

The following observations are made from the results presented

in Tables 10.5 and 10.6.

(i)   The total torque obtained by measurement of the power flow
       differs from that measured by the torque transducer by less
       than 9% (torque by power flow as base).

(ii)   The percentage of the total power flow at the ends of the machine
       is greater than at the centre of the machine for all values of
       excitation and frequency within the range of the tests carried
       out.   Since the eddy-current reaction is least at the ends of
       the machine and greatest at the centre of the machine this may
       appear incorrect, but it may be reasoned that the increase in
       radial flux density in the air gap and thereby the increase in
       power flow is not only due to a decrease in $\dot{H}_x$ but also to an
       increase in $\dot{H}_z$.

(iii) The percentage of the total power flow at the ends of the machine
       increases with excitation and/or frequency and conversely the
       percentage of the total power flow at the centre of the machine
       decreases with increase of excitation and/or frequency.   The
       variation in the distribution of power density with frequency
       and excitation, is consistent with the observed variation of
       the distribution of radial flux in the air gap.

(iv)   The power density at the axial centre of the stator is greater
       than that for the end-ring stator for all excitations and
       frequencies, and is due to the relatively small ratio of
       $\frac{\text{active length}}{\text{pole pitch}}$ for the experimental machine.

10.7.4   Phase Angle $\underline{/\dot{B}}_{yg}$

The phase angle $\underline{/\dot{B}}_{yg}$, i.e. the angle between the primary excitation
(current sheet) and the air gap flux density, may be obtained by the
method described in Section 10.5.2.1, for the measurement of power flow.
The angle $\underline{/\dot{B}}_{yg}$ is given by that method as the angle between the voltage
from the search coils and the integrated output from the linear coupler.

The angle between the waveforms was obtained by the analysis of oscillograms. The results of the measurements are given in Table 10.7 for excitations of 4800 A/m to 19200 A/m and frequencies of 20 Hz and 50 Hz. The values of flux in coil 7, which is outside the active length, was too small to give reliable results.

It is seen from Table 10.7 that $\underline{/\dot{B}}_{yg}$ at the axial centre of the stator decreases with increase in excitation and frequency, i.e. as the eddy-current reaction increases. At the end of the active length however, $\underline{/\dot{B}}_{yg}$ does not approach 90° as might be supposed if the energy transfer decreases to zero. This may be due, either to eddy current reaction in this region due to the circulation of eddy currents outside the active length of the stator, or hysteresis of the primary or secondary iron.

10.8 CONCLUSION

The measured and calculated torque for the continuous stator have been compared in Section 10.1, both directly (Fig. 10.1), and by means of the finite length factor, R_L, in Table 10.1. The deviation between measured and calculated values of R_L vary generally from -14 to $+14\%$, (except for the value at 4800 A/m at 5 Hz which is $+20\%$), the calculated value being the base. The deviation between measured and calculated flux/pole is generally $< 10\%$ between 2 Hz and 20 Hz, but increases to -23% at 100 Hz; no calculations of flux/pole are given in the publications discussed in Section 9.2 to compare with these figures. The experimental investigation was carried out on a machine of small (length/pole pitch), ratio (0.58) in which finite length effects are large, so that agreement between measured and calculated results should be even better on a machine of larger (length/pole pitch) ratio, in which the least saturated regions at the ends of the machine are less significant.

Considering the approximations made, these results justify the definition of equivalent constant permeability, μ_e, and the mathematical model, for the experimental range of frequency and excitation.

The value of $|\mu_e|$ is obtained from a knowledge of the dimensions and parameters of the machine, the frequency and primary excitation, and the normal B-H curve of the material; values of the linear permeability in previous publications (Section 9.2) were arbitrarily chosen and iterative solutions were required. The definition of μ_e accounts for changes in the level of saturation at the axial centre of the stator, and would appear from the results to account approximately for the variation in the mean level of saturation throughout the stator with excitation and frequency. Measurements of surface current density show that there is probably little difference between the maximum levels of saturation for the peripheral and axial components of the magnetic

field. The agreement between measured values of surface current density

at the centre of the continuous and the end-ring stators verify that μ_e

may be determined from the two-dimensional field distribution at the

axial centre of the stator.

It was stated in Section 10.2.3.1 that although the calculated

value of R_L at low frequencies could be increased to reduce the difference

between R_L and R_{Lm} by decreasing μ_e, this would be contrary to physical

reasoning. An increase in permeability to decrease the difference

between R_L and R_{Lm} at high frequencies (50 to 100 Hz), is not contrary

to physical reasoning, since the reduction in surface magnetic field

strength in the end regions of the machine may cause an increase in the mean

level of permeability for the stator. It is interesting to consider why

the measured torque is larger than the calculated torque at low frequencies.

Hysteresis may contribute to the torque due to the increase in the air

gap flux density, and the reduction of eddy-current reaction, at the ends

of the machine; its contribution would be greatest at low frequencies.

The nett effect of an increase in R_L at the lower frequencies, due to

hysteresis torque, and a reduction in R_L at the higher frequencies, due to

the circulation of eddy currents outside the active length of the machine,

would be relatively little change in the value of R_L. This is observed

in Table 10.1 for frequencies between 5 to 100 Hz.

The significance of the developed length for the stator is shown

in the computation of the finite length factor R_L, (Section 10.2.3.1), and

is justified by the measurements of surface current density (Section 10.6).

If the actual length of the stator had been used, R_L would be some 30%

greater than that for the developed length at all values of frequency.

Angst[55] based his analysis on the model of Wood and Concordia,[54] but used

the actual length of the machine in his calculations of torque. He

found that the calculated torque was 26% greater than the measured torque

for a machine whose (length/pole pitch) ratio was greater than one, but the difference was even greater for a machine whose (length/pole pitch) ratio was less than one. He therefore used an empirical factor to reduce the calculated torque - but only for machines whose (length/pole pitch) ratio was less than one. The rapid convergence of the solution for R_L eliminates the need for a more precise definition of the current sheet (Fig. 9.5), although the effects of its inaccuracy are seen in the computed curves of surface current density distribution (Fig. 10.9).

The main deficiency in the theory is its inability to account for the change in the air gap length at the ends of the machine. The concentration of peripheral eddy-currents at the ends of the active length increases with frequency and the level of saturation at the axial centre of the stator. The change in air gap length at the ends of the machine causes the eddy currents to seek paths of minimum impedance outside the active length and in so doing increase the effective length of the stator and the total eddy-current reaction. The nature and magnitude of these effects have been clearly shown by measuresments of flux/pole, surface current density and power flow to the stator, which therefore indicate the areas of the theory that may be improved.

CHAPTER 11

GENERAL CONCLUSIONS AND FURTHER WORK

11.1   GENERAL CONCLUSION

Analytic solutions have been derived in this thesis for the loss
in solid iron due to a single travelling mmf wave, taking into account
the effects of both magnetic non-linearity and finite length.   The
analysis has been divided into two main parts;   a solution is derived
in the first part for a two-dimensional model, including non-linearity,
and in the second part is extended to a three-dimensional model.

The two-dimensional solution contains factors which,

(i)   represent the shape of the normal B-H curve,

(ii)   account for the effect of the shape of the normal B-H curve on

         the penetration of the electromagnetic wave into the iron,   and

(iii)   account for the effects of saturation harmonics.

The solution for the loss is expressed in terms of the primary
excitation and is applicable to machines of any air-gap length.

Generalised torque/frequency characteristics have been given in
which the eddy-current reaction is implicit;   the torque, or loss, may
be obtained from this characteristic together with the expressions for
the peak torque and the frequency at peak torque.

The two-dimensional theory was verified on the experimental machine
with the end-ring stator.   The deviation between measured and calculated
values of loss, flux/pole, and surface current density is within $\pm$ 9%
for the experimental range of frequency and excitation.

A relationship between the peripheral component of the magnetic
field on the surface of the seconday H_{xg}, and the primary excitation K
has been given, and discussed with reference to the experimental machine.

e error in the loss calculation by assuming $|\dot{H}_{xg}| = \hat{K}$, for the non-linear case, is shown, particularly at low frequencies. This does not appear to have been studied previously.

The relation between the loss and the machine parameters has been shown and three distinct modes of operation of the machine are defined; these can be identified by the value of the non-dimensional quantity, Q_n, so that, when,

(i) $Q_n \gg 1$, the eddy-current field is strong and the loss is 'current dependent' ($P_n \alpha \rho^{\frac{1}{2}}$),

(ii) $Q_n \ll 1$, the eddy-current field is weak and the loss is 'voltage dependent' ($P_n \alpha \left[\frac{1}{\rho}\right]^{\frac{1}{b+1}}$) and

(iii) $Q_n = 1$, when maximum loss occurs in the iron.

Additional verification of the theory for the solid iron region was obtained by measurement of loss and current density on the round mild steel bar. Significant errors in the calculation of the loss occur only when the value of the surface magnetic field strength is below the knee of the normal B-H curve.

The flux penetration tests were successful only at high excitations and low frequencies. Since the attenuation and change of phase of the electromagnetic field with depth into the iron may be considerable compared to the width of the search coils, it would be of more value to measure the penetration of the electric field rather than the magnetic field into the iron.

The more important features of the work on the combined effects of magnetic non-linearity and finite length are:

(i)   the three-dimensional linear analysis of a model in which the axial component of the primary excitation is set equal to zero in the passive end regions and the stator cross-section is developed on to the air-gap surface,

(ii)   the definition of an equivalent constant permeability for the
        iron to account approximately for magnetic non-linearity, and

(iii)   a method of calculating the loss, or torque and the flux/pole.

The analytic solution was verified by means of an experimental
investigation on the machine with the continuous stator. The deviation
between measured and calculated values of finite length factor, R_L, and
flux/pole, is within $\mp$ 14% and +2% and -23% respectively, the calculated
values being the base.

Measurements of flux/pole and surface current density have clearly
shown that an increasing proportion of the crosspole currents exist outside
the active length of the machine as the frequency and excitation increases.

The objectives of the work contained in this thesis were not only
to obtain and verify an analytic solution, but also to demonstrate its
strengths and weaknesses and to gain an understanding of the variation
in the loss with the machine parameters;   it is believed that these
objectives have been achieved, and it is hoped that the results of this
work will be useful in the design of machines with solid iron members.

11.2   FURTHER WORK

The results of the theoretical and experimental investigation
given in this thesis has led to work on an axially slotted solid-iron
stator;   measurement of loss, flux/pole and current-density distribution
on this stator may be compared directly with the experimental results
given here since the end-ring, continuous and slotted stators have the
same main dimensions.

Further work should also include the effect, on the loss in solid
iron, of superposing several travelling mmf waves and a d.c. field;   the
results of this work would be relevant to the calculation of mmf harmonic
and negative sequence losses.

To advance the theory for the combined effect of finite length

and magnetic non-linearity, both the increase in air-gap length at the axial ends of the machine and the variation of permeability with axial length must be accounted for; the latter effect is, in some part, dependent on the former. To take account of the change in air-gap length at the ends of the machine, a model may be considered which is similar to Fig. 9.2 in all respects except that the primary iron is assumed to extend over a length L_p, where $L_p < L$. Analysis of this model, which must also include the effects of magnetic non-linearity, may prove intractable unless approximations are made. These approximations may, in turn, obviate any advantages that this analysis should have over the present analysis. Finite difference, or finite element,[66] solutions may provide information which will enable suitable approximations to be made.

APPENDICES

APPENDIX I

AMPLITUDE OF THE FUNDAMENTAL COMPONENT OF THE FLUX DENSITY WAVEFORM

A1.1   GENERAL

This Appendix contains the derivation of the fundamental component of the flux density waveform, which is obtained from the normal B-H curve for the steel for a stated waveform of magnetic field strength (Section 4.6).

A1.2   ANALYTIC EXPRESSION FOR THE FLUX DENSITY WAVEFORM

If the magnetic field strength is given by

$$h = \frac{H \sin \omega t}{1 - U \sin \omega t} \qquad \qquad \text{A1.1}$$

and the normal B-H curve is represented by the Frohlich expression, so that,

$$b = \frac{h}{d + kh}, \qquad \qquad \text{A1.2}$$

the flux density waveform is given by,

$$b_{(\omega t)} = \frac{H}{(kH - dU)} \left[\frac{\sin \omega t}{c + \sin \omega t} \right], \quad 0 < \omega t < \pi \qquad \text{A1.3}$$

and

$$b(\omega t) = \frac{-H}{(kH - dU)} \left[\frac{\sin \omega t}{c + \sin \omega t} \right], \pi < \omega t < 2\pi$$

where $c = \dfrac{d}{(kH - dU)}$ '   A1.4

A1.3   FUNDAMENTAL COMPONENT OF $b_{(\omega t)}$

If $b_{(\omega t)}$ may be expressed as a Fourier series so that

$$b_{(\omega t)} = \sum_{n = 1}^{n = \infty} A_n \sin(n \omega t) \quad ,$$

where the fundamental component is $(A_1 \sin \omega t)$.

A_1 is given by,

$$A_1 = \frac{1}{\pi} \int_0^{2\pi} b_{(\omega t)} \sin \omega t \, d(\omega t)$$

$$= \frac{1}{\pi} \int_0^{\pi} b_{(\omega t)} \sin \omega t . d(\omega t) + \int_{\pi}^{2\pi} b_{(\omega t)} \sin \omega t \, d(\omega t) \quad \text{A1.5}$$

From Equations A1.5 and A1.3,

$$I_1 = \int_0^\pi b_{(\omega t)} \sin \omega t \, d(\omega t) = \frac{H}{kH - dU} \int_0^\pi \frac{\sin^2 \omega t}{c + \sin \omega t} \cdot d(\omega t), \quad 0 < \omega t < \pi$$

A1.6

and

$$I_2 = \int_\pi^{2\pi} b_{(\omega t)} \sin \omega t \, d(\omega t) = \frac{-H}{kH - dU} \int_\pi^{2\pi} \frac{\sin \omega t \, \sin(\omega t - \pi)}{c + \sin(\omega t - \pi)} d(\omega t), \quad \pi < \omega t < 2\pi$$

A1.7

Letting $\left. \begin{array}{l} \tau = t - \pi \\ t = \tau + \pi \end{array} \right\}$ Equation A1.7 becomes,

$$I_2 = + \frac{H}{kH - dU} \int_0^\pi \frac{\sin^2(\omega \tau) \cdot d(\omega \tau)}{c + \sin(\omega \tau)}$$

A1.8

In Equations A1.6 and A1.8, the integral,

$$\int_0^\pi \frac{\sin^2 x}{c + \sin x} = \left[-\cos x - cx \right]_0^\pi + c^2 \int_0^\pi \frac{dx}{c + \sin x}$$

A1.9

The solution of the integral in Equation A1.9, I_3, has two forms,

(i) $c^2 < 1$

$$I_3 = c^2 \int_0^\pi \frac{dx}{c + \sin x} = \frac{\mp c^2}{1 + c^2} \cdot \ln \left[\frac{1 - \sqrt{1 - c^2}}{1 + \sqrt{1 - c^2}} \right]$$

A1.10

(ii) $c^2 > 1$

$$I_3 = c^2 \int_0^\pi \frac{dx}{c + \sin x} = \frac{\pm c^2}{\sqrt{c^2 - 1}} \left[\pi - 2 \tan \left| \frac{\pm 1}{\sqrt{c^2 - 1}} \right| \right]$$

A1.11

where the upper signs are for $c > 0$

and the lower signs are for $c < 0$

Thus, the fundamental component of the flux density waveform, A_1

is obtained from Equation A1.5, as,

$$A_1 = \frac{2H}{\pi(kH - dU)} \left[2 - c\pi + I_3 \right]$$

A1.12

APPENDIX II

LINEAR THEORY FOR THE ROUND BAR

A2.1 GENERAL

This Appendix compares the linear analysis for the electro-magnetic fields and power loss in a specimen of cylindrical cross section, e.g. the round bar (Section 5.4   ), with that for a flat, semi-infinite specimen.

A2.2 ANALYSIS IN CYLINDRICAL CO-ORDINATES

The co-ordinate system referred to in this analysis is shown in Fig. A2.1.

The magnetic field strength at the surface of the bar is known directly from the a.c. supply current which flows axially through the bar. The current-density distribution within the bar is governed by the diffusion equation:
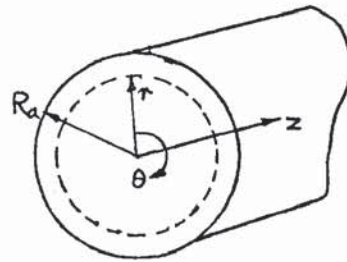
Fig. A2.1

$$\nabla^2 \underline{J} = \frac{\mu_o \mu_r}{\rho} \cdot \frac{\partial \underline{J}}{\partial r} \qquad\qquad\text{A2.1}$$

Equation A2.1 reduces to the form,

$$\frac{\partial^2 J_z}{\partial r^2} + \frac{1}{r} \cdot \frac{\partial J_z}{\partial r} = \frac{\mu_o \mu_r}{\rho} \cdot \frac{\partial J_z}{\partial t} \qquad\qquad\text{A2.2}$$

By writing $J_z = \text{Re } \dot{j} \, e^{j\omega t}$

where $\dot{j}$ is a function of r only, Equation A2.2 becomes

$$\frac{\partial \dot{j}^2}{\partial r^2} + \frac{1}{r} \cdot \frac{\partial \dot{H}}{\partial r} - jm^2 = 0 \qquad\qquad\text{A2.3}$$

where
$$m = \sqrt{\frac{\omega \mu_o \mu_r}{\rho}} \qquad\qquad A2.4$$

The solution of Equation A2.3 is obtained, with due regard to the boundary conditions, as

$$\dot{J} = J_R \, \frac{M_o(m \, r)}{M_o(mR_a)} \cdot e^{j\left(\phi_o(mr) - \phi_o(mR_a)\right)} \qquad\qquad A2.5$$

where J_R is the surface current density (i.e. $\dot{J} = J_R$ at $r = R_a$)

$$M_n(mr) = \left| J_n(j^{3/2} \, mr) \right| \qquad\qquad A2.6$$

and

$$\phi_n(mr) = \angle J_n(j^{3/2} \, mr) \qquad\qquad A2.7$$

where J_n is the Bessel function of the first kind of order n (n = 0,1,2...)

From curl $\underline{H} = \underline{J}$,

$$\frac{\partial H_\theta}{\partial r} = J_z \qquad\qquad A2.8$$

Letting $H_\theta = \text{Re} \, \dot{H} \, e^{j\omega t}$, Equations A2.8 and A2.5 give,

$$J_R = \frac{H_R m}{M_R} \cdot e^{j\phi_R}; \qquad\qquad A2.9$$

where H_R is the surface magnetic field strength, $\qquad\qquad$ A2.10

$$M_R = \frac{M_1(mR_a)}{M_o(mR_a)} , \qquad\qquad A2.11$$

and

$$\phi_R = \left[\phi_o(mR_a) - \phi_1(mR_a) + 3/4 \, \pi \right] \qquad\qquad A2.12$$

ϕ_R is the 'power factor angle' by which the surface current density, J_R, leads the surface magnetic field strength H_R (Equation A2.9).

The power loss/unit surface area in the bar may be obtained as

$$P_R = \frac{|J_R|^2 \, \rho}{m} \, M_R \cos \phi_R \qquad\qquad A2.13$$

Tables of M_1, M_o, ϕ_o and ϕ_1 are given by Mclachlan so that P_R and J_R may be obtained from Equations A2.13 and A2.9 respectively.

A2.3 COMPARISON WITH THE ANALYSIS FOR FLAT PLATE

When $(mR_a) \to \infty$, Equations A2.9, A2.11, 12, and 13 become

$$\cos\phi_R \to \cos\phi_\infty = 0.707 \qquad\qquad A2.14$$

$$M_R \to M_\infty = 1.0$$

$$P_R \to P_\infty = \frac{J_R^2 \, \rho}{2 \sqrt{2} \, m} \qquad\qquad A2.15$$

$$J_R \rightarrow J_\infty = H_R m \, e^{j \, 45^o} \qquad\qquad A2.16$$

Equations A2.15 and A2.16 are equal to those obtained by considering a flat, semi-infinite plate . (note $m = \sqrt{2}\,\alpha$).

The ratio of the power $\mathrm{loss/m}^2$ in the bar to the power $\mathrm{loss/m}^2$ in a flat plate is obtained from Equations A2.11 and A2.15 as,

$$\frac{P_R}{P_\infty} = \sqrt{2}\, M_R \, \cos\phi_R \qquad\qquad A2.17$$

The ratio of the surface current density in the bar to the surface current density in a flat plate is obtained from Equations A2.9 and A2.16 as,

$$\frac{|J_R|}{|J_\infty|} = \frac{1}{M_R} \qquad\qquad A2.18$$

The ratios P_R/P_∞, $|J_R|/|J_\infty|$ and $\cos\phi_R$ are plotted in Fig.A2.2 against (mR_a).

A2.4   CALCULATIONS FOR THE ROUND BAR (7.6 cm diameter).

For the bar of EN1A steel used in the experimental investigation (Section 5.3),

$\omega = 314$ rad/sec.

$\rho = 1.9 \times 10^{-7} \ \Omega - m$

A value of 100 was chosen for the relative permeability of the steel μ_r; this is approximately equal to the value of μ_r corresponding to

$H_R = 15000$ A/m (Fig. 5.2).

Thus, from Equation 3.4, $m = 455.0 \ (m^{-1})$

For a bar diameter of 0.076 m

$(mR_a) = 17.8$

From Fig. A2.2,

$$\left. \begin{array}{ll} \dfrac{P_R}{P_\infty} & = \ 0.96 \\[2em] \dfrac{J_R}{J_\infty} & = \ 1.02 \end{array} \right\} \quad (mR_a) \ = 17.8$$

APPENDIX III

FINITE-DIFFERENCE SOLUTION OF EQUATION 4.13

In this Appendix, a brief description is given of the finite-difference solution of Equation 4.13.

Equations 4.11 and 4.12, from which Equation 4.13 is derived may be written in finite difference form, as

$$H_{m+1} - 2H_m + H_{m-1} = H_m . \xi^2 . \Delta y^2 \qquad\qquad A3.1$$

$$H_m (\xi_{m+1} - \xi_{m-1}) = \frac{\omega}{\rho} . \Delta y . B_m - \xi (H_{m+1} - H_{m-1}) \qquad A3.2$$

where $\quad \xi = \dfrac{\partial \varepsilon}{\partial y} \qquad\qquad A3.3$

and H_m and B_m correspond at a depth of y_m - see Fig. A3.1 below.
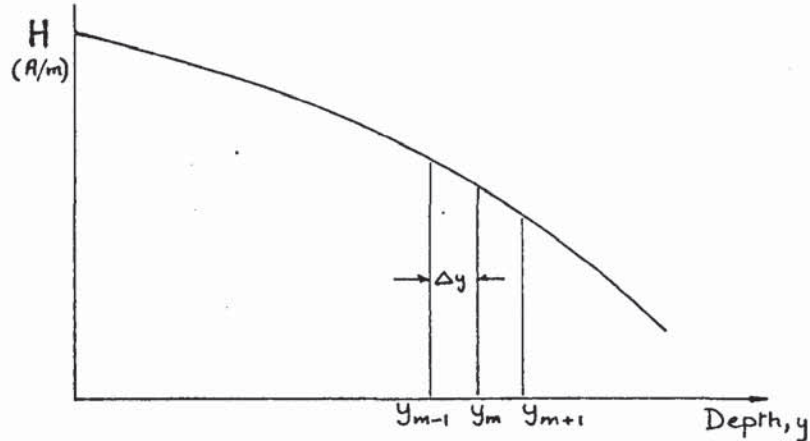
Fig. A3.1

Thus,

$$H_{m-1} = 2 H_m - H_{m+1} + H_m \xi^2 \Delta y^2 \qquad\qquad A3.4$$

and
$$\xi_{m-1} = \xi_{m+1} + 2 \xi_m \frac{(H_{m+1} - H_{m-1})}{H_m} + \frac{2\omega}{\rho H_m} B_m . \Delta y \qquad A3.5$$

so that evaluation of H_{m-1} from Equation A3.4 enables ξ to be

obtained from Equation A3.5.

Initial values of H_m and H_{m+1} were obtained by assuming the region of the normal B-H curve between H = 0 and H = 250 A/m to be linear. Thus,

$$H = H_i \, e^{-\sqrt{\dfrac{\omega \mu_o \mu_r}{2\rho}} \cdot y} \qquad\qquad A3.6$$

where H and H_i are values of the magnetic field strength $\leqslant$ 250 A/m, and, from Fig. 5.2, $\mu_o \mu_r = 120 \times 10^{-6}$ at H = 250 A/m. $\qquad$ A3.7

Equation A3.6 is a particular solution of the differential equations 4.11 and 4.12, so that

$$\frac{\partial \varepsilon}{\partial y} = \sqrt{\frac{\omega \mu_o \mu_r}{2\rho}} \qquad\qquad A3.8$$

B_m is read directly from the B-H curve. Sixty three ordinates of the B-H curve were stored in the computer for o < H < 15000 A/m. Intermediate values were obtained by interpolation.

APPENDIX IV

FINITE DIFFERENCE SOLUTION OF THE DIFFUSION EQUATION

This Appendix gives a brief account of the finite difference
solution of the diffusion equation (Equation 4.2), proposed by
Gillot and Calvert[42]. A flat, infinitely long plate of thickness
2d is considered, with a time varying magnetic field applied parallel
to its surfaces; the co-ordinate system used is shown in Fig. A4.1.

The space-time grid used in the
solution is shown in Fig. A4.2. The
region $0 < y < d$ is divided into (M-1)
equal rows of width Δy, i.e.
$d = (M-1). \Delta y$. Similarly, the
time ordinate is divided into columns
Δt apart so that $t = (J - 1). \Delta t$.
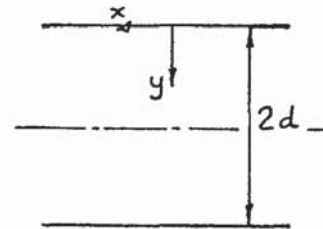
Fig. A4.1

If at $t = 0$, the surface magnetic field is $H = H \sin \omega t$, the
known boundary conditions are,

$$H (i,j) = H \sin (\omega (J-1) \Delta t), \quad i = 1, j \geq 1 \tag{A4.1}$$

$$H (i, j) = 0.0 \quad , \quad 1 \leq i \leq M, j = 1$$

and at the centre of the plate $(i = M)$,

$\frac{\partial B}{\partial y} (M, t) = 0$ which in finite difference form is

$$\frac{B((M + 1), j) - B ((M - 1), j)}{2 \Delta y} = 0 \tag{A4.2}$$

The differential equation (Equation 4.2), transforms into

$$B(i, j + 1) = \frac{\Delta t.\rho}{\Delta y^2} \quad H (i +1,j) - 2H(i,j) + H(i-1,j) + B(i,j) \tag{A4.3}$$

taking forward time difference and central space difference.

The flux density at the point (2,2), Fig. A4.2, may be obtained

from Equation A4.3 since H (1,1), H (1,2) and H (1,3) may be obtained
from the initial conditions (Equation A4.1). The value of B (1,2) is
obtained from the B-H curve corresponding to H (1,2). In the
computational method this value was interpolated from the values of
the B-H curve stored in the computer in the manner described in
Appendix III. This calculation may be repeated for all points in the
range $2 \leq i \leq M - 1$. At the centre plane (i = M), Equation A4.2 is
used. This procedure is repeated for successive time columns until
the point j = J and i = M is reached. If j = 1 and j = J are a time
cycle apart, the values of flux density should correspond. Thus the
values of flux density computed at each point on the line j = 1 and
j = J are compared. If their difference is greater than a specified
acceptable error, the values of B and H at j = 1 are replaced by the
values of B and H at j = J and the cycle of computation is repeated.
This procedure is continued until difference values within the specified
limit, (1%), are reached.

The power loss/m^2 in the plate is

$$P = \frac{\rho}{T} \int_0^T \int_0^d J_z \, (y,t)^2 \, . \, \Delta y \, . \, \Delta t \qquad \text{A4.4}$$

where T is the period of the applied field strength.

This may be written in finite difference form as:

$$P = \frac{4 \rho}{T} \int_0^T \int_0^d \left[\frac{H (i,j) - H (i + 1, j)}{\Delta y} \right]^2 \Delta t \qquad \text{A4.5}$$

APPENDIX V

THE PRELIMINARY FLUX PENETRATION TESTS

A5.1 General

Two sets of measurements were taken with the search coil array shown in Fig. 7.1 (Section 7.2.3.2); these consisted of

(a) the peak value of the mean flux density over the width of each search coil, and

(b) the phase angle between the flux linking each search coil and the total peripheral flux.

Both sets of measurements were taken for a range of frequency and excitation.   Figs. A5.1 and A5.2 show the variation of the peak value of the mean flux density and the variation of phase angle, respectively, with depth into the iron.   The general form of these curves are given in Fig. A5.3 below.
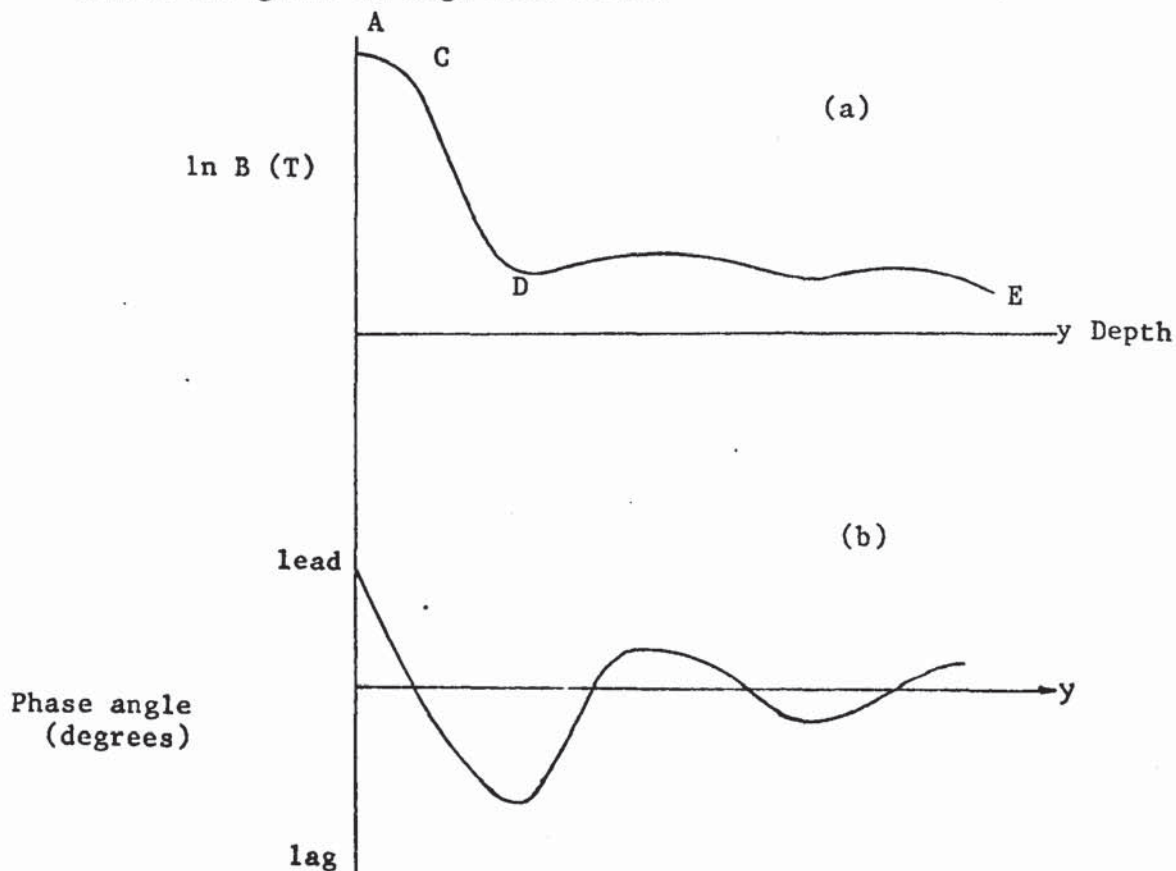
Fig. A5.3   Form of Penetration Curves given in Figs. A5.1 and A5.2

A5.2 Finite Length Effects

The flux penetration curve shown in Fig. A5.3a may be divided into three regions:

A-C; a region of fairly constant flux density,

C-D; a region where the attenuation is approximately exponential,

D-E; a region of fairly constant flux density.

The values of flux density in region D-E are much greater than those predicted theoretically (Fig. 5β). By summing the flux progressively through the stator, it was found that approximately 20% of the peripheral component of the flux in the stator penetrated into the region D-E.

To indicate that the flux in region D-E existed mainly at the axial ends of the stator, a matrix of search coils was inserted between the stator halves; the half-stators were separated by pieces of 0.08 mm sheet steel to allow the search coils to be inserted. Penetration curves, taken with the original axial search coils in the grooves (Fig. 7.1), showed little change in the overall flux distribution due to the insertion of the sheet steel. Fig. A5.4 shows a typical distribution of flux over the cross section of the stator obtained with the matrix of search coils; there is considerable flux in the end regions of the stator which are outside the active length of the rotor.

The average value of the flux density in the stator end region is 0.02T, which is approximately equal to the flux density shown in the region D-E of the corresponding penetration curve (Fig. A5.2).

REFERENCES

REFERENCES

1. Chalmers, B.J.: 'Electromagnetic problems of a.c. machines'
    (Chapman and Hall, 1965)

2. Jackson, W.B. and Winchester, R.L.: 'Direct and quadrature-axis
    equivalent circuits for solid-rotor turbine generators'
    IEEE Trans., 1969, PAS-88, pp.1121.

3. Widger, G.F.T. and Adkins, B.: 'Starting performance of synchronous
    motors with solid salient poles', Proc. IEE, 1968,
    115, (10), pp. 1471.

4. Lim, K.K. and Hammond, P.: 'Universal loss chart for the calculation
    of eddy-current losses in thick steel plates'
    Proc. IEE, 1970, (4), pp.857.

5. Davies, E.J.: 'An experimental and theoretical study of eddy-
    current couplings and brakes', Trans. IEEE, 1963,
    PAS-67, pp. 401.

6. Lasocinski, J.: 'Electromagnetic field in the air gap of an infinitely
    long machine with solid ferromagnetic rotor',
    Rozprawy Elektrotechniczne, 1965, 11, (4), pp. 743.

7. Davies, E.J.: 'General theory of eddy-current couplings and brakes',
    Proc.IEE, 1966, 113, pp.825.

8. Wood, A.J. and Concordia, C.: 'An analysis of solid rotor machines ,
    Pt.II. Effect of curvature', Trans.IEEE, 1960,
    78, (III), pp. 1666.

9. Lawrenson, P.J., Reece, P. and Ralph, M.C.: 'Tooth-ripple losses in
    solid poles', Proc.IEE, 1966, 113, pp. 657.
    Correspondence: Proc.IEE, 113, pp. 1846 and 114,
    pp. 275.

10. Hammond, P.: 'Electric and magnetic images', Proc.IEE, 1960, 107 C, pp. 306.

11. Concordia, L. and Poritsky, H.: 'Synchronous machine with cylindrical rotor', Trans. AIEE, 1937, 56, pp.49.

12. Kuyper, W.W.: 'Pole-face losses in solid-rotor turbine generators', Trans. AIEE, 1943, 62, pp. 827.

13. Postnikov, I.M.: 'Eddy currents in synchronous and asynchronous machines with unlaminated rotors', Elektrichestvo, 1958, 10, pp.7. In Russian (Translation: Electric Technology, 1959, 4, pp. 463.)

14. Mukherji, K.C.: 'Reaction of eddy currents induced in a ferro-magnetic medium on the inducing field', Proc. IEE, 1965, 112, (2), pp. 444.

15. Stoll, R.L. and Hammond, P.: 'Calculation of the magnetic field of rotating machines. Part 4. Approximate determination of the field and the losses associated with eddy currents in conducting surfaces', Proc. IEE, 1965, 112, (11), pp. 2085.

16. Rudenberg, R. :'The energy of eddy currents', Sammlung Elektro-technischer Vortrage, 1906, pp. 269. In German.

17. Bozorth, R.M. : 'Ferromagnetism', D.Van Nostrand Company.

18. Woolman, J. and Mottram, R.A. : 'Mechanical and physical properties of British Standard EN steels'.

19. Randall, W.F. and Scholefield, H.H. : 'Some metallurgical and structural factors affecting properties of soft magnetic materials', Proc. IEE, 1950, 97, (II), pp. 133.

20. Jackson, W.J.   : ' The effect of heat-treatment on the magnetic
    properties of carbon-steel castings',   J. Iron and
    Steel Inst., 1960, pp.29.

21. The Institution of Electrical Engineers : 'Electrical methods of
    machining and forming', Conference Publication
    No. 38,   1967.

22. Aspden, H.   : 'Eddy-currents in solid cylindrical cores having
    non-uniform permeability' J. Appl. Phys., 1952,
    23, pp. 523.

23. Pohl, R.   : 'Electromagnetic and mechanical effects in solid
    iron due to alternating or rotating magnetic fields',
    Proc. IEE, 1944, 91, pp.239.

24. Rao, V.S.   : 'Non-linear magnetisation in thin ferromagnetic
    plate', Proc. IEE, 1966, 113, pp. 1125.

25. Poritsky, H. and Butler, J.M.: 'A.C. flux penetration into magnetic
    materials and saturation', IEEE Trans. Communi-
    cations and Electronics, 1964, 83, pp. 99.

26. Chow, S.H.   : 'On a non-linear diffusion equation applied to the
    magnetisation of saturable reactors',   J.Appl. Phys.,
    1954, 25, (3), pp. 377.

27. Haberland, F. and Haberland, G.: 'The alternating field in saturated
    solid iron', Archiv Elektrotechnik, 1936, 19, pp.126.

28. MacLean, W.   ; 'Theory of strong electromagnetic waves in massive
    iron', J. Appl. Phys., 1954, 25, (10), pp. 1267.

29. Shevel, W.L.   : 'A modified limiting non-linear theory of eddy
    current phenomena in solid iron', Trans. AIEE, 1962,
    81, (1), pp. 48.

30. Lammeraner, J. and Stafl, M. : 'Eddy currents', Iliffe, 1966, pp.45.

31. Raghunathji, B. and Krishnamurthy, M.R.: 'Eddy-current effects in solid unslotted iron rotors', Proc. IEE, 1969, 116, (4), pp. 612.

32. Agarwal, P.D. : 'Eddy current losses in solid and laminated iron', Trans. IEEE, 1969, 78, (1), pp. 169.

33. Thornton, C.A.M.: 'Resistance heating of mild-steel containers at power frequencies', Proc. IEE, 1952, 99, (II) pp.85.

34. McConnell, H.M. : 'Eddy current phenomena in ferromagnetic materials', AIEE.Trans. 1954, 73, (I), pp.226.

35. Pry, R.H. and Bean, C.P.:' Calculation of the energy loss in magnetic sheet materials using a domain model', J. Appl. Phys. 1958, 29, (3), pp. 532.

36. Anderson, J.C. :'Magnetism and magnetic materials', Chapman & Hall, 1968, pp. 174.

37. Fischer, J. and Moser, H.: 'The representation of the magneticsation curve by simple algebraic and transcendental functions', Archiv Elektrotechnik, 1956, 42, pp. 286. In German.

38. Pillai, K.P.P. :' Fundamental-frequency eddy-current loss due to rotating magnetic field. Part 1. Eddy-current loss in solid rotors', Proc.IEE, 1969, 116, (3), pp. 407.

39. Ollendorf, F. :'Das eindringen elektromagnetischer wellen usw', Z.Tech. Phys. 1931, 12, pp.39.

40. Nejman, L.R. :'Skin effect in ferromagnetic bodies', Gosenergoizdat, Leningrad, 1949. (In Russian).

41. Kesavamurthy, N. and Rajagopalan, P.K.:'Eddy currents in solid iron due to an alternating magnetic flux', Proc.IEE, 1959, 105C, pp.207.

42. Gillott, D.H. and Calvert, J.F.:'Eddy current losses in saturated solid magnetic plates, rods and conductors', IEEE., Trans. Magnetics, 1965, 1, pp. 126.

43. Gillott, D.H. and Abrams, M.D.:'Numerical analysis of hysteresis and eddy current losses in solid cylindrical rods of No. 1010 steel', IEEE. Trans. Power App. and Systems, 1967, PAS-86, (9), pp. 1077.

44. Hensman, G.O. and Norris, W.T.:'Universal loss chart for the calculation of eddy-current losses in thick steel plates', Proc. IEE. 1971, 118, (1), pp. 277.

45. Gokhale, S.L. :'Law of magnetization', Trans.AIEE, 1926, pp.1013.

46. Gonnen, D. and Stricker,S.: 'Analysis of an eddy-current brake', Trans. IEE, 1965, 84, pp.357.

47. Dorairaj, K.R. and Krishnamurthy, M.R.:'Polyphase induction machines with a slitted ferromagnetic rotor', Trans. IEEE, 1967, PAS-86, (7), pp. 844. (Part II).

48. McConnell, H.M. and Sverdrup, E.F.:'The induction machine with solid iron rotor', Trans. IEEE, 1955, 74, (III), pp. 343.

49. Gibbs, W.J. :'Theory and design of eddy current slip coupling', The Beama Journal, 1946, 53, pp. 5, 123, 172, 219.

50. McLachlan, N.W. :'Bessel functions for engineers', (Oxford, 1934).

51. Davies, E.J. and Bowden, A.L.:'Direct Resistance Heating of Ferromagnetic Billets', 7th International Congress on Electro-heat, Warsaw 1972.

52. Wagner, C.F. and Evans, R.D.:'Symmetrical components', (McGraw-Hill 1933), pp. 92.

53. Burke, E. and Alden, S.:'Current density probe', Trans. IEEE, 1969, PAS-88, (2), pp. 181.

54. Wood, A.J. and Concordia, C.:'An analysis of solid rotor machines. Pt. III. Finite length effects', Trans. IEEE, 1960 (III), pp. 21.

55. Angst, G. :'Polyphase induction motor with solid rotor effects of saturation and finite length', ibid. 1962, 80 pp. 902.

56. Lasocinski, J. :'Electromagnetic field in air gap of finite length machine with solid iron rotor', Rozprawy Elektrotech., 1966, 12, pp. 69.

57. Preston, T.W. and Reece, A.B.J.: 'Transverse edge effects in linear induction motors', Proc. IEE, 1969, 116, (6), pp. 973. Corrigenda, 1970, 117 (9), pp. 1808. Correspondence: Proc. IEE, 1971, 118 (12) pp. 1820.

58. Bondi, M.A. and Mukherji, B.E.: 'An analysis to tooth-ripple phenomena in smooth laminated pole shoes', Proc. IEE, 1957, 104C, pp. 349.

59. Vilnitis, A.Ya. :'Transverse edge effect of flat induction magneto-hydrodynamic machines', Inst. of Latvian Academy of Sciences monograph, 1966, pp.63.

60. Veske, T.A. :'Solution of the electromagnetic field equations for a plane, linear induction machine with allowance for secondary transverse edge effects', Magnitnaya Gidrodinamika, 1965, 1(1), pp.87.

61. Yee, H. :'Effects of finite length in solid rotor induction machines', Proc. IEE, 1971, 118, (8), pp. 1025.

62. Stratton, J.A. :'Electromagnetic theory', (McGraw-Hill 1941), pp. 135.

63. Yee, H. and Wilson, T.:'Saturation and finite-length effects in
solid-rotor induction machines', Proc. IEE, 1972,
119, pp.877.

64. Harris, M.R. and Fam, W.Z.:'Analysis and measurement of radial power
flow in machine air gaps', Proc. IEE, 1966, 113, (10),
pp. 1607.

65. Fam, W.Z.   :'Direct measurement of the fundamental and harmonic
tooth-ripple losses in solid poles. Part II.
Experimental Investigation', Trans. IEEE, 1971, 90
(2), pp. 602.

66. Silvester, P. and Chari, M.V.K.:'Finite element solution of saturable
magnetic fields', Trans. IEEE, 1970, PAS-89, (7)
pp. 1642.

67. Chalmers, B.J. and Woolley, I.:'General theory of solid-rotor induction
machines', Proc. IEE, 1972, 119, (9), pp. 1301.

68. Bratoljić, T.   :'Recent studies of stray losses in solid pole-pieces
of synchronous machines', Brown Boveri Review, 1966,
53, pp. 521.

TABLES.

TABLE 4.1

LOSS, CALCULATED BY THE PRESENT THEORY AND THE LIMITING NON-LINEAR THEORY

Present Theory			Limiting Non-linear theory	
(1) and (2) P_n/P (4)			(3) P_L/P	
$B = aH^b$	$B_1 = 1.25(0.664H_1^b)$ (5)		$B_s = \hat{B}_{xg}$	$B_s = 0.75\,\hat{B}_{xg}$ (6)
b = 0	b = 0	b = 0.112		
1.375	1.54	1.465	1.7	1.47
b = 0.112				
1.31				

NOTES:
(1) P_n : Equation 4.45
(2) P_L : Equation 3.4
(3) P : Loss when permeability is constant and equal to μ_g
(4) Fundamental sinusoids of B_x and H_x related by $B = 0.664H^b$
(5) Fundamental sinusoids of B_x and H_x related by $B_1 = 1.25(0.664H_1^b)$ (Equation 4.59)
(6) Agarwal's empirical relationship.

TABLE 5.1

LOSS IN THE BAR - MEASURED AND CALCULATED VALUES

Bar Excitation		Loss (KW/m^2)					
I_{RMS} (A)	$\hat{H}_R$ (A/m)	Measured	Non-Linear[1] Theory $B_l = AH_l^b$	Agarwal's[2] Theory	Linear[3] Theory $\mu_r = f(\hat{H}_R)$	Linear Theory $\mu_r = 250$	Linear Theory $\mu_r = 1000$
500	2950	0.79	0.79	0.8	0.55	0.43	0.86
1000	5900	2.34	2.34	2.48	1.72	1.75	3.5
1500	8850	4.42	4.52	4.6	3.18	3.88	7.76
2000	11800	7.23	7.31	7.25	4.92	6.95	13.9
2500	14720	10.3	10.32	10.24	6.95	10.78	21.6

Notes: (1) $B_l = 1.25 \, (0.664 \, H_l^{0.112})$

(2) Agarwal's limiting non-linear theory; $B_S = 0.75 \, \hat{B}_R$ where $\hat{B}_R$ corresponds to $\hat{H}_R$ on normal B-H curve. (Fig. 5.1).

(3) Linear theory where μ_r corresponds to $\hat{H}_R$ on the μ_r-H curve (Fig. 5.1).

TABLE 5.2

SURFACE CURRENT DENSITY IN THE BAR - MEASURED AND CALCULATED VALUES

Bar Excitation		Surface Current Density (MA/m^2)		
I_{RMS} (A)	$\hat{H}_R$ (A/m)	Measured: Peak Value	Measured: fundamental amplitude	Calculated fundamental amplitude (1)
200	1180	1.88	1.73	1.7
500	2950	3.14	2.93	2.95
1000	5900	4.84	4.56	4.5
1500	8850	6.12	5.75	5.75
2000	11800	7.44	7.1	6.88
2500	14750	8.18	7.82	7.85

NOTE (1)   For $\hat{H}_R > 2500$ A/m, $B_1 = 1.25 \left(0.664 H_1^{0.112} \right)$ (Equation 5.2)

For $\hat{H}_R < 2500$ A/m, $B_1 = R_b \left(0.664 H_1^{0.112} \right)$

where R_b is obtained from Fig. 4.6 for U = 0

TABLE 5.3

ANALYSIS OF OSCILLOGRAMS OF VOLTAGES FROM SURFACE CURRENT DENSITY PROBES

Bar Excitation		Amplitude (per cent of fundamental)		
I_{RMS} (A)	$\hat{H}_R$ (A/m)	3rd Harmonic	5th Harmonic	7th Harmonic
500	2950	17.4	7.5	6.2
1000	5900	19.0	9.1	5.8
2000	11800	21.5	11.2	6.2

TABLE 5.4

LOSS OBTAINED BY FINITE DIFFERENCE SOLUTION OF THE DIFFUSION
EQUATION (EQUATION 4.2)

Surface Magnetic Field Strength (H_o) (A/m)	Loss (KW/m^2)
5000	2.75
10000	5.47

TABLE 5.5

PENETRATION OF MAGNETIC FIELD OBTAINED BY FINITE DIFFERENCE
SOLUTION OF THE DIFFUSION EQUATION (EQUATION 4.2)

Depth from Surface (mm)	Magnetic Field Strength (A/m)		Flux Density (T)		$R_b^{(1)}$
	Peak Value	Fundamental	Peak Value	Fundamental (B_1)	
0	10000	10000	1.854	2.26	1.22
1	5500	4807	1.75	2.01	1.17
2	2630	1846	1.6	1.7	1.14
3	500	476	0.91	0.962	1.10

NOTE (1)

R_b = (Fundamental Flux Density (B_1))/(Flux Density corresponding to
Fundamental magnetic field strength on normal B-H curve (B_{h1}))

TABLE 7.1

CONTACT RESISTANCE DROP   TESTS

| | | | Resistance between Electrodes[1] (p.u.) | | |
			C.P.= 140	C.P.= 280	C.P.= 550
Surface Conditions	lapped 0. 4 μm	A	4000	4000	4000
		B	12	9	5
	ground 1.4 μm	A	350	200	100
		B	12	7	3.5
	sand-blasted 3.0 μm	A	90	30	13
		B	7	4	2.5

Note (1) : Resistances given as multiples of that of solid block of EN1A steel.

A : steel/steel surfaces.

B : mating surfaces with deposition of copper.

C.P. : clamping pressure between electrodes (p.s.i)

Test Rig
(full scale)

d.c. current flow : voltage measured between electrodes

Copper electrodes

Blocks of EN1A steel

mating surfaces
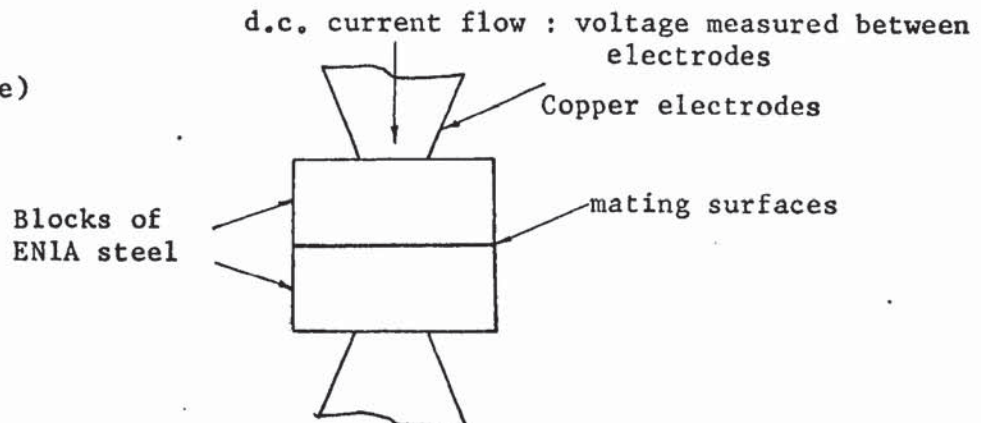
TABLE 7.2

DATA OF EXPERIMENTAL MACHINE

Rotor

Number of phases		3
Number of poles	2p	4
Number of slots		36
Pitch (p.u.)		0.778
Rated current/phase (A)		17.0
Active length (mm)	L_A	104.8

Stators (1)

Outer Diameter (mm)		371.0
Inner Diameter (mm)	D	228.4
Effective air-gap length (mm)	g	0.838
Pole pitch (mm)	$\frac{\lambda}{2}$	179.6
Active length (mm) of end-ring stator.	L_A	104.8
Axial length (mm) of continuous stator	L_s	134.0

Copper Rings (2)

Thickness (mm)		12.7
Outer diameter (mm)		304.5
Inner diameter (mm)	D	228.4

NOTES (1) Dimensions are the same for both stators, unless stated.

   (2) End-ring stator.

TABLE 7.3

ROTOR EXCITATION OF THE EXPERIMENTAL MACHINE

Rotor Current (A, rms)	MMF $\lvert\dot{F}_c\rvert$ (At/pole)	Current Sheet $\hat{K}$ (A/m)
2	109.8	1920
5	275.0	4800
7.5	410.0	7200
10	550.0	9600
12.5	685.0	12000
15	820.0	14420
17.5	960.0	16820
20	1100.0	19200

NOTE : $\hat{K} = \lvert\dot{F}_c\rvert \cdot q$

TABLE 7.4

AREAS AND MEAN DEPTHS OF SEARCH COILS IN THE PLATE

Search coils, numbered from air-gap surface	Area[1] of search coil (sq. cm)	Mean depth [2] of search coil from air-gap surface (mm)
1	0.90	0.475
2	1.15	1.54
3	1.22	2.72
4	1.16	3.9
5	1.24	5.1
6	1.22	6.33
7	2.52	8.2
8	0.95	9.95
9	1.2	11.0
10	1.17	12.2
11	3.44	14.5
12	1.18	16.9
13	1.15	18.0
14	2.45	19.85
15	2.45	22.3
16	2.39	24.7
17	2.32	27.1

NOTES : (1) Area of search coil = (mean spacing between search wires) x L_A

(2) Distance from the surface to the mean centre line of the search coil.

TABLE 8.1

MEASURED TORQUES FOR THE END RING AND THE CONTINUOUS STATORS

Rotor Excitation (At/pole) [1]	Torque (N-m)							
	275		550		820		1100	
Frequency (Hz)	E [2]	C [2]	E	C	E	C	E	C
1.5	2.12	1.35	8.55	7.51	18.35	16.8	_[3]	_[3]
2	1.98	1.85	7.9	8.0	16.9	18.2	28.4	29.0
5	1.58	2.0	6.0	7.8	12.3	17.0	20.0	27.5
10	1.35	1.75	4.7	6.9	8.9	14.05	14.7	23.4
20	0.98	1.5	3.21	5.4	6.65	11.1	10.3	18.1
50	0.65	1.07	2.1	3.83	4.2	7.4	6.7	12.2
100	0.55	0.84	1.5	3.3	3.1	5.7	4.8	9.35

Notes: (1) See Fig. 7.3

(2) E : End-Ring Stator

C : Continuous Stator

(3) 1100 At/pole at 1.5 Hz could not be obtained.

TABLE 8.2

CALCULATED VALUES OF THE NON-DIMENSIONAL QUANTITY Q_n AND NORMALISED TORQUE AT VARIOUS EXCITATIONS AND FREQUENCIES

FOR THE MACHINE WITH THE END-RING STATOR

Frequency (Hz)	Rotor Excitation (At/pole) 275 T_{nm} = 2.22 (N-m), f_{nm} = 1.03 (Hz)					Rotor Excitation (At/pole) 550 T_{nm} = 8.85, f_{nm} = 0.55					Rotor Excitation (At/pole) 1100 T_{nm} = 35.8, f_{nm} = 0.30				
	N_Δ	Q_n	Δ_n	T_n/T_{nm}	ω/ω_{nm}	N_Δ	Q_n	Δ_n	T_n/T_{nm}	ω/ω_{nm}	N_Δ	Q_n	Δ_n	T_n/T_{nm}	ω/ω_{nm}
1.5	2.46	1.3	0.307	0.978	1.5	4.56	1.9	0.276	0.89	2.73	8.44	2.61	0.238	0.792	5
2.0	3.24	1.55	0.295	0.945	2	6.02	2.2	0.260	0.845	3.64	11.1	3.1	0.216	0.692	6.67
5.0	8.1	2.59	0.239	0.762	5	15.05	3.61	0.195	0.626	9.1	27.75	5.0	0.155	0.517	16.7
10.0	16.2	3.75	0.19	0.612	10	30.1	5.25	0.149	0.5	18.2	55.5	7.25	0.116	0.372	33.4
50.0	81.0	8.7	0.1	0.32	50	150.5	11.9	0.076	0.23	91	277.5	16.4	0.0565	0.184	167
100.0	162	12.35	0.073	0.236	100	301	17.05	0.054	0.176	182	555	23.3	0.041	0.132	334

$$N_\Delta = (Q_n)^{\frac{b+3}{2}} \cdot \Delta_n^2 \cdot \frac{b-1}{2} = \frac{2\,\mu_0^2\,\omega\,|\dot{F}_c|^{(1-b)}}{q\,(b+1)^2\,\rho R_n^2 K_b^2 A \tanh^2 qg} \cdot \cosh^{b-1} qg \;\; ; \;\; \Delta_n = (Q_n + Q_n^{-1} + 2\sin\emptyset_n)^{-1} \; ;$$

$$\frac{T_n}{T_{nm}} = (2 + 2\sin\emptyset_n) \cdot \Delta_n \;\; ; \;\; \sin\emptyset_n = \frac{Y_n}{R_n} \;\; ; \;\; b = 0.112 \;\; \text{(Equation 5.2)}$$

Calculated torques are plotted in Figs. 8.1 and 8.2 against frequency for various excitations.

TABLE 8.3

VARIATION OF MEASURED CURRENT DENSITY OVER THE SURFACE OF THE END-RING STATOR

Frequency Hz	Rotor Excitation (At/pole)	Fundamental component of Surface Current Density (MA/m^2)					
		A[1]	B	C	D	E	Plate[2]
2	275	0.544	0.55	0.53	0.5	0.58	0.52
	550	0.89	0.88	0.87	0.81	0.95	0.87
	1100	1.36	1.4	1.31	1.3	1.58	1.38
10	275	1.0	1.03	0.97	0.9	1.03	1.0
	550	1.62	1.67	1.58	1.47	1.88	1.58
	1100	2.46	2.46	2.4	2.28	2.75	2.45
50	275	3.84	3.9	3.7	3.5	3.9	3.67
	550	5.8	5.97	5.6	5.4	6.13	5.63
	1100	8.7	8.94	8.5	8.25	9.5	8.7

Notes: (1) The location of the probes, indicated by the letters A to E, is given in Fig. 7.4.

(2) Current density probe on air-gap surface of plate at axial centre of stator.

TABLE 8.4

COMPARISON OF MEASURED LOSS AND SURFACE CURRENT DENSITY IN THE BAR AND END-RING STATOR AT VARIOUS VALUES OF SURFACE MAGNETIC FIELD STRENGTH

Surface Magnetic Field Strength	Current Surface Density (MA/m^2)		Loss, (KW/m^2)	
	Bar	End-Ring Stator	Bar	End-Ring Stator
2850	3.0	2.72	0.794	0.84
5900	4.75	4.63	2.342	2.441
8850	5.75	5.9	4.42	4.56
11800	7.0	7.025	7.23	7.12
14720	7.95	8.15	10.29	10.4

TABLE 8.5

RATIO OF FUNDAMENTAL AMPLITUDE TO PEAK VALUE OF INTEGRATED VOLTAGES FROM SEARCH COILS (α FLUX) IN PLATE AND SPLIT SURFACES.

Frequency: 2 Hz;   Primary Excitation; 19200 A/m.
Surface Magnetic Field Strength (calculated):   15250 A/m.
Search coils are numbered from the air-gap surface.

Search Coil No.	Fundamental/Peak	
	Plate Surface Nominal width of search coils 1.25 mm.	Split Surface Nominal width of search coils 2.5 mm
1	1.16	1.15
2	1.16	1.08
3	1.15	1.08
4	1.12	1.06
5	1.10	
6	1.07	
7	1.06	

TABLE 9.1

COMPARISON BETWEEN VALUES OF FIELD QUANTITIES CALCULATED BY THE TWO-DIMENSIONAL AND THREE-DIMENSIONAL LINEAR THEORIES. (SECTION 9.6.3).

ROTOR EXCITATION (A/m)	4800					19200				
Frequency (Hz)	$\lvert\mu_e\rvert$	$\lvert\dot{H}_{xg}\rvert$ (A/m)	$\lvert\dot{H}_{xgh}\rvert_{z=0}$ (A/m)	$\lvert\dot{J}_{zg}\rvert$ (MA/m^2)	$\lvert\dot{J}_{zgh}\rvert_{z=0}$ (MA/m^2)	$\lvert\mu_e\rvert$	$\lvert\dot{H}_{xg}\rvert$ (A/m)	$\lvert\dot{H}_{xgh}\rvert_{z=0}$ (A/m)	$\lvert\dot{J}_{zg}\rvert$ (MA/m^2)	$\lvert\dot{J}_{zgh}\rvert_{z=0}$ (MA/m^2)
2	770	2400	2230	0.65	0.530	169	1820	1670	1.6	1.35
5	617	3600	2880	1.16	1.0	170	1670	1470	2.65	2.65
50	497	4500	4180	4.0	4.14	152	1520	1220	9.1	9.9

$\left.\begin{array}{l} \lvert\dot{H}_{xg}\rvert \\ \lvert\dot{J}_{zg}\rvert \end{array}\right\}$ two-dimensional linear theory; $\left.\begin{array}{l} \lvert\dot{H}_{xgh}\rvert_{z=0} \\ \lvert\dot{J}_{zgh}\rvert_{z=0} \end{array}\right\}$ three dimensional linear theory.

TABLE 10.1

CALCULATED AND MEASURED FINITE LENGTH FACTOR, R_L, FOR THE EXPERIMENTAL MACHINE

Rotor Excitation (A/m)	Frequency (Hz)	Surface MagneticField Strength $\lvert \dot{H}_{xg} \rvert$ (A/m)	Equivalent constant Permeability $\lvert \mu_e \rvert$	Finite Length Factor		
				R_L	R_{Lm}	$\dfrac{R_{Lm}}{R_L}$
4800	2	2400	770	0.81	0.925	1.14
	5	3600	617	1.01	1.23	1.20
	10	4000	550	1.16	1.35	1.12
	20	4200	506	1.32	1.50	1.12
	50	4500	497	1.59	1.59	1.0
	100	4600	486	1.74	1.56	0.90
9600	2	6600	351	0.94	1.03	1.07
	5	7950	300	1.13	1.3	1.14
	10	8400	284	1.31	1.5	1.14
	20	8800	275	1.48	1.6	1.10
	50	9150	270	1.74	1.66	0.96
	100	9250 =	266	1.92	1.73	0.90
19200	2	15250	175	1.02	1.05	1.01
	5	16700	170	1.23	1.45	1.11
	10	17400	155	1.44	1.6	1.10
	20	17900	153	1.63	1.73	1.06
	50	18200	152	1.89	1.78	0.94
	100	18800	150	2.08	1.79	0.86

R_L : calculated finite length factor. R_{Lm} : measured finite length factor

$\lvert \dot{H}_{xg} \rvert$: calculated from Equation 6.19 $\mu_e = \dfrac{\mu_g}{\mu_o} R_b (K_b^2 R_n^2)/2$ (Equation 9.42)

TABLE 10.2

MEASURED AND CALCULATED FLUX/POLE FOR THE EXPERIMENTAL MACHINE WITH THE CONTINUOUS STATOR

FLUX/POLE (mWb)

Rotor Excitation (A/m)	4800				9600				19200			
Frequency (Hz)	Φ_{hm}	Φ_{ha}	$\dfrac{\Phi_{hm}}{\Phi}$	$\dfrac{\Phi_{ha}}{\Phi}$	Φ_{hm}	Φ_{ha}	$\dfrac{\Phi_{hm}}{\Phi}$	$\dfrac{\Phi_{ha}}{\Phi}$	Φ_{hm}	Φ_{ha}	$\dfrac{\Phi_{hm}}{\Phi}$	$\dfrac{\Phi_{ha}}{\Phi}$
2	3.25	3.18	1.66	1.63	5.65	5.5	1.7	1.68	8.8	9.2	1.7	1.77
5	2.45	2.48	1.7	1.7	4.2	4.3	1.87	1.91	6.65	7.1	1.84	1.96
10	2.05	2.1	1.95	2.0	3.35	3.55	2.09	2.22	5.1	5.76	2.03	2.29
20	1.6	1.8	2.11	2.38	2.55	2.85	2.13	2.38	3.95	4.6	2.19	2.55
50	1.08	1.28	2.07	2.45	1.7	2.11	2.12	2.63	2.61	3.45	2.18	2.88
100	0.80	1.05	1.91	2.5	1.32	1.72	2.10	2.74	1.96	2.5	2.23	2.85

Φ_{hm} measured flux/pole - continuous stator

Φ_{ha} calculated flux/pole - continuous stator

Φ measured flux/pole - end-ring stator.

TABLE 10.3

SURFACE CURRENT DENSITY AND (FLUX/POLE)/cm. MEASURED AT THE AXIAL CENTRE OF THE END-RING AND THE CONTINUOUS STATORS

Rotor (A/m) Excitation	4800					9600					19200				
	Current Density (MA/m²)		(Flux/pole)cm. (mWb)			Current Density (MA/m²)		(Flux/pole)cm. (mWb)			Current Density (MA/m²)		(Flux/pole)cm. (mWb)		
Frequency (Hz)	J_{zc1}	J_{z1}	Φ_{hc}	Φ_c	$\dfrac{\Phi_{hc}}{\Phi_c}$	J_{zc1}	J_{z1}	Φ_{hc}	Φ_c	$\dfrac{\Phi_{hc}}{\Phi_c}$	J_{zc1}	J_{z1}	Φ_{hc}	Φ_c	$\dfrac{\Phi_{hc}}{\Phi_c}$
2	0.48	0.6	.242	.192	1.26	0.95	1.03	.424	.314	1.25	1.45	1.56	.71	.481	1.47
5	1.1	1.2	.202	.14	1.44	1.74	1.7	.344	.218	1.56	2.65	2.5	.53	.336	1.58
10	1.69	1.6	.154	.103	1.5	2.6	2.52	.25	.16	1.56	3.9	3.6	.38	.241	1.58
20	2.47	2.26	.121	.074	1.64	3.7	3.5	.187	.11	1.64	5.5	5.24	.27	.174	1.56
30	—	—	.097	.064	1.52	—	—	.144	.094	1.54	—	—	.212	.15	1.45
50	3.95	3.8	.064	.051	1.265	5.7	5.76	.10	.079	1.27	8.45	8.84	.15	.12	1.24
100	5.52	5.8	.05	.04	1.25	8.2	8.8	.073	.058	1.26	11.8	12.3	.102	.084	1.22

J_{zc1} : fundamental current density, continuous stator; J_{z1} : fundamental current density, end ring stator.

Φ_{hc} : measured (flux/pole)/cm., continuous stator; Φ_c : measured (flux/pole)/cm., end ring stator.

TABLE 10.4

MEASURED SURFACE CURRENT DENSITY IN END FACES AND OUTER SURFACE OF CONTINUOUS STATOR

Rotor Excitation :   4800 A/m;   Frequency: 50 Hz.

Surface Current Density expressed as a p.u to base of 4.14 MA/m^2 (2)		
Location of Probe (1)	J_{xhl}	J_{zhl}
At outer edge of end face	0.07	0.26
At axial centre of outer surface.	0.0	0.168

$\left.\begin{array}{l} J_{xhl} \\ J_{zhl} \end{array}\right\}$ see Section 10.6.2

NOTES :   (1)   Fig. 9.1

(2)   Value at centre of stator - see Fig. 10.9

TABLE 10.5

COMPARISON OF TORQUES FOR THE END-RING STATOR OBTAINED BY POWER FLOW MEASUREMENT AND TORQUE TRANSDUCER

Frequency: 50 Hz

	Torque (N - m)			
Rotor (A/m) Excitation	4800	9600	14400	19200
Torque obtained by power flow	0.71	2.29	4.5	7.0
Torque obtained by Transducer (1)	0.65	2.1	4.2	6.7

NOTE (1)   Section 7.3

TABLE 10.6

TORQUES OBTAINED BY POWER FLOW MEASUREMENTS FOR THE EXPERIMENTAL MACHINE WITH THE CONTINUOUS STATOR

Torque/cm as p.u. of mean torque/cm over active length

Rotor Excitation (A/m)	2400		4800		9600		19200	
Frequency (Hz)	20	50	20	50	20	50	20	50
Coil No. (1)	A	B	A	B	A	B	A	B
1	1.05	0.995	0.99	0.97	0.97	0.92	0.925	0.832
2	1.12	1.04	1.05	1.02	1.02	0.97	0.99	0.895
3	1.065	1.03	1.05	1.032	1.02	1.01	1.02	0.955
4	1.10	1.07	1.11	1.1	1.12	1.12	1.15	1.12
5	1.07	1.05	1.1	1.11	1.15	1.175	1.20	1.23
6	0.6	0.73	0.621	0.78	0.65	0.835	0.67	0.88
Total Torque by Power Flow (N-m)	0.46	0.40	1.5	1.28	5.6	3.96	17.7	12.7
Torque by Transducer (N-m) (2)			1.5	1.07	5.4	3.85	18.1	12.2
$T_{cu/cm}$ (N-m) (3)			0.624	0.58	0.55	0.52	0.55	0.52

NOTES
(1) Search coil numbers refer to Fig. 7.7
(2) Section 7.3.
(3) $T_{cu/cm}$ = torque/cm of end-ring stator expressed as p.u. of mean torque/cm of continuous stator.

TABLE 10.7 PHASE ANGLE $\underline{/\dot{B}_{yg}}$

PHASE ANGLE $\underline{/\dot{B}_{yg}}$ (degrees)

Rotor Excitation (A/m)	4800		9600		19200	
Frequency (Hz) (1)	20	50	20	50	20	50
Coil 1	34.5	27.1	31.5	23.4	25.7	23.2
Coil 2	34.8	28.7	32.2	25.0	26.3	24.5
Coil 3	37.3	32.4	34.6	28.8	30.2	28.4
Coil 4	42.8	39.7	40.8	36.5	36.5	35.7
Coil 5	49.6	49.7	48.4	48.5	46.5	47.8
Coil 6	59.7	54.8	60.2	55.4	59.8	55.5

Note (1)   See Fig. 7.7 for location of the coils.

FIGURES.

Fig. 2.2. Variation of β/α and γ/α with $q^2/2\alpha^2$ $(\propto \delta^2/\lambda^2)$

Curve	a	b	c	d	e	f	g
qg	0.014	1.0	0.10	0.033	0.014	0.033	0.014
	1	70	10	30	30	70	70

$$qg = \frac{2\pi g}{\lambda} \quad ; \quad \eta = \frac{q\mu_s}{\alpha}$$
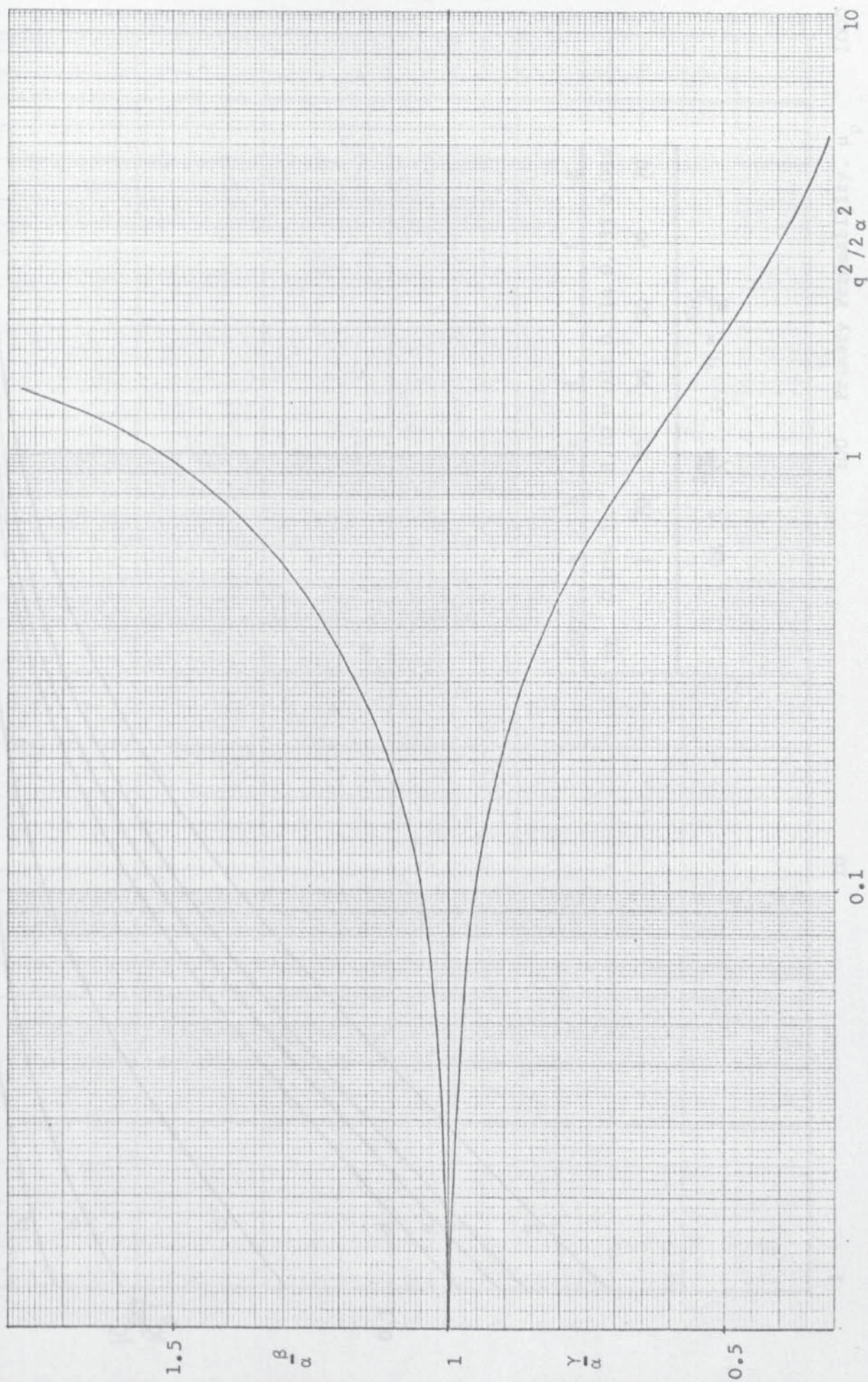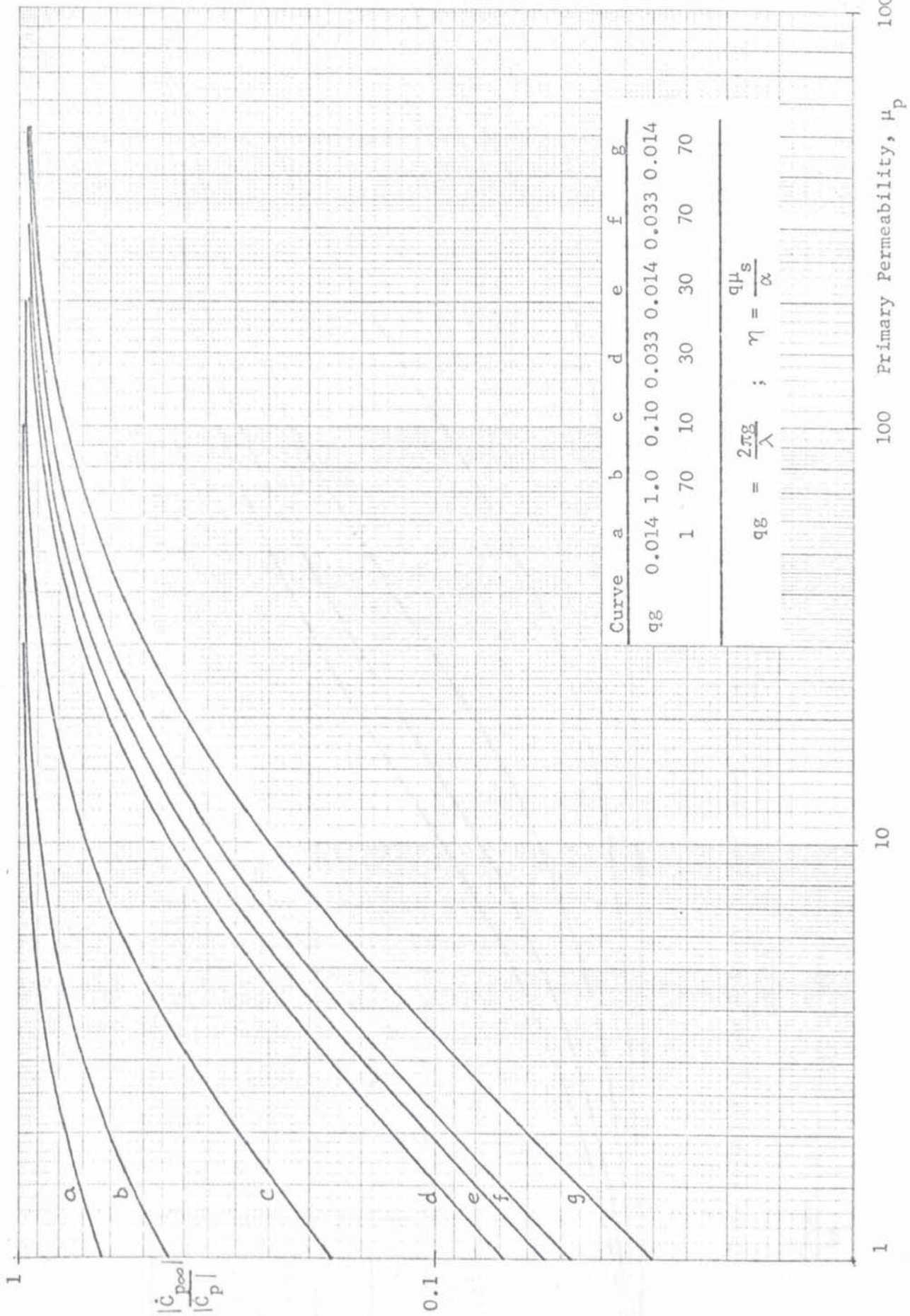
Fig. 2.3   Illustrating the Effect of the Primary Iron on the Field Distribution in the Linear Model (Fig.2.1)
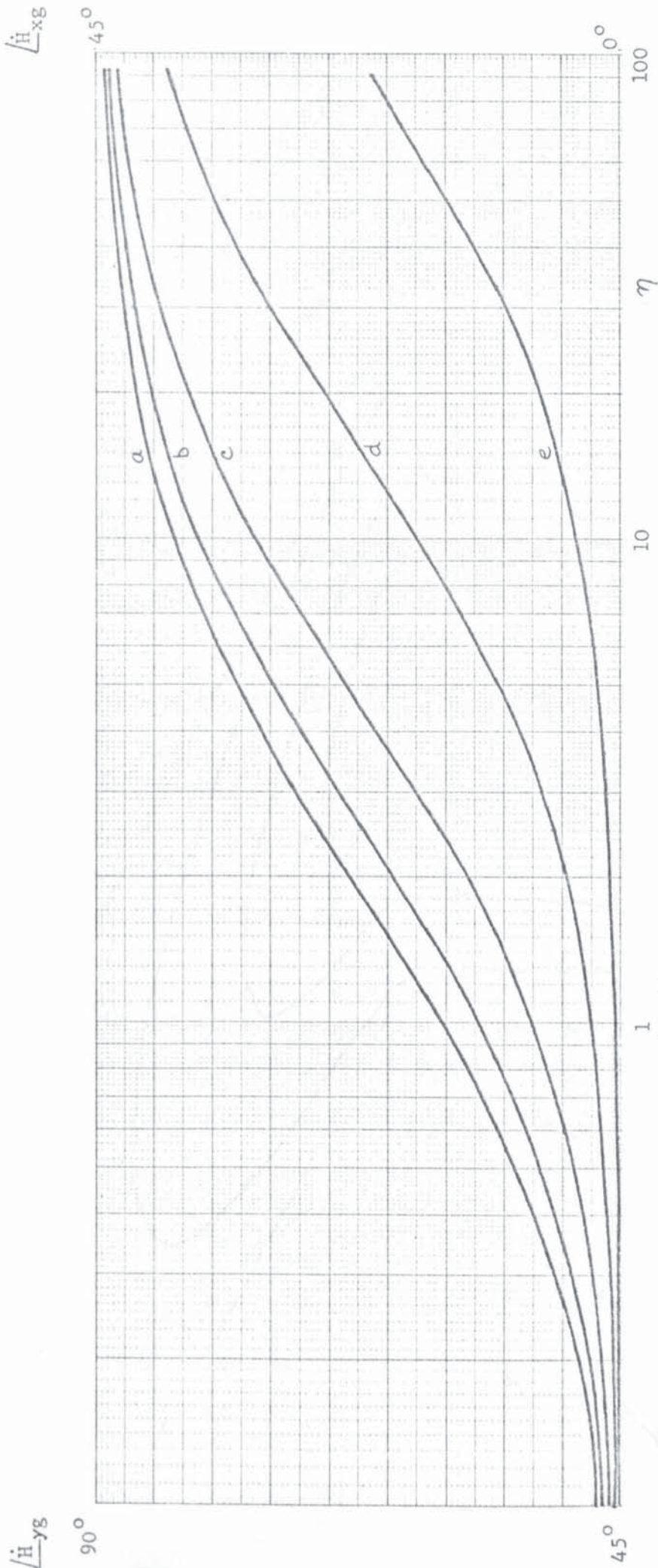
Fig. 2.5   Phase, Relative to the Primary Current Sheet, of the Radial and Peripheral Components of the Magnetic Field Strength at the Surface of the Secondary (y = g). $\eta = \dfrac{q\mu s}{\propto}$.

Curve	a	b	c	d	e
$\dfrac{q}{g}$	1.0	0.625	0.33	0.1	0.014
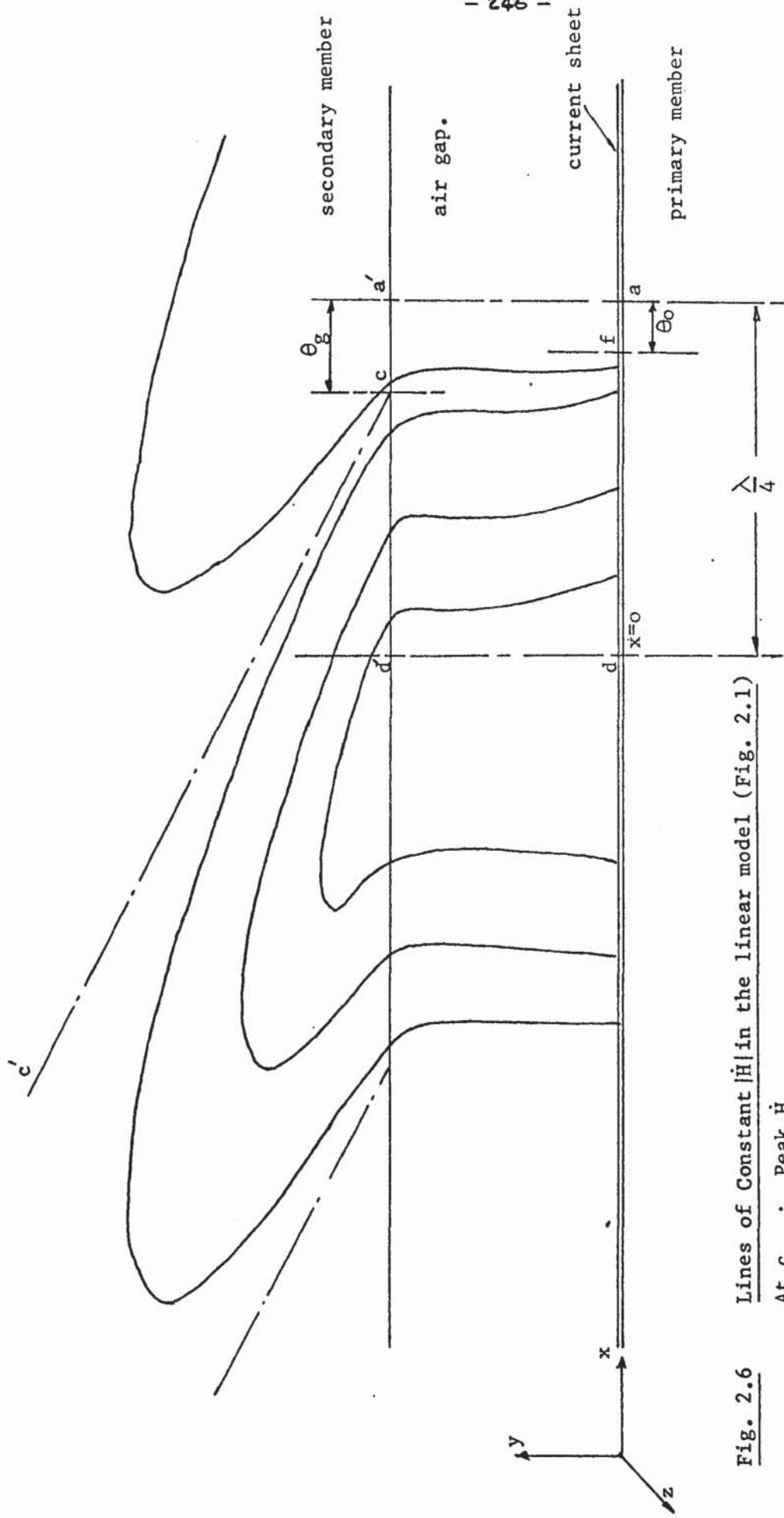
Fig. 2.6   Lines of Constant $|\dot{H}|$ in the linear model (Fig. 2.1)

At c   : Peak $\dot{H}_{yg}$

f   : Peak $\dot{H}_{yo}$

a-a': Peak primary mmf

d   : Peak primary current density.
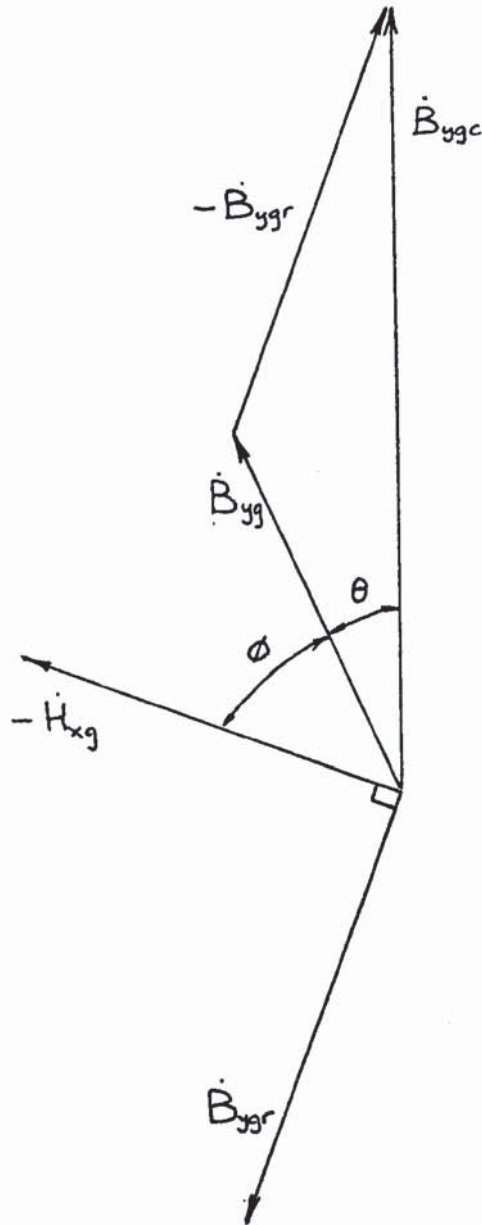
Fig. 2.7   Vector Diagram of Radial Flux Densities at the Surface
of the secondary (y = g)

$\dot{B}_{yg}$:   resultant flux density

$\dot{B}_{ygc}$:   flux density due to the applied field of the
primary current sheet

$\dot{B}_{ygr}$:   flux density due to eddy currents in the secondary

Assumptions: $\mu_p \rightarrow \infty$, μ_s tanhqg $\gg$ 1 and $\sqrt{2}\alpha > q$.
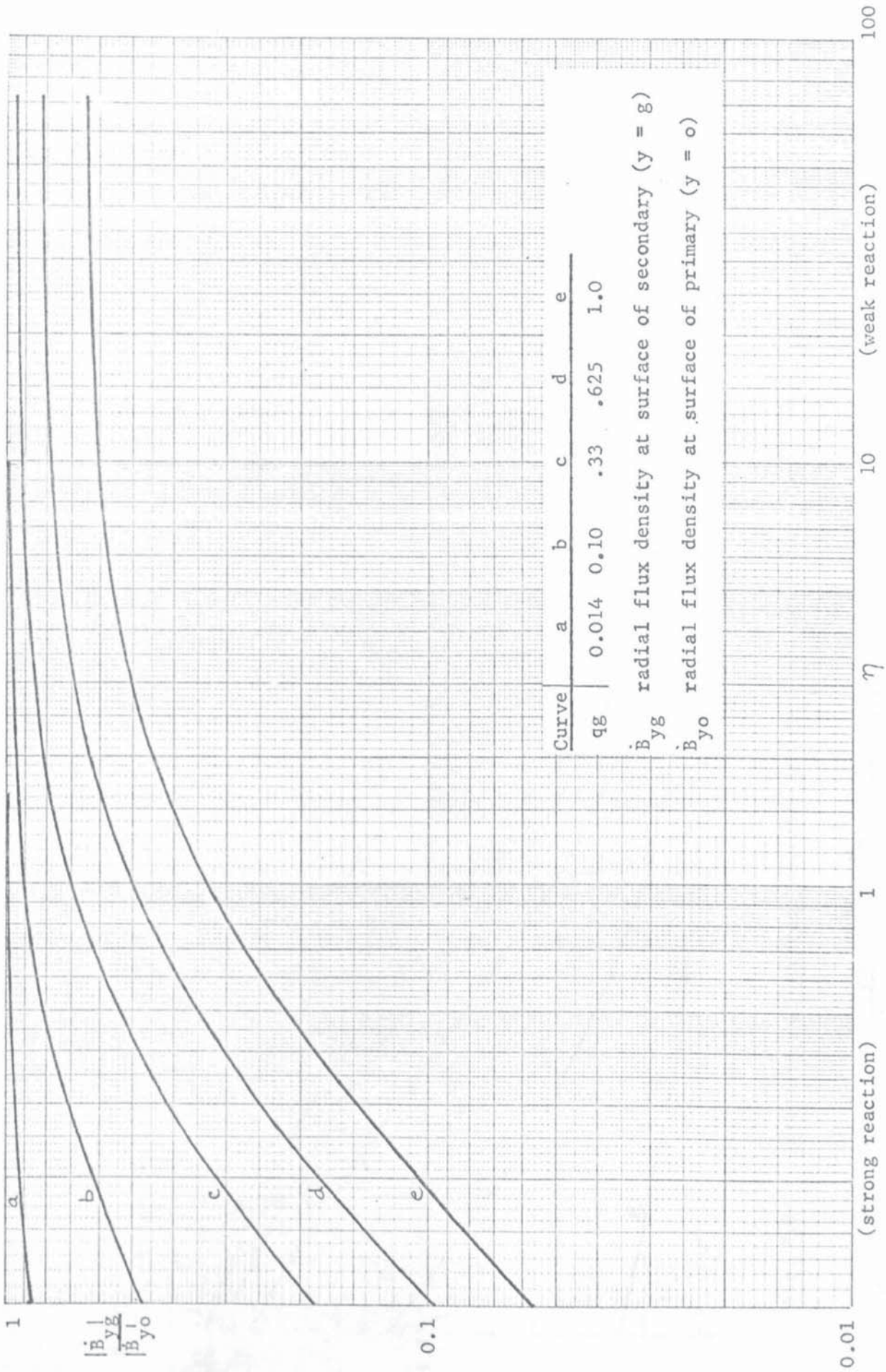
Fig. 2.8   Effect of Eddy Current reaction on the Field in the Air Gap;   Magnitude of Radial Flux Density.
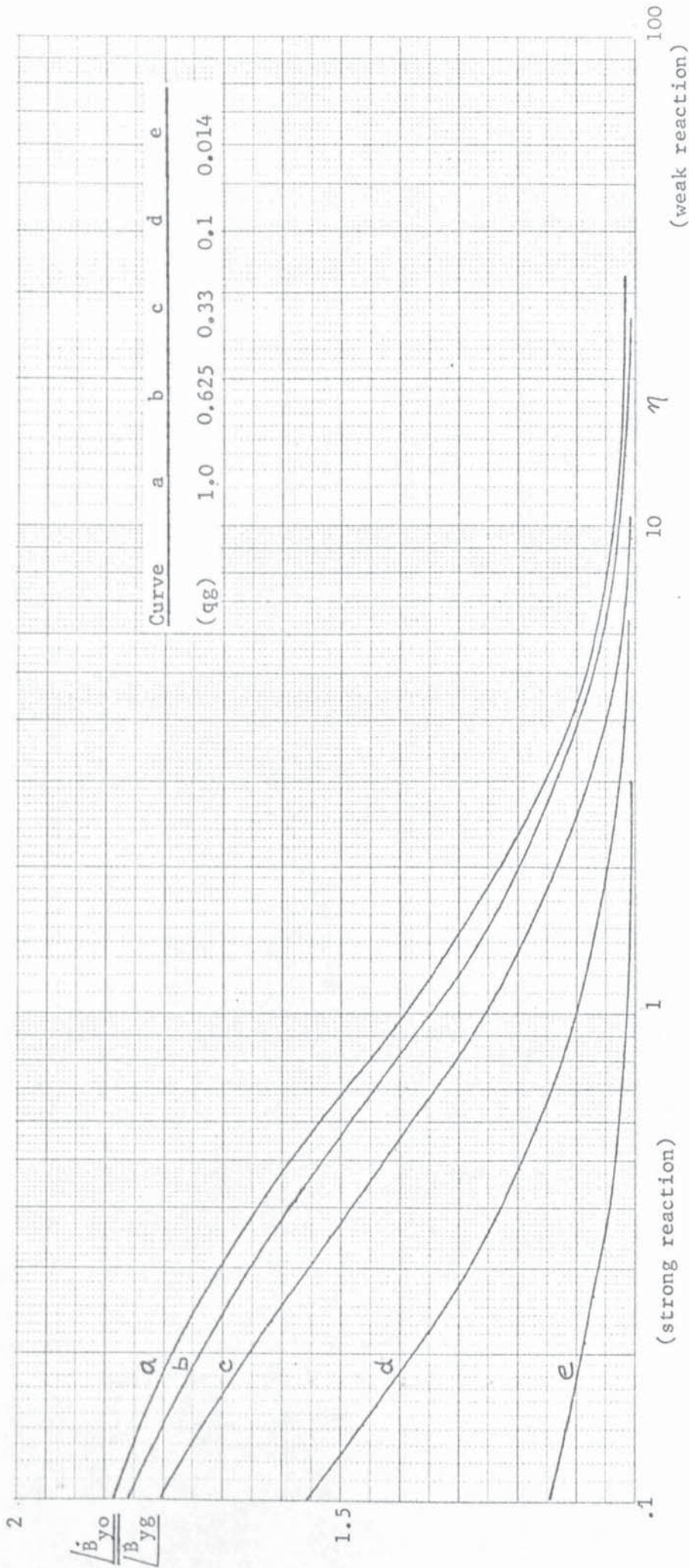
Fig. 2.9   Effect of Eddy-Current Reaction on the field in the Air Gap;   Phase of Radial Flux Density Relative
to Primary Current Sheet (K)

$$\underline{/B_{yo}} = (90 - \theta_o)$$
$$\underline{/B_{yg}} = (90 - \theta_g)$$

Fig. 2.6

Curve	a	b	c	d	e
(qg)	1.0	0.625	0.33	0.1	0.014

Curve	a	b	c	d	d'	e	f'	f
(qg)	.014	.033	.1	.33	.33	.625	1.0	1.0

For curves d' and f', it was assumed that qg << 1 (Equation 2.96)
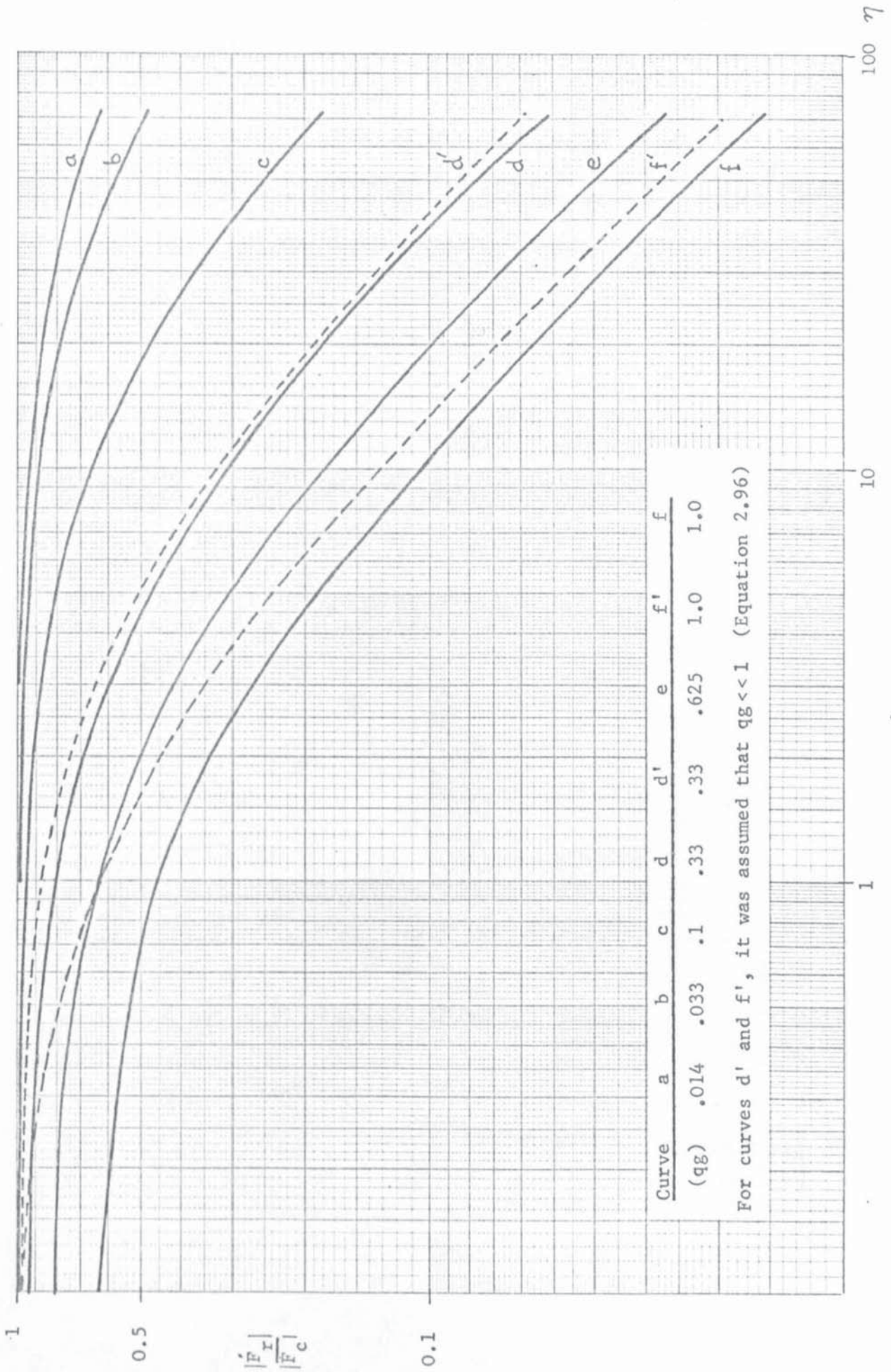
Fig. 2.10   Normalised Curves of the mmf $\dot{F}_r = \int \dot{H}_{xg} dx$, which includes the Reaction Field of the Eddy Currents, as functions of η and (qg)
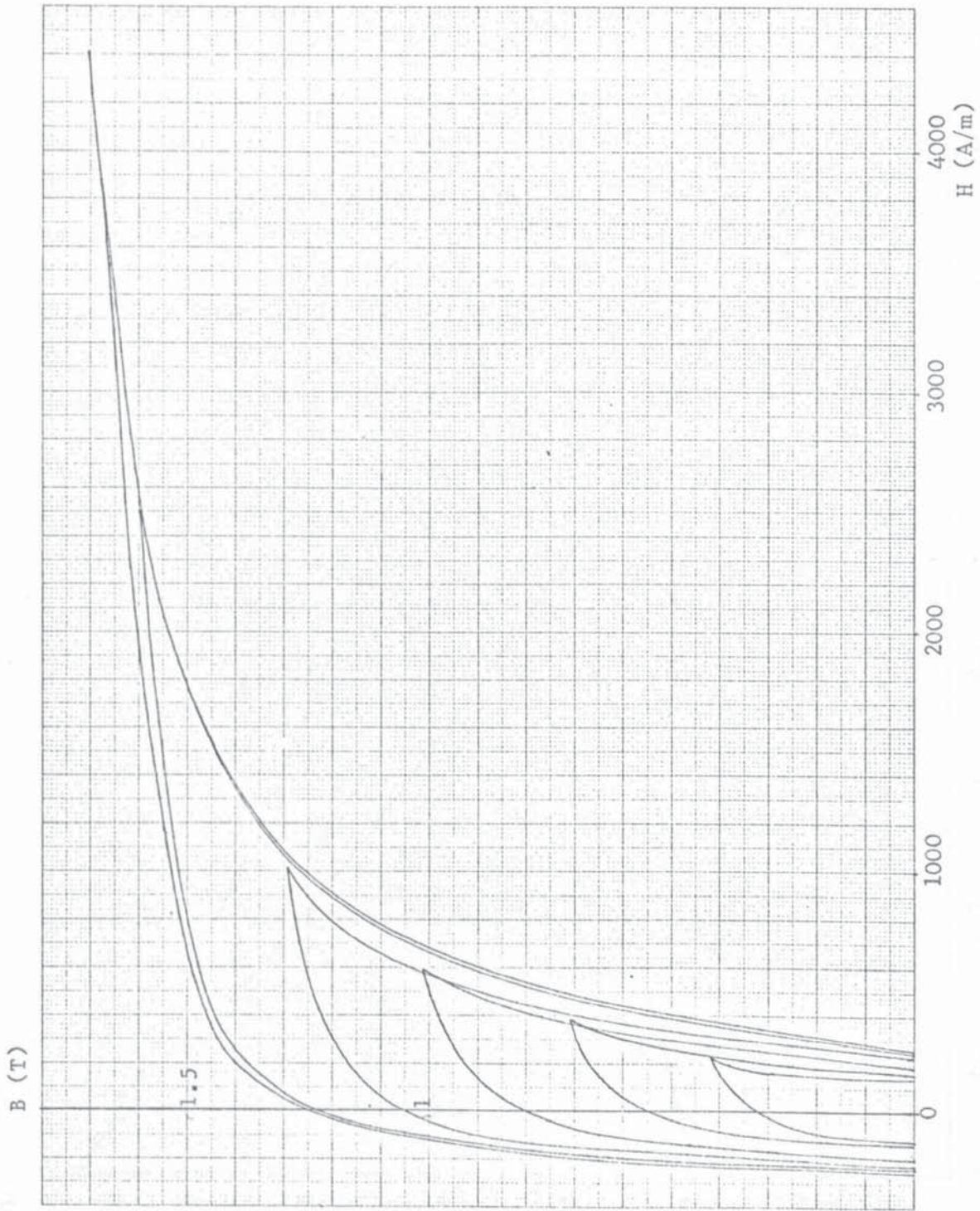
Fig. 3.2   Hysteresis loops for a Sample of EN1A mild steel
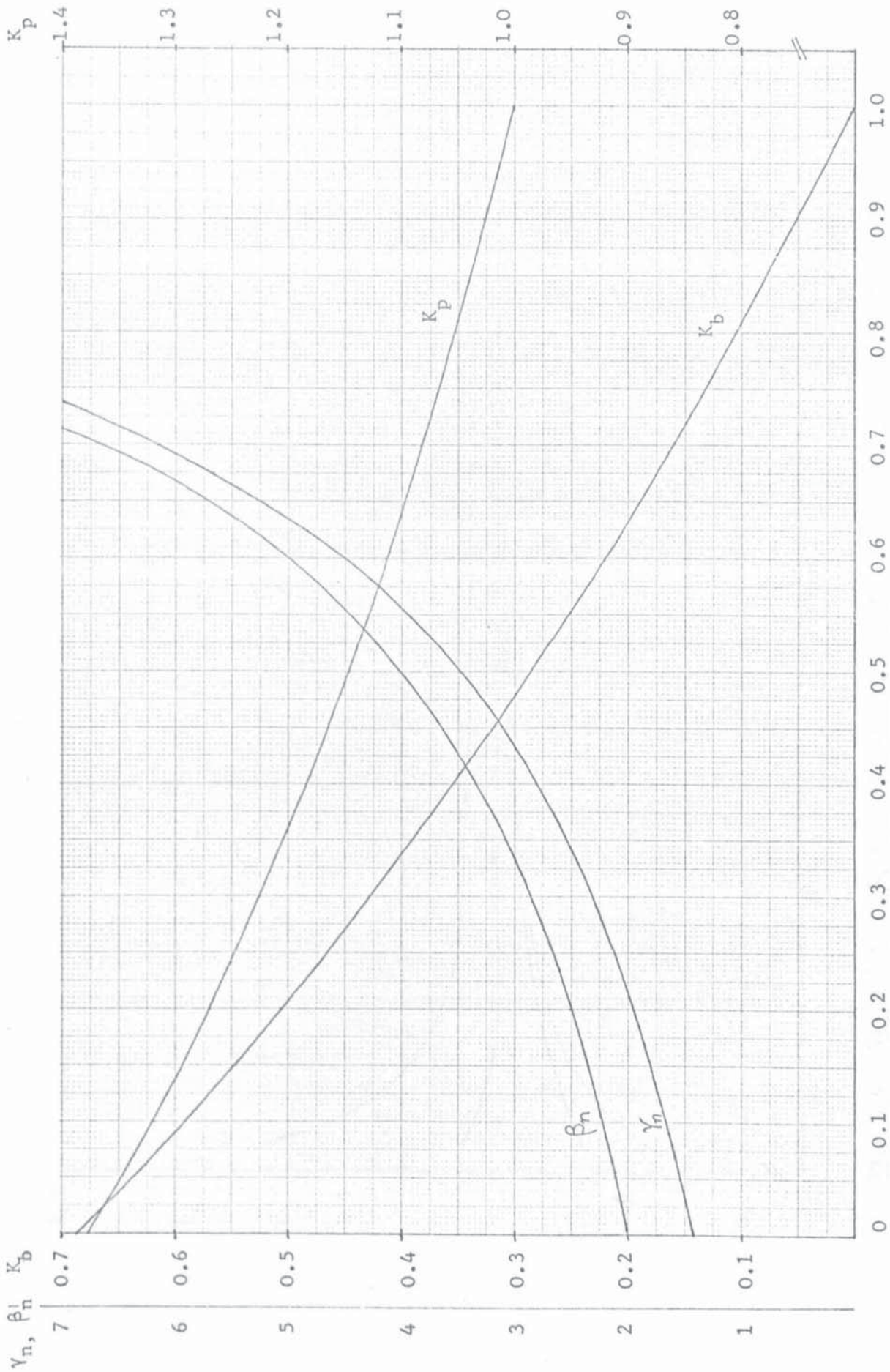
Fig. 4.2   Variation of γ_n, β_n, K_b and K_p with the Exponent b.

(Equations for these quantities are given in a 'list of important formula' at the end of the thesis.)
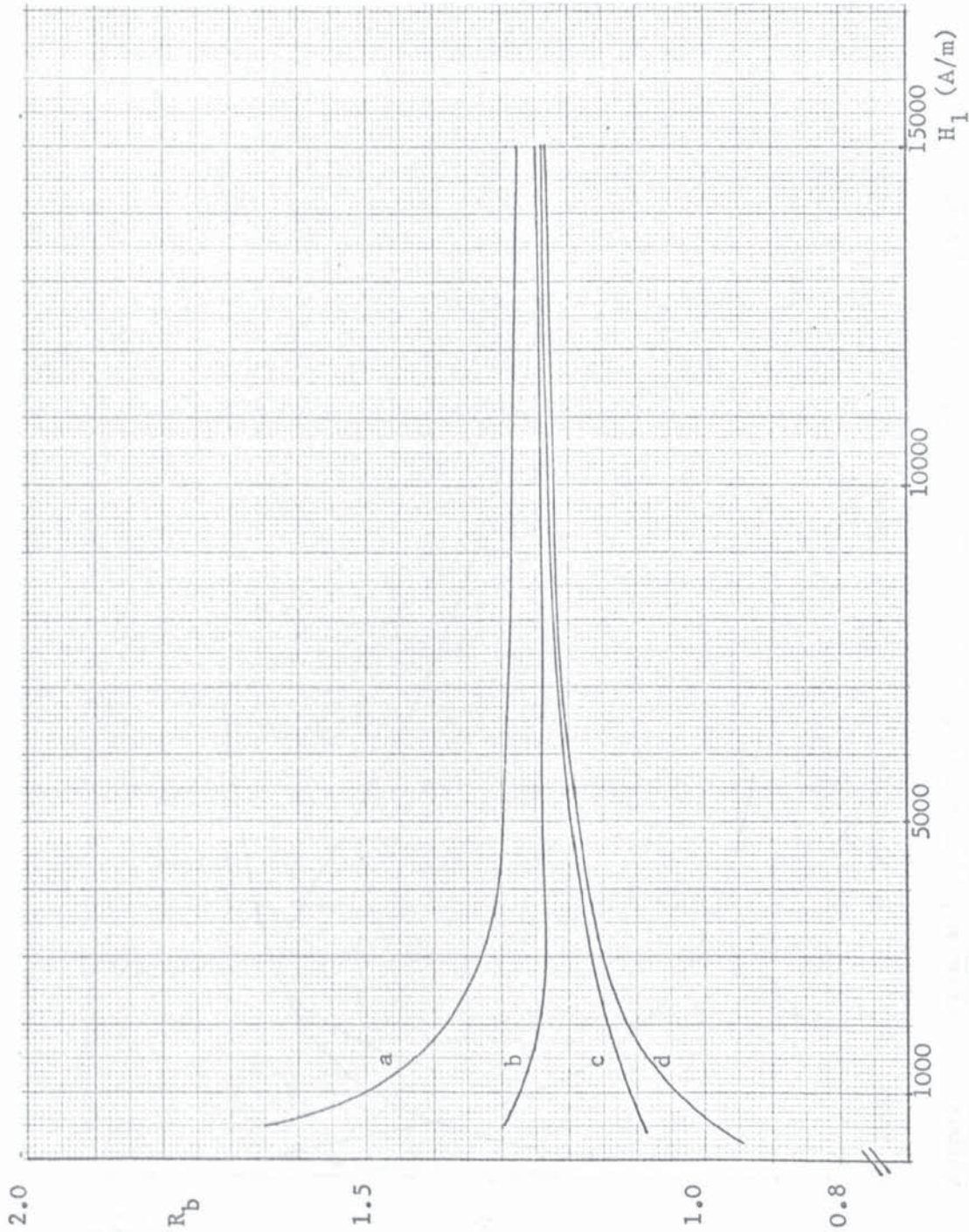
Fig. 4.6   Variation of R_b with the Fundament Component of the Magnetic Field Strength, H_1 for EN1A steel

$R_b = B_1/B_{h1}$ Curve (a) : U = 0.5   Curve (b) : U = 0,   Curve (c) : U = 0.2
                    Curve (d) : U =-0.1.
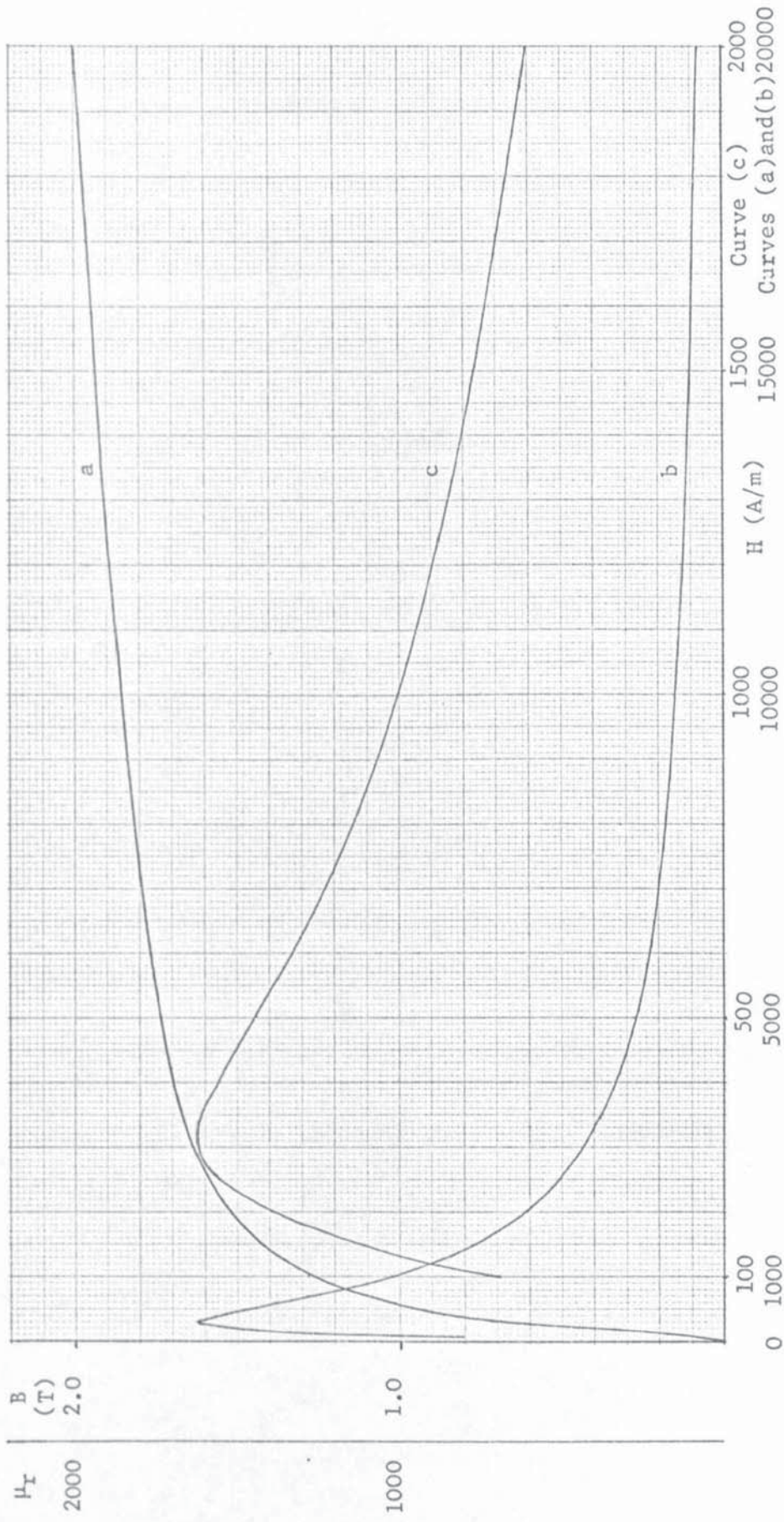
Fig. 5.1   Normal B-H Curve and μ_r-H curve for the EN1A Steel used in the Experimental Investigations.

(a) : normal B-H curve.;   (b) & (c) : μ_r - H curve.
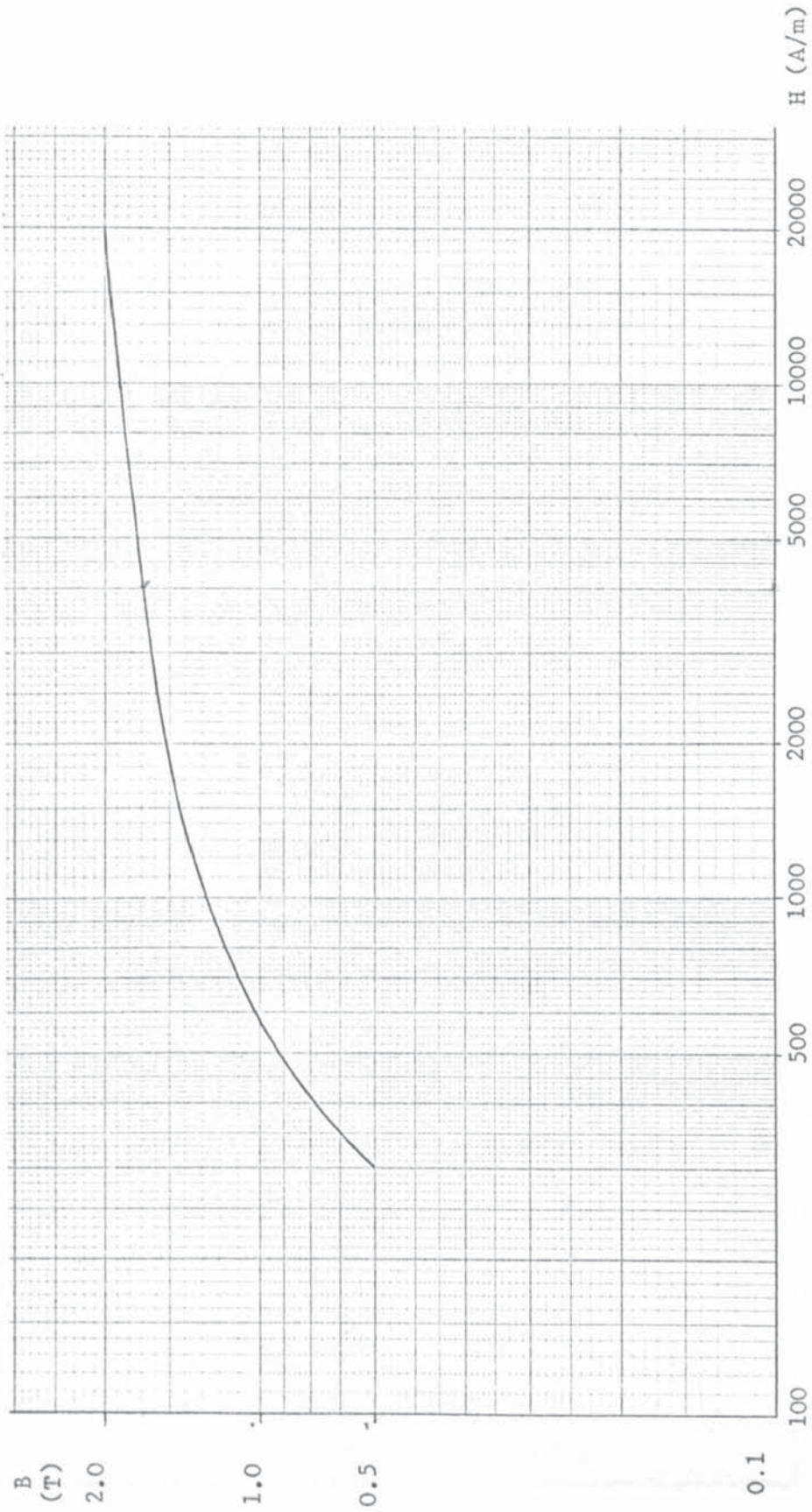
Fig. 5.2   Log B against Log H for the EN1A Steel used in the Experimental Investigation.
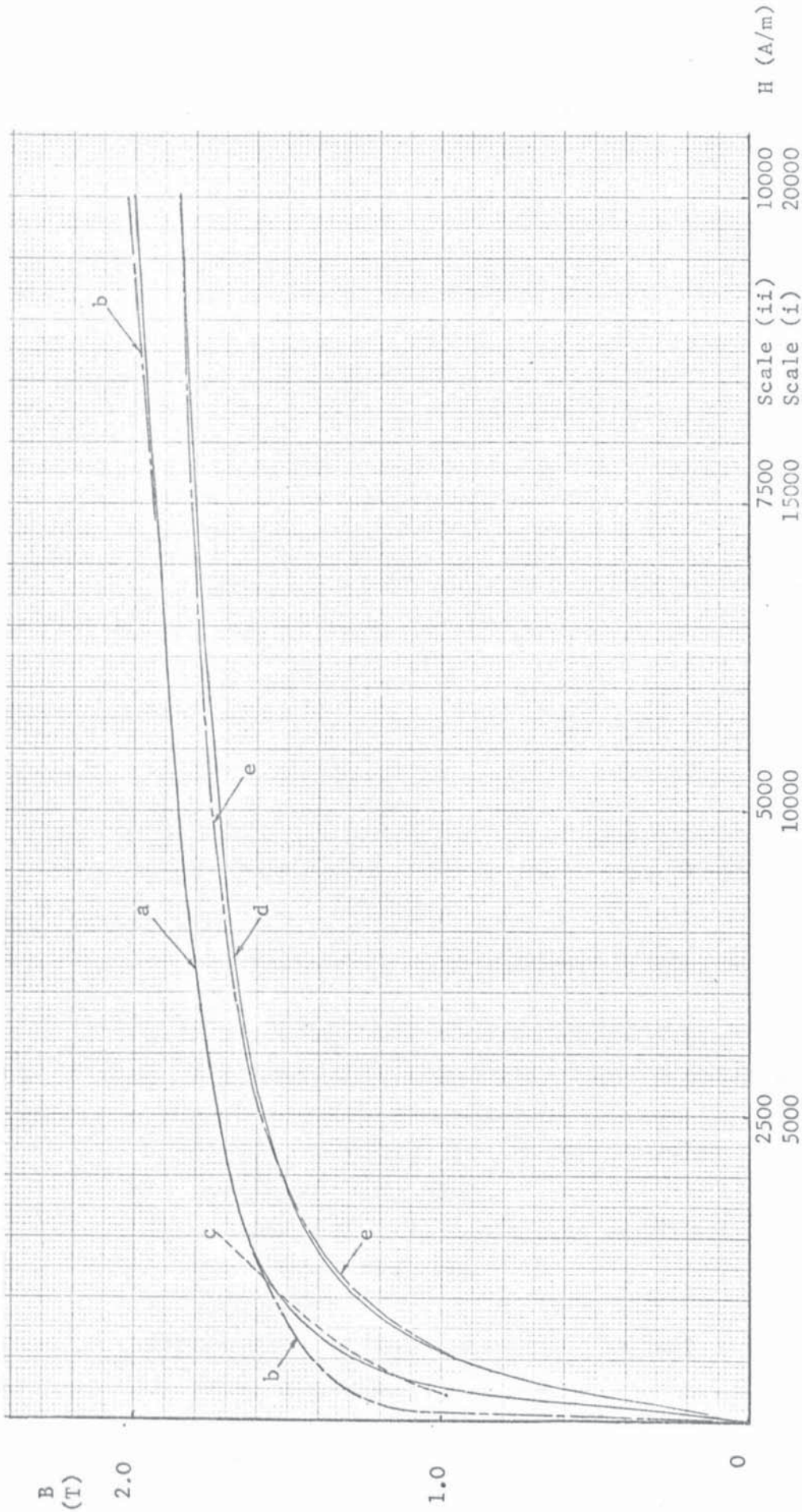
Fig. 5.3   Comparison between the Normal B-H curve for EN1A Steel (Fig. 5.1) and Curves obtained from the

Function $B = aH^b$ and $B = H/(d + kH)$

Curve (a): normal B-H curve;   Curve (b): $B = 0.664H^{0.112}$;   Curve (c): $B = 0.214H^{0.258}$;

Curve (d): normal B-H curve;   Curve (e): $B = H/(288 + 0.512 H)$

Scale (i): curves (a), (b) and (c);   Scale (ii): curves (d) and (e).
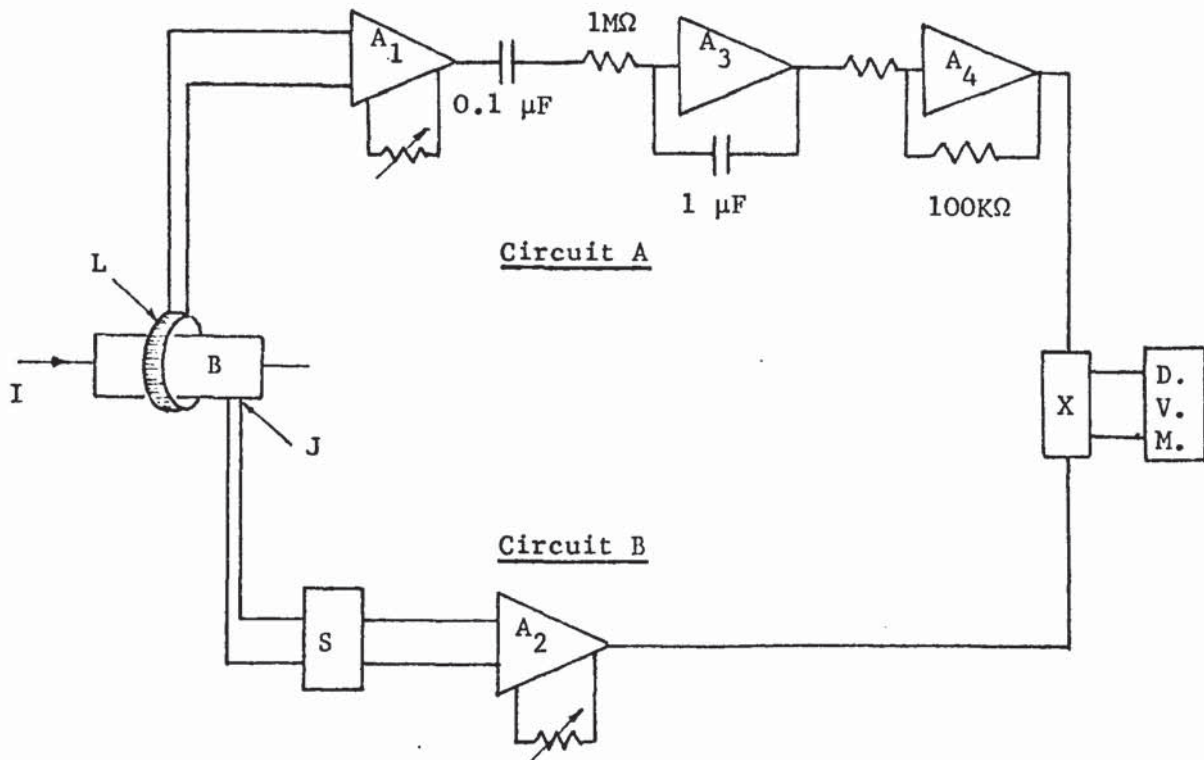
Fig. 5.5 <u>Circuits for Measurement of Loss in the Bar.</u>

Circuits A and B were also used in the measurement of flux and surface current density on the experimental machine. (Chapters 7, 8 and 10).

L   Linear Coupler;   non-integrated output: 0.41mV/A

B   Bar

J   Current Density Probe (Section 5.4.2.1)

A_1, A_2 Instrumentation Amplifiers;   Burr Brown, model 3061.
Gain :   x 1000 (variable).

A_3 Chopper-stabilised operational amplifier;
Burr Brown model 3071.

A_4 Chopper-stabilised operational amplifier;
Burr Brown model 3071.

X   Multiplier;   Burr Brown, model 4029

DVM Solartron Digital Voltmeter.   LM 1402

S   Reversing switch.

Loss
(KW/m^2)
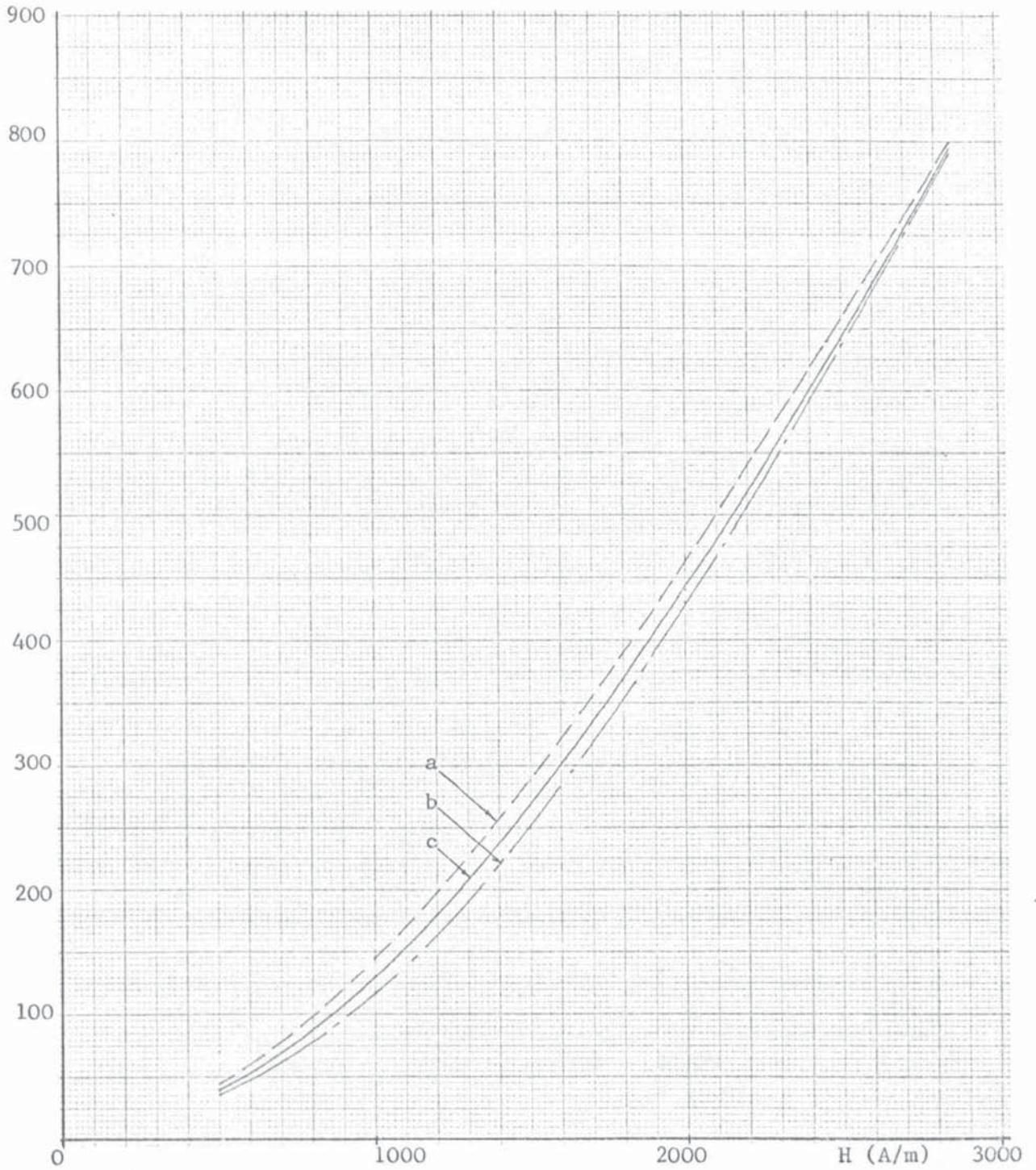
<u>Fig. 5.6</u>   <u>Measured and Calculated Loss/Unit Area as a Function of the
Surface Magnetic Field Strength, Ĥ.</u>

Curve (a) : Calculated loss, Agarwal's theory.

Curve (b) : Calculated loss, present non-linear theory
$(B_1 = AH_1^b.)$

Curve (c) : Measured loss in the Bar.
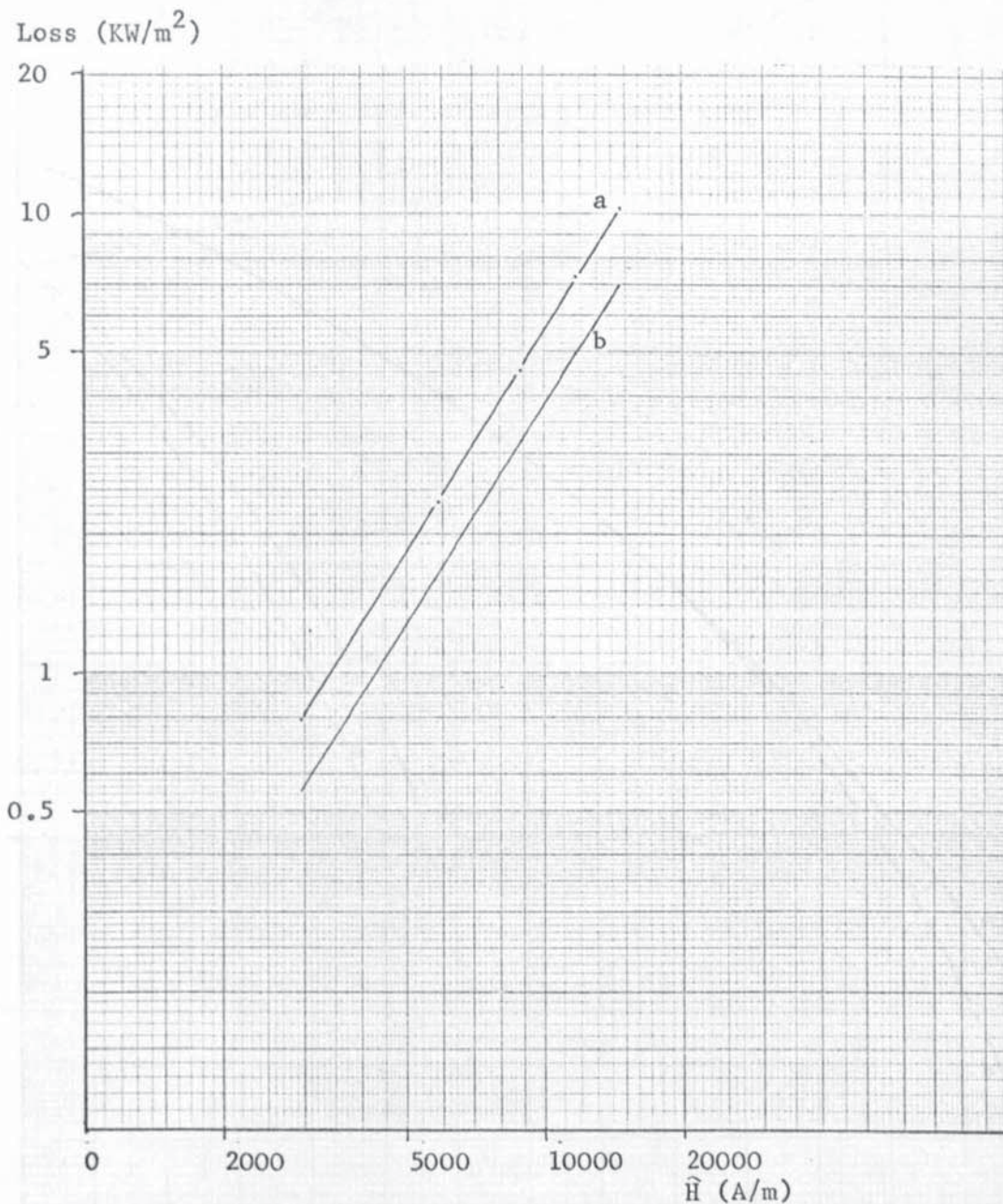
Fig. 5.7 Loss/Unit Area as a Function of the Surface Magnetic
Field Strength $\hat{H}$.

Curve (a) : Measured loss in the bar;   gradient: 1.57

Curve (b) : Calculated loss, linear theory, $\mu_r = f(\hat{H})$;
gradient : 1.59
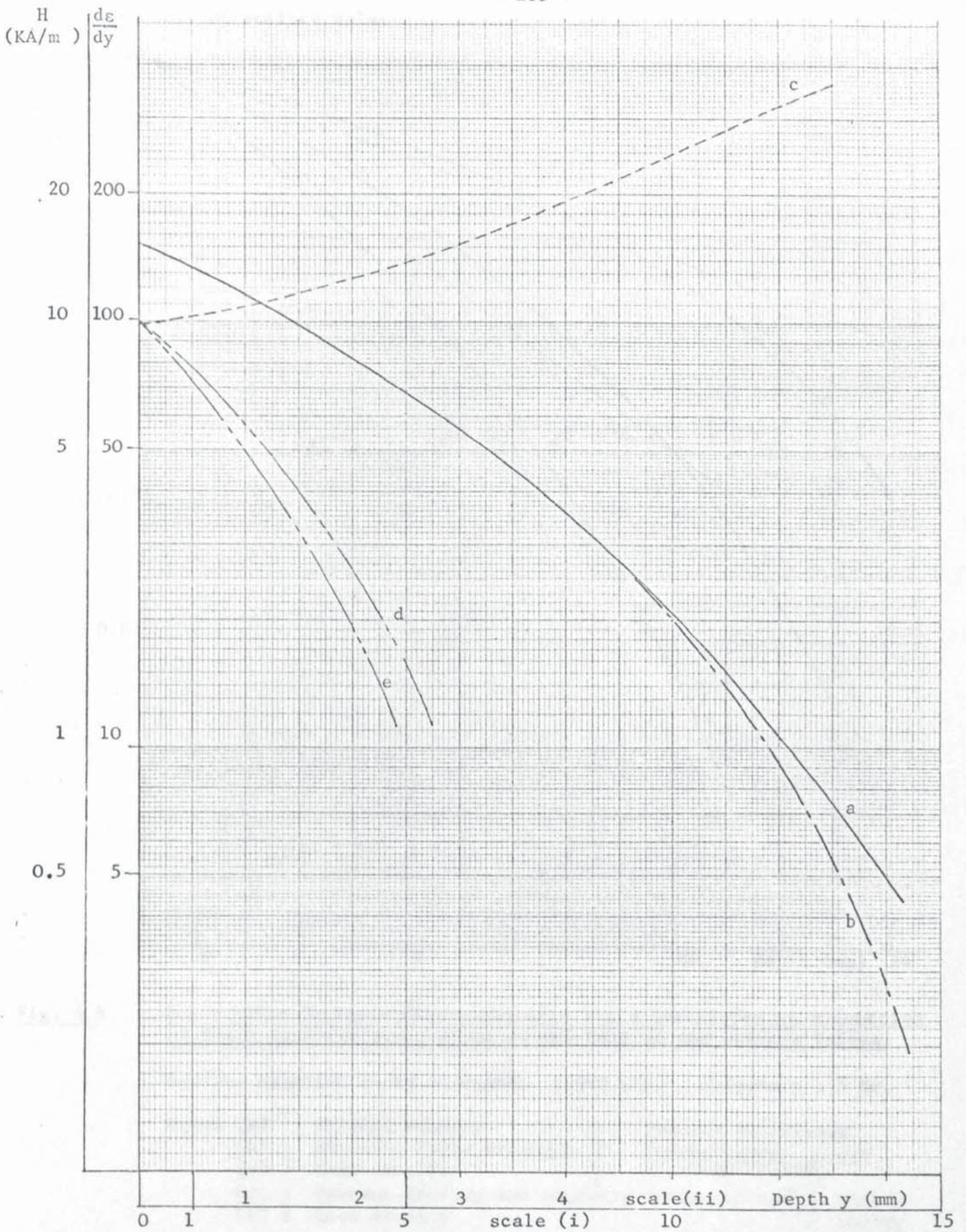
Fig. 5.8   Penetration Curves - Magnetic Field Strength as a
Function of Depth into the Iron.

Curve (a) : Finite difference solution of Equation 4.13 } 5 Hz
Curve (b) : Analytic Solution using $B = 0.66H^{0.112}$ } scale (i)
Curve (c) : $d\varepsilon/dy$ - see Appendix III
Curve (d) : Analytic solution using $B = 0.66H^{0.112}$ } 50 Hz
Curve (e) : Analytic solution using $B_1 = 1.25 (0.66H_1^{0.112})$ } scale (ii)

Per unit of surface value
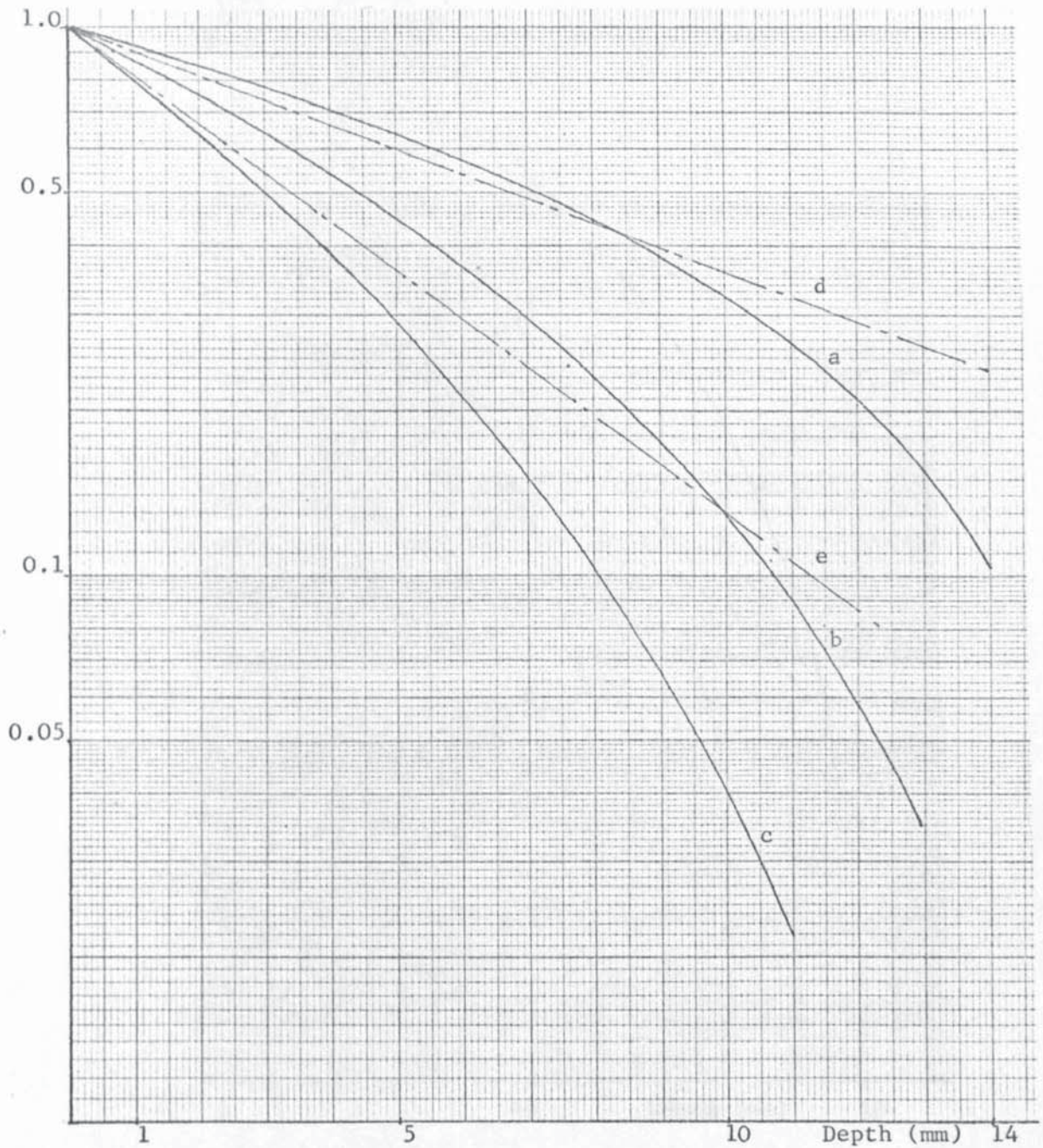
Fig. 5.9 Penetration Curves:- Electromagnetic Field Quantities as a Function of Depth into the Iron, given as per Unit of the Surface Values.

Surface magnetic field strength: 15000 A/m; frequency : 5 Hz.

Curve (a) : Current density   } Present non-linear
      (b) : Magnetic field strength } theory using
      (c) : Loss density   } $B_1 = 0.66 H_1^{0.112}$
      (d) : Current density and magnetic field strength } Linear
      (e) : Loss density   } theory
                                                                       $\mu = \mu_g$

Fig. 5.10   Penetration Curves - Electromagnetic Field Quantities as a
Function of Depth into the Iron, given as per unit of the
Surface Values.

Surface magnetic field strength : 5000 A/m; frequency 5 Hz.

Curve (a) : Current density   ⎫ Present non-linear
       (b) : Magnetic field strength   ⎬ theory using
       (c) : Loss density   ⎭ $B_1 = 0.66 H_1^{0.112}$
       (d) : Current density and magnetic field strength ⎫ linear
       (e) : Loss density   ⎬ theory
                                                               ⎭ $\mu = \mu_g$

Fig. 5.11.   Waveforms (half cycles only) of Flux Density and

Magnetic Field Strength obtained by a Finite

Difference Solution of the Diffusion Equation.

Surface Excitation : 10000A/m   (Equation 4.2)
Frequency : 50 Hz.
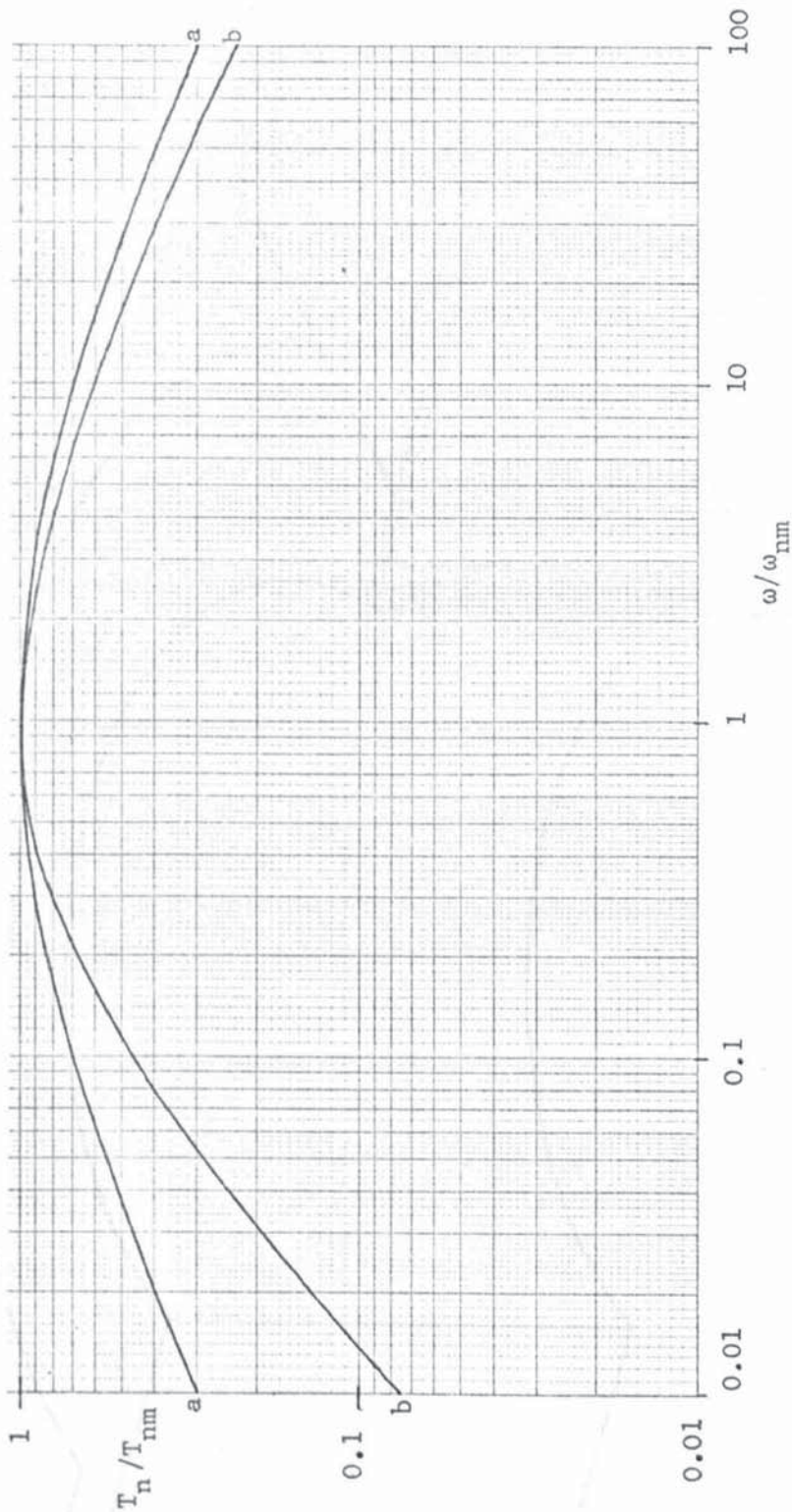
Fig. 6.1   Generalised Torque/Frequency Characteristics.

Curve (a) : b = 1
Curve (b) : b = 0.112

Search wires connected to a common strip.

Wires, Twisted and connected to Selector Switch
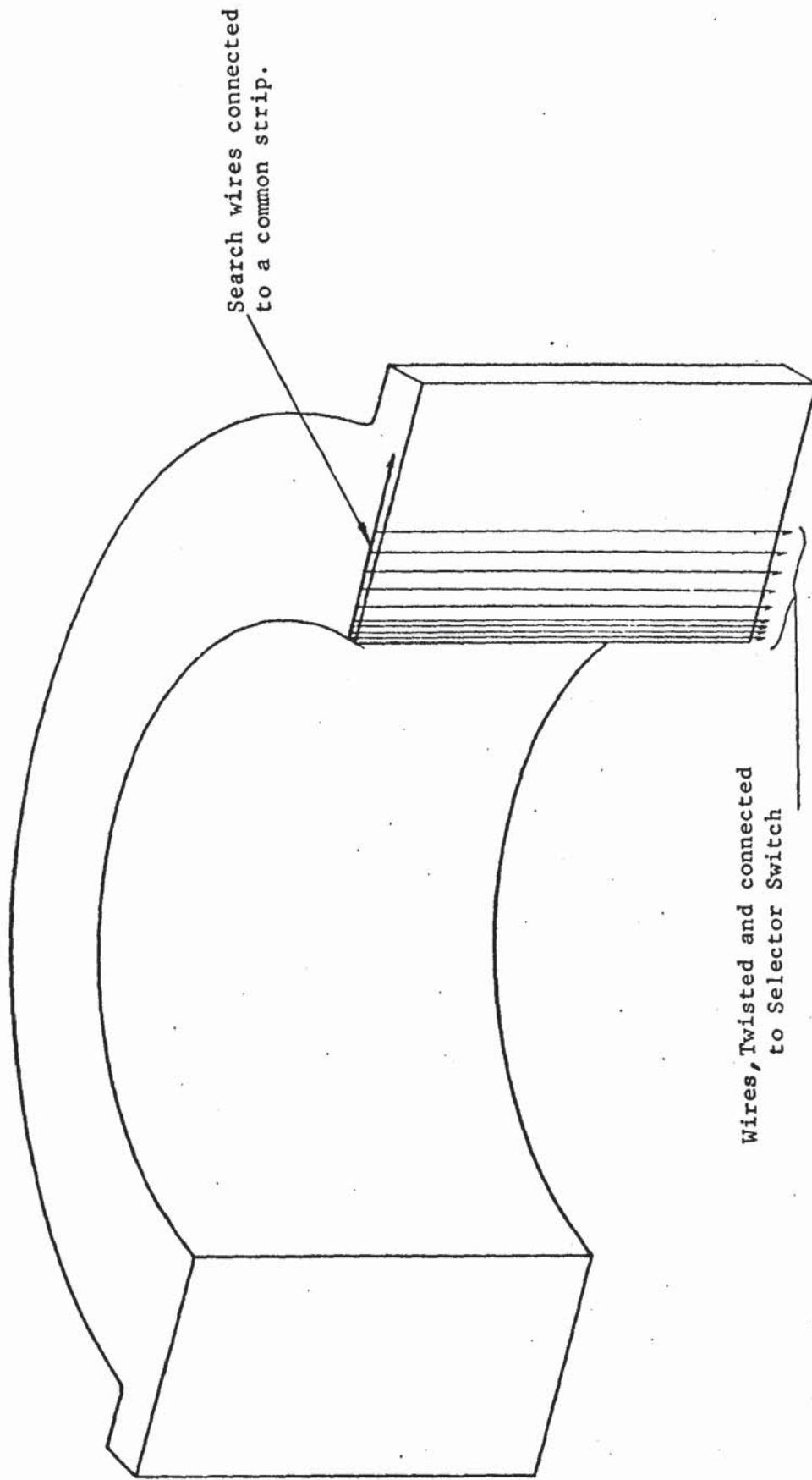
Fig. 7.1   Half of Stator used in the Preliminary Investigation, showing location of search coils to measure flux penetration.
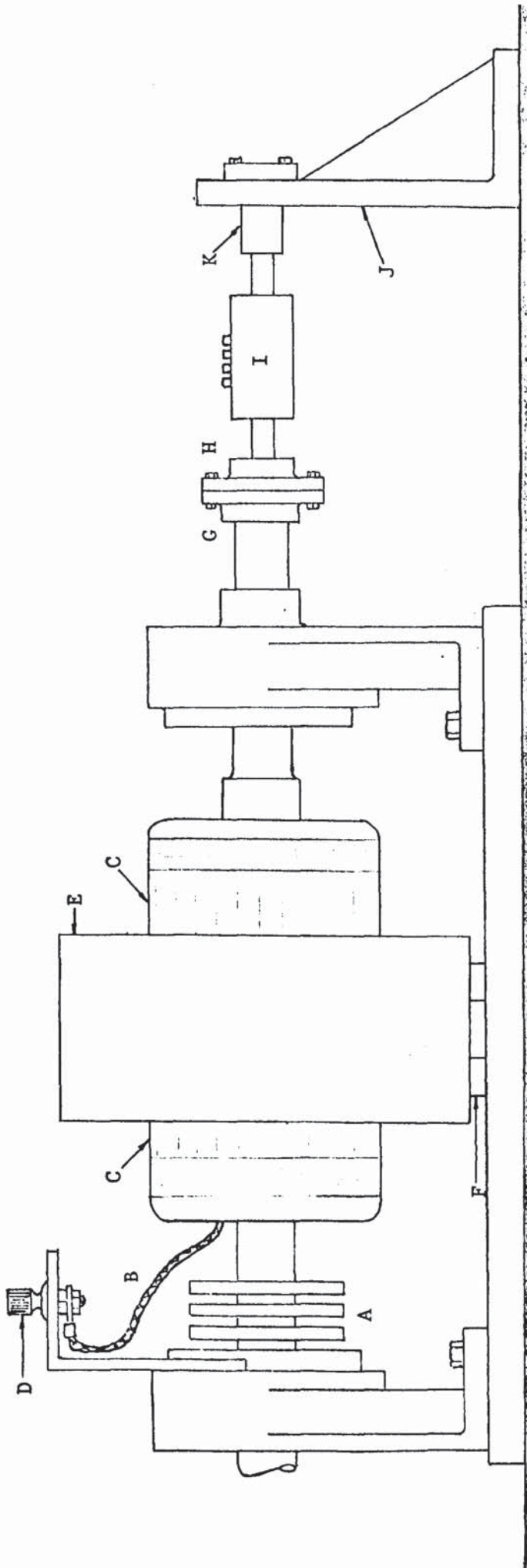
Bedplate

FIG. 7.2   THE EXPERIMENTAL RIG

A : slip rings (not used);   B : braided copper conductors (3), brazed onto rotor winding terminations;

C : rotor   D : supply terminals (3) mounted on bakelite board;   E : stator;

F : support shoes (tufnol) see plate 7.2,   G & H : half couplings keyed to rotor shaft and torque transducer shaft,

I : torque transducer,   J : Fixed support bracket,   K : coupling keyed to torque transducer and bracket J,

Notes : coupling H may be replaced by a bracket, similar to K, for locking the rotor in any position. Further
         details of the machine are shown in Plate 7.1 and Plate 7.2;   the clamping arrangement for the stator
         is omitted from this Figure, but is included in the Plates.
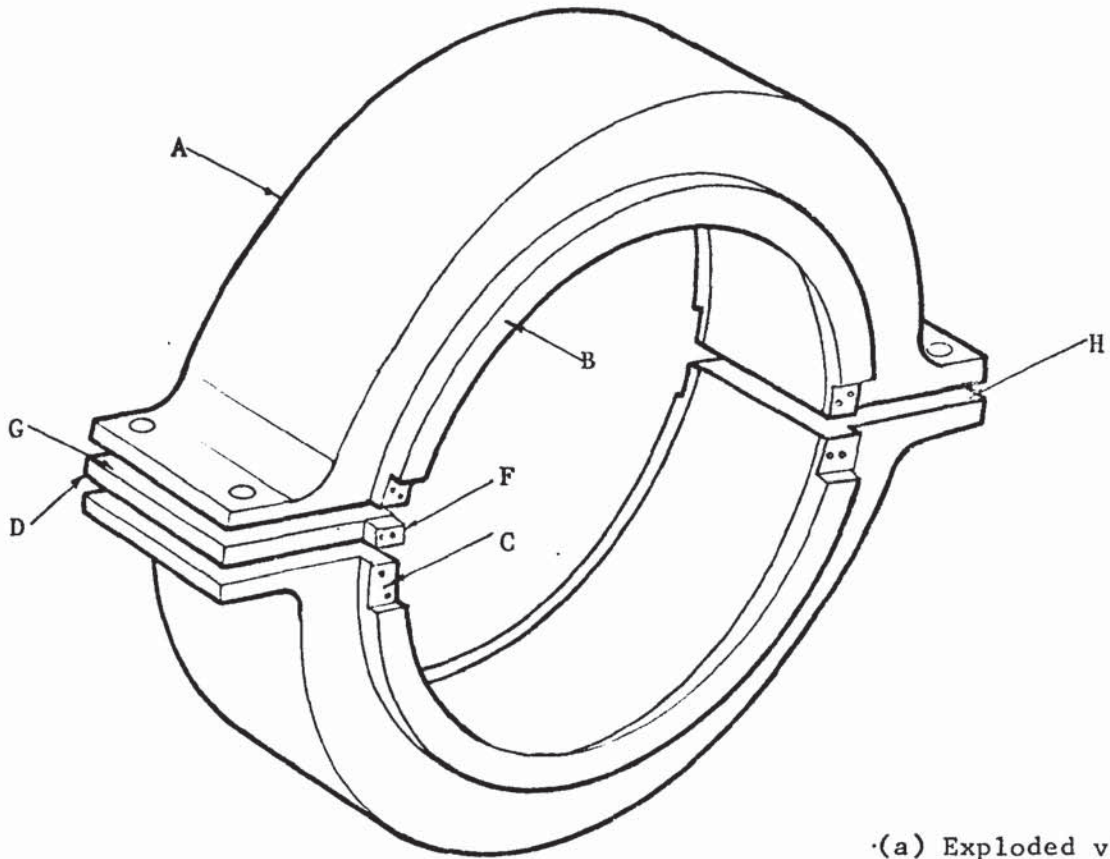
·(a) Exploded view.
(bridging pieces
removed).
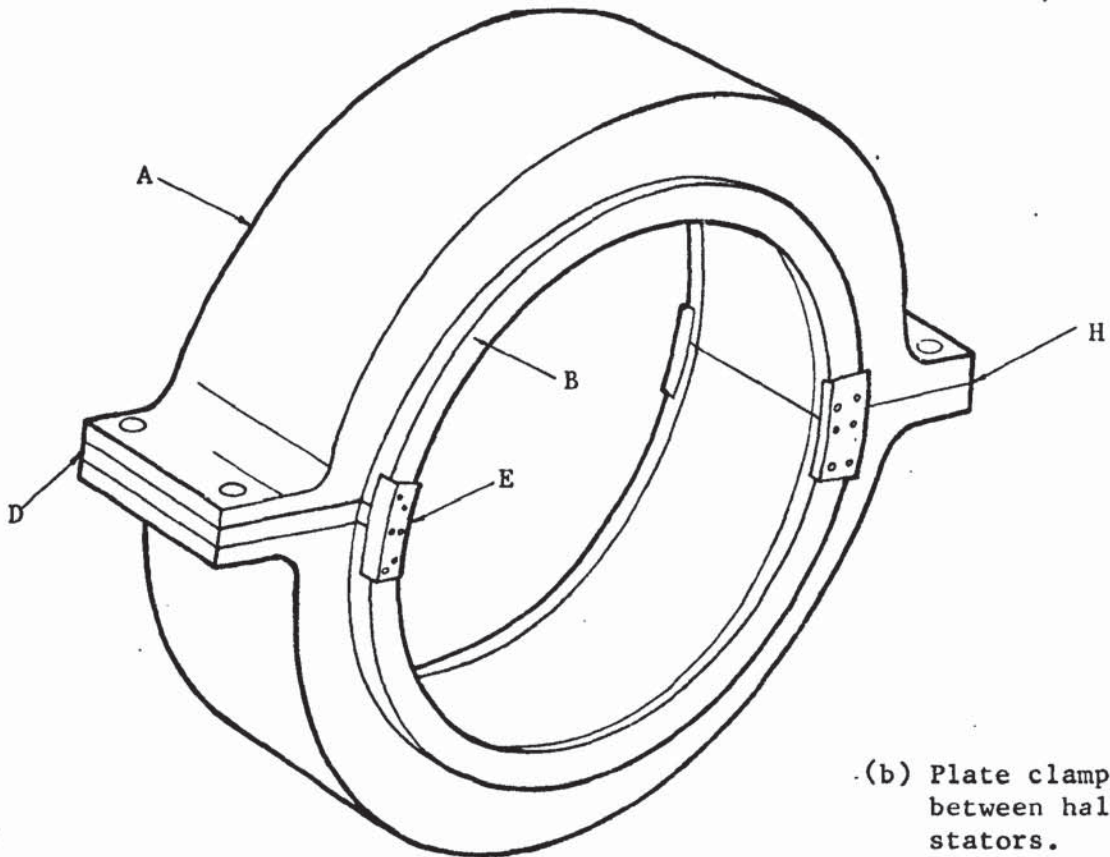
·(b) Plate clamped
between half
stators.

·Fig. 7.3   THE END RING STATOR.

·A : stator,   B : copper rings,   C : recessed surfaces for bridging pieces,

D : plate,   E : copper bridging pieces,   F : copper pieces brazed to plate

G : plate surface   ⎞ surfaces in which grooves

H : split surface (diametrically opposite G) ⎠ were machined for location
of search coils.
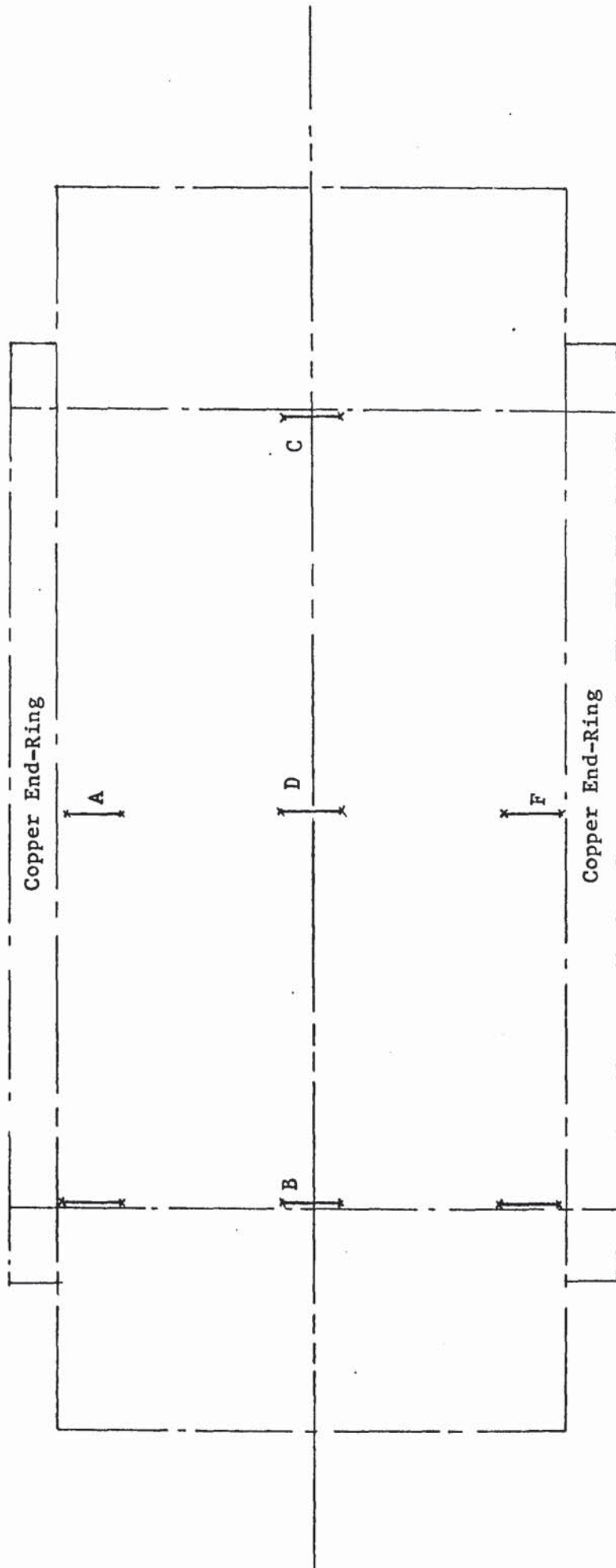
Fig. 7.4 Plan view of Half-Stator with Copper End Rings, showing Location of Current Density Probes

——— stator outline

—✗— current density probes (1 cm pitch)

(Both half stators had the arrangement of probes shown in this figure).
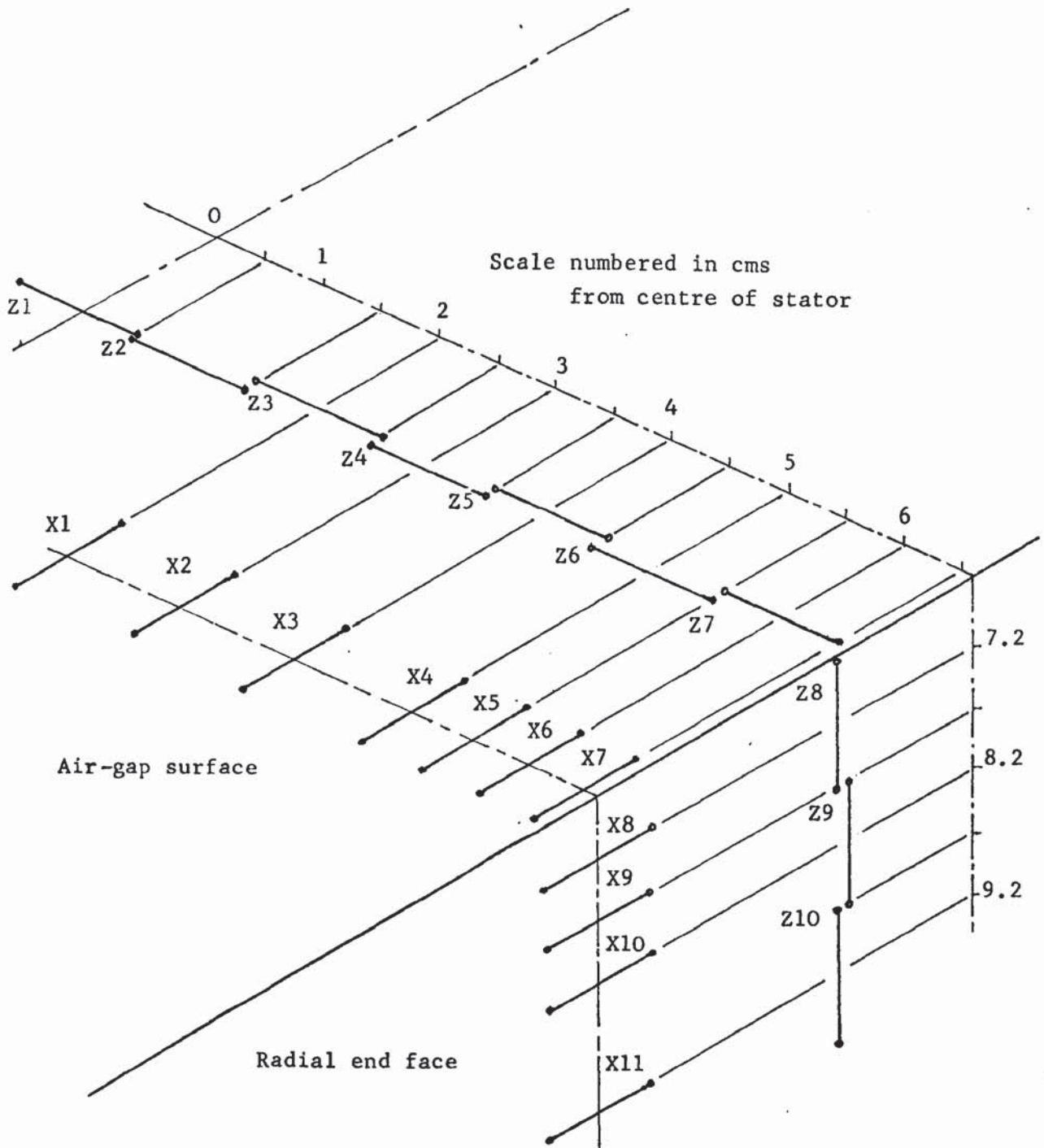
FIG. 7.5   Location of Current-Density Probes on the Airgap Surface
and Radial End Faces of the Continuous Stator

x : Peripheral probes, to measure J_x.

z : Axial probes, to measure J_z.

Note: the axial and peripheral probes were placed on the same
axial line on the stator, but have been separated for
clarity in this figure. This set of probes was duplicated
on a diamentrically opposite line on the stator.
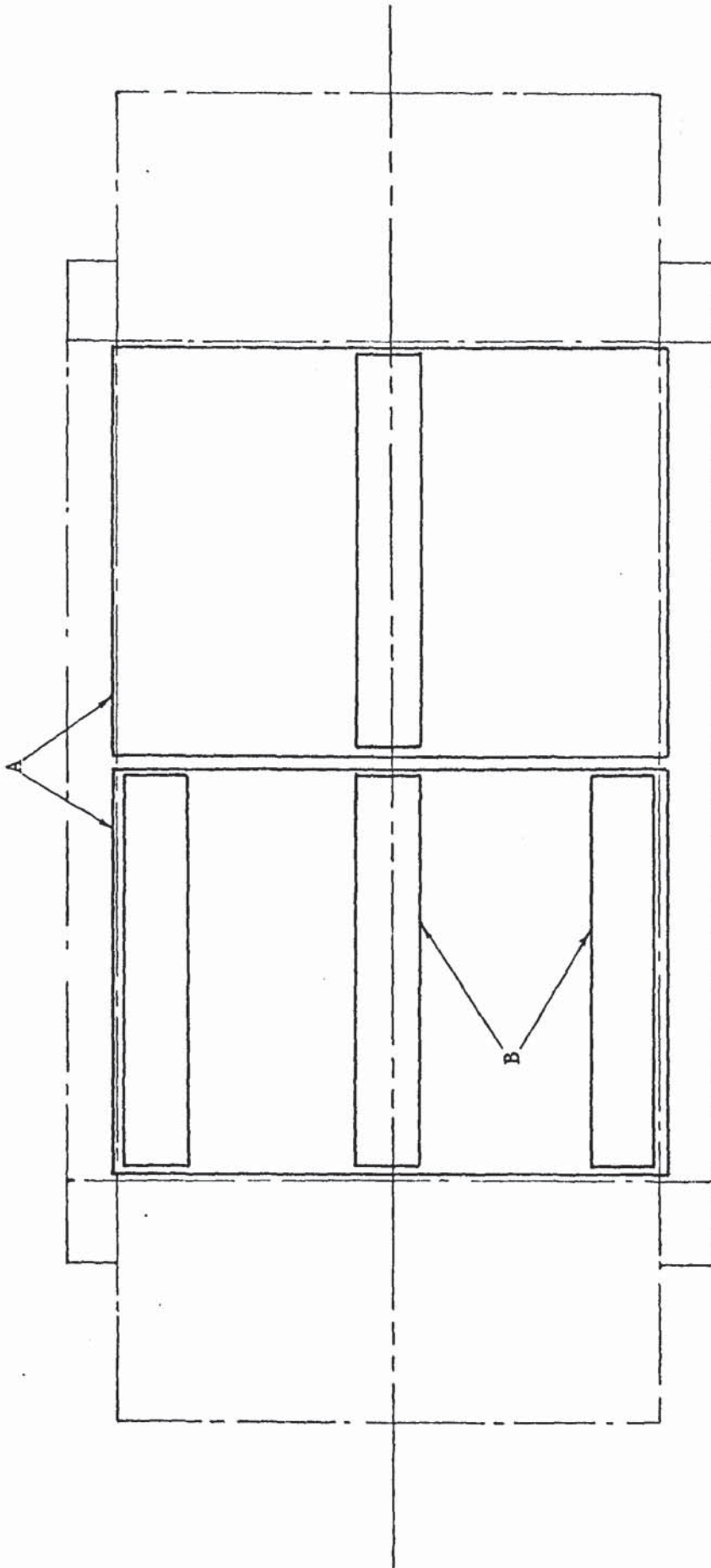
FIG. 7.6   Plan view of Half Stator with Copper End Rings, showing Search Coil arrangement for

Flux measurement

A : (full pitch) x (active length of stator)

B : (full pitch) x 1 cm.

——— outline of stator

——— Search coils

(Both half stators had the arrangement of search coils shown in this figure).
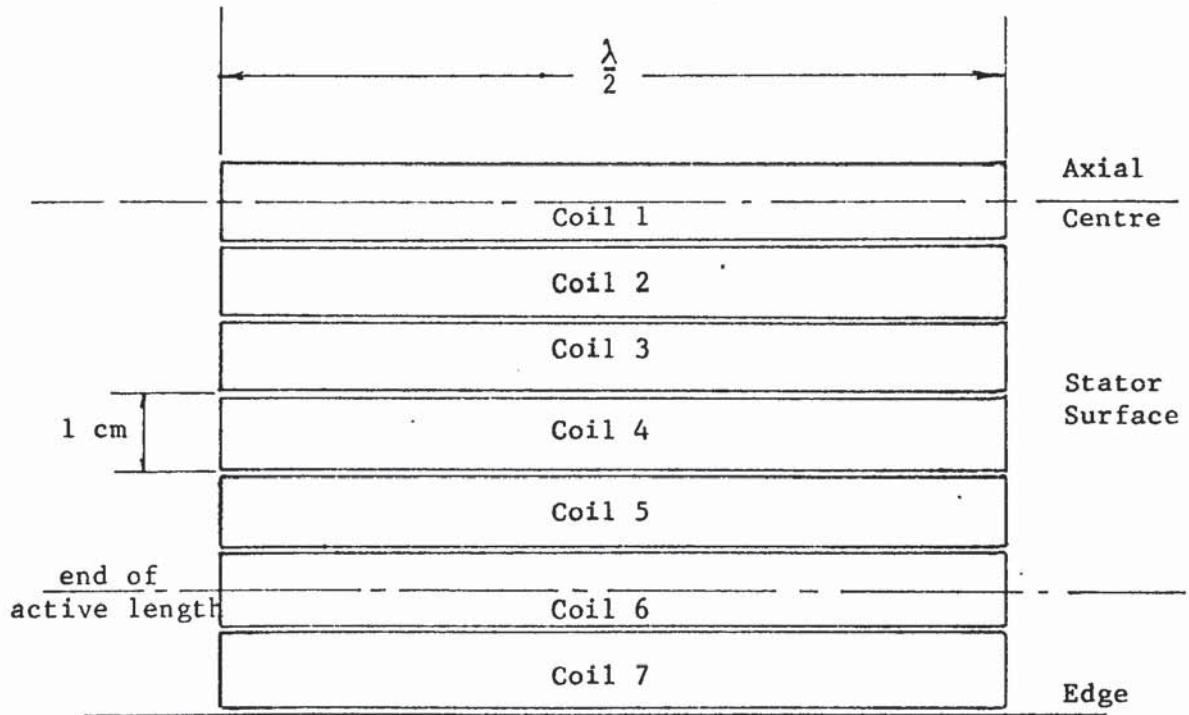
FIG. 7.7   Location of Full-pitch Search Coils on the
Surface of the Continuous Stator
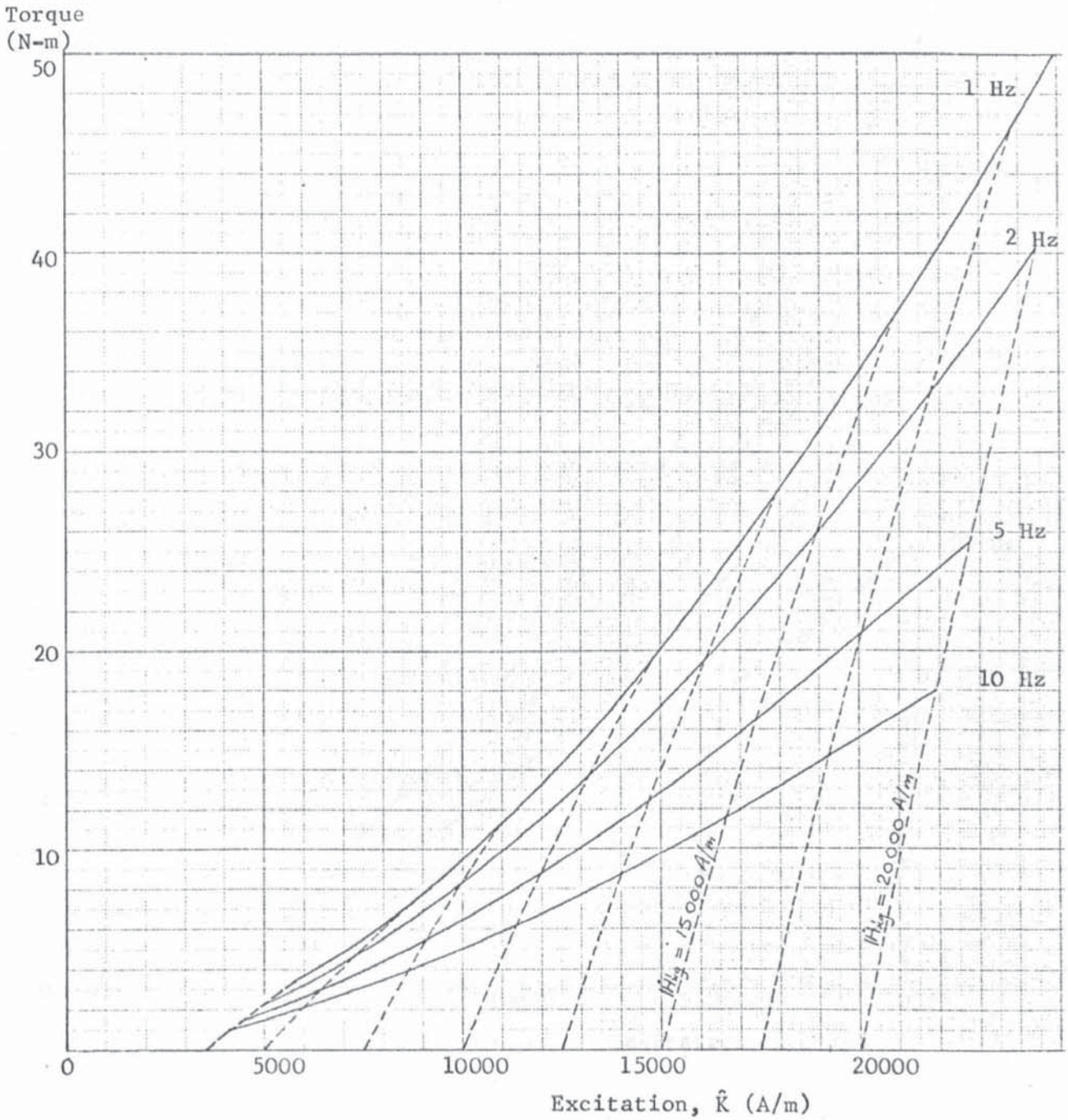
Fig. 8.1 Variation of Calculated Torque T_n, with Excitation $\hat{K}$,
at various Frequencies (1 - 10 Hz), for the End Ring
Stator.

———— torque lines
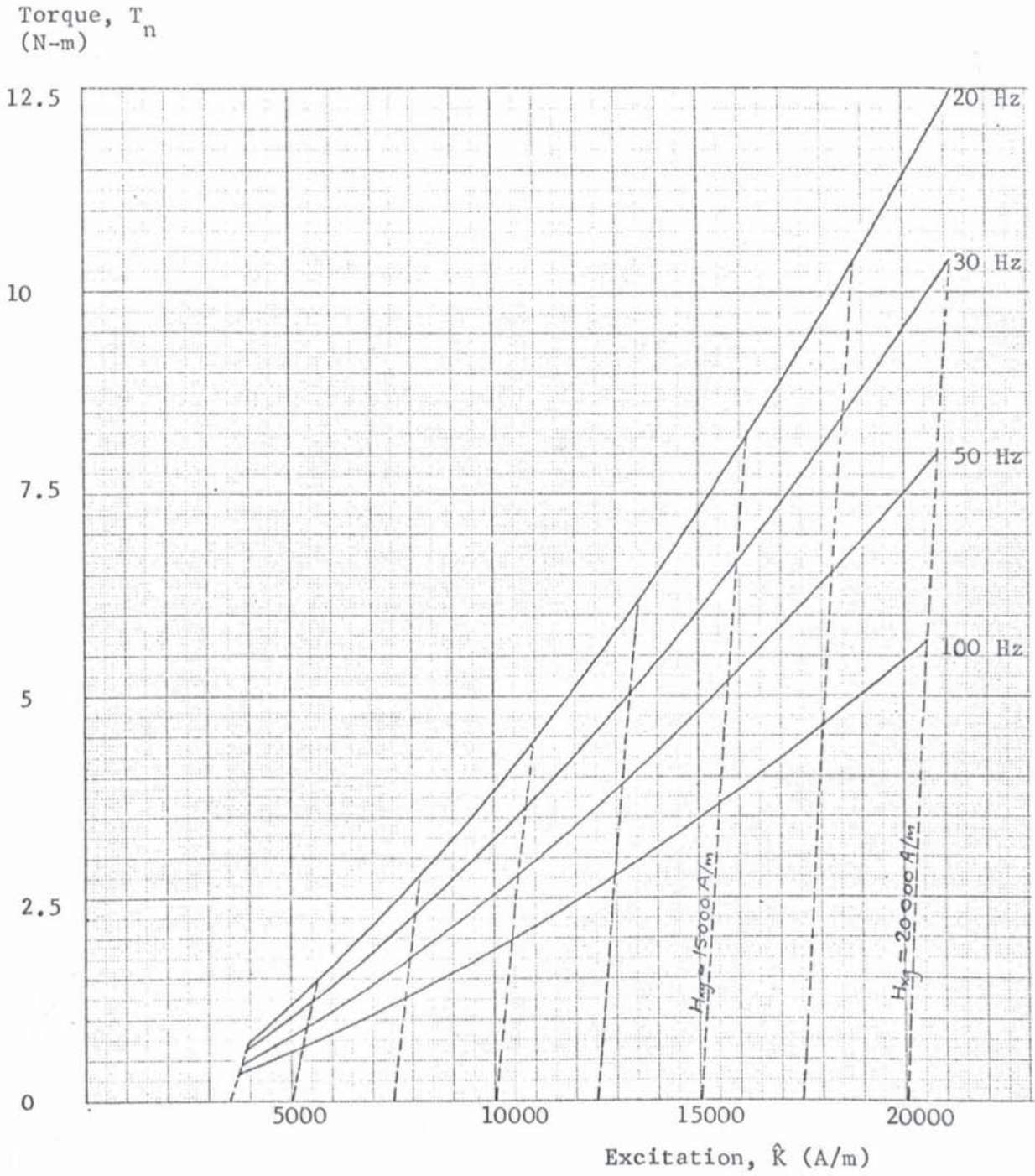
-------- constant $|\dot{H}_{xg}|$ lines

<u>Fig. 8.2</u>   <u>Variation of Calculated Torque, T_n, with Excitation $\hat{K}$,</u>
<u>at Various Frequencies (20-100 Hz) for the End-Ring Stator.</u>

_____ torque lines

--------------- constant $|\dot{H}_{xg}|$ lines.
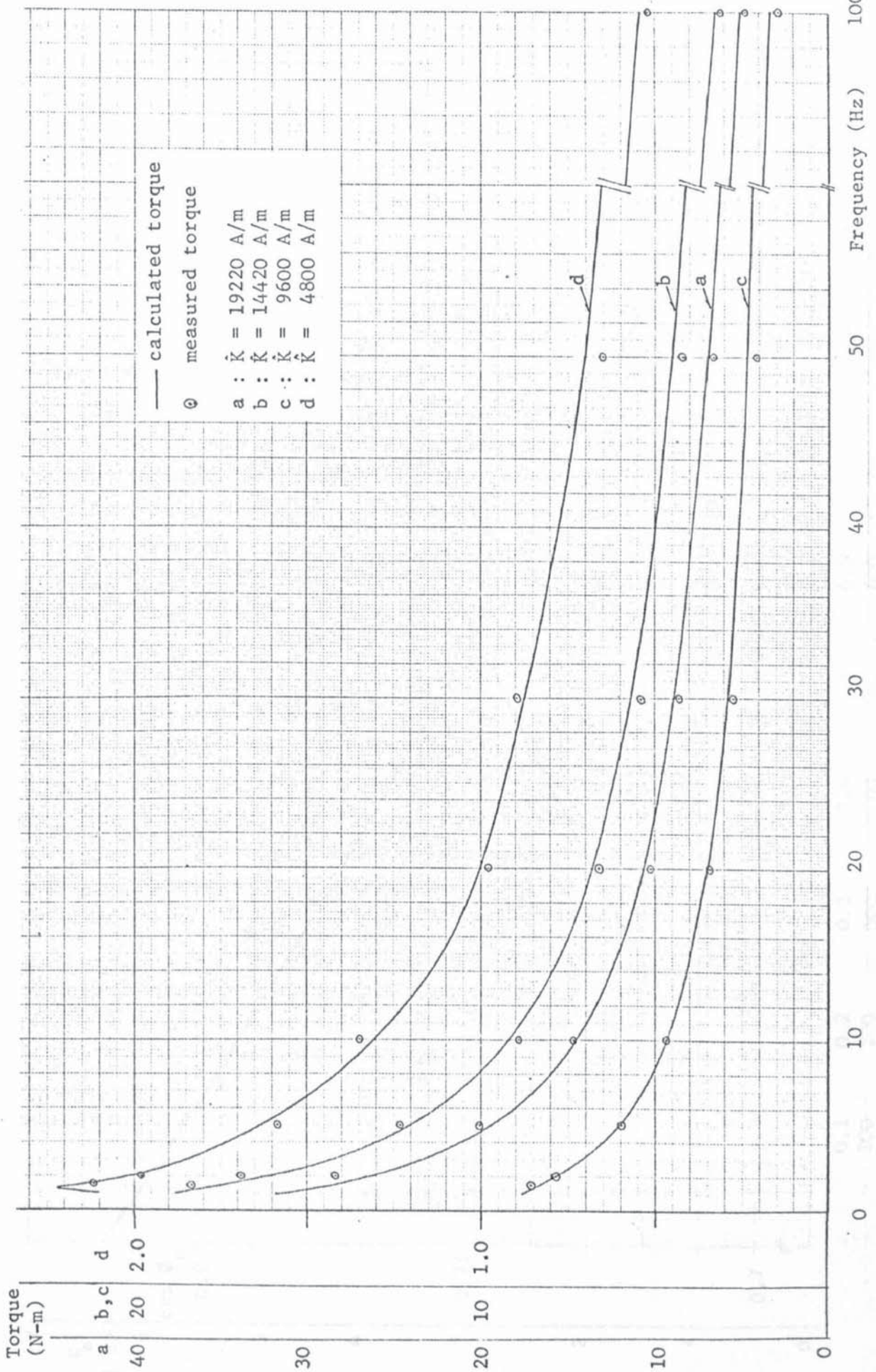
Fig. 8.3 Comparison of Measured and Calculated Torques at various Excitations, $\hat{K}$, and Frequencies for the End Ring Stator.
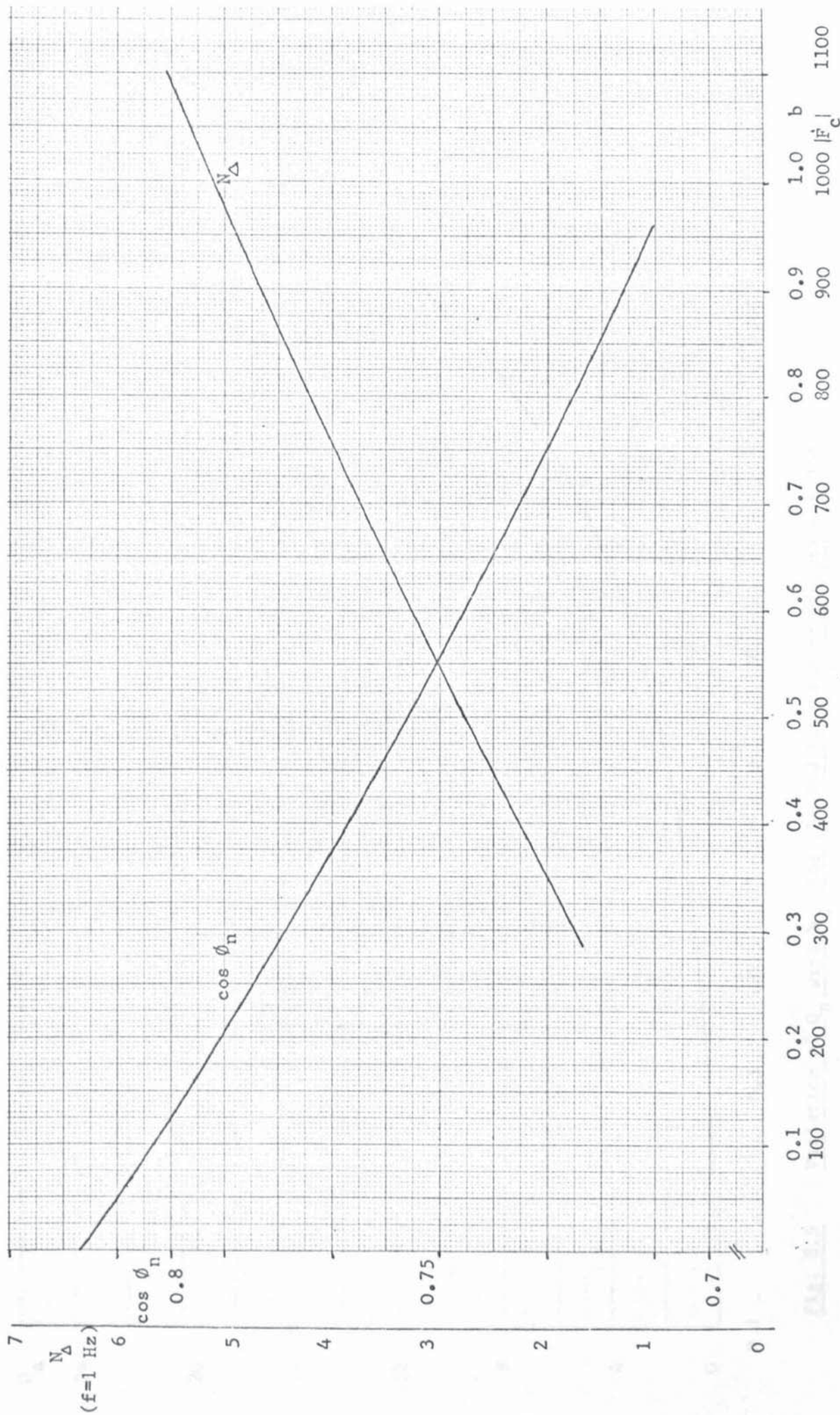
Fig. 8.4   Variation of (i) N_Δ with Excitation, $|\dot{F}_c'|$, for the End Ring Stator and (ii) $\cos\phi_n$ with b.
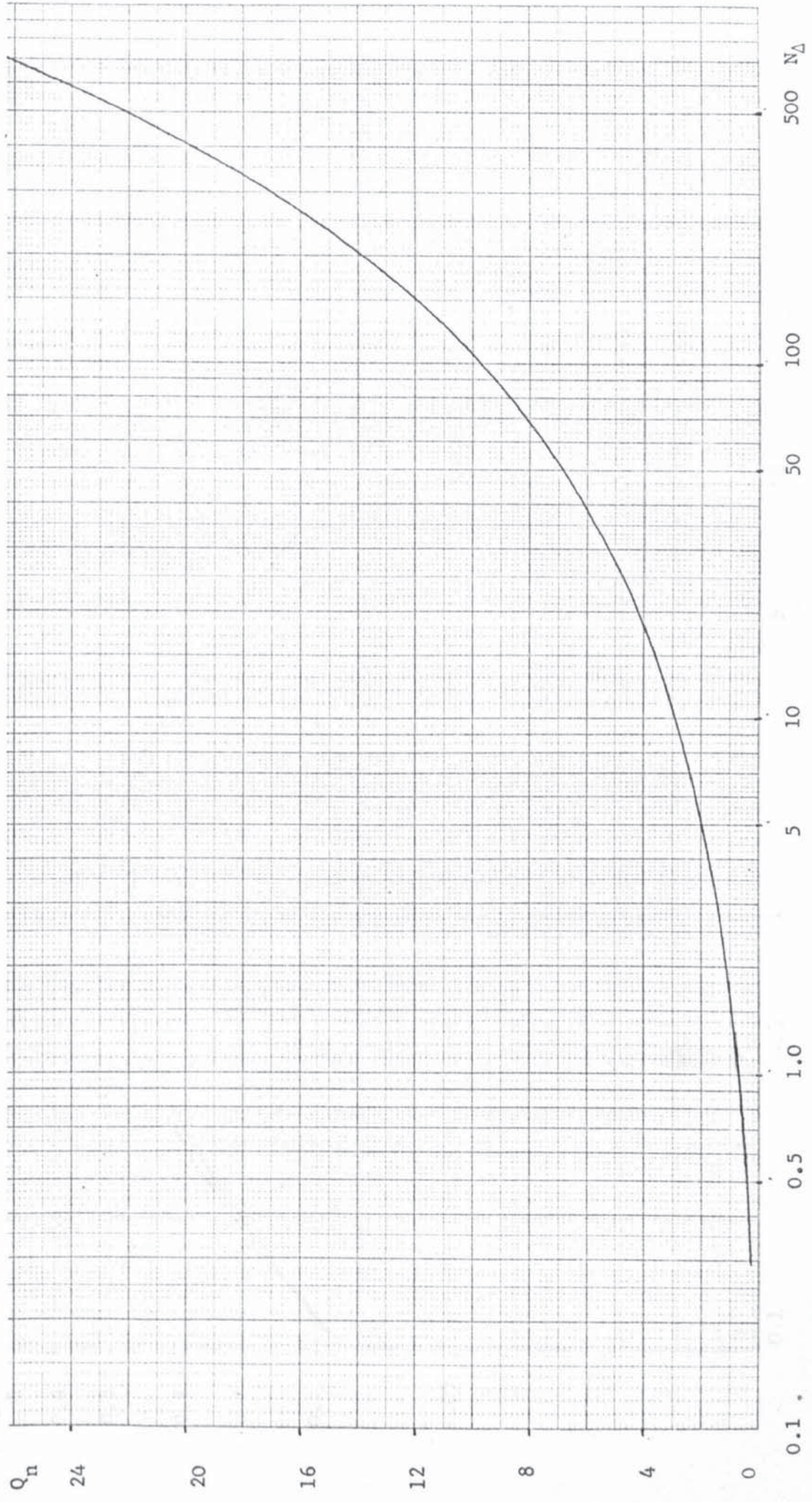
Fig. 8.5   Variation of Q_n with N_Δ for the End Ring Stator (Equation 6.35)
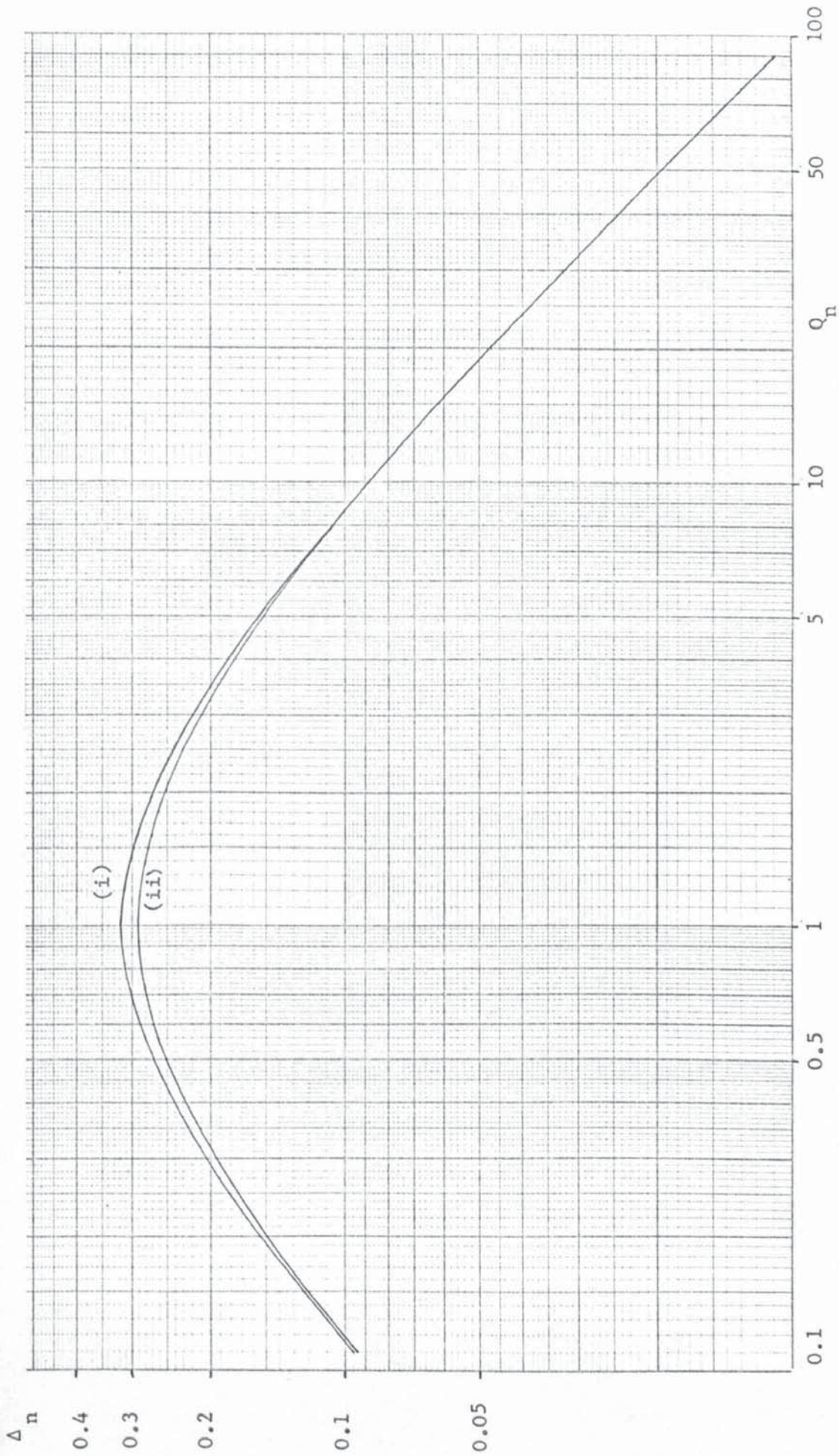
Fig. 8.6   Variation of Δ_n with Q_n (Equation 6.29)

Curve (i) b = 0.112;   Curve (ii) b = 1.0.
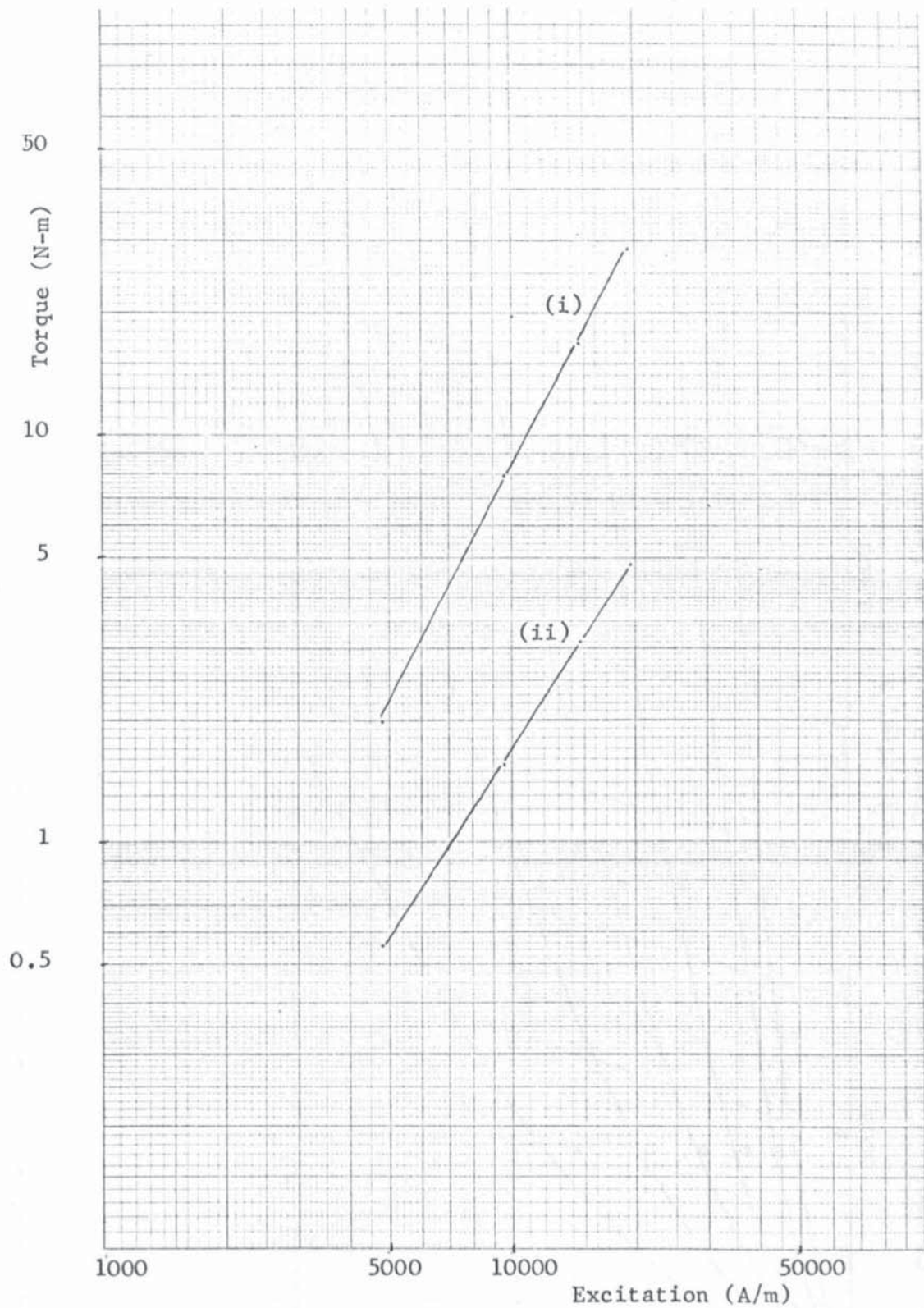
Fig. 8.7   Variation of Measured Torque with Excitation
for the End Ring Stator.

(i) 2 Hz : slope ≈ 1.9;   (ii) 100 Hz : slope ≈ 1.6
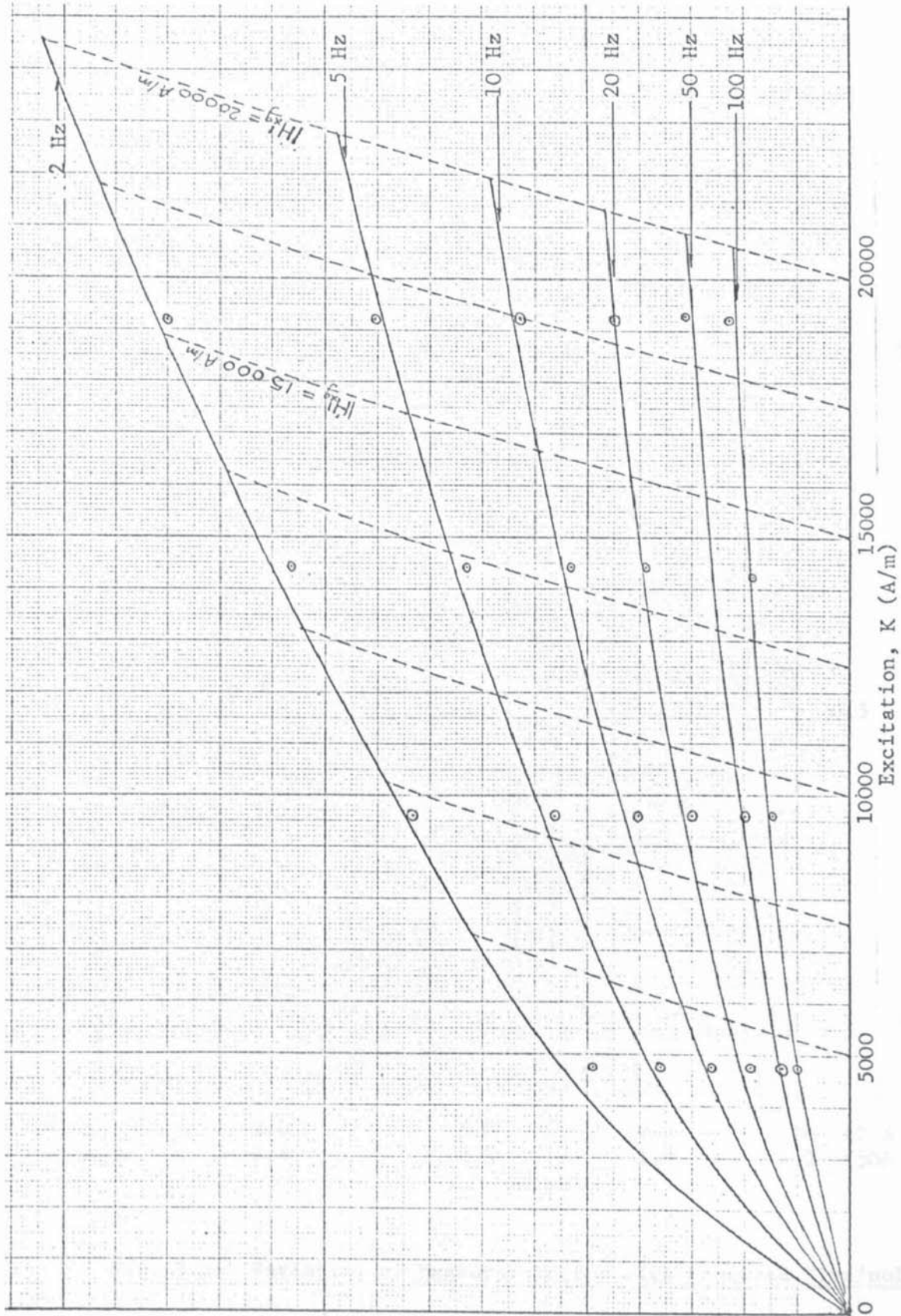
Fig. 8.8 Comparisons of Measured and Calculated Flux/pole at Various Excitations, K, and Frequencies for the End-Ring Stator. ⊙ measured ———— calculated ; ——— constant |H̊ₓg| lines.
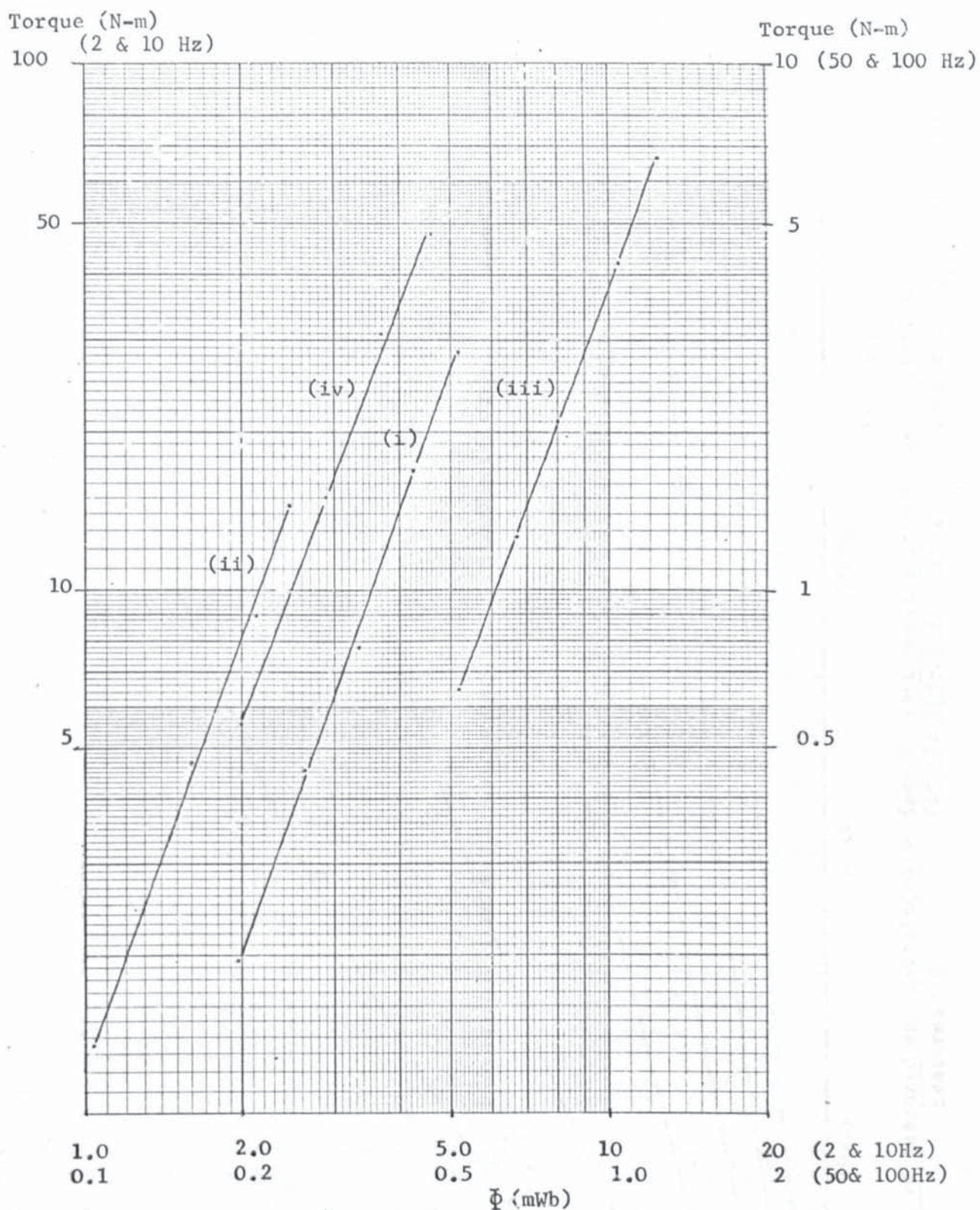
Fig. 8.3   Variation of Measured Torque with Measured Flux/pole.

Curve :	frequency :	slope
(i) :	2 Hz :	2.74
(ii) :	10 Hz :	2.77
(iii) :	50 Hz :	2.69
(iv) :	100 Hz :	2.67
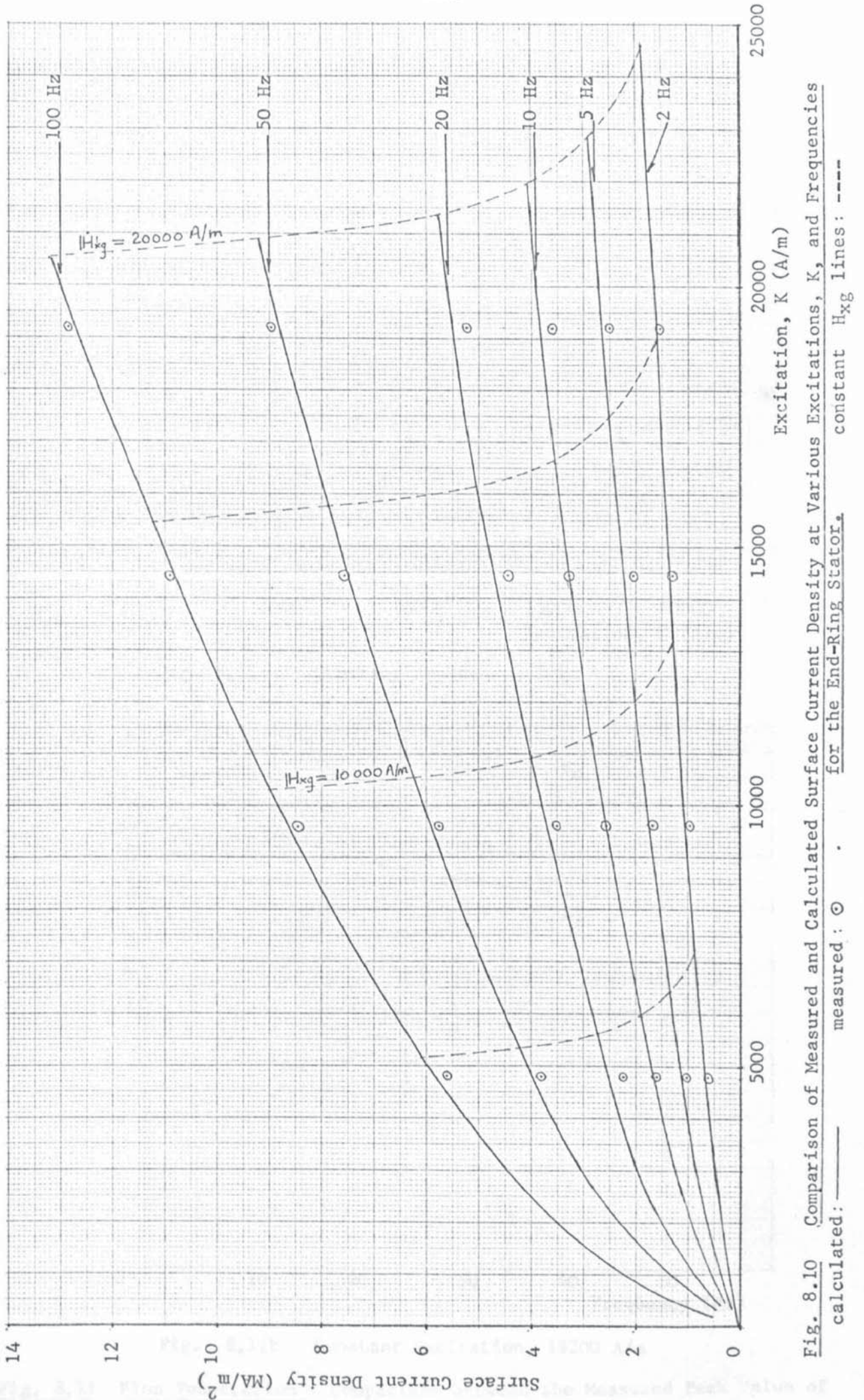
Fig. 8.10 Comparison of Measured and Calculated Surface Current Density at Various Excitations, K, and Frequencies for the End-Ring Stator.

measured : ⊙ .   calculated: ———   constant H_{xg} lines : –––
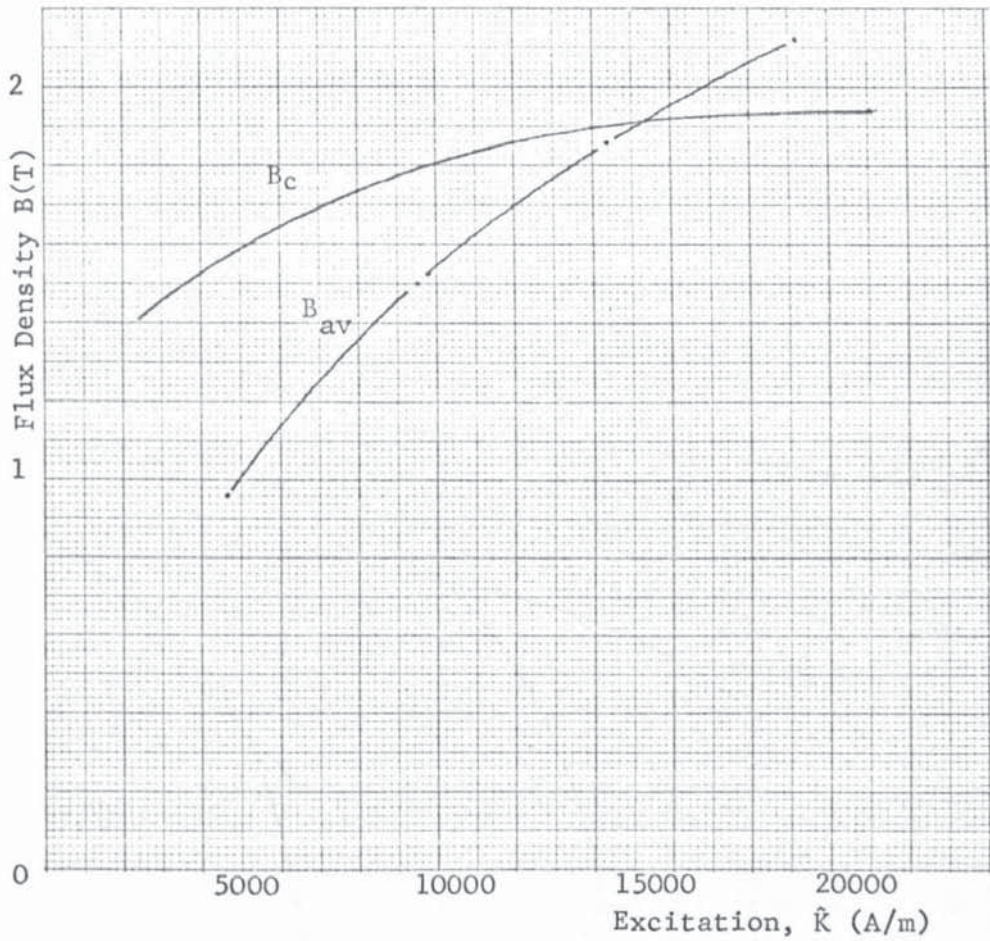
Fig. 8.11a   Constant Frequency, 2 Hz
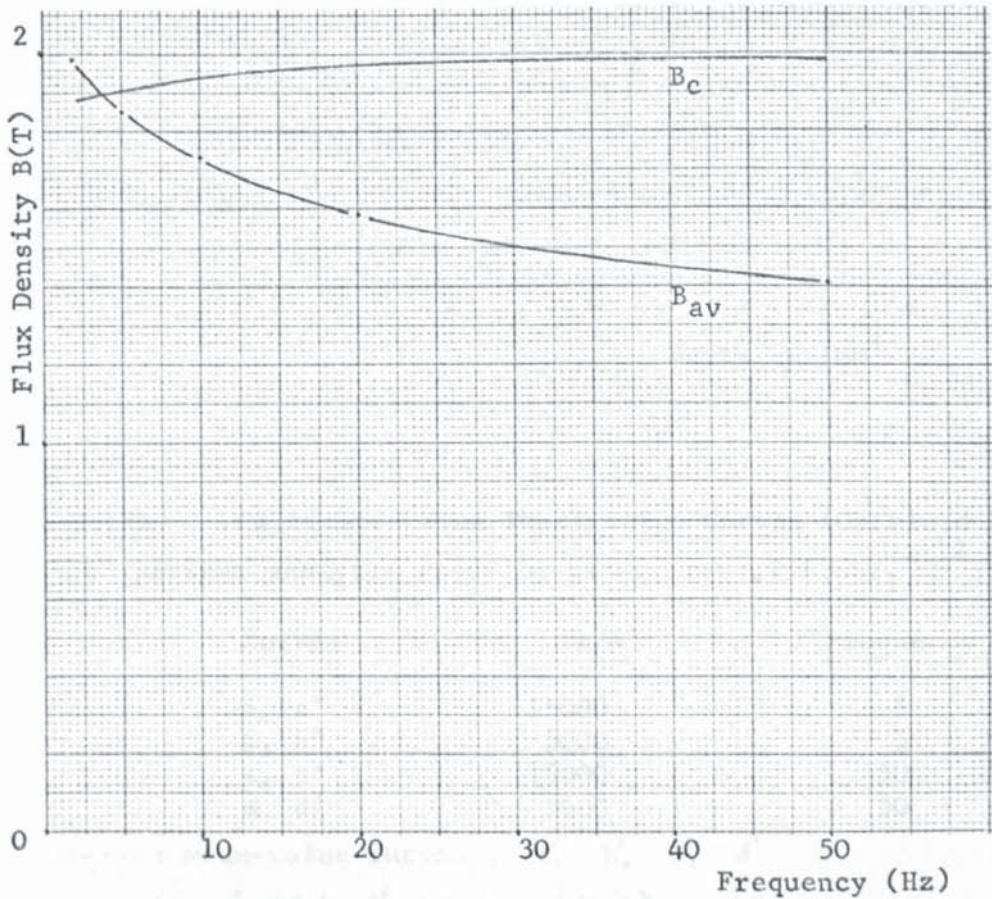
Fig. 8.11b   Constant Excitation, 19200 A/m

<u>Fig. 8.11</u> <u>Flux Penetration</u> : Comparison between the Measured Peak Value of
the Mean Flux Density, B_{av} , and the Calculated Value of Flux
Density, B_c , at the Surface of the End Ring Stator.
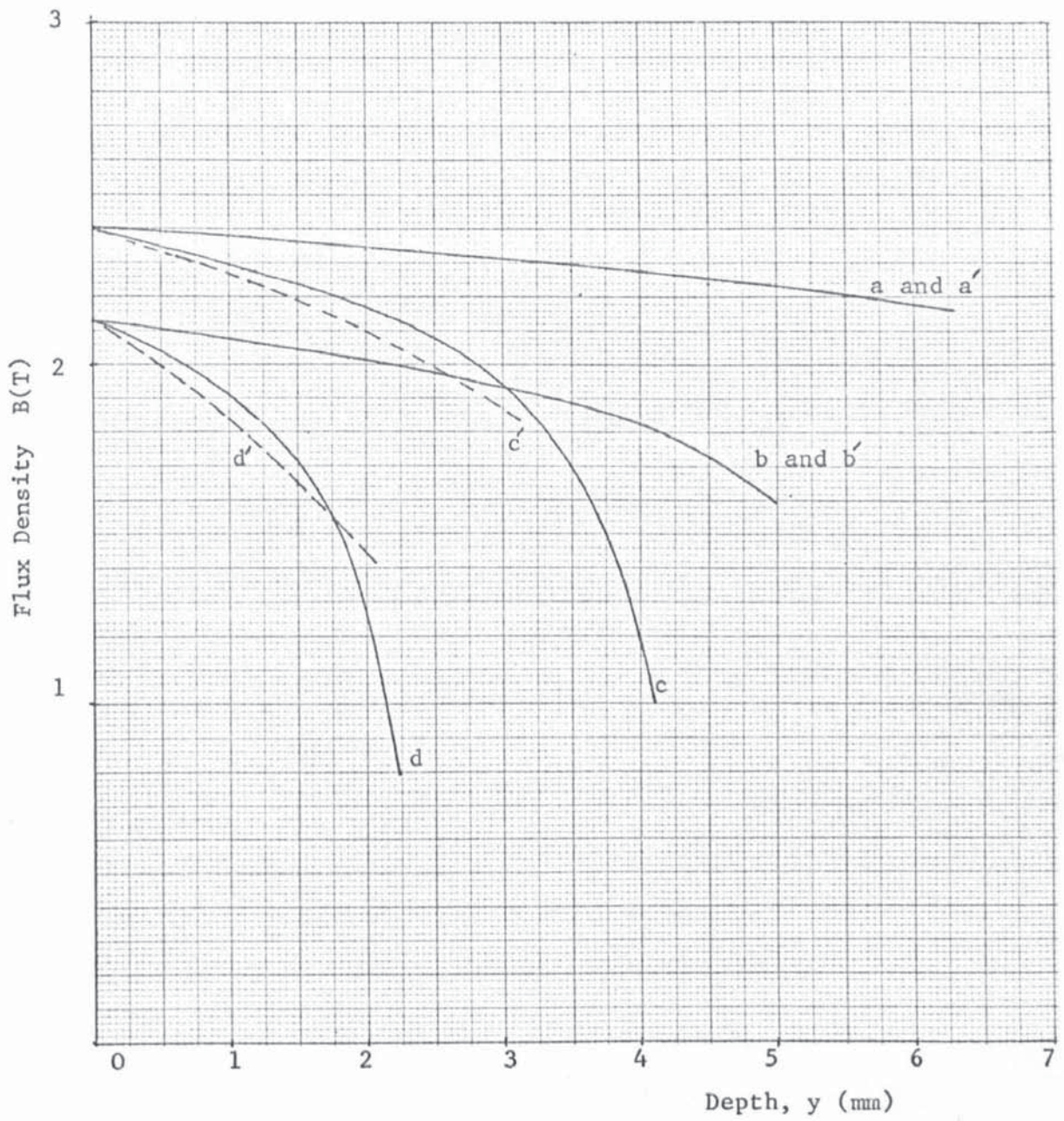
Fig. 8.12a   Calculated Flux Penetration Curves (Obtained by the present analytic solution using $B_1 = 1.25(.66H_1^{0.112})$

Curves	:	$\hat{H}_{-xg}$ (A/m)	:	Frequency (Hz)
a, a'		15000		5
b, b'		5000		5
c, c'		15000		50
d, d'		5000		50

---- : mean-value curves ; a', b', c', d'

(a, a' and b, b' are coincident)
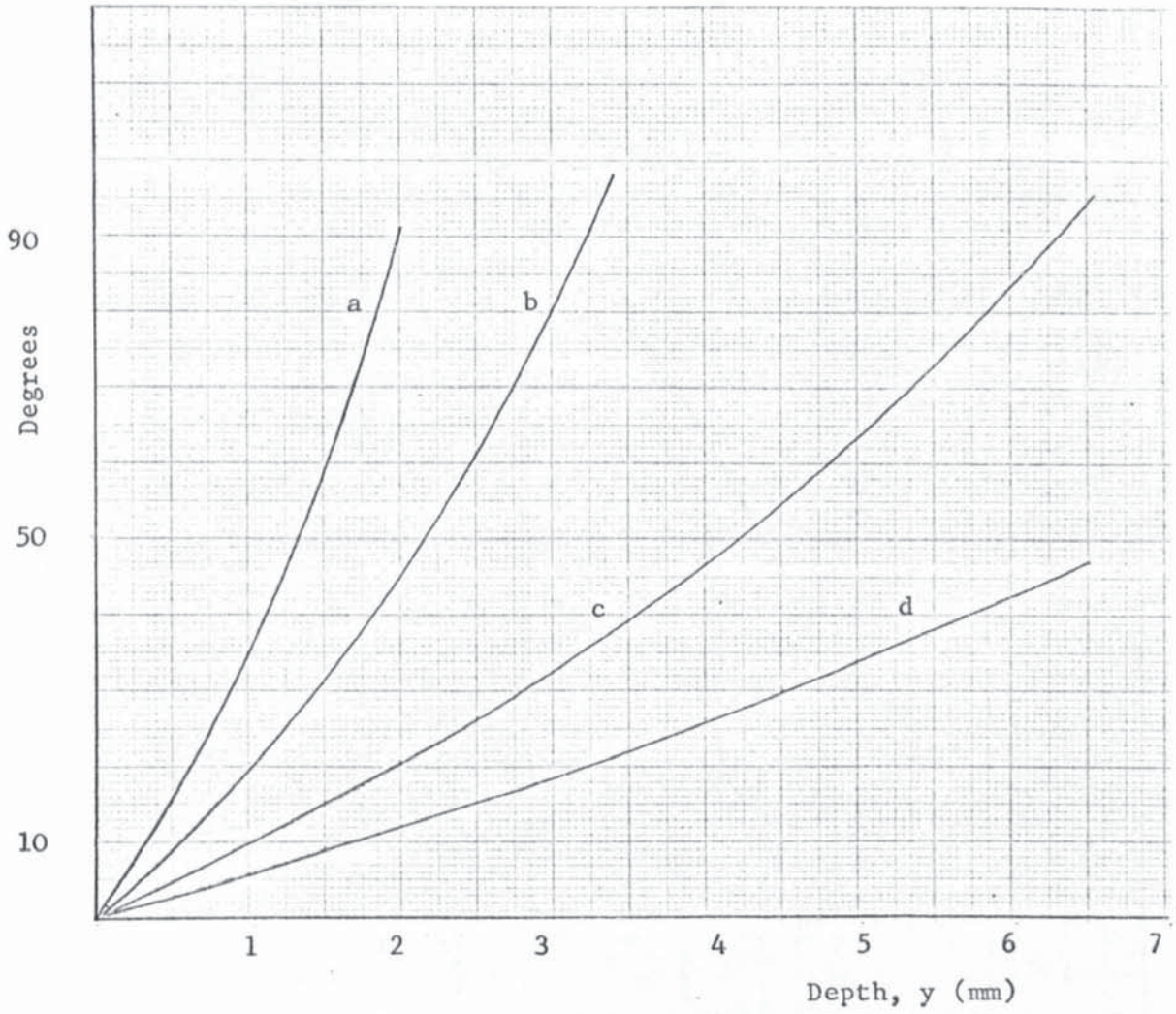
Fig. 8.12b   Calculated Change of Phase of Flux Density with Depth.

Curve	:	$\hat{H}_{xg}$ (A/m)	:	Frequency (Hz)
a		5000		50
b		15000		50
c		5000		5
d		15000		5
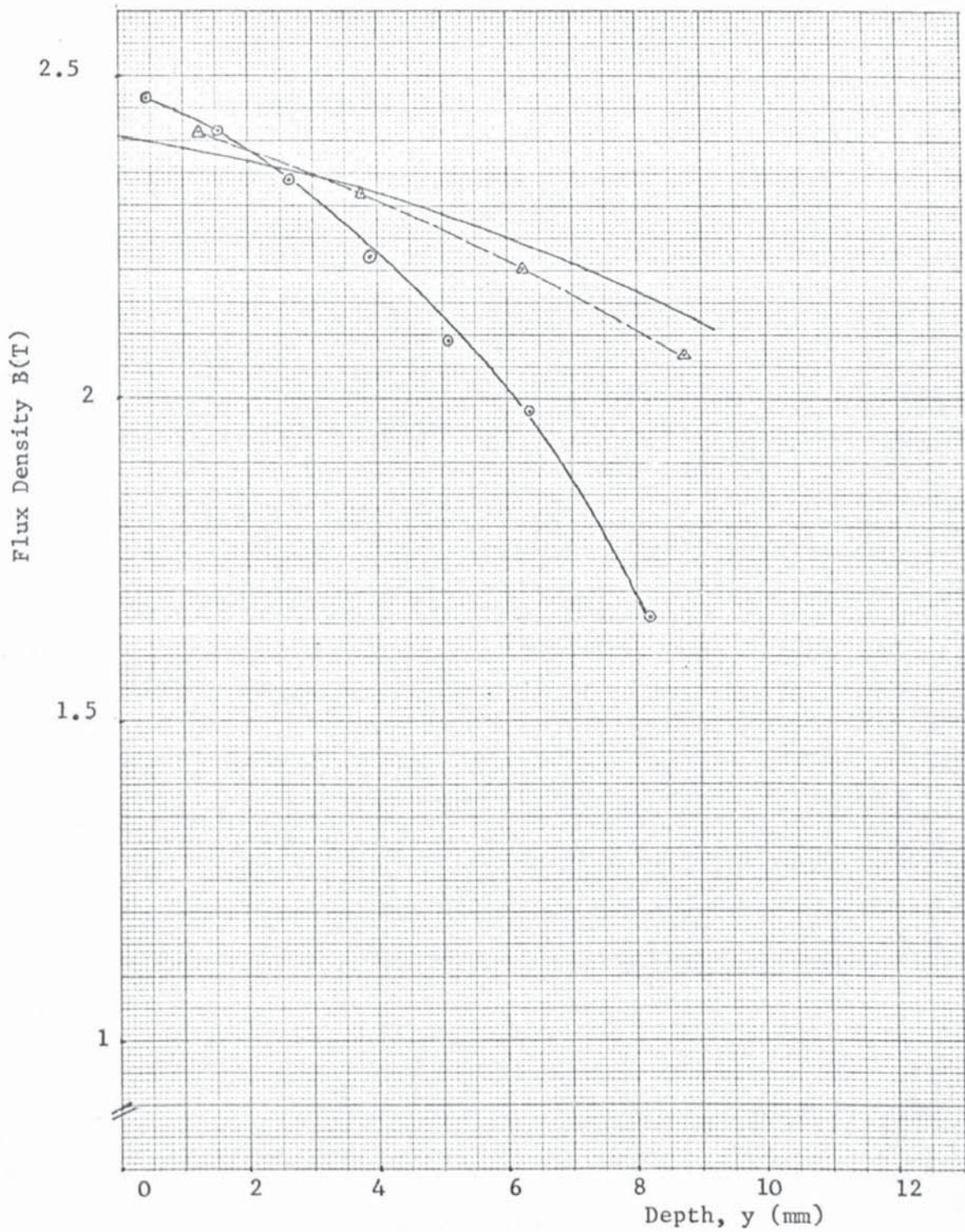
Fig. 8.13   Comparison of Experimental and Theoretical Flux
Penetration Curves.

Excitation : 19200 A/m ;   Frequency : 2 Hz

——————— present theory using $B_1 = 1.25 \ (0.66H_1^{0.112})$

— ⊙ — measured in the plate   } fundamental components

-- △ -- measured in the split surface
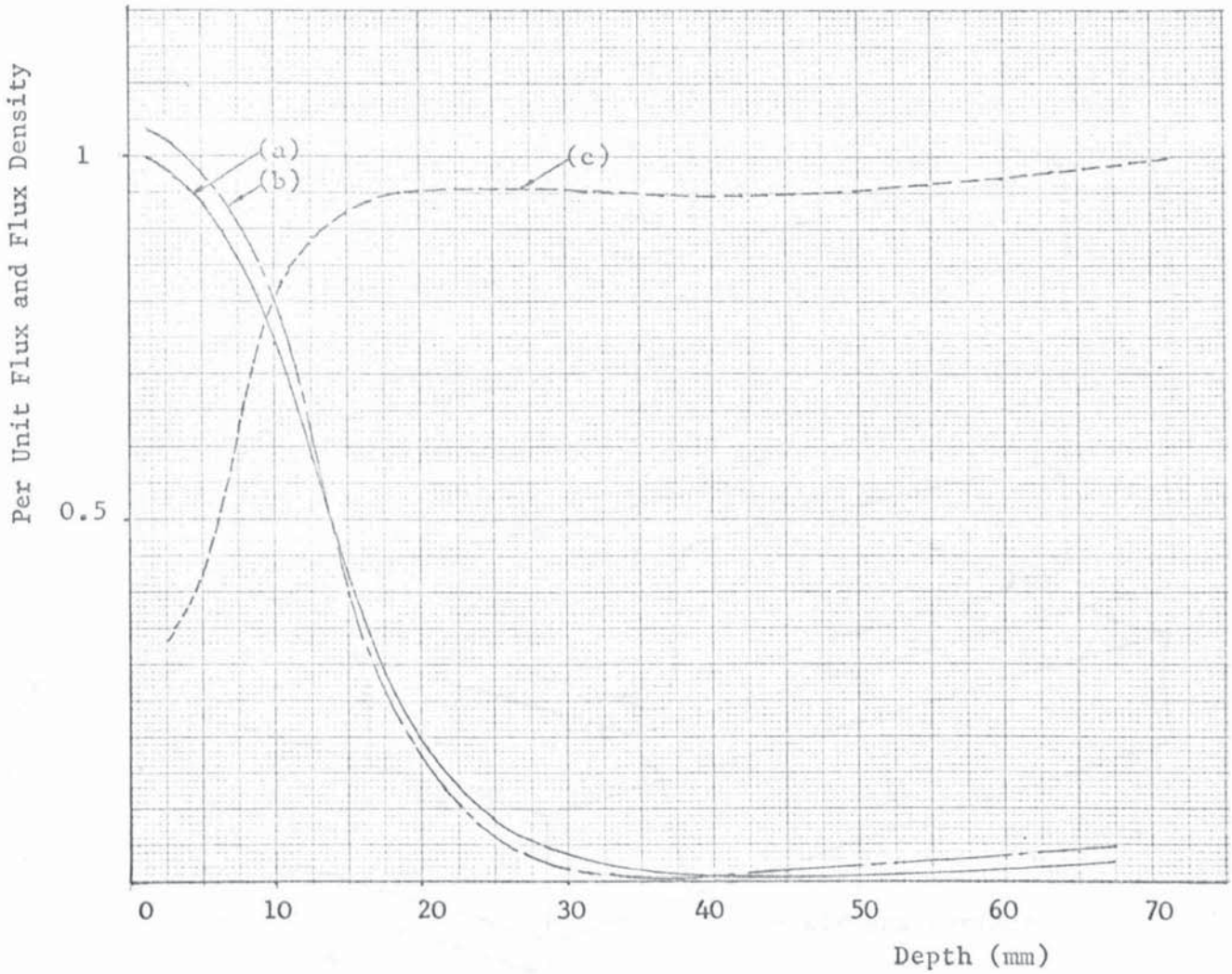
Fig. 8.14   Flux Penetration Curves obtained at the Split Surface,
             Showing the Effects of Finite Depth and the Removal of
             the Copper Bridging Pieces.
             Excitation : 14420 A/m ; Frequency : 2 Hz

Curve (a)   : with bridging pieces   ⎫ P.u. to a base of
Curve (b)   : without bridging pieces ⎬ flux density at the
                                        ⎭ surface (curve (a)).
Curve (c)   : summation of flux across the split surface, p.u.
                to a base of the total peripheral flux.
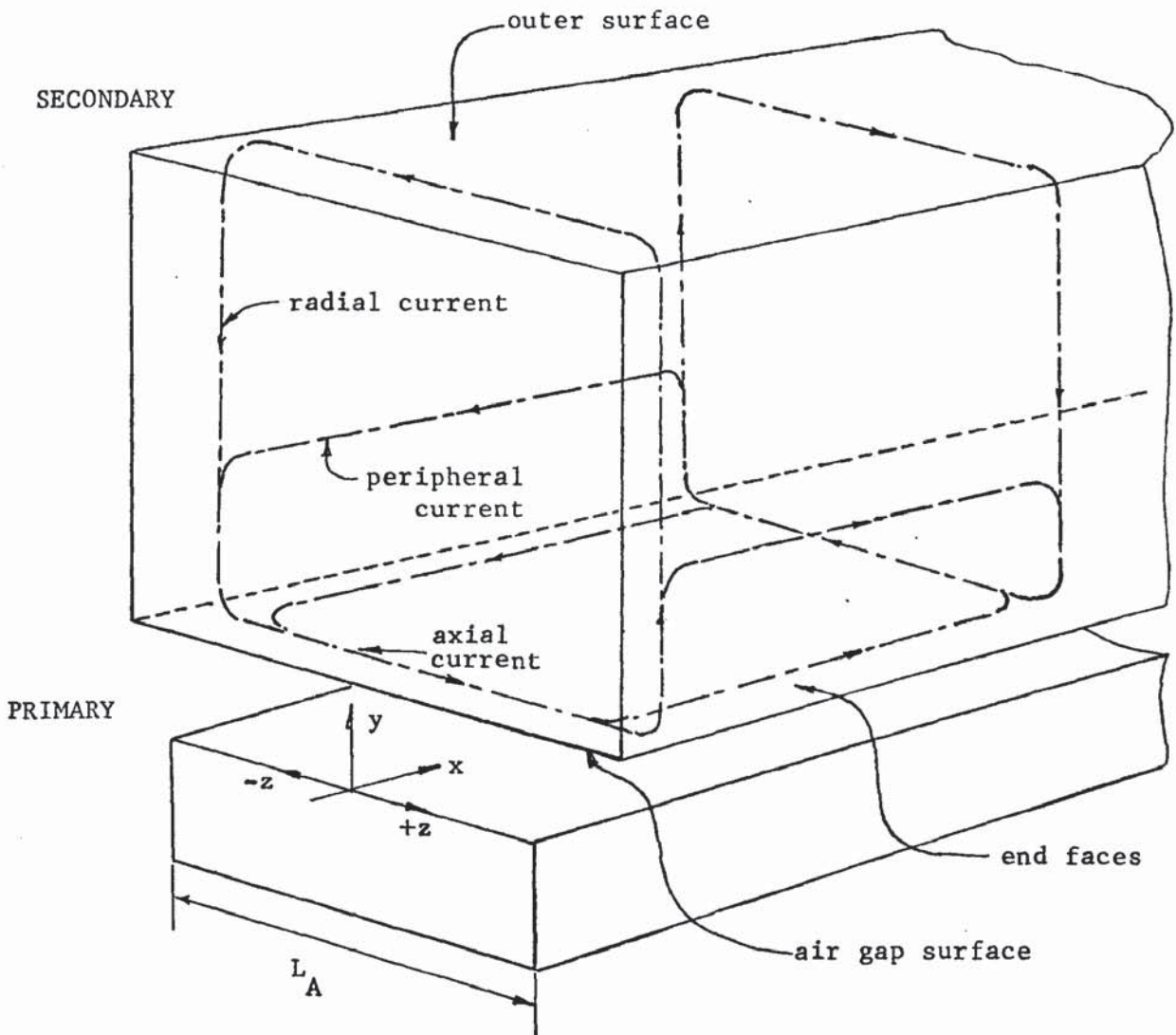
Fig. 9.1 Idealised Eddy-Current Distribution in a Developed Model of the Experimental Machine.
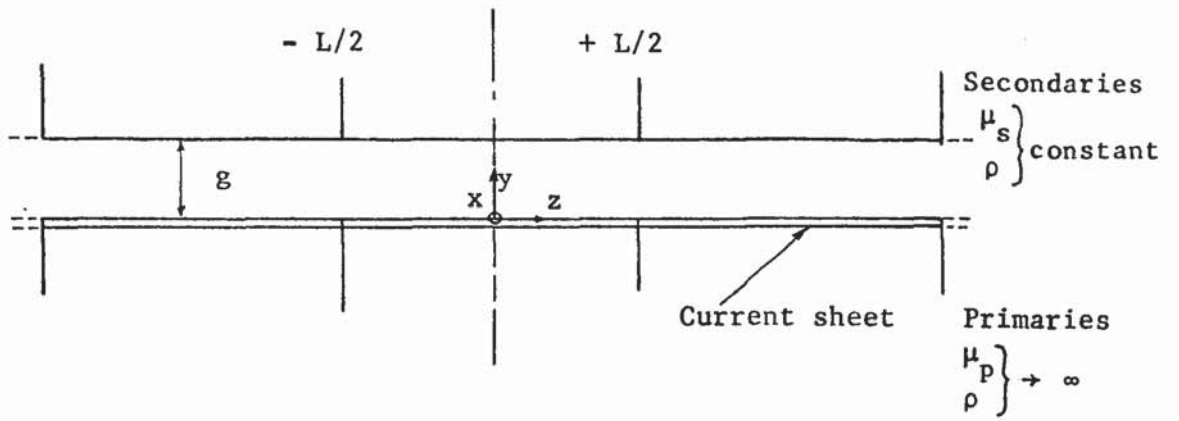
Fig. 9.2   Model Proposed by Wood and Concordia for
Three-dimensional Analysis
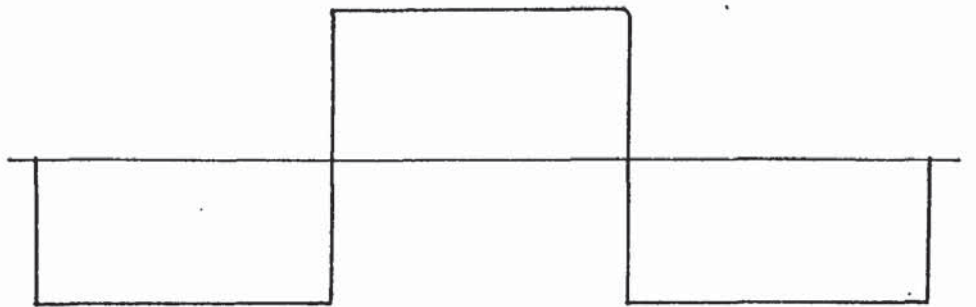
(a) Axial component
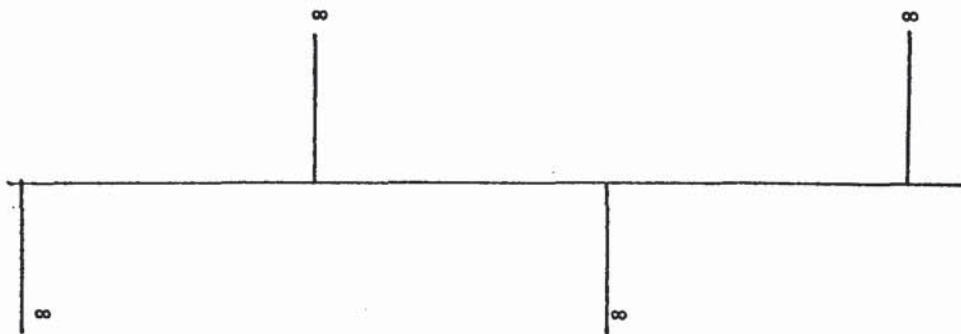
(b) Peripheral component

Fig. 9.3   Primary Current Sheet Proposed by Wood and Concordia

Type (a)

$H_z = 0$, $h = 1$

——— J_z, H_x, H_y

——— J_x, J_y

Type (b)

$J_z = 0$, $h = 2$

——— H_z, J_x, J_y

——— H_x, H_y

Type (c)

$H_z = J_z = 0$

——— H_y, H_x

——— J_y, J_x
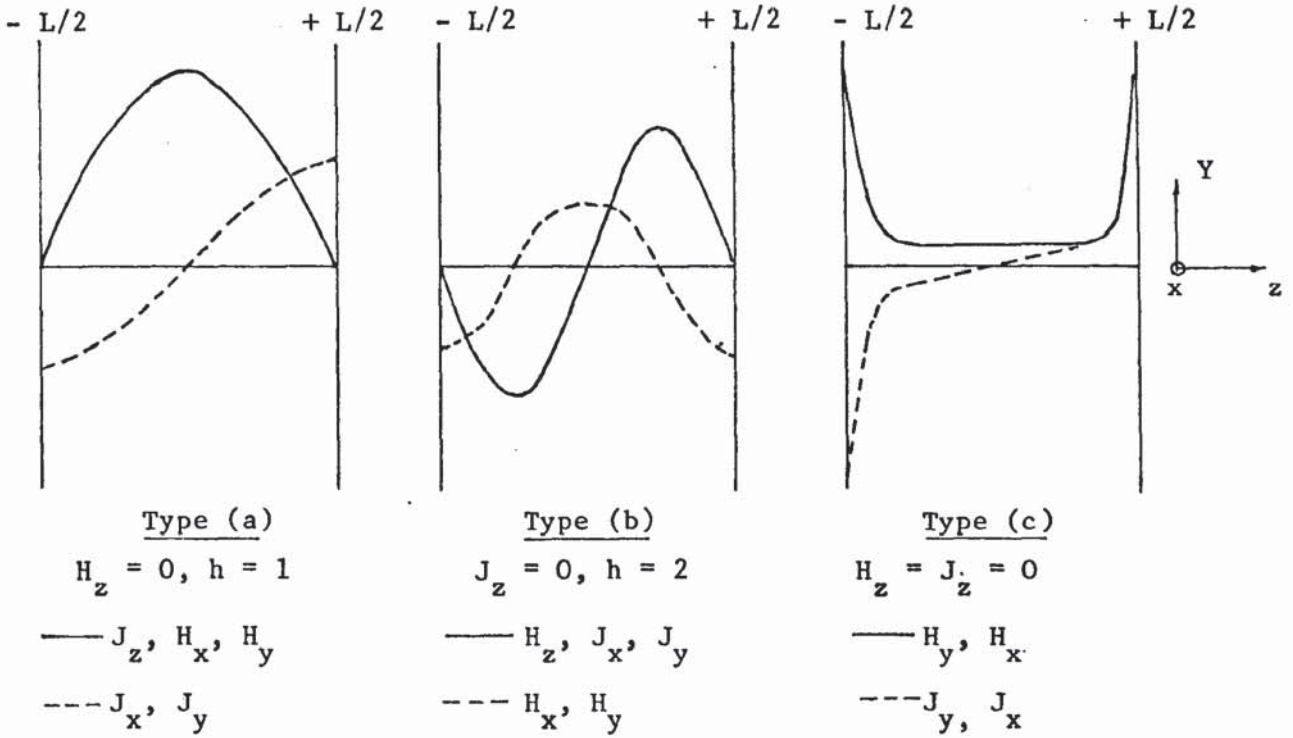
Fig. 9.4   Illustrating the Solution of Bondi and Mukherji[58]

(a)

(b)
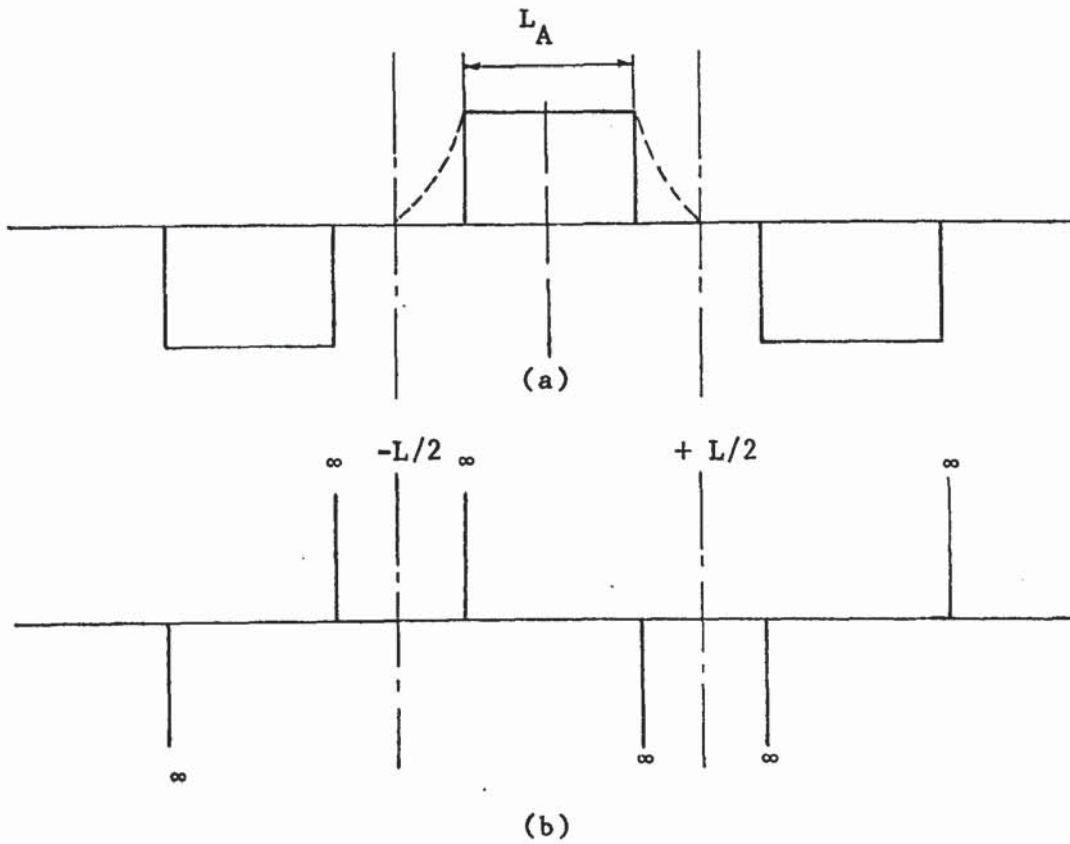
Fig. 9.5   Primary Current Sheet used in Present Analysis

(a)   axial component,
        ----- waveform proposed by Preston and Reece[57]
        L_A : active length.

(a)

L/2   Secondary

L_s

L_A Primary

(b)

L   Developed
                                                       Secondary
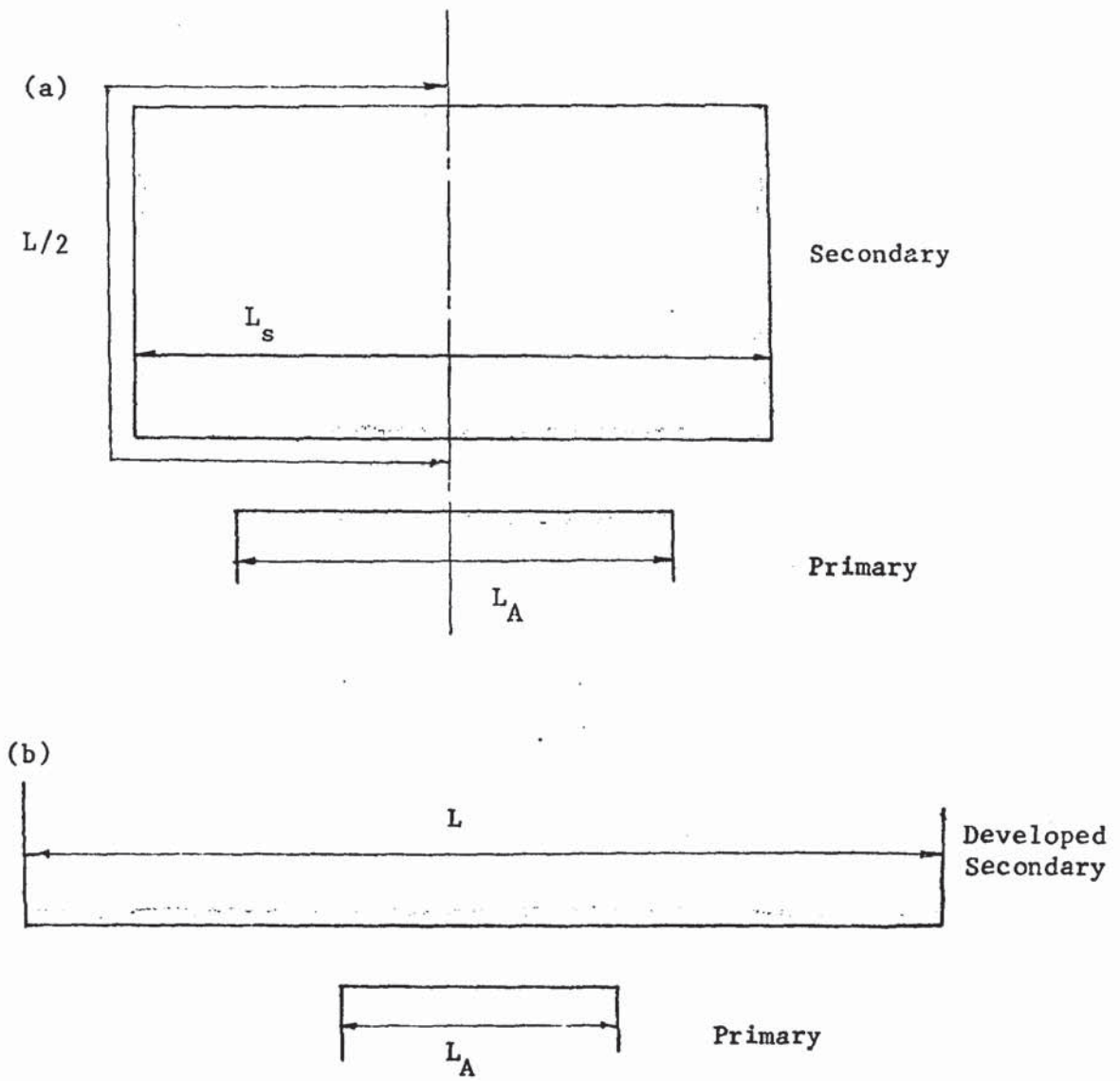
L_A Primary

FIG. 9.6   Developed Length of Secondary, L
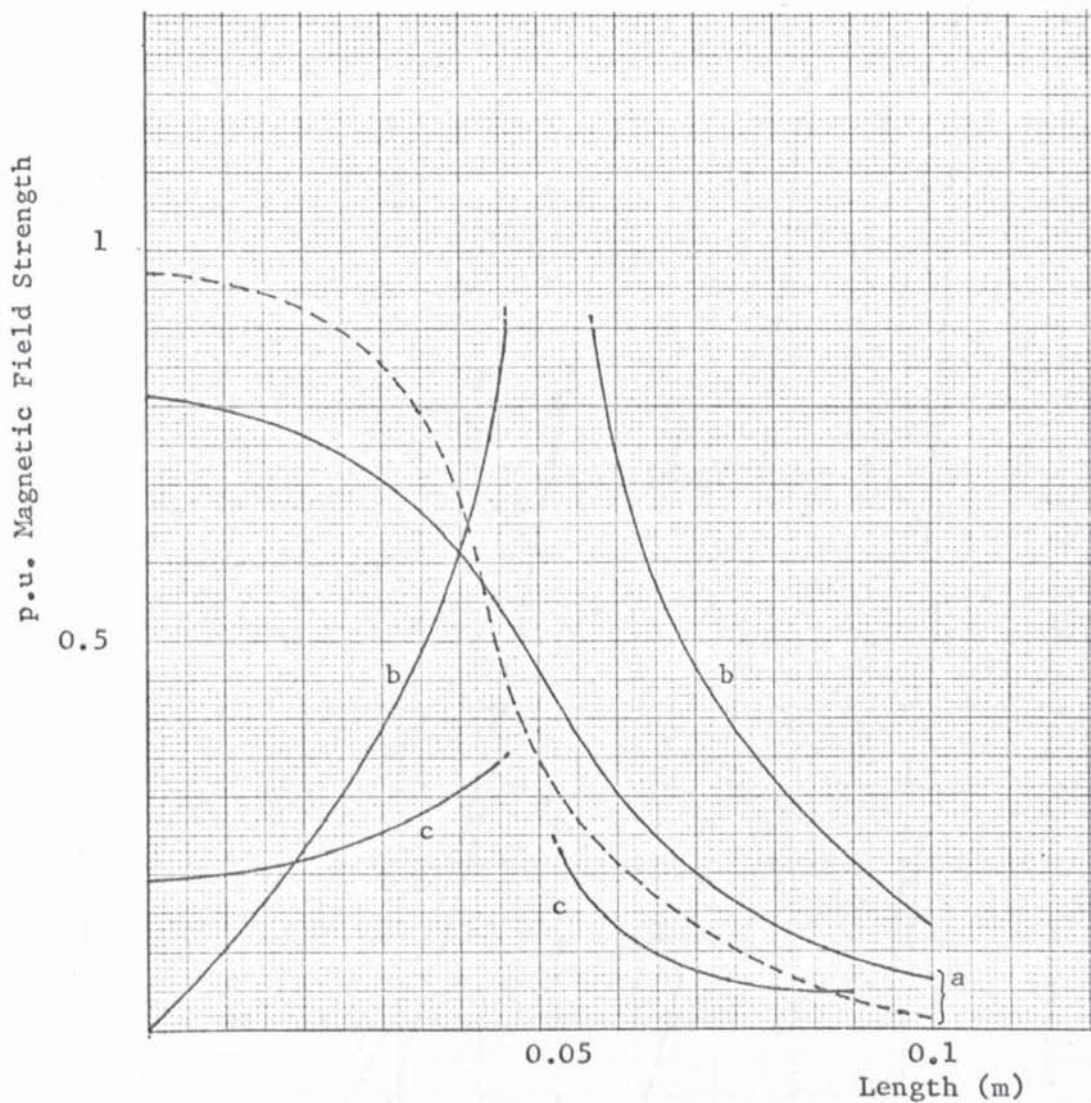
a. $|\dot{H}_{xgh}|$ ⎫
b. $|\dot{H}_{zgh}|$ ⎬ Expressed as p.u. of primary excitation $\hat{K}$ (A/m)
c. $|\dot{H}_{ygh}|$ ⎭

——— 5 Hz
----- 50 Hz

Fig. 9.7   Distribution, with Axial Length, of the Components of
the Magnetic Field Strength at the Surface of the
Secondary of the Experimental Machine, Obtained with
the Present Linear Three-dimensional Analysis.
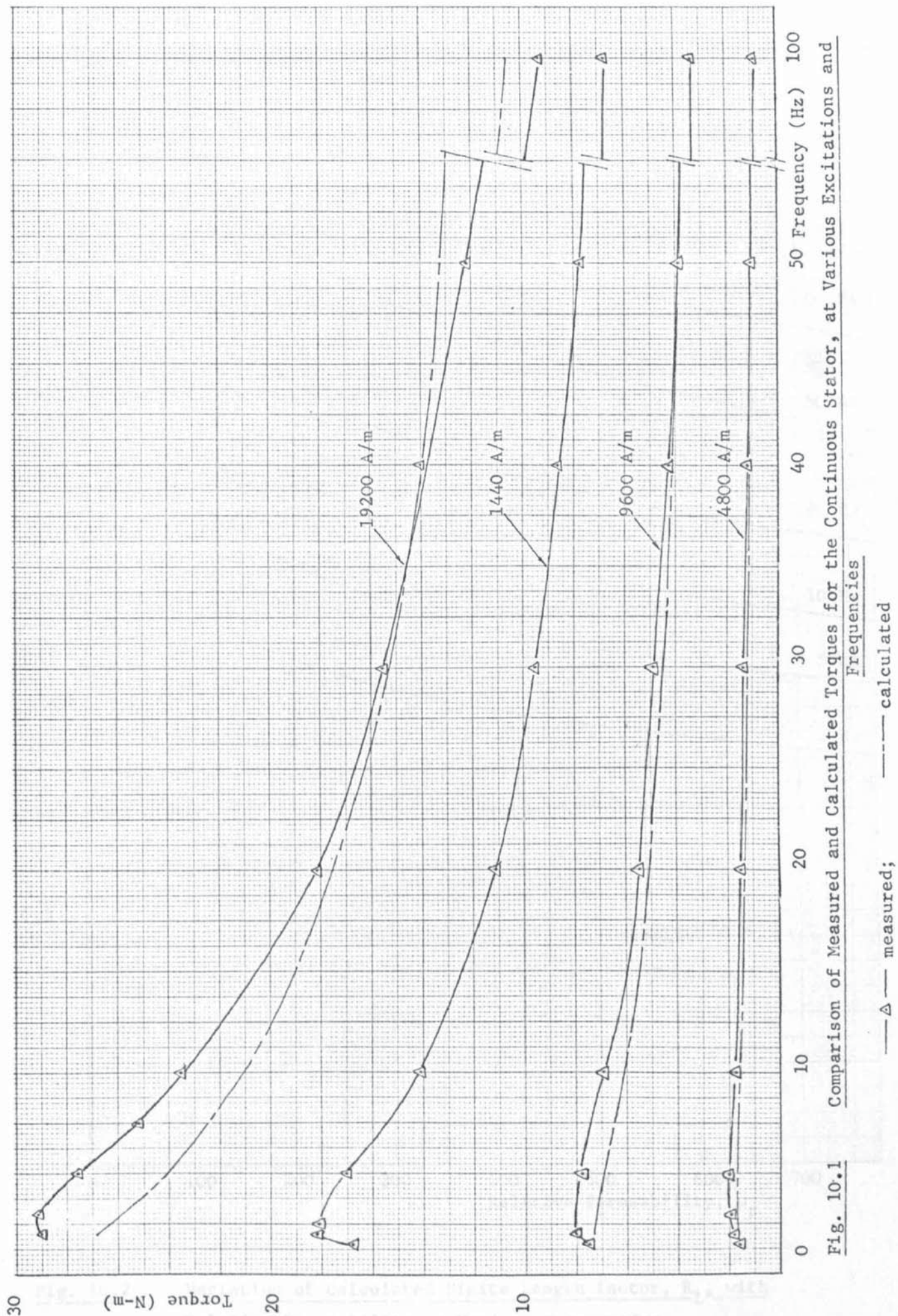
Fig. 10.1 Comparison of Measured and Calculated Torques for the Continuous Stator, at Various Excitations and Frequencies

———— measured; ———— calculated
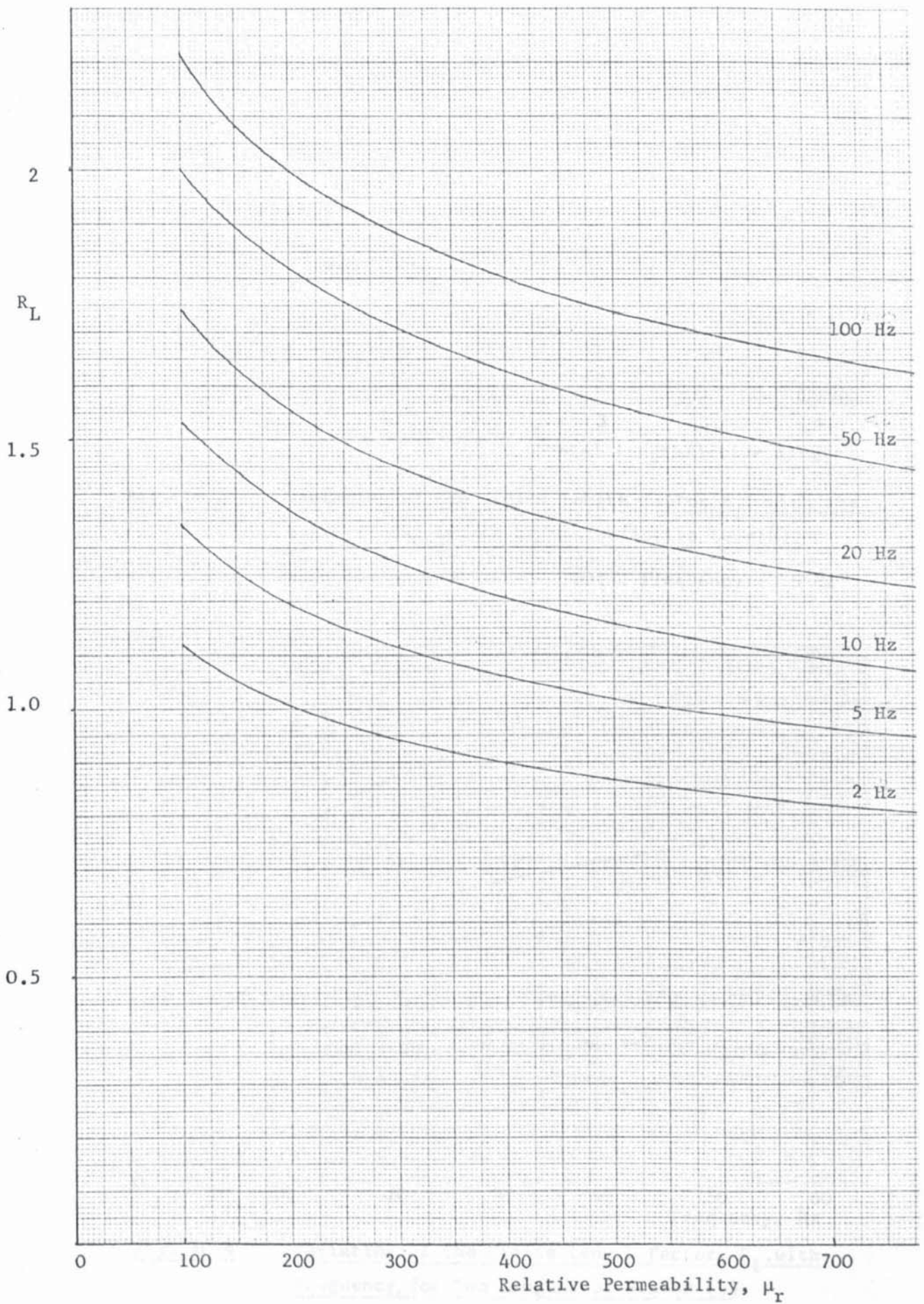
Fig. 10.2   Variation of Calculated Finite Length factor, R_L, with
Relative Permeability at Various Frequencies.
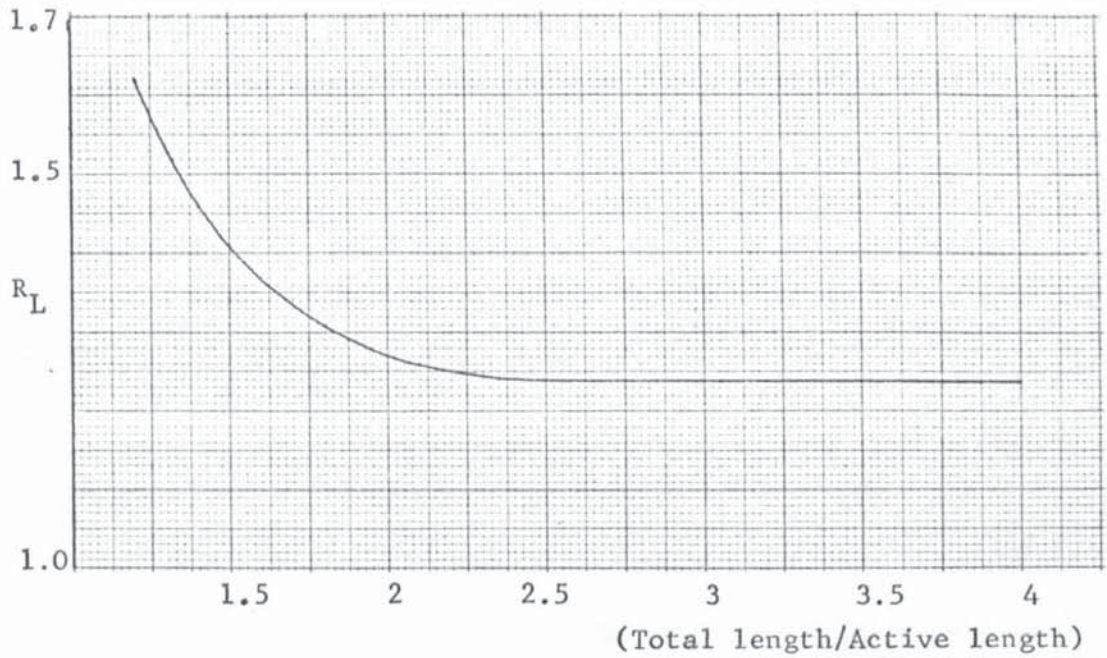
Fig. 10.3   Variation of the Finite Length factor R_L, with the
Ratio (Total Length of Stator/Active Length).

Relative permeability: 180;   Frequency : 5 Hz
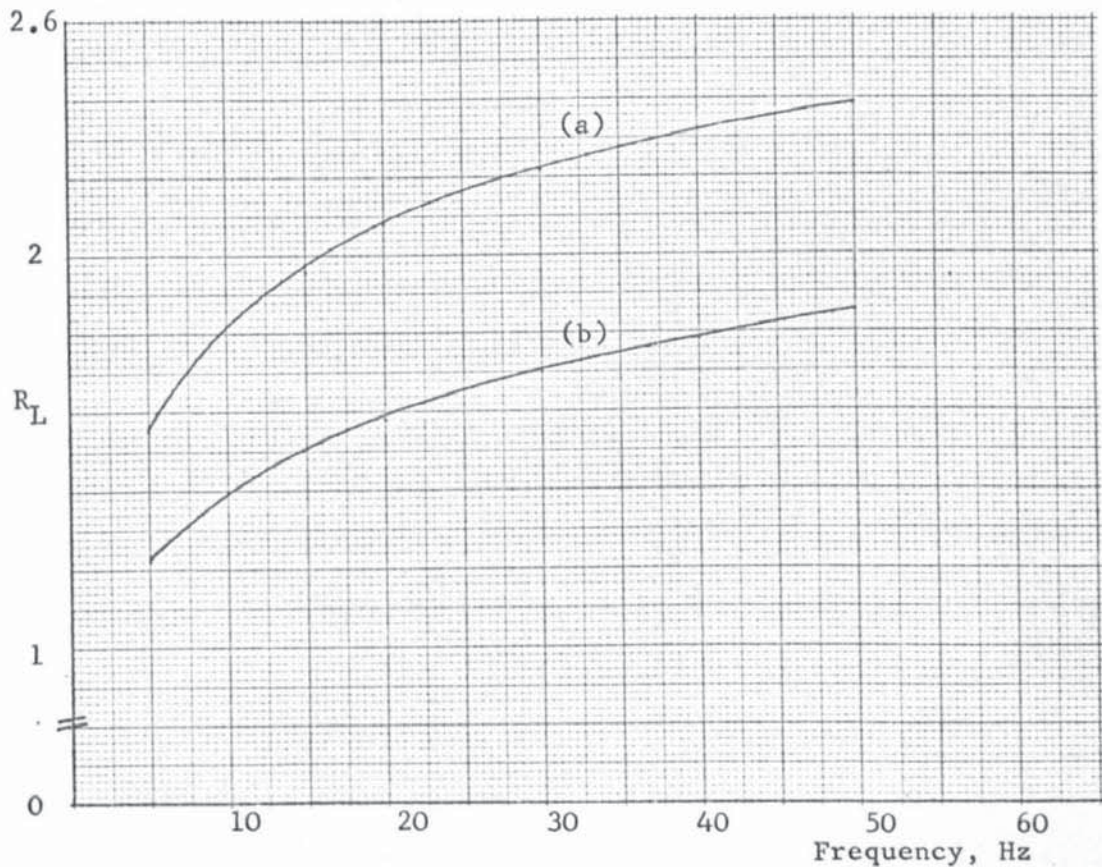
Fig. 10.4   Variation of the Finite Length Factor, R_L, with
Frequency, for Two Lengths of Stator (L)

Curve (a) : L = 0.133m;   Curve (b) : L = 0.406m
Active Length = 0.1048m in both cases.
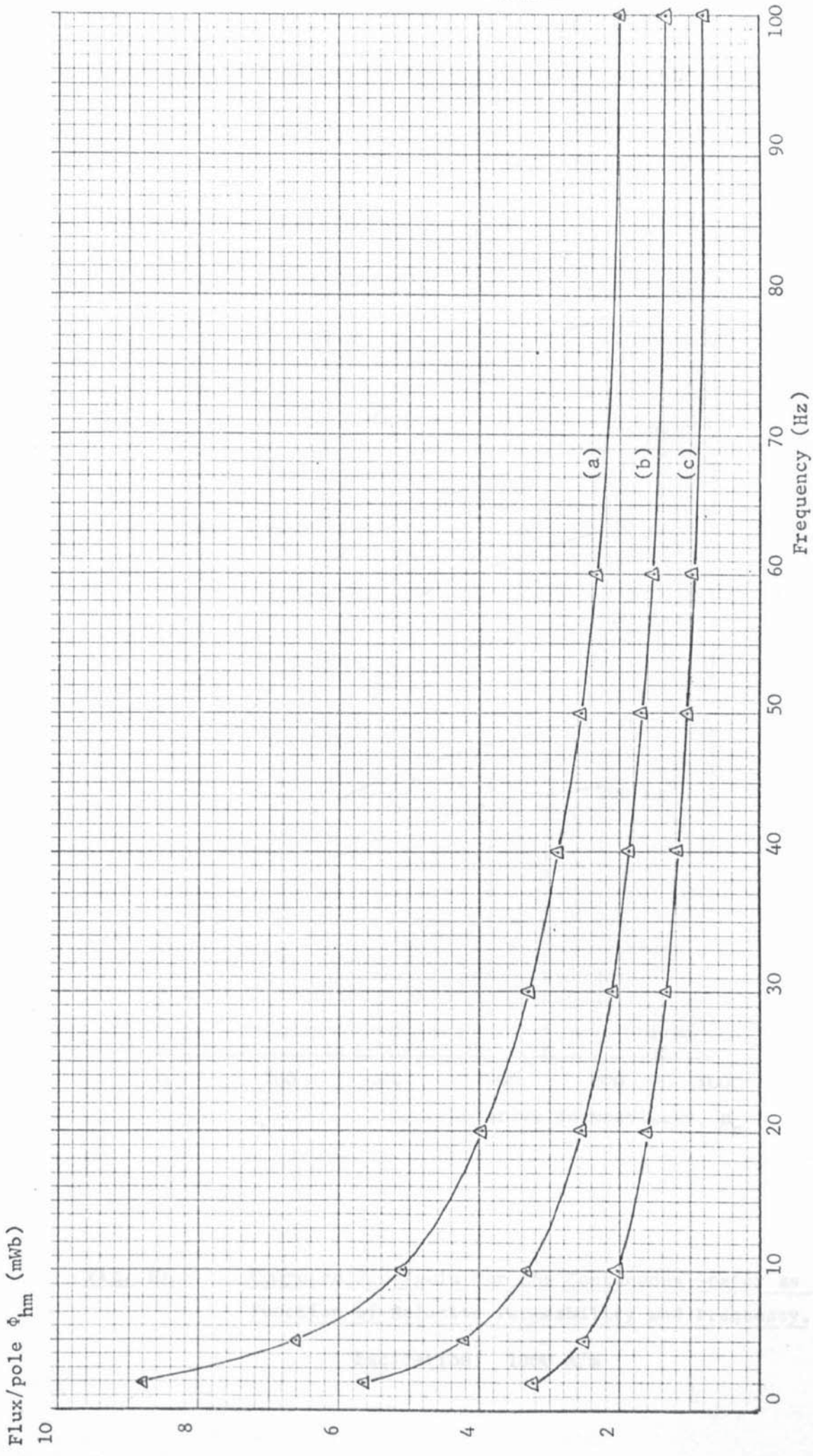
Fig. 10.5   Variation of Measured Flux/Pole for the Continuous Stator

Curve	:	Primary Excitation (A/m)
(a)		19200
(b)		9600
(c)		4800
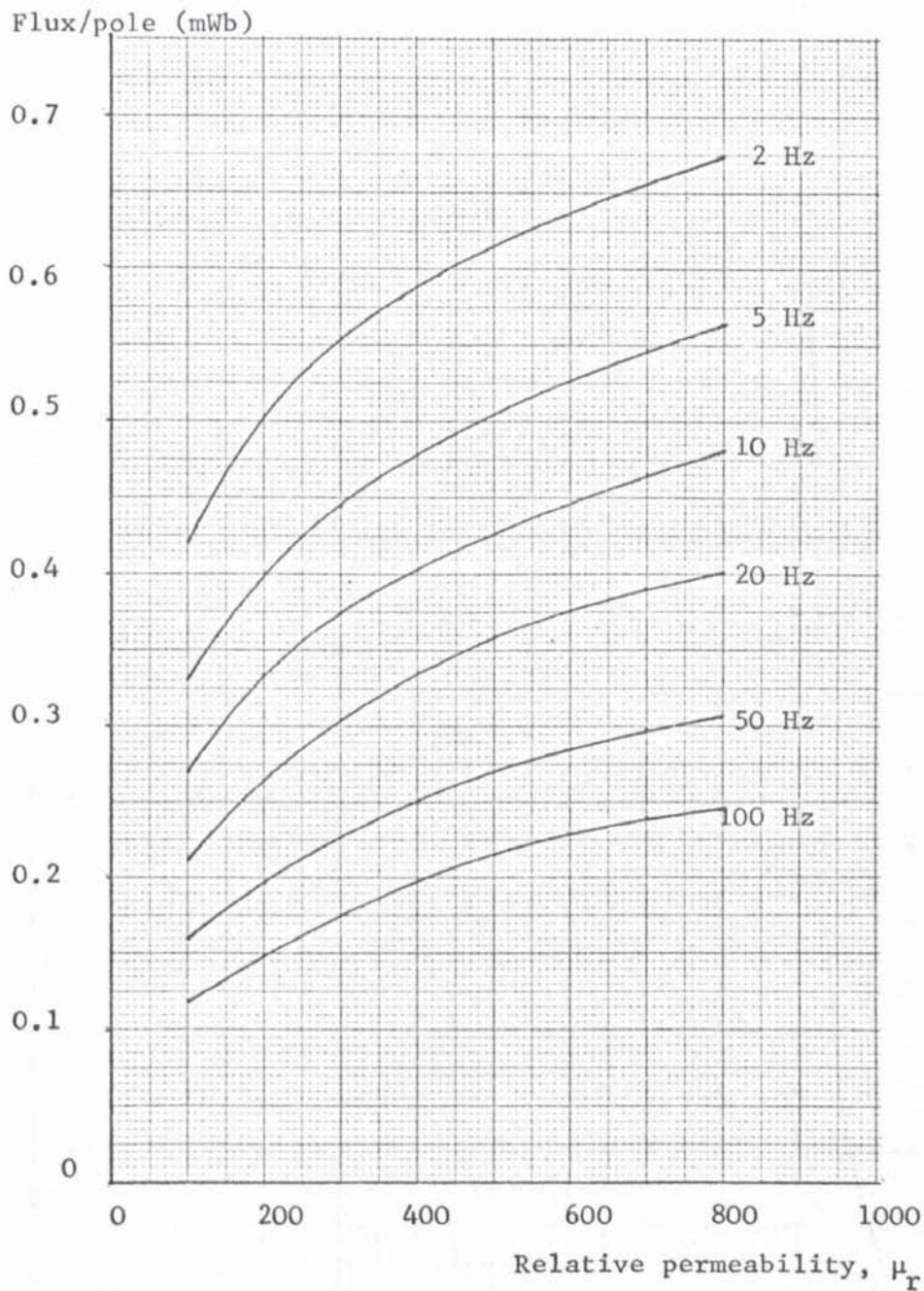
Fig. 10.6   Computed Flux/pole for the Continuous Stator as a
             Function of Relative Permeability and Frequency.

             Excitation: 1000 A/m

<u>Fig. 10.7</u> The Distribution of Air-Gap Flux with Axial Length - a
Comparison between Measurements taken by a Hall Probe and
Search Coils (Fig. 7.7).   Frequency, 50 Hz.

Values are given as per unit of the values at the axial centre of the stator.
Excitation : 4800 A/m   Excitation : 9600 A/m
△ : Search coil; --- Hall Probe   □ : Search coil; —— Hall Probe
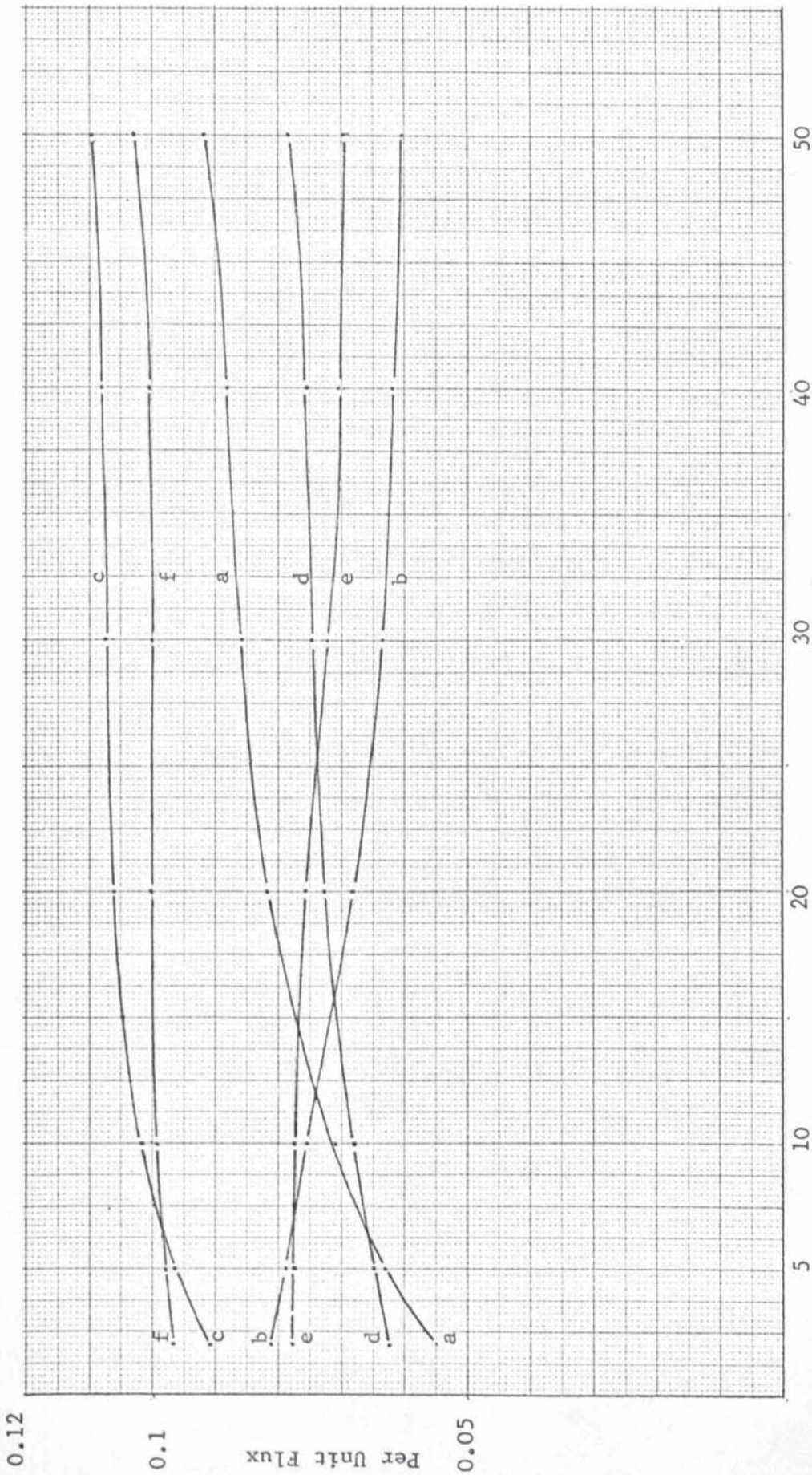
Fig. 10.8   Variation of the (Flux/pole)/cm with Frequency at Two Values of Excitation.

Coil 6 (5 cm from centre of stator) ; $\begin{cases} \text{curve a : } 19200 \text{ A/m} \\ \text{curve d : } 4800 \text{ A/m} \end{cases}$

Coil 1 (centre of stator) : $\begin{cases} \text{curve b : } 19200 \text{ A/m} \\ \text{curve e : } 4800 \text{ A/m} \end{cases}$

Coil 5 (4 cm from centre of stator); $\begin{cases} \text{curve c : } 19200 \text{ A/m} \\ \text{curve f : } 4800 \text{ A/m} \end{cases}$

Coil numbers refer to Fig. 7.7

1 p.u. $= \bar{\Phi}_{hm}$
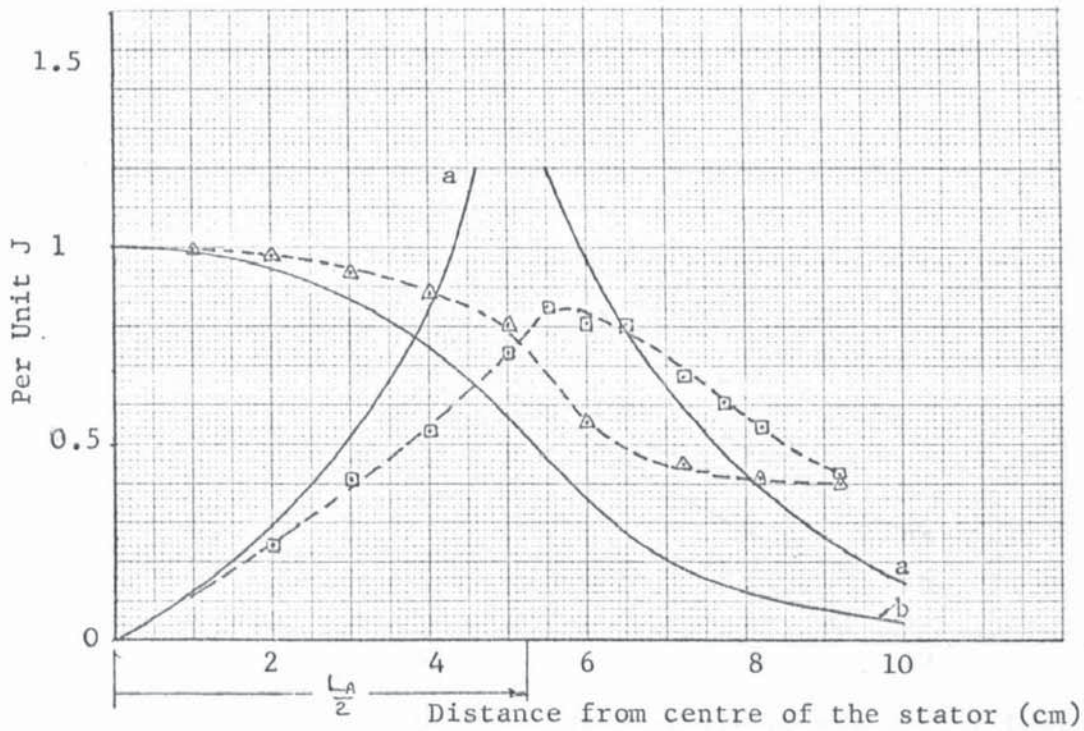
(a) Excitation : 4800 A/m;   Frequency : 50 Hz
    1 p.u. = 4.14 MA/m^2
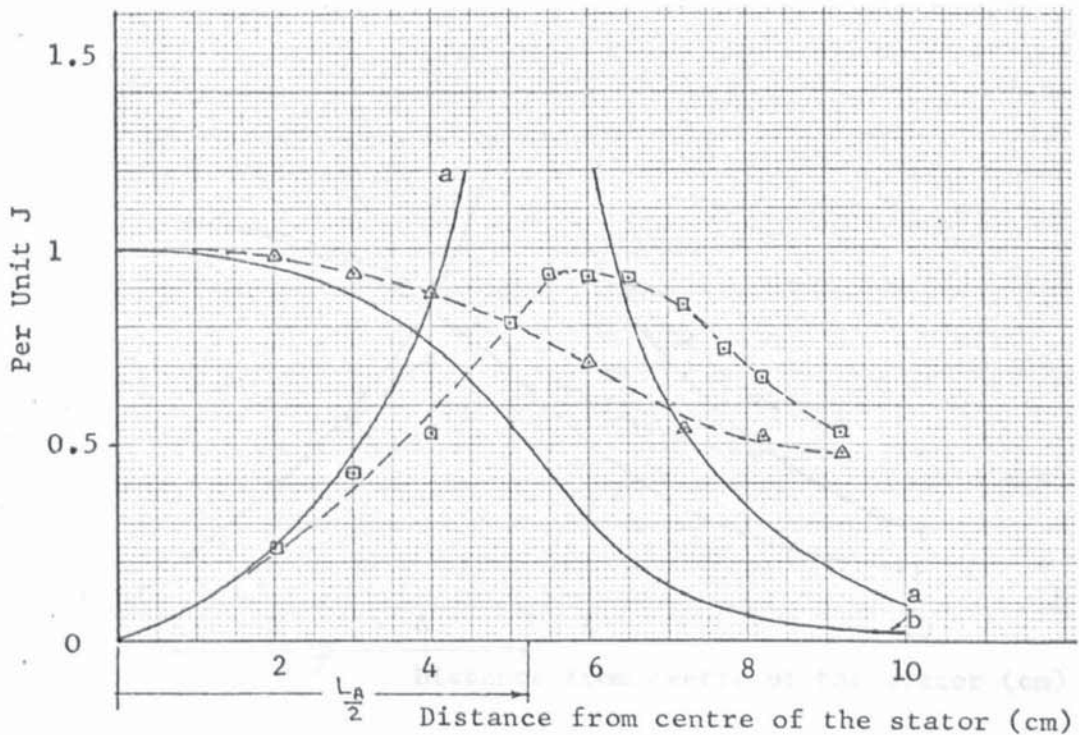
(b) Excitation : 19200 A/m;   Frequency : 50 Hz
    1 p.u. = 9.9 MA/m^2

Fig. 10.9   Surface Current-Density Distribution - a Comparison
            of Measured and Calculated Values.

Calculated: $\begin{cases} \text{Curves (a) }, |J'_{xhg}| \\ \text{Curves (b) }, |J_{zhg}| \end{cases}$; Measured: $\begin{cases} -\square- J_{xhl} \\ -\triangle- J_{zhl} \end{cases}$
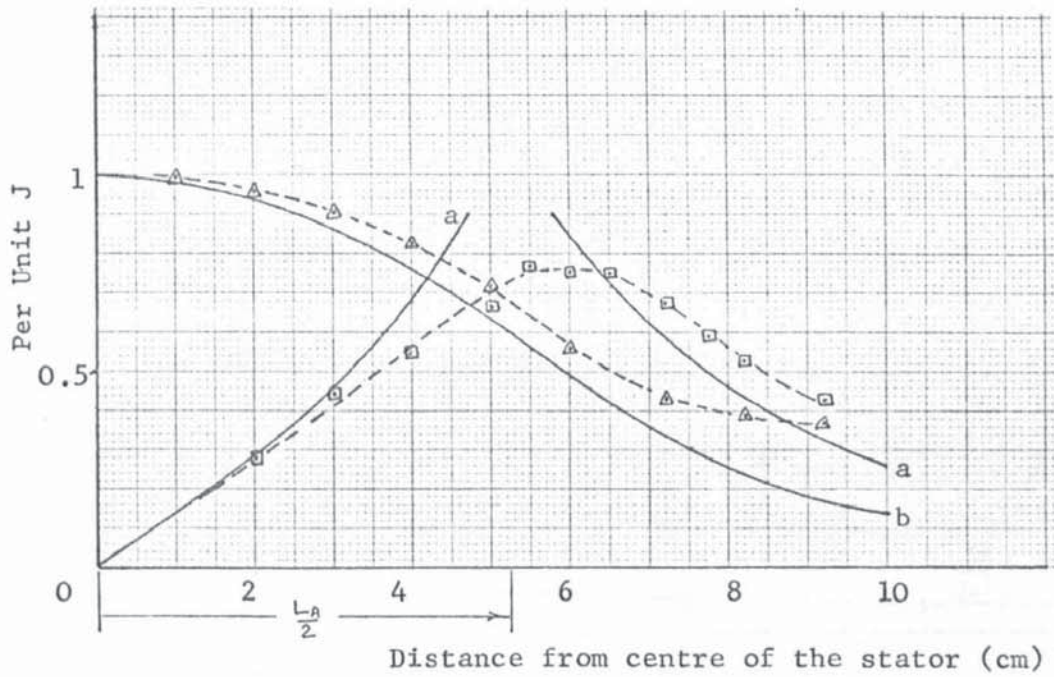
(c) Excitation : 4800 A/m;   Frequency : 5 Hz
   1 p.u. = 0.99 MA/m^2
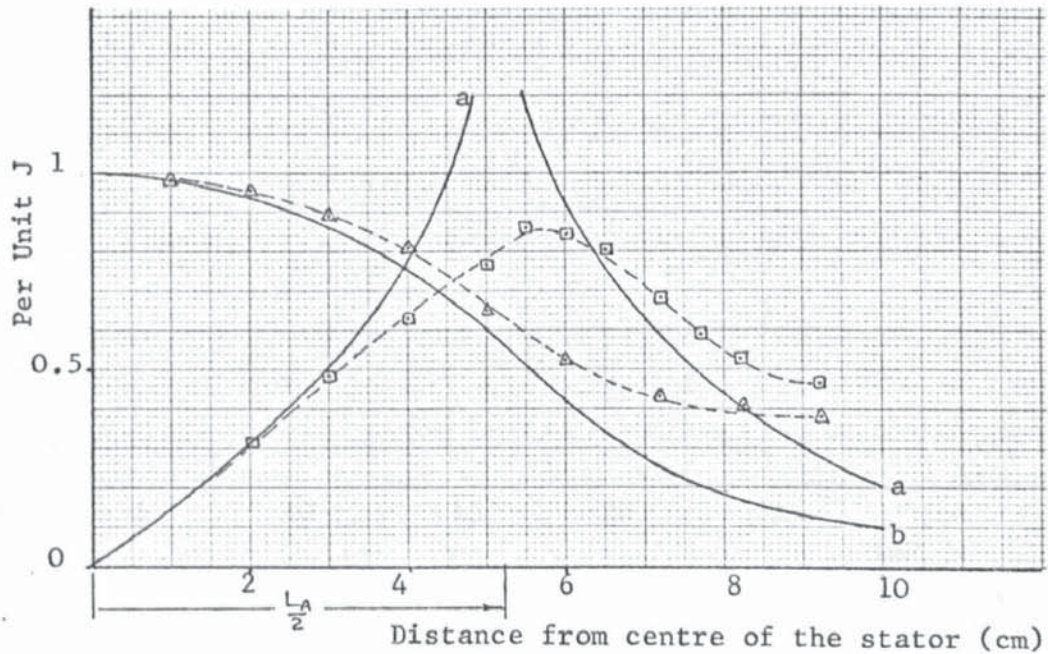
(d) Excitation : 19200 A/m;   Frequency : 5 Hz
   1 p.u. = 2.65 MA/m^2

Fig. 10.9   Surface Current Density Distribution - a comparison of Measured and Calculated Values.

Calculated: $\begin{cases} \text{Curves (a),} & |J_{xhg}| \\ \text{Curves (b),} & |J_{zhg}| \end{cases}$;   Measured: $\begin{cases} \text{---}\square\text{---,} & J_{xhl} \\ \text{---}\triangle\text{---,} & J_{zhl} \end{cases}$
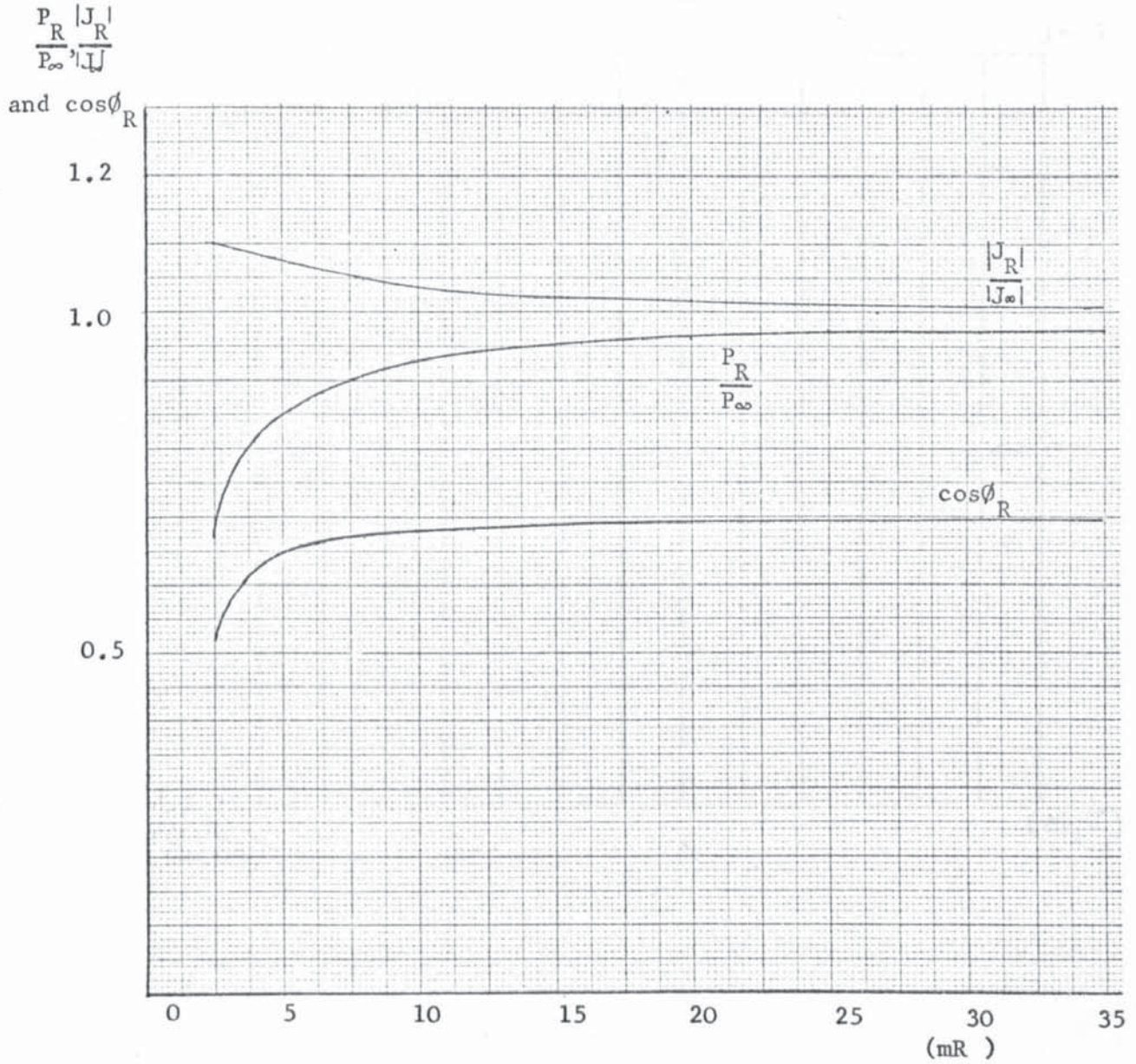
Fig. A2.2   Variation of $\frac{P_R}{P_\infty}$, $\frac{J_R}{J_\infty}$ and $\cos\phi_R$ with (mR_a) for a Round

Ferromagnetic Bar.

$$m = \sqrt{\frac{\omega\mu_o\mu_r}{\rho}}$$
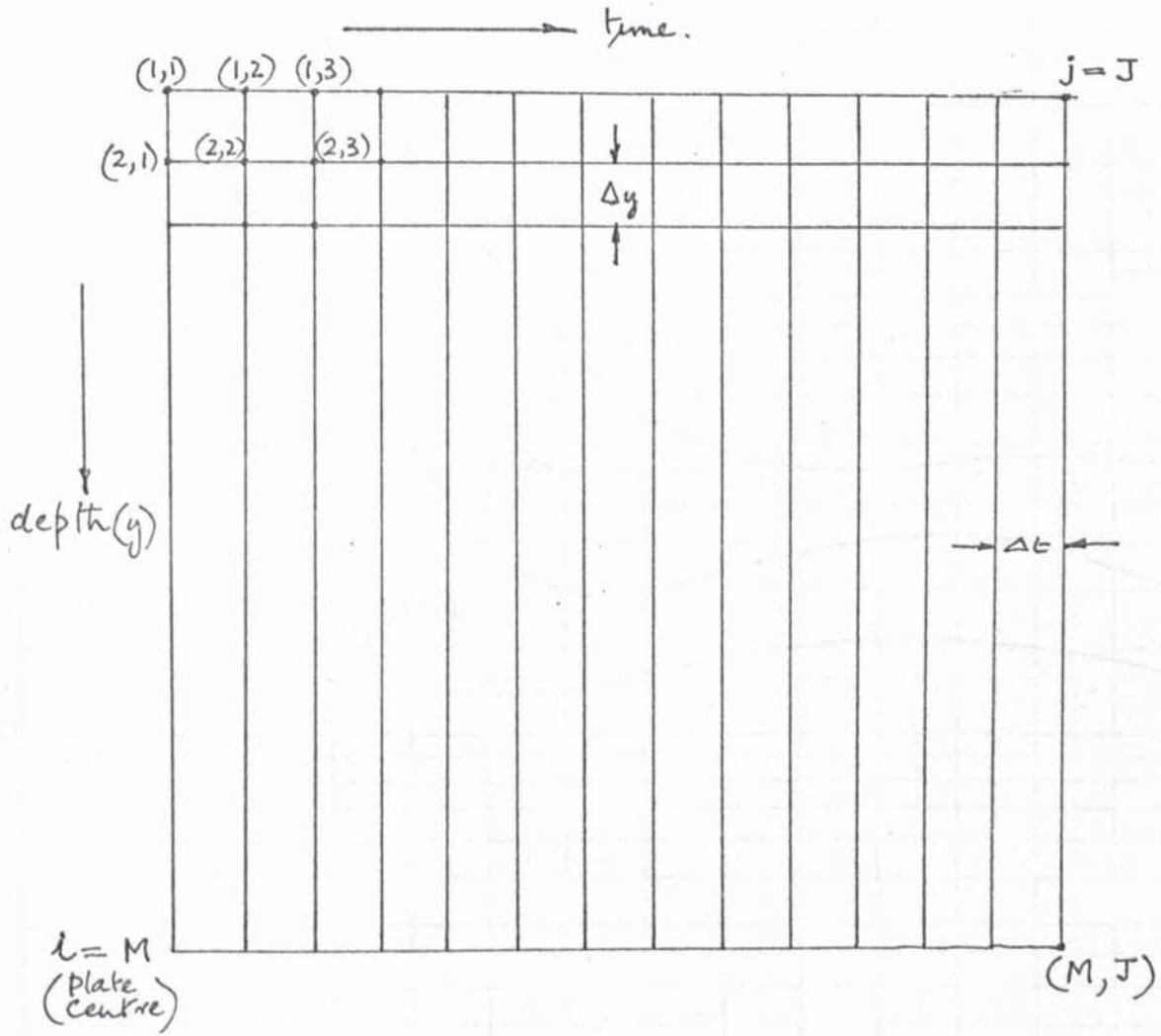
Fig. A4.2   Computational Grid for Finite Difference.
Solution of the Diffusion Equarion.
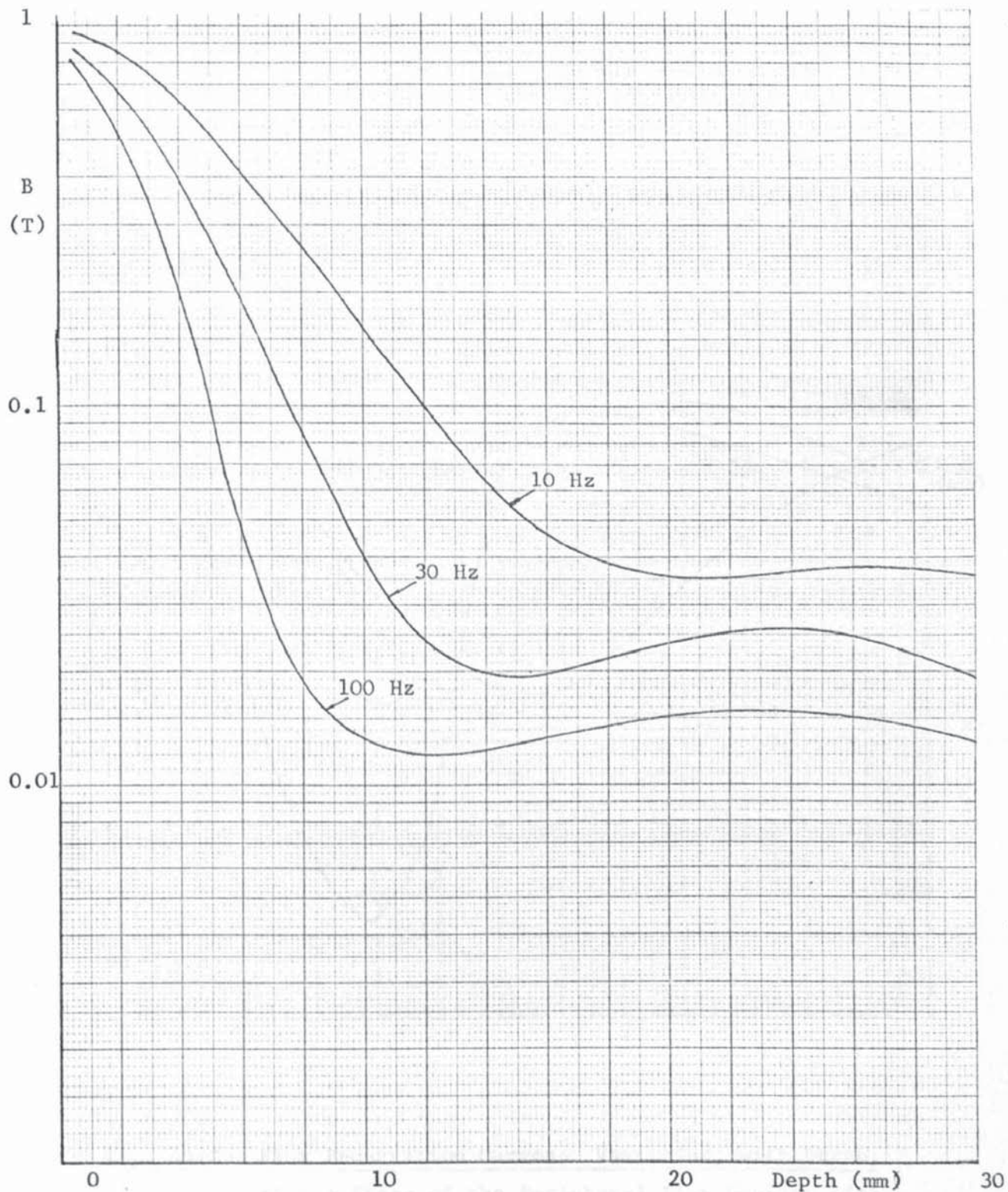
Fig. A5.1   Flux Penetration Curves: Variation of the Peak
Value of the Mean Flux Density with Depth into the Stator.

Constant Excitation: 7700 A/m
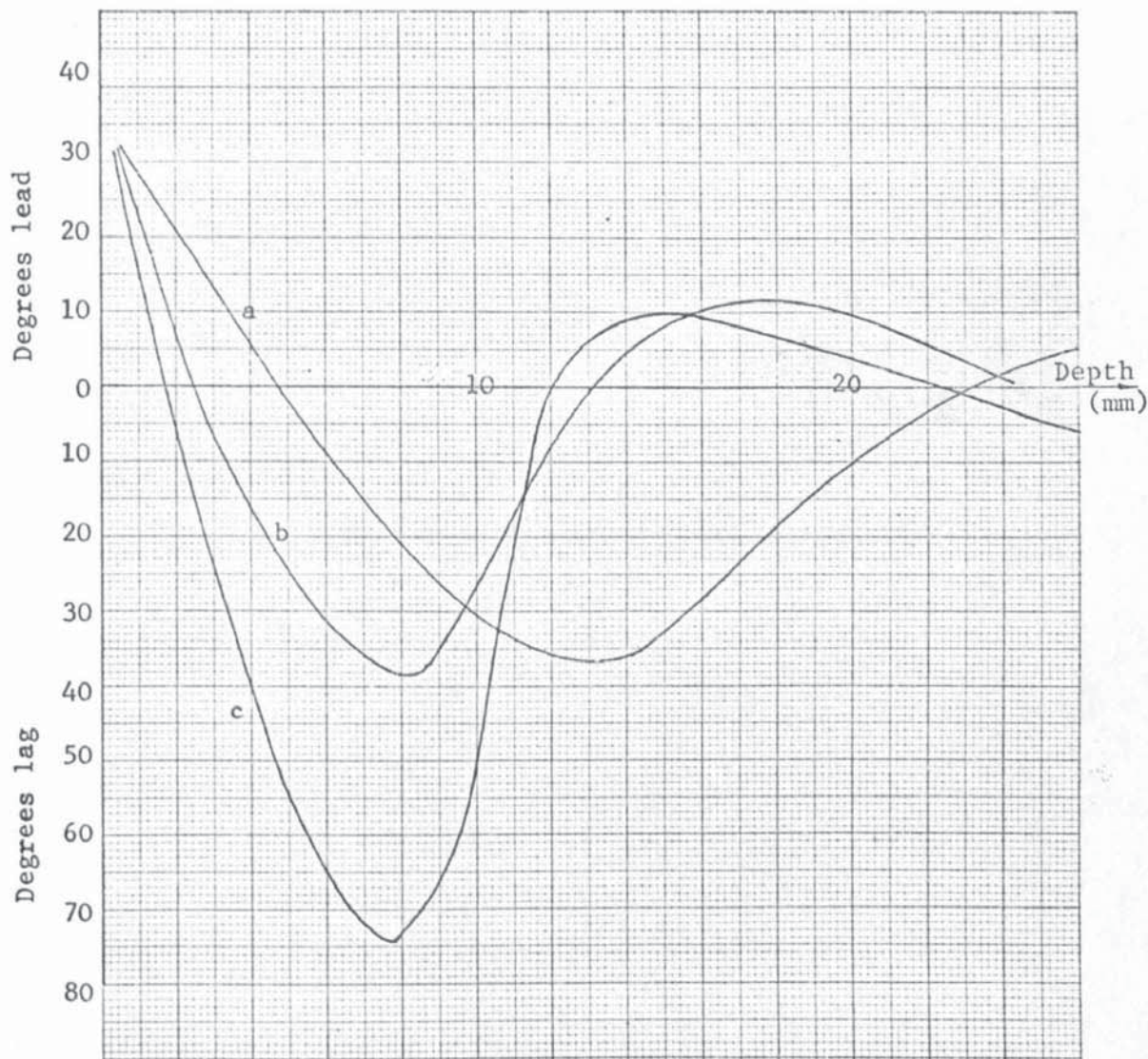
Fig. A5.2   Flux Penetration Curves: Variation, with Depth,
of the Phase of the Peripheral Flux Density with
respect to the Total Peripheral Flux.

Curve :	Excitation (A/m) :	Frequency (Hz)
a	7700	10
b	7700	50
c	23000	50
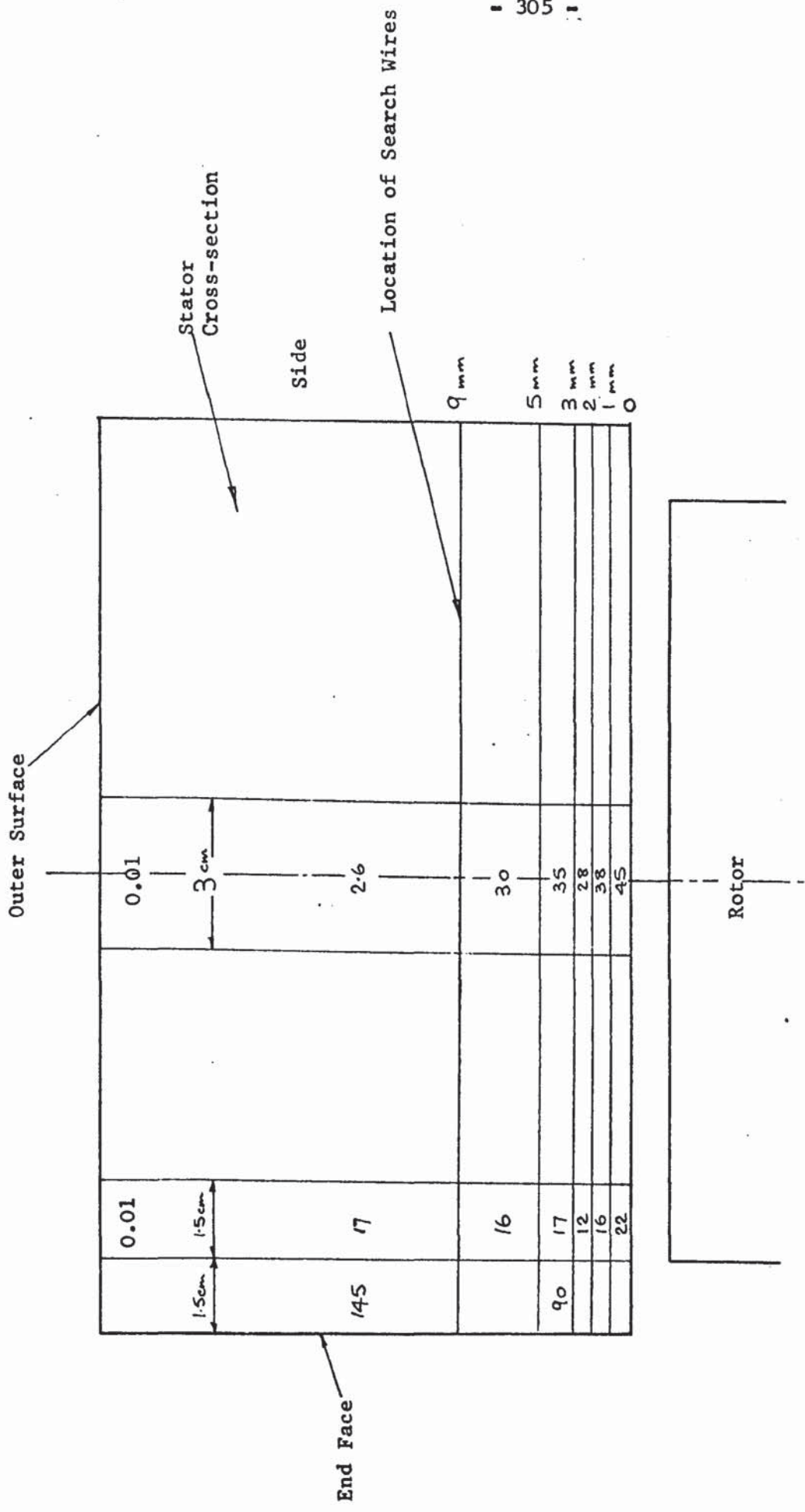
Fig. A5.4   Flux Distribution over Stator Cross-section.

Excitation : 7700 A/m;   frequency 50 Hz.

Values given are (mV), where 1 mV = 1.6 x 10⁻² T

PHOTOGRAPHIC

PLATES
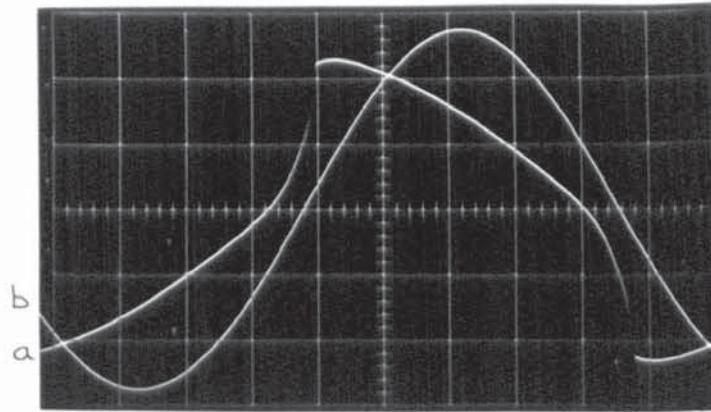
H$_R$ = 2850 A/m

(a) 2V/cm

Amplification: 300

(b) 0.05V/cm

2 msec/cm.
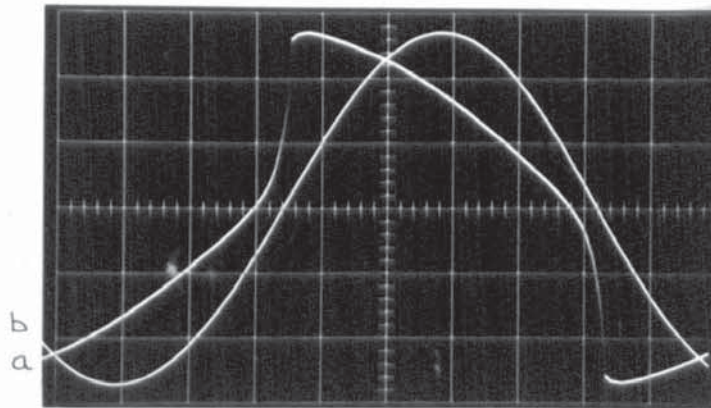
H$_R$ = 5900 A/m

(a) 2V/cm

Amplification: 250

(b) 0.05V/cm

2 msec/cm.
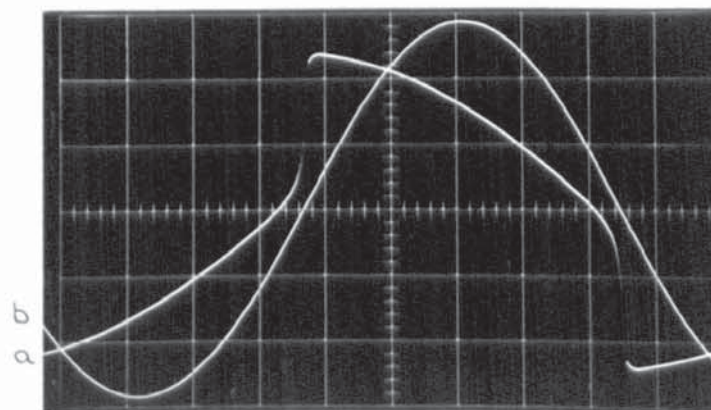
H$_R$ = 11800 A/m

(a) 2V/cm

Amplification: 150

(b) 0.05V/cm.

2 msec/cm.

PLATE 5.1   Oscillograms of Voltages proportional to the Current Density
at the Surface of the Bar (waveform (a)), and the Current
through the Bar (waveforms (b)).   (Section 5.4.2 and 5.4.3.2).
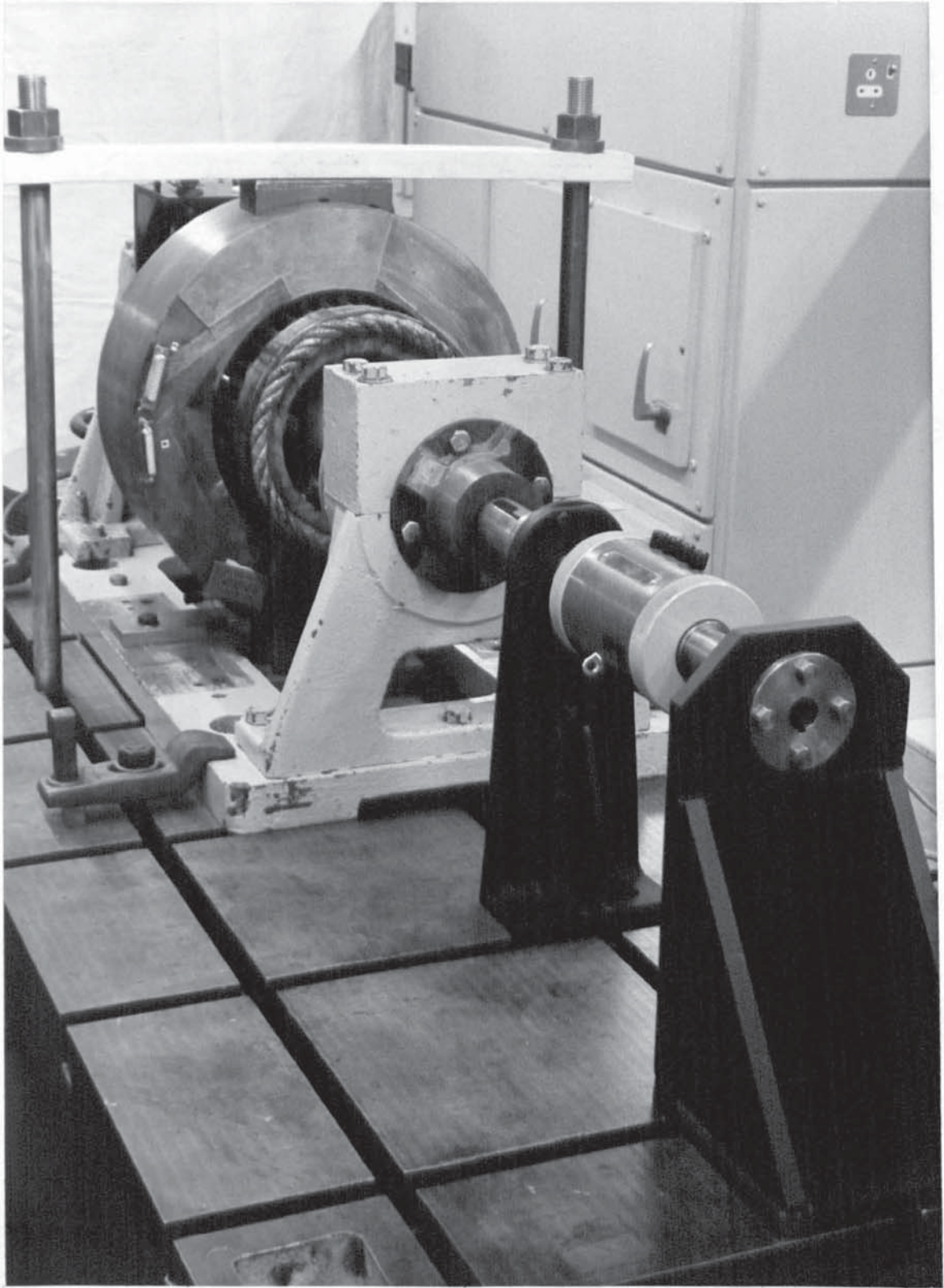
Plate 7.1   The Experimental Machine with the Continuous Stator, and Torque Transducer
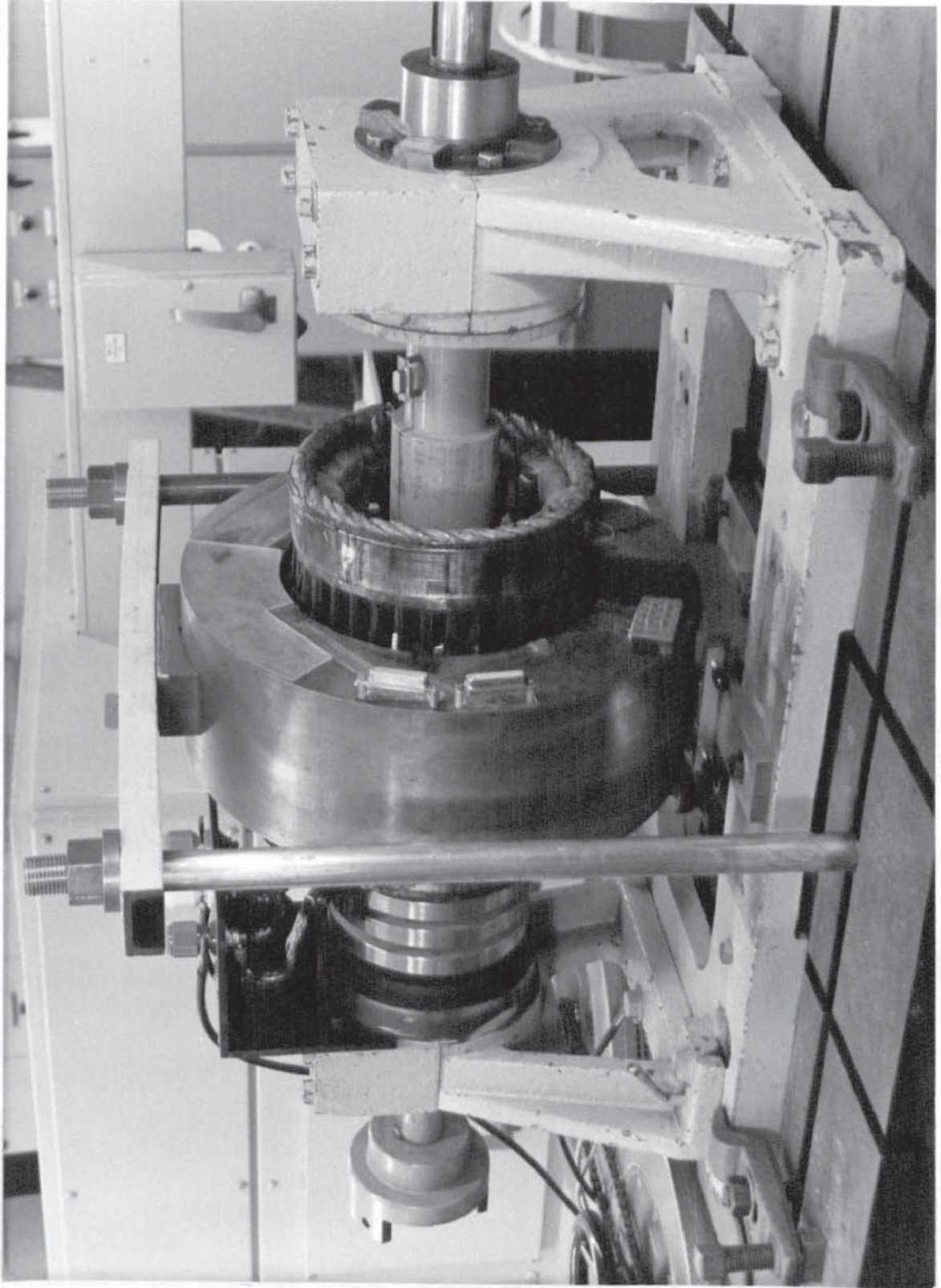
Plate 7.2   The Experimental Machine with the Continuous Stator
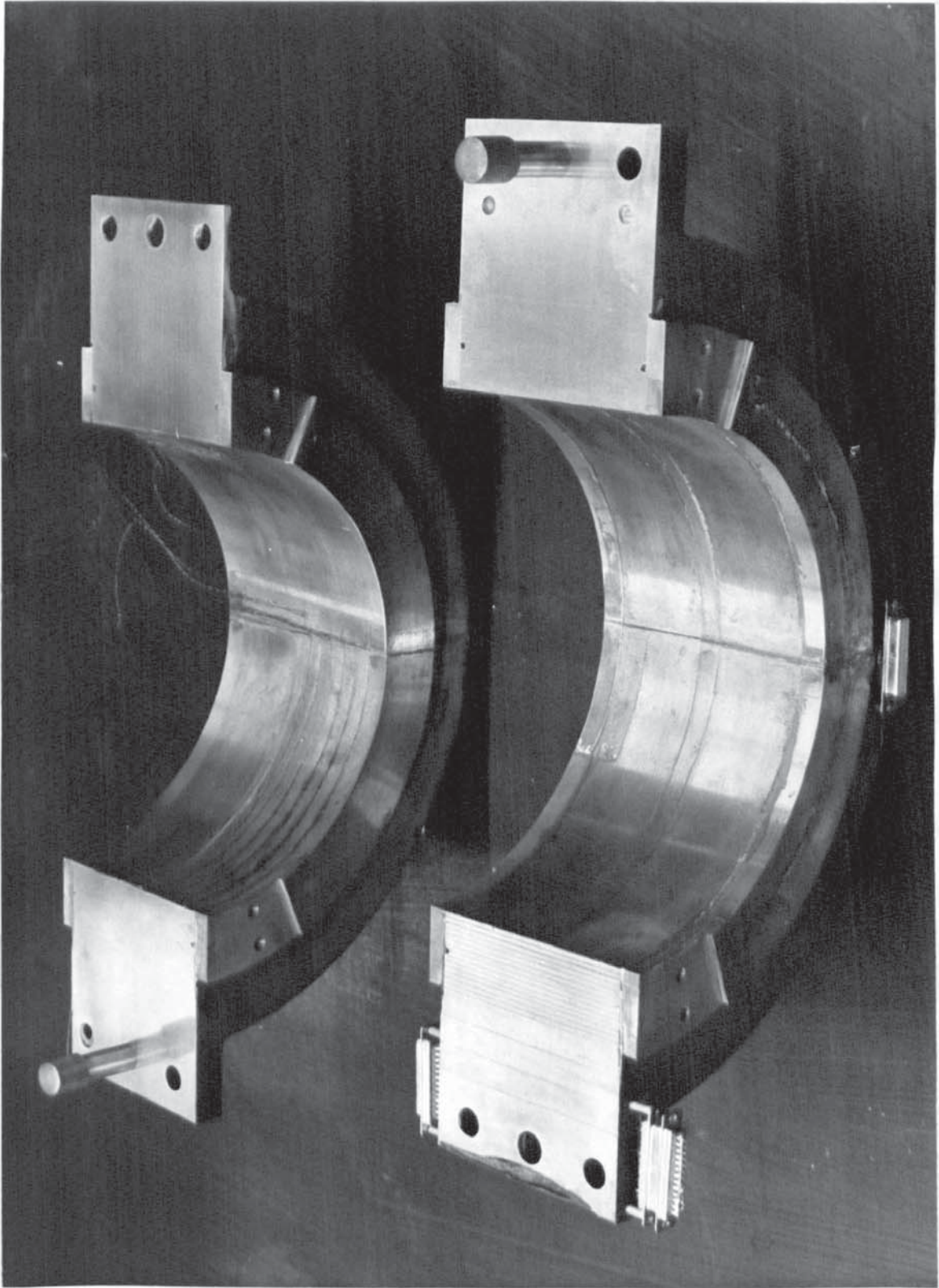
The End-Ring Stator
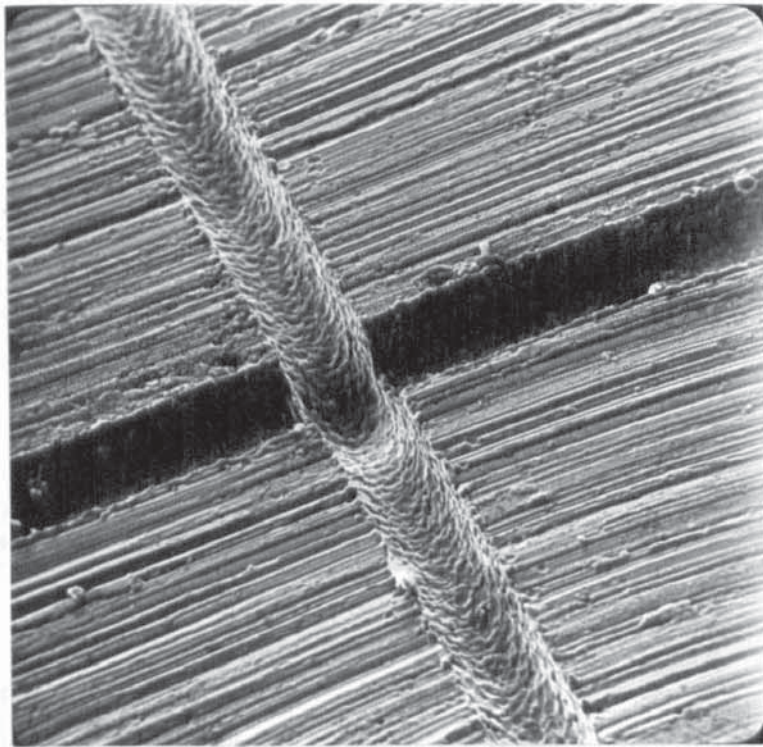
Plate 7.3

Plate 7.4   Grooves, Spark Machined (Magnified x 150)

Plate 7.5   ·   Weld, between a Nickel-Copper Wire (0.1 mm diameter)
                  and a Steel Surface (magnified x 260)

These photographs were taken with a Stereoscan Electron Microscope.
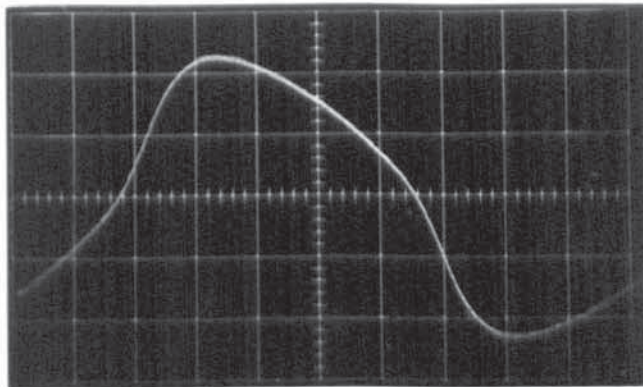
Voltages from a Current
Density Probe (Fig. 7.4)

(i) Excitation 4800 A/m
     0.2V/cm
     Amplification: 600
     (Fig. 5.5B)
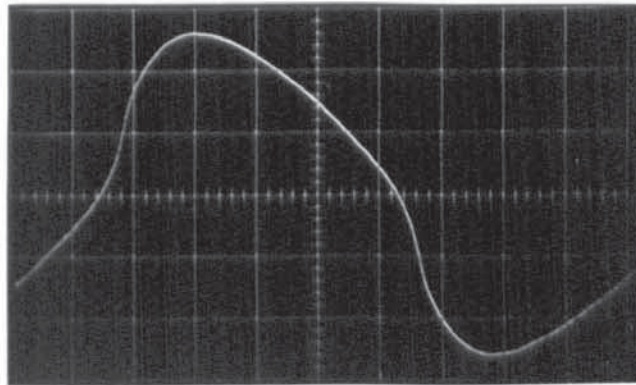
(ii) Excitation 19200 A/m
     0.2V/cm
     Amplification: 300

Voltages from a Full-Pitch
search coil (waveform (a)),
and proportional to
excitation, K, (waveform (b)).
        (Fig. 7.6)

(i) Excitation 4800 A/m
    (a) 2V/cm
    Amplification:300
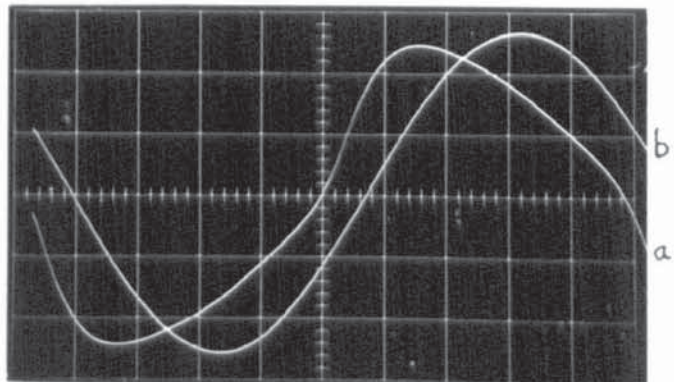
(ii) Excitation 19200 A/m
     (a) 2V/cm
     Amplification: 150
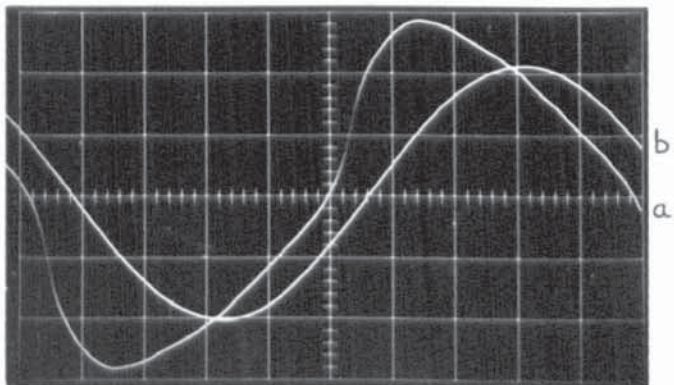
PLATE 8.1   Oscillograms of Voltages from Current Density Probes and Full-
             Pitch Search Coils on the End Ring Stator.

             Frequency in all cases: 50 Hz.
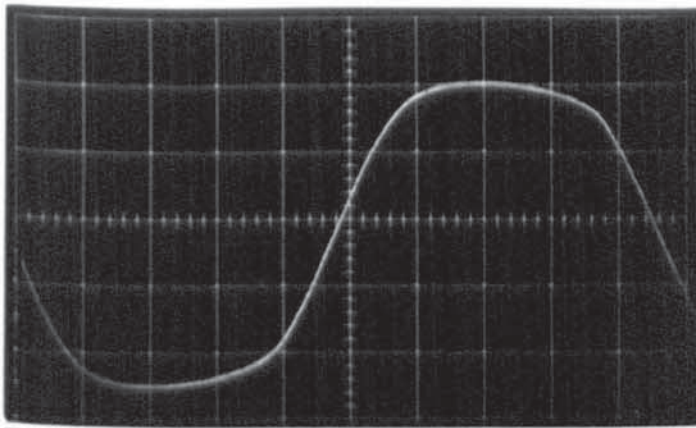
Search Coil (1) :
Mean depth: 0.475 mm,
Fundamental amplitude
$\hat{=}$ 2.46 T
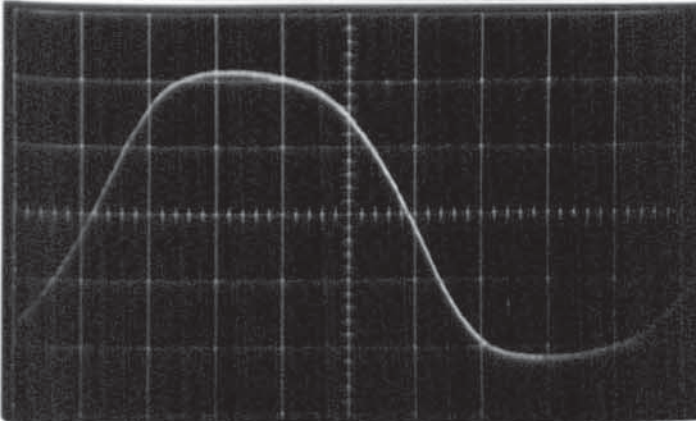
Search Coil (5) :
Mean depth: 5.1 mm,
Fundamental amplitude
$\hat{=}$ 2.09 T
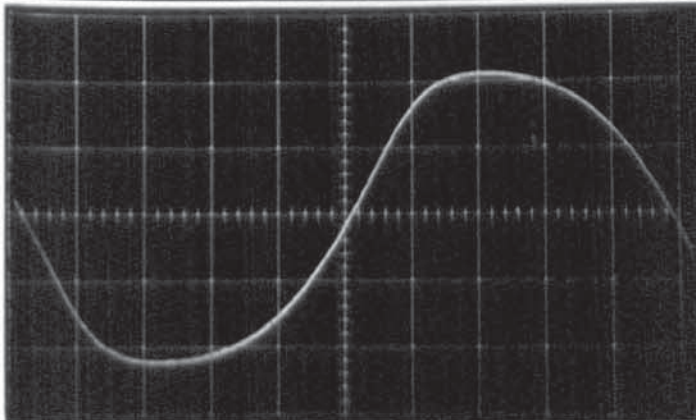
Search Coil (6) :
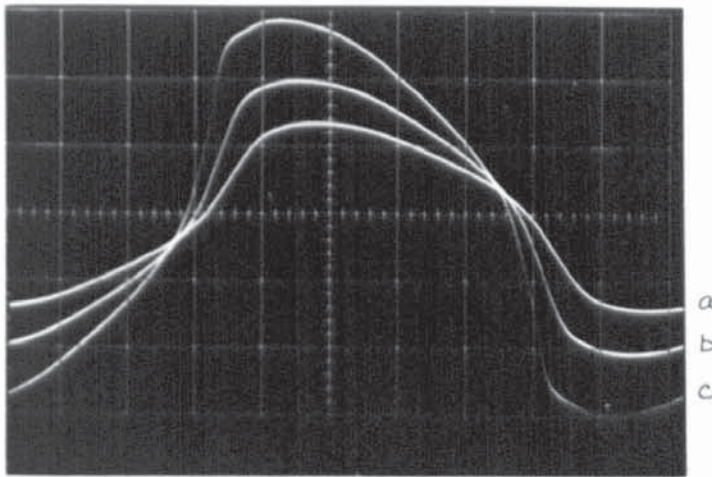Mean depth: 6.33 mm,
Fundamental amplitude
$\hat{=}$ 1.98 T
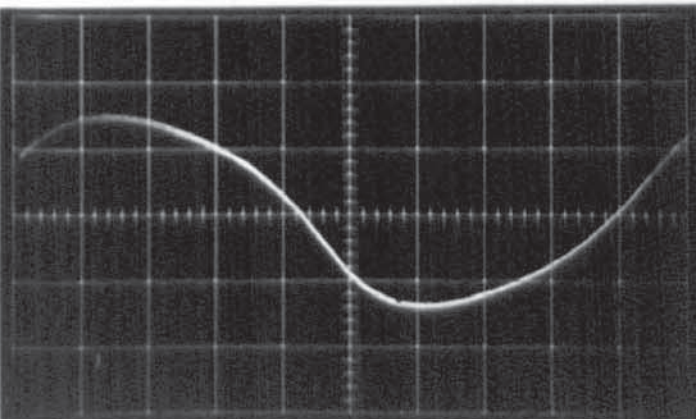
Search Coil (8) :
Mean depth: 9.95 mm,
Fundamental amplitude
$\hat{=}$ 0.94 T

PLATE 8.2   Oscillograms of Integrated Voltages from the Search Coils
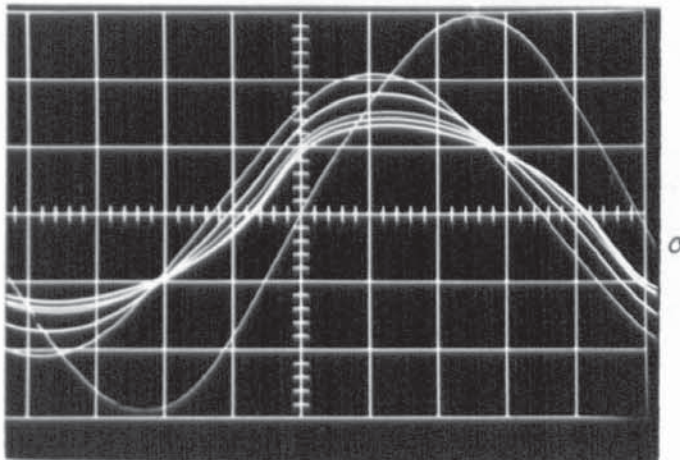($\propto$ Flux) in the Plate.   Excitation: 19200 A/m, Frequency 2 Hz.

Search coils numbered from the surface — see Fig. 7.4.
Circuit used: Fig. 5.5, amplification variable.

0.5V/cm

2 msec/cm

PLATE 10.1a   Oscillogram of Voltages from a Full-pitch Search Coil ($\propto B_y$)
               at the centre of the Continuous Stator (Fig. 7.7).

              Waveform : Excitation A/m
                (a)   4800
                (b)   9600
                (c)   19200

10 msec/cm.
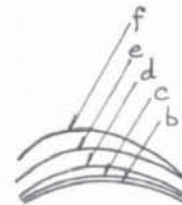Waveform (a), 0.02V/cm
Waveforms(b)-(f), 1V/cm
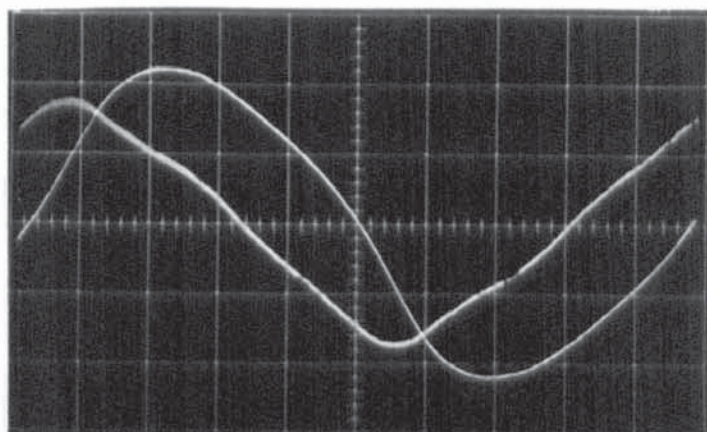Amplification: x 150

PLATE 10.1b   Oscillogram of Voltages from the Full-Pitch Search Coils
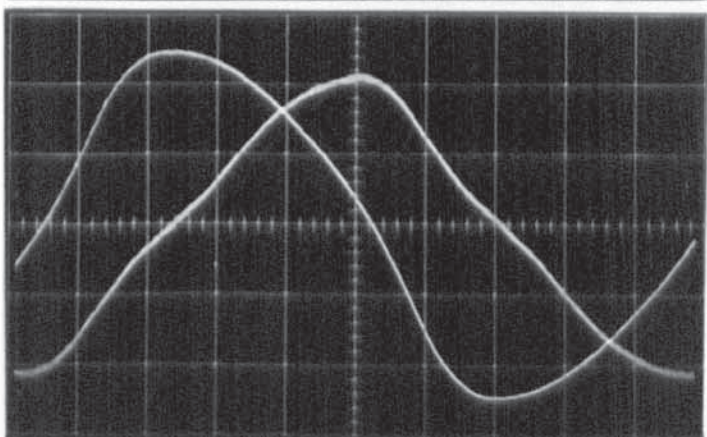   on the Surface of the Continuous Stator (Fig. 7.7).

               Excitation: 4800 A/m; frequency:10 Hz.

               Waveform:
                 (a) Voltage proportional to rotor mmf (Section 7.7.3)
                 (b) Coil 1
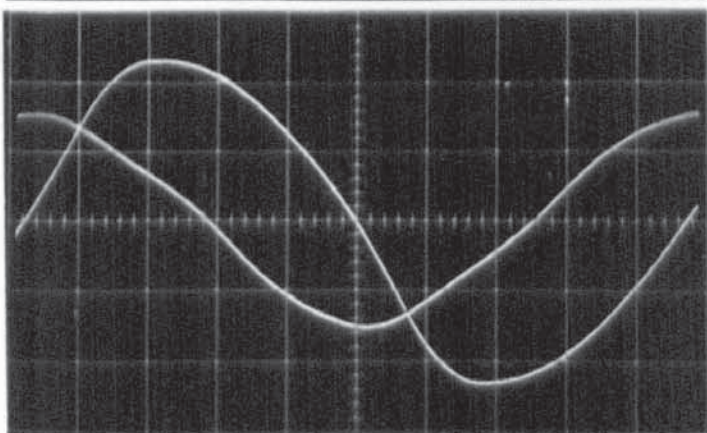   (c) Coil 3
                 (d) Coil 4 } Fig. 7.7.
                 (e) Coil 5
                 (f) Coil 6

a : probe Z3 ⎱
b : probe X1 ⎰ 2 cm
(Fig. 7.5)
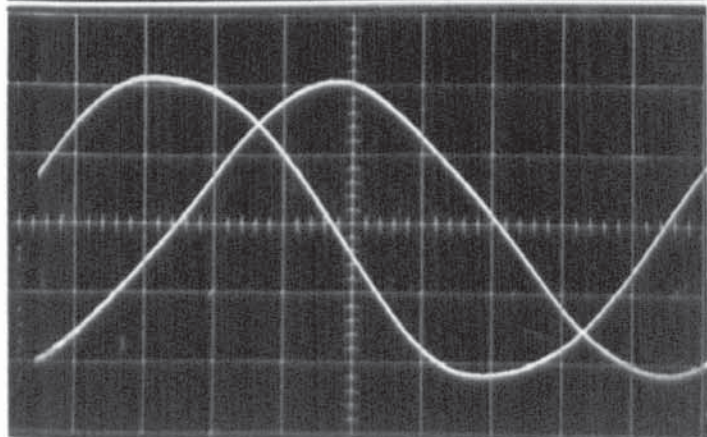
a : 1V/cm_ x 650
b : 0.5V/cm x 800

a : probe Z4 ⎱
b : probe X2 ⎰ 3 cm

a : 1V/cm ⎱
b : 0.5V/cm ⎰ x 800

a : probe Z5 ⎱
b : probe X3 ⎰ 4 cm

a : 1V/cm ⎱
b : 1V/cm ⎰ x 800

a : probe Z6 ⎱
b : probe X4 ⎰ 5 cm

a : 1V/cm ⎱
b : 1V/cm ⎰ x 900

PLATE 10.2b Oscillograms of Voltages from Current Density Probes
on the Continuous Stator (Fig. 7.5).

Excitation: 4800 A/m; frequency: 10 Hz.

2.34 : $\eta = \dfrac{q\mu_s}{\alpha} = \dfrac{2\pi}{\lambda} \cdot \dfrac{\mu_s}{\alpha}$

2.42 : $|\dot{M}| = \cosh qg \left[(\eta \tanh qg + 1)^2 + 1 \right]^{\frac{1}{2}}$

4.13 : $\dfrac{d}{dy} \left[\hat{H}_x^{1.5} \left(\dfrac{d^2 \hat{H}_x}{dy^2} \right)^{\frac{1}{2}} \right] = \dfrac{\omega a}{\rho} \cdot \hat{H}_x^{(b+1)}$

4.21 : $\mu_g = a \hat{H}_{xg}^{b-1}$

4.23 : $\alpha_g = \sqrt{\dfrac{\omega \mu_g}{2\rho}}$

4.24 : $\alpha_n = K_b \cdot \alpha_g$

4.25 : $K_b = \left[\dfrac{\sqrt{2}\ (1-b)^2}{(3+b)(1+b)^{\frac{1}{2}}} \right]^{\frac{1}{2}}$

4.26 : $\beta_n = \dfrac{2}{1-b}$

4.29 : $\gamma_n = \dfrac{\sqrt{2(1+b)}}{1-b}$

4.38 : $\begin{cases} R_n = \sqrt{\beta_n^2 + \gamma_n^2} \\ R_n = \dfrac{\sqrt{6+2b}}{1-b} \end{cases}$

4.40 : $\cos \phi_n = \beta_n / R_n$

4.41 : $\sin \phi_n = \gamma_n / R_n$

4.45 : $P_n = \dfrac{\hat{H}_{xg}^2}{2} \rho \cdot \beta_n \cdot \alpha_n$

4.50 : $K_p = \left[\dfrac{4\sqrt{2}}{(3+b)(1+b)^{\frac{1}{2}}} \right]^{\frac{1}{2}}$

4.58 : $\begin{cases} B_1 = AH_1^b \\ A \simeq a R_b \end{cases}$, for $H_1 > 5000 A/m$, $R_b \simeq 1.25$

6.14 : $\dot{S} = \dfrac{-q \cdot \rho \cdot \alpha_n}{\omega \mu_o} (\beta_n + j\gamma_n)$

6.16 : $K_s = \dfrac{q \cdot \rho \cdot \alpha_n}{\omega \mu_o} \cdot \tanh qg$

6.19 : $|\dot{H}_{xg}| = \dfrac{\hat{K}}{\cosh qg \left[1 + 2\sin\phi_n K_s R_n + K_s^2 R_n^2 \right]^{\frac{1}{2}}}$

6.27 : $P_n = \dfrac{|\dot{F}_c|^2 \mu_o \omega q \cos\phi_n}{2 \sinh qg \cosh qg} \cdot \Delta_n$

6.29 : $\Delta_n = \dfrac{1}{Q_n^{-1} + Q_n + 2\sin\phi_n}$

6.30 : $P_{nm} = \dfrac{|\dot{F}_c|^2 \mu_o \omega q \cos\phi_n}{4 (1+\sin\phi_n)\sinh qg \cosh qg}$

6.32 : $\dfrac{T_n}{T_{nm}} = \dfrac{2 + 2\sin\phi_n}{Q_n^{-1} + Q_n + 2\sin\phi_n}$

6.33 : $\omega_{nm} = \dfrac{q^{(b+1)} A \rho R_n^2 K_b^2 \sinh^2 qg \left[2 + 2\sin\phi_n \right]^{\frac{(1-b)}{2}}}{2 |\dot{F}_c|^{(1-b)} \mu_o^2 \cosh^{(b+1)} qg}$

6.34 : $N_\Delta = \dfrac{2 \mu_o^2 \omega |\dot{F}_c|^{(1-b)} \cosh^{(b-1)} qg}{q^{(b+1)} \rho R_n^2 K_b^2 A \tanh^2 qg}$

6.35 : $N_\Delta = \left(Q_n^{\frac{b+3}{2}} \cdot \Delta_n^{\frac{b-1}{2}} \right)$

6.36 : $Q_n = \dfrac{\omega}{\omega_{nm}}^{\frac{2}{3+b}} \cdot \dfrac{T_n}{T_{nm}}^{\frac{1-b}{3+b}}$

9.32 : $\dot{M}_h = \left[(\beta_h \cosh s_h g + \mu_{s_h} s_h \sinh s_h g) + j\gamma_h \cosh s_h g \right]$

9.35 : $R_L = \displaystyle\sum_{h=1,3}^{\infty} \dfrac{K_h^2 \cdot \gamma_h \cdot R_n |\dot{M}|^2 \cdot L \cdot \left[1 + \dfrac{w_h}{q^2} \right]}{2 K^2 |\dot{M}_h|^2 L_A}$

9.38 : $\dot{\phi}_{ha} = \dfrac{4}{q} \displaystyle\sum_{h=1,3}^{\infty} \dfrac{K_h^2 s_h^2 \mu_s}{w_h |\dot{M}_h|} \angle \dot{H}_{xgh} \sin \dfrac{\pi h L_A}{2L}$

9.42 : $\begin{cases} \mu_e = \dfrac{\mu_g}{\mu_o} K_e \angle 2\phi - 90 \\ K_e = R_b (K_b^2 R_n^2) / 2 \end{cases}$